

2011

Investigation of Ultrasonic Wave Scattering Effects using Computational Methods

Cara Ann Campbell Leckey
College of William & Mary - Arts & Sciences

Follow this and additional works at: <https://scholarworks.wm.edu/etd>



Part of the [Acoustics, Dynamics, and Controls Commons](#)

Recommended Citation

Campbell Leckey, Cara Ann, "Investigation of Ultrasonic Wave Scattering Effects using Computational Methods" (2011). *Dissertations, Theses, and Masters Projects*. Paper 1539623348.
<https://dx.doi.org/doi:10.21220/s2-e5vv-6092>

This Dissertation is brought to you for free and open access by the Theses, Dissertations, & Master Projects at W&M ScholarWorks. It has been accepted for inclusion in Dissertations, Theses, and Masters Projects by an authorized administrator of W&M ScholarWorks. For more information, please contact scholarworks@wm.edu.

Investigation of Ultrasonic Wave Scattering Effects
using Computational Methods

Cara Ann Campbell Leckey

Charleston, South Carolina

M.S. Physics, The College of William and Mary, 2008
B.S. Physics, University of Mary Washington, 2006

A Dissertation presented to the Graduate Faculty
of the College of William and Mary in Candidacy for the Degree of
Doctor of Philosophy

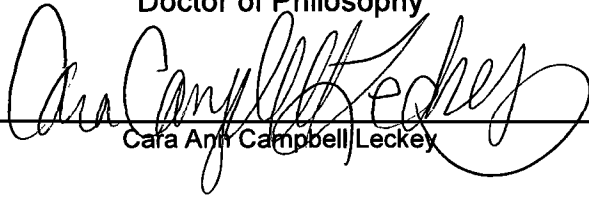
Department of Physics

The College of William and Mary
February, 2011

APPROVAL PAGE

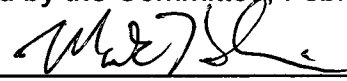
This Dissertation is submitted in partial fulfillment of
the requirements for the degree of

Doctor of Philosophy




Cara Ann Campbell Leckey


Approved by the Committee, February, 2011



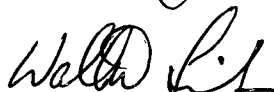
Committee Chair
Professor Mark Hinders, Applied Science
The College of William & Mary



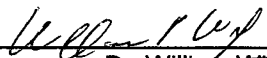
Professor William Kossler, Physics
The College of William & Mary



Chancellor Professor Eugene Tracy, Physics
The College of William & Mary



Dr. Walter Silva
NASA Langley Research Center



Dr. William Winfree
NASA Langley Research Center

ABSTRACT PAGE

Advances in computational power and expanded access to computing clusters has made mathematical modeling of complex wave effects possible. We have used multi-core and cluster computing to implement analytical and numerical models of ultrasonic wave scattering in fluid and solid media (acoustic and elastic waves). We begin by implementing complicated analytical equations that describe the force upon spheres immersed in inviscid and viscous fluids due to an incident plane wave. Two real-world applications of acoustic force upon spheres are investigated using the mathematical formulations: emboli removal from cardiopulmonary bypass circuits using traveling waves and the micromanipulation of algal cells with standing waves to aid in biomass processing for algae biofuels. We then move on to consider wave scattering situations where analytical models do not exist: scattering of acoustic waves from multiple scatterers in fluids and Lamb wave scattering in solids. We use a numerical method called finite integration technique (FIT) to simulate wave behavior in three dimensions. The 3D simulations provide insight into experimental results for situations where 2D simulations would not be sufficient. The diverse set of scattering situations explored in this work show the broad applicability of the underlying principles and the computational tools that we have developed. Overall, our work shows that the movement towards better availability of large computational resources is opening up new ways to investigate complicated physics phenomena.

Contents

List of Tables	iii
List of Figures	iv
Acknowledgments	viii
1 Introduction	1
2 Acoustic Radiation Force: Incident Plane Progressive Wave	10
2.1 Background	10
2.2 Radiation Force Derivation - Compressible sphere in a viscous fluid	13
2.3 Reduction to Inviscid Equations - Compressible sphere in an inviscid fluid	26
2.4 Viscous Model Code Verification and Convergence	33
2.5 Viscous Model Results	37
3 Emboli Removal from Extracorporeal Circuits	42
3.1 Emboli in Cardiac Surgery	42
3.2 Results for Emboli in Blood	44
3.2.1 Discussion of Results	47
3.3 Bulk Viscosity	49
4 Acoustic Radiation Force: Plane Stationary Wave	51
4.1 Compressible Sphere in a Viscous Fluid	51
4.2 Compressible Sphere in an Inviscid Fluid	54
4.3 Standing Wave Results	56
5 Acoustic Particle Separation for Microalgae Biofuels	71
5.1 Background	71
5.1.1 Acoustic Sorting	73
5.1.2 Separation Via Acoustically Enhanced Sedimentation	77
5.1.3 Acoustic Separation of Liquid-Liquid Mixtures	81
5.1.4 Acoustic Streaming	86
5.2 Microalgae Biofuels	87
5.3 Modeling Results	92
5.3.1 Discussion of Algae Modeling Results	97

5.4	3D Acoustic Finite Integration Simulations	99
5.5	AFIT Simulation Results	110
5.6	Discussion of AFIT Results	129
6	Ultrasonic Waves in Solid Media	131
6.1	3D Elastodynamic Wave Simulations	132
6.2	Stress-free Boundary Conditions	139
6.3	Parallel Processing	139
6.4	EFIT Code Verification	140
6.4.1	Analytical Solution Comparison	149
6.4.2	Discussion of Results	157
7	Lamb Wave Scattering	158
7.1	Guided Waves	158
7.2	EFIT Simulation Results	160
7.2.1	Discussion of Results	216
8	Conclusions and Future Work	217
8.1	Acoustic Force Models	217
8.2	Numerical Scattering Simulations	219
8.2.1	AFIT	219
8.2.2	EFIT	223
	Appendix A: Surface Tension Values	227
	Appendix B: Viscous Fluid Equations	228
	Appendix C: Elastic Scattering from a Sphere: Matrix Equations	235
	Bibliography	239

List of Tables

2.1	Notation for Acoustic Force Equations	13
2.2	Material Properties Used for Inviscid Model Comparison	33
2.3	n Dependent Contribution to Acoustic Radiation Force, Progressive Wave: for n values of 40 to 48 at $ka = 10$	36
2.4	n Dependent Contribution to Acoustic Radiation Force, Standing Wave: for n values of 40 to 48 at $ka = 10$ and $d = (1/8)\lambda$	37
2.5	Material Properties	41
3.1	CPB Material Properties Range	46
3.2	Percent Difference in Force due to Changes in Bulk Viscosity	50
5.1	Summary of Experimental Specifications in the Literature	84
5.2	Summary of Experimental Specifications in the Literature	85
5.3	Material Properties	93
7.1	Void Depth	165
8.1	Surface Tension	242
8.2	Surface Tension	242

List of Figures

2.1	Diagram for equation (2.15)	17
2.2	Comparison between our results and Hasegawa's results	32
2.3	Air in glycerol	34
2.4	Resonance peak positions for a blood droplet in air	35
2.5	Radiation force for various material combinations	39
2.6	Radiation force for various material combinations	40
3.1	Radiation force for an air bubble in blood	45
3.2	Radiation force for a lipid sphere in blood	46
3.3	Emboli removal chamber	48
4.1	Standing wave field.	52
4.2	Distance, d .	53
4.3	Polymethylmethacrylate sphere in water	56
4.4	Radiation force for various material combinations	59
4.5	Radiation force for various material combinations	60
4.6	Radiation force for various material combinations	61
4.7	Radiation force for various material combinations	62
4.8	Air bubble in glycerol.	63
4.9	Glycerol droplet in air.	64
4.10	Air bubble in water.	65
4.11	Water droplet in air.	66
4.12	Water droplet in glycerol.	67
4.13	Glycerol droplet in water.	68
4.14	Ethanol droplet in glycerol.	69
4.15	Glycerol droplet in ethanol.	70
5.1	Acoustic standing wave particle separation	73
5.2	Mandralis and Feke flow path diagram.	75
5.3	Particle separation using a microfluidic chip	76
5.4	Spengler and Jekel experimental setup.	79
5.5	<i>BioSep</i> ^(R) device(Applikon Biotechnology, Schiedam, Netherlands)	80
5.6	Srinivas experimental setup.	83
5.7	Acoustic streaming.	87

5.8	Raceway ponds	89
5.9	Photobioreactors	90
5.10	Ocean dead zone map	91
5.11	Algal cell in seawater.	94
5.12	Algal cell in seawater at $d = \lambda/8$	95
5.13	Algal cell in seawater.	96
5.14	Algal cell in freshwater at $d = \lambda/8$	97
5.15	Algal cell shapes.	98
5.16	AFIT spatial grid.	103
5.17	1D Virtual Topology.	105
5.18	Scattering example from AFIT.	105
5.19	Scattering from a fishing vest.	107
5.20	Scattering from a human torso.	108
5.21	Scattering from a C4 block.	109
5.22	Standing wave in AFIT simulation space.	111
5.23	Standing wave rounding error	113
5.24	Standing wave ripple	114
5.25	Standing wave field with scatterers.	116
5.26	A-line plot, standing wave field.	117
5.27	2.2×10^7 particles per mL.	118
5.28	2.2×10^7 rigid scatterers per mL evenly dispersed.	119
5.29	2.2×10^7 particles per mL.	120
5.30	Standing wave field with increased particle concentration.	122
5.31	Force on an algal cell.	123
5.32	A-line plot, standing wave field with algae.	125
5.33	Standing wave with random particle distribution.	126
5.34	Standing wave with algal cells distribution.	127
5.35	A-line result with increased algal cell concentration.	128
5.36	Force with increased algal cell concentration.	129
6.1	EFIT grid.	135
6.2	EFIT variable passing.	140
6.3	Steel block: drive function and transducer frequency.	143
6.4	Elastic wave scattering from an angled free surface.	144
6.5	Elastic wave in steel scattering from a brass angled boundary.	145
6.6	Elastic wave in steel scattering from a brass angled boundary.	145
6.7	Verification of analytical model implementation.	149
6.8	Incident wave and backscattering.	152
6.9	Gating results.	153
6.10	Scattering from an aluminum sphere in brass.	154
6.11	EFIT backscattering versus analytical result.	156
7.1	Guided waves.	159

7.2	EFIT result showing Lamb wave modes.	160
7.3	Experimental setup.	162
7.4	Photo of experimental setup.	163
7.5	Al 2024 group velocity dispersion curves.	163
7.6	Al 2024 phase velocity dispersion curves.	164
7.7	Plate with no flaw: EFIT result, top view	168
7.8	Plate with no flaw: EFIT result, thickness	169
7.9	Plate with no flaw: raw experimental data compared to EFIT	170
7.10	Spectrograms for plate with no flaw.	173
7.11	Transducer position 1.	174
7.12	10% material loss, transducer position 1: EFIT result	175
7.13	59% material loss, transducer position 1: top view	177
7.14	59% material loss, transducer position 1: top view of void region	178
7.15	59% material loss, transducer position 1: spectrogram plots	179
7.16	Experimental waveforms for 59% material loss: transducer position 1	180
7.17	85% material loss, transducer position 1: top view	183
7.18	85% material loss: spectrogram plots for transducer position 1	184
7.19	Experimental waveforms for 85% material loss: transducer position 1	185
7.20	2D EFIT thickness slices for $y=0.083$ m	187
7.21	2D EFIT thickness slices for $y=0.095$ m	188
7.22	Transducer position 2	189
7.23	Spectrogram ray path for transducer position 2	190
7.24	Plate with 68% material loss, transducer position 2	192
7.25	68% material loss, transducer position 2: spectrogram plots	193
7.26	Experimental waveforms for 68% material loss: transducer position 2	194
7.27	2D EFIT thickness slices, transducer position 2	196
7.28	Transducer position 3	198
7.29	59% material loss, transducer position 3: top view	199
7.30	59% material loss, transducer position 3: thickness	200
7.31	59% material loss, transducer position 3: spectrogram plots	201
7.32	59% material loss, transducer position 3: spectrogram plots	202
7.33	Experimental waveforms for 59% material loss: transducer position 3	204
7.34	Tomographic flaw reconstruction.	205
7.35	Ray paths for Figure 7.36.	206
7.36	59% material loss, transducer position 3: spectrograms for various y positions	207
7.37	59% material loss, transducer position 3: thickness plots for various y positions	208
7.38	Transducer position 4.	209
7.39	59% material loss, transducer position 4, EFIT results	211
7.40	59% material loss, transducer position 4, EFIT results	212
7.41	59% material loss, transducer position 4: spectrogram plots	213

7.42 Experimental waveforms for 59% material loss: transducer position 4 215

Acknowledgements

I would like to thank my advisor Dr. Mark Hinders for his guidance on this work. Thanks also to Dr. Ted Lynch, Dr. Kevin Rudd, Dr. Matt Rogge, Dr. Jill Bingham, and Chris Bording for helpful discussions, and also to Corey Miller. This work was performed in part using the Sciclone Computing Cluster at the College of William and Mary which was provided with the assistance of the National Science Foundation, the Virginia Port Authority, Sun Microsystems, and Virginia's Commonwealth Technology Research Fund. Thanks to Tom Crockett for assistance using Sciclone and to the Virginia Space Grant Consortium for partial funding.

Chapter 1

Introduction

Advances in computational power and expanded access to computing clusters has made mathematical modeling of complex 3-dimensional wave effects possible. In this work we use multi-core and cluster computing to implement analytical and numerical models of wave scattering. The scattering cases that we explore involve ultrasonic waves, which are sound waves with frequencies above 20 kHz . We investigate the scattering behavior of waves in fluid and solid media (acoustic and elastic waves). Acoustic waves are traditionally modeled as longitudinal waves, however, viscous fluids can support both longitudinal and shear wave motion, with the latter being strongly damped. Elastic media support the independent propagation of both longitudinal and shear waves, although scattering converts energy between them.

The first step in a mathematical description of scattering is to write the appropriate equations describing wave propagation. An educated decision must be made about the level of complexity that needs to be included in the equations. The partial differential equations that describe wave motion are usually linearized by dropping higher order terms. However, for some cases linearization is not appropriate. For example, in order to describe the acoustic force on a scatterer due to an incident

ultrasonic wave, nonlinear terms must be included since acoustic force is a nonlinear effect. Beyond the decision of what order of terms can be neglected, one must choose how much of the relevant physics should be included. For example, in some situations thermal effects may be small enough to be considered negligible. As we show in the first few chapters, the decision to include additional physics phenomena, such as viscosity, can greatly increase the complexity of the formulation. It does not take much to get to the point where the resulting equations become so complicated that they are not usable.

For acoustic waves in a fluid the basic equations are the Navier-Stokes equations and an equation of state:

$$\partial_t \rho + \partial_j(\rho v_j) = 0 , \tag{1.1}$$

$$\partial_t \rho v_i + \rho v_j \partial_j v_i = \partial_j \sigma_{ij} + f_i , \tag{1.2}$$

$$p = \rho c^2 , \tag{1.3}$$

where $\partial_t = \frac{\partial}{\partial t}$, $\partial_j = \frac{\partial}{\partial x_j}$, ρ is density, σ_{ij} is the stress tensor, v_i is velocity, and f_i is a source term, p is pressure, and c is the speed of sound. In these equations $i, j = 1, 2, 3$ and summation over repeated indices is assumed. Various assumptions are generally made to make these equations easier to solve for specific applications. Since sound waves are small fluctuations in the variables of the Navier-Stokes equations, velocity, pressure and density are usually linearized to first-order. This means that if we expand velocity as $v = v_0 + v^{(1)} + v^{(2)} + \dots$, all terms above $v^{(1)}$ are dropped ($v_0 = 0$ unless there is mean fluid flow). The assumption of negligible higher-order terms also usually results in dropping the nonlinear term on the left side of equation (1.2) [1]. The linearized version of the Navier-Stokes equations can be solved via a Helmholtz decomposition and separation of variables. If the fluid is assumed to be inviscid then the linear equations are simplified further since there will be no support

of transverse waves, resulting in velocity being defined in terms of only a scalar potential. For a small number of cases separation of variables and boundary/initial conditions can lead to a fairly straight-forward analytical solution which can be used to find scattering information such as reflection and transmission coefficients, scattering cross-section, etc. As mentioned above, in order to describe acoustic force nonlinear terms and higher order descriptions of variables in the Navier-Stokes equations cannot be ignored.

A further potential complication of the fluid equations shows up in the stress tensor in equation (1.2). In its full form the stress tensor includes terms that depend on shear and bulk viscosity (η and ξ) [2]:

$$\sigma_{ij} = -p\delta_{ij} + \eta \left(\partial_j v_i + \partial_i v_j - \frac{2}{3} \partial_k v_k \delta_{ij} \right) + \xi \partial_k v_k \delta_{ij} . \quad (1.4)$$

Viscosity is usually neglected under the assumption that the particle diameter is much smaller than the wavelength and much larger than the viscous boundary layer, $\delta = \sqrt{2\eta/(\rho\omega)}$ [3]. If viscous terms are included, as in chapter 2, the resulting analytical equations for describing the acoustic force on a sphere due to an incident plane wave (first published in the literature 15 years ago) become so complicated that until now they have not been implemented numerically. Thermal effects are also usually neglected. If heat conduction in the fluid is taken into account then additional equations must be included to account for energy dissipated as heat [4], [5]. Furthermore, including thermal effects leads to compressional and thermal waves that are coupled [6]. Complicated analytical solutions, as we show in the first few chapters of this dissertation, are only useful if they can be implemented to yield relevant information. It is crucial to use good scientific judgment when choosing/deriving the appropriate analytical model for a specific application.

For elastic waves in a solid the basic equations are:

$$\rho \partial_t^2 u_i = \partial_j T_{ij} + f_i \quad , \quad (1.5)$$

$$T_{ij} = C_{ijkl} \epsilon_{kl} \quad , \quad (1.6)$$

$$\epsilon_{kl} = \frac{1}{2} (\partial_l u_k + \partial_k u_l - \partial_k u_j \partial_l u_j) \quad (1.7)$$

where u_j is displacement, T_{ij} is the stress tensor, f_i is a source term, ϵ_{kl} is the strain tensor, and C_{ijkl} is the stiffness tensor [7]. First, it is important to point out that the elastic equations are inherently more complicated than the acoustic equations. In the acoustic case shear waves are only supported in a viscous fluid and are strongly damped. In elastodynamics there is no sensible basic assumption to remove the presence of shear wave propagation since it is the ability to resist shear that distinguishes a solid from a fluid. As with the acoustic equations, higher order terms can be dropped in the appropriate situations. The strain tensor is usually linearized by dropping the last term on the right side of equation (1.7). Our implementation of the elastodynamic equations in chapter 6 uses the linearized elastodynamic equations.

The elastodynamic equations can also get complicated when considering what level of physics needs to be included in the stress tensor for a specific application. For an isotropic media the stress tensor reduces to a simple expression, $T_{ij} = \lambda \epsilon_{kk} \delta_{ij} + 2\mu \epsilon_{ij}$, where longitudinal and transverse wave speeds are related to the Lamé parameters by

$$\begin{aligned} c_L &= \sqrt{(\lambda + 2\mu)/\rho}, \\ c_T &= \sqrt{\mu/\rho} \quad . \end{aligned} \quad (1.8)$$

As the level of physics included in the formulation increases, the equations quickly

become much more unwieldy. For anisotropic media the stiffness tensor is directional (wave speeds depend on direction), which leads to a far more complicated expression for the stress tensor. If viscoelastic effects are included in the formulation then attenuation is introduced through complex wavenumbers [8]. Another phenomenon that can be included in elastodynamic equations, if required by an application, is plasticity. Plasticity is a non-reversible deformation of a material that could, for example, be caused by the propagation of high amplitude waves due to an impact [9]. In this case the relationship between stress and strain is often strongly nonlinear and can depend on the rate of strain for a viscoplastic situation [10]. Even in isotropic media the interaction of shear and longitudinal waves with boundaries can lead to situations where an analytical solution cannot be derived. These examples reiterate the importance of making an educated choice of what physics to include in a model.

This work begins by considering analytical equations that describe the force upon spheres immersed in fluids due to an incident plane wave. We implement both inviscid and viscous fluid models that have appeared in the literature. Due to the complexity of the viscous equations we are the first, that we are aware of, to numerically implement them in order to explore their behavior. Two real-world applications of acoustic force upon spheres in a fluid are investigated using the formulations: emboli removal from cardiopulmonary bypass circuits using traveling waves and the micromanipulation of algal cells with standing waves to aid in biomass processing for algae biofuels. In the first application we find ultimately that a complicated viscous formulation is not necessary to describe the acoustic force. In the second application the models predict that viscosity has a significant practical effect on algal cell manipulation.

The extremely complicated analytical equations in chapter 2 are for the case of scattering from a sphere. Since a sphere is the simplest 3D shape, one can imagine how much more complicated the resulting analytical equations are for non-spherical

shapes. In fact, basic analytical scattering solutions for an incident plane wave via separation of variables is only possible in a few coordinate systems (spherical, cylindrical, prolate and oblate spheroidal, ellipsoidal, etc) [11]. Still, scattering from these basic shapes can lead to very complicated equations involving special functions that may be difficult to implement numerically. For example, scattering from a single spheroid requires computation of various spheroidal wave functions (analogous to spherical Bessel functions) [12], [13]. Furthermore, the orientation of a non-spherical scatterer relative to the incident wave must be accounted for in the formulation [12].

Describing multiple scattering adds more layers of complication. In fact, accounting for multiple scattering with analytical equations requires assumptions that are unrealistic for most applications. Common assumptions are that all scatterers are identical and are either a basic geometric shape (such as a sphere or infinitely long cylinder) or are much smaller than the sound wavelength so that geometric details can be ignored [14]. Furthermore, for random distributions of scatterers the assumption of very dilute concentration is usually made in order to calculate the total scattering as the summation of fields due to single scatterers [15]. If the constraints on shape, number, and distribution are relaxed it is necessary to use numerical methods to explore scattering behavior.

As stated above, in cases where an analytical solution cannot be found, numerical methods can be used to explore scattering behavior. Like the analytical methods, numerical methods also tend to make simplifications which drop higher order terms. Solutions to the (often linearized) partial differential equations are approximated over a small discrete volume (a single grid space), which can allow for the equations to be expressed as simple algebraic equations with boundary/initial conditions taken into account. The wave field throughout the entire larger volume (the entire grid) is calculated for every step in time. This method clearly requires a computer when

there are more than a few time and spatial steps.

The benefit of numerical methods is that they provide almost complete flexibility in the choice of scatterer shape, number, and distribution. Additionally, as long as boundaries are incorporated correctly, numerical methods can handle situations where the interaction of waves with boundaries would prevent an analytical solution. Another benefit of numerical methods is that no assumptions have to be made about the incident wave field. Essentially any source function can be incorporated into the models and can be applied over any section of the grid. Yet, care must be taken when discretizing the scatterer(s) and surrounding media. Numerical wave propagation models are often implemented in time domain and stability conditions must be met for both the spatial and time step sizes in order to correctly capture the behavior of the highest frequency waves (smallest wavelength). Furthermore, numerical methods can be extremely costly computationally, requiring large amounts of time to complete a single simulation on a multi-core computer or computing cluster. Current computing power can handle 3-dimensional scattering simulations, but the need for large simulation spaces in order to simulate waves in real materials/structures brings us up against the limits of available computational resources.

In later chapters of this work we consider wave scattering situations where exact analytical models do not exist: scattering of acoustic waves from multiple scatterers in fluids and Lamb wave scattering in solids. We use a numerical method, finite integration technique (FIT), to investigate these cases in three dimensions. We chose FIT over other numerical techniques such as Finite Difference Time Domain (FDTD) and Finite Element Methods (FEM) for several reasons. FIT differs from traditional FDTD approaches by naturally requiring staggered spatial and temporal grids which lead to better stability [16]. Boundary conditions are also easily incorporated into FIT [17]. Another important reason for choosing FIT is that the mathematical anal-

ysis is straight-forward and leads to equations that are easy to implement in any programming language (we have chosen C++). By developing our own code, as opposed to using commercial FEM or other software, we are able to maintain complete control over the equations and solving steps in the simulation. If, for example, we decide to add in viscoelastic effects we are able to make direct changes to the EFIT equations to incorporate the additional physics. Furthermore, we can use Message Passing Interface (MPI) to parallelize the code in an optimized fashion for efficient computation of scattering in large simulation spaces. Even with the use of customized parallel code, the three dimensional simulations are computationally expensive.

FIT multiple scattering simulations are applied as a continuation of investigations into algal cell manipulation using standing waves, and allow us to investigate scattering from numerous non-spherical algal cells. We find that the material properties and distribution of scatterers affect the standing wave field. Additionally, our results show that large increases in the number of scatterers can lead to significant changes in the standing wave field.

The elastic wave modeling focuses on Lamb wave propagation in thin plates. We use elastodynamic finite integration simulations to investigate frequency-thickness regimes where the dispersive behavior of Lamb wave modes leads to the existence of multiple modes that are closely grouped in phase and/or group velocity. Using 3-dimensional simulations we can investigate Lamb wave scattering in ways that are not possible analytically, experimentally, or with 2D models. We find that 2D modeling for flaw shapes such as the one explored in this work (a rounded rectangle) is not sufficient for describing Lamb wave behavior. The EFIT simulations expand our comprehension of complicated scattering situations and help us understand experimental data.

The topics explored in this work deliberately fall into a wide range of areas

(medicine, alternative energy, aerospace) and are connected by the same basic underlying principles which transcend any particular application. The specific physical situations were chosen as a diverse set of cases where modeling and simulation were needed to understand the complicated scattering physics involved. Modern computational resources have allowed us to push the envelope of modeling and simulation to gain insight into this complex wave behavior. We have purposefully constructed the computational tools so that as computer power improves they can become even more broadly applicable through the straight-forward addition of further physical phenomena. Overall, our work shows that the movement towards better availability of large computational resources is opening up new ways to investigate complicated physics.

Chapter 2

Acoustic Radiation Force: Incident Plane Progressive Wave

2.1 Background

Acoustic radiation force is the force exerted upon an object by an incident sound wave. Over the past century numerous authors have modeled acoustic radiation force. In this work we will analyze calculations for acoustic radiation force exerted by incident plane progressive and standing waves upon freely suspended compressible spheres immersed in fluids. We will discuss the derivation of the force of an incident wave on a sphere of radius a in a viscous fluid, as well as the simplified case of a sphere in an inviscid fluid.

In the literature there are two primary formulations for the acoustic radiation force upon spheres. One is an inviscid model that appeared in the literature as early as the 1930s in a paper by L.V. King [18]. King's work is focused on calculating the force of plane progressive and plane stationary waves upon a rigid sphere immersed in an inviscid fluid. Yosioka and Kawasima extended King's derivation to account for

sphere compressibility [19]. The inviscid formulation for incident plane progressive waves has been studied extensively by Takahi Hasegawa [20], [21]. The second model was developed by Alexander A. Doinikov in the 1990s and includes the effects of viscosity. Doinikov derived an equation for the force of plane progressive and standing waves upon a rigid or compressible sphere immersed in a viscous fluid. In this work we will outline Doinikov's derivation for a wave incident upon a compressible sphere. When the compressible-inviscid case is expanded to include viscosity, the complexity of the derivation increases in a number of ways: 1) a shear wavenumber must be included both outside and inside the sphere, 2) longitudinal and shear wavenumbers are now complex and depend on density, speed of sound, frequency, and viscosity, 3) viscous terms must be included in the stress tensor.

We will first outline the approach used by Doinikov to derive the radiation force from an incident progressive wave upon a freely suspended compressible sphere in a viscous fluid (with thermal effects neglected) [22]. Following Doinikov, we include terms up to second order and will not include thermal effects, which are small compared to the effects of viscosity [23]. There are no published plots made using Doinikov's equations for acoustic radiation force, that we are aware of, possibly due to the lack of computing power available at the time. We will then show how the viscous case reduces to the familiar inviscid case as described by Takahi Hasegawa [20], [21]. In a later chapter we will discuss stationary wave models.

We will discuss various applications of acoustic radiation force. In Chapter 3 we investigate the removal of emboli from extracorporeal circuits during cardiac surgery using plane progressive sound waves. During surgeries that require the use of cardiopulmonary bypass circuits, air bubbles and lipid emboli can enter the blood stream. If the emboli travel to the brain they can cause ischemia which may lead to brain damage. We investigate the possibility of removing these small emboli using acoustic

radiation force to push emboli out of the blood flow path [24].

In Chapter 5 we will discuss the use of acoustic radiation force from standing waves to sort microalgae based on its content. Microalgae is an environmentally friendly alternative source for biofuels. New harvesting methods and algal sorting could make the production of algae based biofuels more economical.

2.2 Radiation Force Derivation - Compressible sphere in a viscous fluid

Table 2.1: Notation for Acoustic Force Equations

a	radius of the spherical scatterer
c_1	longitudinal speed of sound in the surrounding medium
c_2	longitudinal speed of sound in the sphere medium
C_1	transverse speed of sound in the surrounding medium
C_2	transverse speed of sound in the sphere medium
δ	skin depth
Γ	scalar velocity potential of the second order velocity
Λ	vector velocity potential of the second order velocity
$h_n()$	spherical Hankel function of the first kind
$j_n()$	spherical Bessel function of the first kind
k_1	longitudinal wavenumber in the surrounding medium
k_2	longitudinal wavenumber in the sphere medium
K_1	transverse wavenumber in the surrounding medium
K_2	transverse wavenumber in the sphere medium
η_1	shear viscosity in the surrounding medium
η_2	shear viscosity in the sphere medium
$y_n()$	spherical Bessel function of the second kind (spherical Neumann)
ϕ	scalar velocity potential of the first order velocity
ψ	vector velocity potential of the first order velocity
ρ_1	density in the surrounding medium
ρ_2	density of the sphere medium
$\underline{\underline{\sigma}}$	stress tensor
σ_{ST}	surface tension
\vec{v}	fluid velocity
ω	angular velocity
ξ_1	bulk viscosity in the surrounding medium
ξ_2	bulk viscosity in the sphere medium

The general equation for the force of a sound wave upon on an object in a fluid is

$$\vec{F} = \oint \underline{\underline{\sigma}} \cdot \hat{n} dS , \quad (2.1)$$

where $\underline{\underline{\sigma}}$ is the stress tensor and the integral is taken over the surface area of the object, which we assume to be spherical. In its general form the stress tensor can be written as [11]

$$\underline{\underline{\sigma}} = -p\underline{\underline{I}} + \eta \left(\nabla \vec{v} + \vec{v} \nabla - \frac{2}{3} \underline{\underline{I}} \nabla \cdot \vec{v} \right) + \xi \underline{\underline{I}} \nabla \cdot \vec{v} , \quad (2.2)$$

where p is pressure, \vec{v} is fluid velocity, η is shear viscosity, ξ is bulk viscosity, and $\underline{\underline{I}}$ is the identity matrix.

In order to find expressions for velocity and pressure we will begin with the Navier-Stokes equations (the same equations listed in section 1),

$$\partial_t \rho + \nabla \cdot (\rho \vec{v}) = 0 , \quad (2.3)$$

$$\partial_t \vec{v} + (\vec{v} \cdot \nabla) \vec{v} = \frac{1}{\rho} \nabla \cdot \underline{\underline{\sigma}} . \quad (2.4)$$

The divergence of the stress tensor can be written as

$$\nabla \cdot \underline{\underline{\sigma}} = -\nabla p + \frac{1}{3} \eta \nabla (\nabla \cdot \vec{v}) + \xi \nabla (\nabla \cdot \vec{v}) + \eta \nabla^2 \vec{v} . \quad (2.5)$$

Using the identity

$$\nabla \times \nabla \times \vec{v} = \nabla (\nabla \cdot \vec{v}) - \nabla^2 \vec{v} , \quad (2.6)$$

we can rewrite equation (2.5) as:

$$\nabla \cdot \underline{\underline{\sigma}} = -\nabla p + \left(\frac{4}{3}\eta + \xi \right) \nabla(\nabla \cdot \vec{v}) - \eta \nabla \times \nabla \times \vec{v} . \quad (2.7)$$

We will now begin following Doinikov's derivation of force [22]. We expand ρ , \vec{v} , p , and $\underline{\underline{\sigma}}$ up to second order,

$$\begin{aligned} \rho &= \rho^{(0)} + \rho^{(1)} + \rho^{(2)} , \\ \vec{v} &= \vec{v}^{(1)} + \vec{v}^{(2)} , \\ \underline{\underline{\sigma}} &= \underline{\underline{\sigma}}^{(1)} + \underline{\underline{\sigma}}^{(2)} , \\ p &= p^{(1)} + p^{(2)} , \end{aligned} \quad (2.8)$$

in which $\rho^{(0)}$ is equilibrium density, and where the equilibrium fluid velocity and stress tensor are $\vec{v}^{(0)} = 0$ and $\underline{\underline{\sigma}}^{(0)} = 0$. Furthermore, we let the equilibrium gauge pressure equal zero, $p^{(0)} = 0$. The equation of state for the first order pressure is:

$$p^{(1)} = c^2 \rho^{(1)} , \quad (2.9)$$

where c is the speed of sound. Plugging (2.8) into equations (2.3) and (2.4) and neglecting higher order terms, we get a set of linearized first order equations and a set of second order equations.

$$\partial_t \rho_1^{(1)} = -\rho_1^{(0)} \nabla \cdot \vec{v}^{(1)} , \quad (2.10)$$

$$\rho_1^{(0)} \partial_t \vec{v}^{(1)} = \nabla \cdot \underline{\underline{\sigma}}^{(1)} , \quad (2.11)$$

$$\rho_1^{(0)} \nabla \cdot \langle \vec{v}^{(2)} \rangle = -\nabla \cdot \langle \rho_1^{(1)} \vec{v}^{(1)} \rangle , \quad (2.12)$$

$$\nabla \cdot \langle \underline{\underline{\sigma}}^{(2)} \rangle = \rho_1^{(0)} \langle (\vec{v}^{(1)} \cdot \nabla) \vec{v}^{(1)} + \vec{v}^{(1)} (\nabla \cdot \vec{v}^{(1)}) \rangle , \quad (2.13)$$

where $\langle \rangle$ denotes the time average of the quantity enclosed over one cycle. In these equations we have taken the time average of all second order terms. Additionally, the time average over one cycle of the change in time of any second order term equals zero because we are assuming negligible oscillations at second order. We will later use equations (2.10) - (2.13) to find velocity.

Returning to equation (2.1), we write the time averaged acoustic radiation force up to second order as

$$\vec{F} = \langle \int_{S(t)} \underline{\underline{\sigma}}^{(1)} \cdot \hat{n} dS \rangle + \int_{S_0} \langle \underline{\underline{\sigma}}^{(2)} \rangle \cdot \hat{n} dS , \quad (2.14)$$

where $S(t)$ is the sphere surface at time, t , and S_0 is the unperturbed sphere surface. The second order stress integral is taken over the unperturbed sphere surface because second order sphere oscillations are assumed to be negligible. Enclose the sphere surface, $S(t)$ by a stationary surface, S , and label the volume between the two surfaces as $\tau(t)$ (refer to Figure 2.1). Using the divergence theorem, the following relation for the first order force, $F^{(1)}$, is then valid:

$$\langle \int_{S(t)} \underline{\underline{\sigma}}^{(1)} \cdot \hat{n} dS \rangle = \langle \int_S \underline{\underline{\sigma}}^{(1)} \cdot \hat{n} dS \rangle - \langle \int_{\tau(t)} \nabla \cdot \underline{\underline{\sigma}}^{(1)} d\tau \rangle . \quad (2.15)$$

The relationship above simply says that the divergence over the volume τ is equal to the difference in flux through the surfaces enclosing τ .

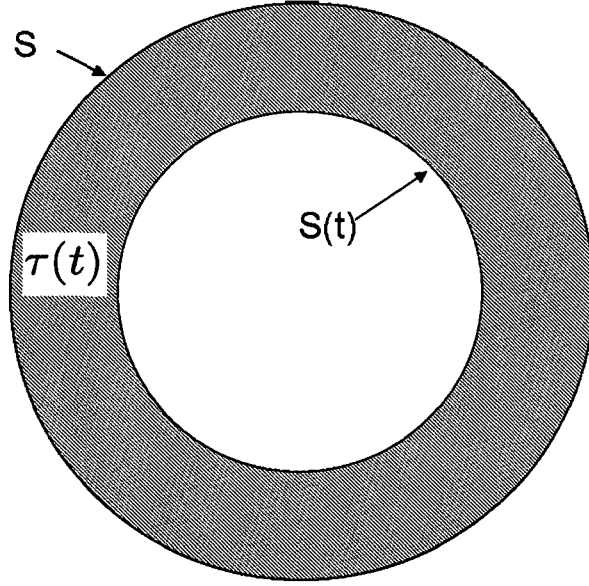


Figure 2.1: Diagram showing surfaces and volume related to equation (2.15).

The average stress over a sound cycle on the stationary surface, S , is equal to zero because the stress over the first half of the sound cycle is opposite in sign from the stress over the second half of the cycle. Therefore, the first term on the right side of (2.15) disappears, and

$$\left\langle \int_{S(t)} \underline{\underline{\sigma}}^{(1)} \cdot \hat{n} dS \right\rangle = - \left\langle \int_{\tau(t)} \nabla \cdot \underline{\underline{\sigma}}^{(1)} d\tau \right\rangle . \quad (2.16)$$

Using (2.11) and the definition of the convective derivative,

$$\frac{d}{dt} = \frac{\partial}{\partial t} + \vec{v} \cdot \nabla , \quad (2.17)$$

we can write the term on the right side of (2.16) as [11]

$$-\rho_1^{(0)} \left\langle \int_{\tau(t)} \partial_t \vec{v}^{(1)} d\tau \right\rangle = -\rho_1^{(0)} \left\langle d_t \int_{\tau(t)} \vec{v}^{(1)} d\tau \right\rangle + \rho_1^{(0)} \left\langle \int_{\tau(t)} (\vec{v}^{(1)} \cdot \nabla) \vec{v}^{(1)} d\tau \right\rangle . \quad (2.18)$$

Equation (2.18) can be written as a surface integral over the unperturbed sphere surface. Using the divergence theorem, equation (2.3), and the relations [25]

$$\rho(\vec{v} \cdot \nabla) \vec{v} = \nabla \cdot (\rho \vec{v} \vec{v}) - \vec{v} \nabla \cdot (\rho \vec{v}) , \quad (2.19)$$

$$\frac{\partial(\rho \vec{v})}{\partial t} = \rho \frac{\partial \vec{v}}{\partial t} + \vec{v} \frac{\partial \rho}{\partial t} , \quad (2.20)$$

we can write the equation

$$\begin{aligned} \rho_1^{(0)} \left\langle \frac{d}{dt} \int_{\tau(t)} \vec{v}^{(1)} d\tau \right\rangle &= \rho_1^{(0)} \left\langle \int_{\tau(t)} \partial_t \vec{v}^{(1)} d\tau \right\rangle + \rho_1^{(0)} \left\langle \int_{S_0} (\vec{v}^{(1)} \vec{v}^{(1)}) \hat{n} \cdot dS \right\rangle \\ &\quad - \rho_1^{(0)} \left\langle \int_{S(t)} (\vec{v}^{(1)} \vec{v}^{(1)}) \cdot \hat{n} dS \right\rangle . \end{aligned} \quad (2.21)$$

The left side of (2.21) and the second term on the right hand side equal to zero since each term for the first half of the sound cycle is opposite in sign from that term for the second half of the cycle. In addition,

$$\rho_1^{(0)} \left\langle \int_{S(t)} (\vec{v}^{(1)} \vec{v}^{(1)}) \cdot \hat{n} dS \right\rangle = \rho_1^{(0)} \int_{S_0} \langle \vec{v}^{(1)} \vec{v}^{(1)} \rangle \cdot \hat{n} dS , \quad (2.22)$$

because the average over one sound cycle of the time harmonic changes over the surface disappear, leaving us with the average of the argument integrated over the unperturbed sphere surface. Therefore, we are left with the relation

$$-\rho_1^{(0)} \left\langle \int_{\tau(t)} \partial_t \vec{v}^{(1)} d\tau \right\rangle = -\rho_1^{(0)} \int_{S_0} \langle \vec{v}^{(1)} \vec{v}^{(1)} \rangle \cdot \hat{n} dS . \quad (2.23)$$

Plugging this result into (2.11) and (2.16), the force can then be expressed as

$$\vec{F} = \int_{S_0} \langle \underline{\underline{\sigma}}^{(2)} \cdot \hat{n} - \rho_1^{(0)} \vec{v}^{(1)} (\vec{v}^{(1)} \cdot \hat{n}) \rangle dS . \quad (2.24)$$

To find a complete expression for force we will use equations (2.10) - (2.13) to solve for the second order stress and first order velocity in equation (2.24). The second order velocity that will appear in the second order stress tensor can be written as a second order velocity in the absence of the sphere plus a streaming velocity due to the sphere boundary

$$\vec{v}^{(2)} = \vec{v}_0^{(2)} + \vec{v}_s^{(2)} . \quad (2.25)$$

Acoustic streaming effects are created due to the presence of the viscous boundary layer of the sphere, which absorbs sound. Acoustic streaming will be discussed in more detail in section 5.1.4.

Via Clebsch's theorem we can write the first order velocity and streaming velocity in terms of scalar and vector potentials

$$\vec{v}^{(1)} = \nabla\phi + \nabla \times \vec{\psi} , \quad (2.26)$$

$$\vec{v}_s^{(2)} = \nabla\Gamma + \nabla \times \vec{\Lambda} , \quad (2.27)$$

where ϕ is the first order scalar velocity potential, $\vec{\psi}$ is the first order vector velocity potential, Γ is the second order scalar velocity potential and $\vec{\Lambda}$ is the second order vector velocity potential. Throughout this paper we will assume that ϕ , ψ , Γ , and Λ have harmonic time dependence described by $e^{-i\omega t}$, which will not be written explicitly.

First we will solve for the first order velocity. Using (2.26), the first order equations

(2.10) and (2.11) can be reduced to the form

$$\begin{aligned}(\nabla^2 + k_1^2)\phi &= 0 \quad , \\ (\nabla^2 + K_1^2)\vec{\psi} &= 0 \quad .\end{aligned}\tag{2.28}$$

The longitudinal and transverse wavenumbers are

$$k_1 = \frac{\omega}{c_1} \left[1 - \frac{i\omega}{\rho_1^{(0)}c_1^2} \left(\frac{4\eta}{3} + \xi \right) \right]^{-\frac{1}{2}} \quad ,\tag{2.29}$$

$$K_1 = (1 + i) \sqrt{\frac{\omega\rho_1^{(0)}}{2\eta}} \quad .$$

A plane progressive wave solution satisfies (2.28). Using Bauer's formula we can write an expression for a plane progressive wave as [26]

$$\begin{aligned}\phi &= e^{ikz} = e^{ikr \cos \theta} \\ &= \sum_{n=0}^{\infty} i^n (2n + 1) j_n(kr) P_n(\cos \theta) \quad ,\end{aligned}\tag{2.30}$$

where $j_n(kr)$ is the spherical Bessel function of the 1st kind and $P_n(\cos \theta)$ is a Legendre

polynomial of order n . The scalar and vector potentials can therefore be written as

$$\begin{aligned}
\phi_{inc} &= \sum_{n=0}^{\infty} i^n (2n+1) j_n(k_1 r) P_n(\cos \theta) \ , \\
\phi_{scat} &= \sum_{n=0}^{\infty} i^n (2n+1) \alpha_n h_n(k_1 r) P_n(\cos \theta) \ , \\
\phi_{trans} &= \sum_{n=0}^{\infty} i^n (2n+1) \tilde{\alpha}_n j_n(k_2 r) P_n(\cos \theta) \ , \\
\psi_{scat} &= \sum_{n=1}^{\infty} i^n (2n+1) \beta_n h_n(K_1 r) P_n^{(1)}(\cos \theta) \ , \\
\psi_{trans} &= \sum_{n=1}^{\infty} i^n (2n+1) \tilde{\beta}_n j_n(K_2 r) P_n^{(1)}(\cos \theta) \ ,
\end{aligned} \tag{2.31}$$

in which $h_n(kr)$ is the spherical Hankel function of the first kind, $P_n^{(1)}(\cos \theta)$ is an Associated Legendre function with $m = 1$, α_n , $\tilde{\alpha}_n$, β_n and $\tilde{\beta}_n$ are coefficients that can be determined using boundary conditions. Only α_n and β_n are needed to find radiation force because the force integral is over the outer surface of the sphere and only incident and scattered fields exist in the exterior region. Note that we are assuming the incident amplitude equals 1. In equation (2.31) the spherical Hankel function, $h_n(kr)$, is used outside the sphere because it satisfies Sommerfeld's radiation conditions. Note that inside the sphere $j_n(kr)$ is used instead of $h_n(kr)$ because the spherical Neumann function, $y_n(kr)$, is singular at the origin (where $h_n(kr) = j_n(kr) + i y_n(kr)$).

Note that, we can now use equation (2.10) to write (2.9) as

$$p^{(1)} = \frac{i \rho_1^{(0)} c^2 k_1^2}{\omega} \phi. \tag{2.32}$$

As mentioned above, only α_n and β_n are needed to find force, and aside from finding these, we now have a complete expression for the first order force. α_n and β_n are listed in the appendix and can be found using the following boundary conditions:

- 1) continuity of normal stress across the boundary
- 2) continuity of shear stress across the boundary
- 3) continuity of normal displacement across the boundary
- 4) continuity of tangential displacement across the boundary

Next we must solve for the second order stress tensor using the nonlinear equations (2.12) - (2.13). This time we cannot simply show that the equations are satisfied by a plane wave solution. Plugging equation (2.27) into equation (2.12), and using the fact that the divergence of a curl is always zero, (2.12) can be written as

$$\nabla^2 \Gamma = -\frac{1}{\rho_1^{(0)}} \nabla \cdot \langle \rho_1^{(1)} \vec{v}^{(1)} \rangle . \quad (2.33)$$

In addition, plugging equations (2.27) and (2.7) into (2.13) and taking the curl of both sides, we get

$$\nabla^2 \nabla^2 \vec{\Lambda} = -\frac{\rho_1^{(0)}}{\eta} (\nabla \times \langle \vec{v}^{(1)} (\nabla \cdot \vec{v}^{(1)}) + (\vec{v}^{(1)} \cdot \nabla) \vec{v}^{(1)} \rangle) . \quad (2.34)$$

We will solve for Γ and Λ using equations (2.33) and (2.34). First we will find Γ . Any function, $f(x)$ on the interval -1 to 1 can be expanded using a Fourier-Legendre series [11], [27]:

$$f(x) = \sum_{n=0}^{\infty} A_n P_n(x) . \quad (2.35)$$

In which

$$A_n = \frac{2n+1}{2} \int_{-1}^1 f(x) P_n(x) dx . \quad (2.36)$$

Thus, following Doinikov, we can write the right hand side of equation (2.33) in terms of Legendre functions as [22]

$$\frac{1}{\rho_1^{(0)}} \nabla \cdot \langle \rho_1^{(1)} \vec{v}^{(1)} \rangle = \sum_{n=0}^{\infty} \frac{(2n+1)}{a^2} \mu_n \left(\frac{r}{a} \right) P_n(\cos \theta) , \quad (2.37)$$

where

$$\mu_n \left(\frac{r}{a} \right) = \frac{a^2}{2\rho_1^{(0)}} \int_0^\pi \nabla \cdot \langle \rho_1^{(1)} \vec{v}^{(1)} \rangle P_n(\cos \theta) \sin \theta d\theta . \quad (2.38)$$

Based on (2.37), we will look for solutions for Γ that are in the form

$$\Gamma = \sum_{n=0}^{\infty} \Gamma_n \left(\frac{r}{a} \right) P_n(\cos \theta) . \quad (2.39)$$

Plugging equations (2.39) and (2.37) into (2.33), and evaluating the Laplacian in polar coordinates, the following differential equation involving Γ can be found

$$\Gamma_n'' \left(\frac{r}{a} \right) + \frac{2a}{r} \Gamma_n' \left(\frac{r}{a} \right) - \frac{n(n+1)a^2}{r^2} \Gamma_n = (2n+1) \mu_n \left(\frac{r}{a} \right) . \quad (2.40)$$

This equation is in the familiar form of Euler's equation [28],

$$Q_n''(q) + \frac{2}{q} Q_n'(q) - \frac{n(n+1)}{q^2} Q_n(q) = 0. \quad (2.41)$$

The solution to Euler's equation is

$$Q_n(q) = f q^n + g q^{-(n+1)} , \quad (2.42)$$

where coefficients f and g are found using boundary conditions. In our case the right hand side of (2.40) is not equal to zero. The specific solution to equation (2.40) is of

the form

$$\begin{aligned} \Gamma_n \left(\frac{r}{a} \right) = & \left(\frac{r}{a} \right)^{-(n+1)} \left(\int_1^{\frac{r}{a}} z^{n+2} \mu_n(z) dz - C_{1n} \right) \\ & - \left(\frac{r}{a} \right)^n \left(\int_1^{\frac{r}{a}} z^{-(n-1)} \mu_n(z) dz - C_{2n} \right) , \end{aligned} \quad (2.43)$$

where C_{1n} is found using boundary conditions and C_{2n} is found using the relation $\nabla\phi \rightarrow 0$ as $r \rightarrow \infty$ [22]. C_{1n} and C_{2n} are shown by Doinikov.

Λ can be found using a method similar to the one used above. The right side of equation (2.34) can be expanded in terms of Legendre polynomials and Associated Legendre polynomials. Using (2.34), an equation in the form of Euler's equation can also be derived for Λ . Again, as with equation (2.40), this equation does not equal zero. A specific solution for Λ can be found and is shown in detail by Doinikov. Once expressions for Γ and Λ are found the second order velocity, $\langle \vec{v}^{(2)} \rangle$, can be found. The resulting $\langle \vec{v}^{(2)} \rangle$ at $r = a$

$$\langle \vec{v}^{(2)} \rangle = \langle \vec{v}_0^{(2)} \rangle + \langle \vec{v}_s^{(2)} \rangle , \quad (2.44)$$

where

$$\langle \vec{v}_s^{(2)} \rangle = \omega^{-2} \langle \partial_t \vec{v}_r^{(1)} \frac{\partial \vec{v}^{(1)}}{\partial r} \rangle - \langle \vec{v}_0^{(2)} \rangle \quad (2.45)$$

and for a plane progressive wave, Doinikov's result for $\langle \vec{v}_0^{(2)} \rangle$ is

$$\langle \vec{v}_0^{(2)} \rangle = \frac{|k_1|^2}{4\omega} (\vec{k}_1 + \vec{k}_1^*) e^{(i\vec{k}_1 \cdot \vec{r} - i\vec{k}_1^* \cdot \vec{r})} . \quad (2.46)$$

Now we only lack an expression for $p^{(2)}$. Using equations (2.7), (2.13), and (2.27) we can write an expression for the gradient of the second order pressure in terms of

Γ and Λ as

$$\begin{aligned}
\nabla \langle p^{(2)} \rangle &= \left(\frac{4}{3} \eta + \xi \right) \langle \nabla \nabla^2 \Gamma \rangle - \eta \langle \nabla \times \nabla \times (\nabla \times \Lambda) \rangle \\
&\quad - \rho_1^{(0)} \langle \vec{v}^{(1)} (\nabla \cdot \vec{v}^{(1)}) + (\vec{v}^{(1)} \cdot \nabla) \vec{v}^{(1)} \rangle \\
&= - \frac{1}{\rho_1^{(0)}} \left(\frac{4}{3} \eta + \xi \right) \nabla (\nabla \cdot \langle \rho_1^{(1)} \vec{v}^{(1)} \rangle) + \eta \nabla^2 (\nabla \times \Lambda) \\
&\quad - \rho_1^{(0)} \langle \vec{v}^{(1)} (\nabla \cdot \vec{v}^{(1)}) + (\vec{v}^{(1)} \cdot \nabla) \vec{v}^{(1)} \rangle .
\end{aligned} \tag{2.47}$$

Second order pressure can be found using equation (2.47) and the full expressions for Γ and Λ (as shown by Doinikov). Once the second order velocity and pressure are known, we have a complete expression for the second order stress tensor. We can then plug the expressions for the first order velocity and the second order stress tensor into equation (2.24), leading to an integral of the form

$$\begin{aligned}
\vec{F} &= 6\pi\eta a^2 \hat{m} (f_1 + 2g_1) + 3\pi \frac{\eta}{\rho_1^{(0)}} \hat{m} \int_1^\infty \int_0^\pi \nabla \cdot \langle \rho_1^{(1)} \vec{v}^{(1)} \rangle \cos \theta \sin \theta d\theta d(r/a) \\
&\quad - 3\pi \rho_1^{(0)} \hat{m} \int_1^\infty \int_0^\pi \left[1 - \left(\frac{r}{a} \right)^{-2} \right] \left[\langle v_r^{(1)} v_r^{(1)} \rangle \cos \theta - v_r^{(1)} v_\theta^{(1)} \sin \theta \right. \\
&\quad \left. + \frac{1}{2} r \hat{\theta} \cdot \langle \vec{v}^{(1)} (\nabla \cdot \vec{v}^{(1)}) + (\vec{v}^{(1)} \cdot \nabla) \vec{v}^{(1)} \rangle \sin \theta \right] a^2 \sin \theta d\theta d(r/a) ,
\end{aligned} \tag{2.48}$$

where unit vector \hat{m} is in the direction of wave propagation [22]. Evaluating the integrals leads to a complicated expression for acoustic radiation force. For a plane progressive incident wave the final expression for acoustic radiation force is [22]

$$\begin{aligned}
F &= \frac{3}{2} i\pi \rho_1^{(0)} \left[\sum_{n=0}^{\infty} (n+1) (D_n - D_n^*) \right. \\
&\quad \left. - \frac{k_1 a k_1^* a}{(K_1 a)^2} (k_1 a + k_1^* a) \left(\frac{\sin(k_1 a + k_1^* a)}{(k_1 a - k_1^* a)} \right) \right] ,
\end{aligned} \tag{2.49}$$

where force is in the direction of wave propagation, D_n^* is the complex conjugate of D_n , and

$$D_n = S_{1n}\alpha_n\alpha_{n+1}^* + S_{2n}\beta_n\beta_{n+1}^* + S_{3n}\alpha_n\beta_{n+1}^* + S_{4n}\beta_n\alpha_{n+1}^* + S_{5n}\alpha_n + S_{6n}\alpha_{n+1}^* + S_{7n}\beta_n + S_{8n}\beta_{n+1}^* + S_{9n} . \quad (2.50)$$

The functions S_{mn} are given in the appendix. Note the correction to Doinikov's expression for $J_{nm}^{(j)}$ that is listed in the appendix.

2.3 Reduction to Inviscid Equations - Compressible sphere in an inviscid fluid

In the case of a freely suspended fluid or solid elastic sphere in an inviscid fluid we will begin the analysis by letting viscosity and bulk viscosity equal zero in equation (2.2). The integral over first order stress, the second term on the right side of equation (2.24), does not depend on viscosity, and therefore does not change. The second order stress, however, is now simplified to $\bar{\sigma}^{(2)} = -p^{(2)}\hat{n}$. We then get the following equation for the time averaged radiation force:

$$\vec{F} = \left\langle \int_{S(t)} (-p^{(2)}\hat{n} - \rho_1^{(0)}\vec{v}^{(1)}(\vec{v}^{(1)} \cdot \hat{n})) dS \right\rangle . \quad (2.51)$$

We let viscosity go to zero in equation (2.47) and integrate both sides to get an expression for the second order pressure in the inviscid case as:

$$\int \nabla \langle p^{(2)} \rangle dx = \int \rho_1^{(0)} \langle \vec{v}^{(1)} (\nabla \cdot \vec{v}^{(1)}) + (\vec{v}^{(1)} \cdot \nabla) \vec{v}^{(1)} \rangle dx . \quad (2.52)$$

In this case there is no vector potential, and therefore velocity is simply described

by

$$\vec{v} = \nabla\phi . \quad (2.53)$$

Using equations (2.10) and (2.32) and integration by parts, the first term in (2.52) can be written as

$$\int \langle \rho_1^{(0)} \vec{v}^{(1)} (\nabla \cdot \vec{v}^{(1)}) \rangle dx = -\frac{1}{2} \frac{\rho_1^{(0)}}{c^2} \dot{\phi}^2 \hat{n} . \quad (2.54)$$

Additionally, using the definition for expanding $\nabla(\vec{a} \cdot \vec{b})$ [11], the second term in equation (2.52) can be written as

$$\int \langle (\vec{v}^{(1)} \cdot \nabla) \vec{v}^{(1)} \rangle dx = \frac{1}{2} \rho_1^{(0)} |\vec{v}^2| \hat{n} . \quad (2.55)$$

We have now reduced the viscous expressions for pressure to inviscid expressions matching those given by King and others [18], [19]:

$$p = \rho_1^{(0)} \vec{v}^{(1)} (\vec{v}^{(1)} \cdot \hat{n}) - \frac{1}{2} \rho_1^{(0)} |\vec{v}^{(1)}|^2 + \frac{1}{2} \frac{\rho_1^{(0)}}{c^2} \dot{\phi}^2 . \quad (2.56)$$

Note that Yosioka and Kawasima show in detail how the first term in (2.56) is equal to the following expression which is the common form given by other authors [19],

$$\rho_1^{(0)} \vec{v}^{(1)} (\vec{v}^{(1)} \cdot \hat{n}) = \rho_1^{(0)} (\dot{\phi}^{(1)} + \dot{\phi}^{(2)}) \hat{n} , \quad (2.57)$$

in which $\dot{\phi}^{(1)}$ and $\dot{\phi}^{(2)}$ are time derivatives of the first and second order velocity potentials. Acoustic radiation force for a compressible sphere in an inviscid fluid is

therefore described by [21]

$$\begin{aligned} \vec{F} = & - \int_{S_o} \langle \rho_1^{(0)} \vec{v}^{(1)} (\vec{v}^{(1)} \cdot \hat{n}) \rangle dS + \int \int_{S_o} \langle \frac{1}{2} \rho_1^{(0)} |\vec{v}^{(1)}|^2 \rangle \hat{n} dS \\ & - \int_{S_o} \langle \frac{1}{2} \frac{\rho_1^{(0)}}{c^2} (\dot{\phi}^{(1)})^2 \rangle \hat{n} dS . \end{aligned} \quad (2.58)$$

Only the incident and scattered longitudinal velocity potentials listed in (2.31) are needed to calculate radiation force for this case. The coefficient α_n can be found using the boundary conditions listed below [21], [29].

For a fluid sphere in an inviscid fluid the boundary conditions are:

- 1) continuity of pressure across the boundary
- 2) continuity of normal displacement across the boundary

For a solid elastic sphere in an inviscid fluid the boundary conditions are:

- 1) the sum of the pressure in the fluid and the normal stress of the sphere at the boundary equals zero
- 2) continuity of normal displacement across the boundary
- 3) tangential shear stress is zero

The velocity components in spherical coordinates are

$$v_r = \left(\frac{\partial \phi}{\partial r} \right)_{r=a} , \quad (2.59)$$

$$v_\theta = \left(\frac{1}{r} \frac{\partial \phi}{\partial \theta} \right)_{r=a} . \quad (2.60)$$

Plugging velocity into equation (2.58) yields the following components for force (in

spherical coordinates)

$$\begin{aligned}
F_r &= -\pi a^2 \rho_1^{(0)} \int_0^\pi \left(\frac{\partial \phi}{\partial r} \right)_{r=a}^2 \sin \theta \cos \theta d\theta \\
F_\theta &= \pi \rho_1^{(0)} \int_0^\pi \left(\frac{\partial \phi}{\partial \theta} \right)_{r=a}^2 \sin \theta \cos \theta d\theta \\
F_{r\theta} &= 2\pi a \rho_1^{(0)} \int_0^\pi \left(\frac{\partial \phi}{\partial r} \right)_{r=a} \left(\frac{\partial \phi}{\partial \theta} \right)_{r=a} \sin^2 \theta d\theta \\
F_t &= -\frac{\pi a^2 \rho_1^{(0)}}{c^2} \int_0^\pi \left(\frac{\partial \phi}{\partial t} \right)_{r=a}^2 \sin^2 \theta \cos \theta d\theta .
\end{aligned} \tag{2.61}$$

Substituting in for ϕ and evaluating the integrals, as shown in detail by Hasegawa, yields the following equation for radiation force [20]:

$$\begin{aligned}
F &= -2\pi \rho k_1 a^2 \sum (n+1)(U'_n V'_{n+1} - V'_n U'_{n+1}) \\
&+ 2\pi \rho \sum_{n=0}^{\infty} n(n+1)(n+2)(U_n V_{n+1} - V_n U_{n+1}) \\
&+ 2\pi \rho k_1 a \sum_{n=0}^{\infty} [n(n+1)(U_n V'_{n+1} \\
&- V_n U'_{n+1}) - (n+1)(n+2)(U'_n V_{n+1} - V'_n U_{n+1})] \\
&- 2\pi \rho k_1 a^2 \sum_{n=0}^{\infty} (n+1)(U_n V_{n+1} - V_n U_{n+1})
\end{aligned} \tag{2.62}$$

where force is in the direction of wave propagation and

$$U_n = j_n(k_1 a)(1 + \zeta_n) + \chi_n y_n(k_1 a) \tag{2.63}$$

$$V_n = \chi_n j_n(k_1 a) - \zeta_n y_n(k_1 a) \tag{2.64}$$

$$U'_n = \left[\frac{n}{k_1 a} j_n(k_1 a) - j_{n+1}(k_1 a) \right] (1 + \zeta_n) + \left[\frac{n}{k_1 a} y_n(k_1 a) - y_{n+1}(k_1 a) \right] \chi_n, \tag{2.65}$$

$$V'_n = \left[\frac{n}{k_1 a} j_n(k_1 a) - j_{n+1}(k_1 a) \right] \chi_n - \left[\frac{n}{k_1 a} y_n(k_1 a) - y_{n+1}(k_1 a) \right] \zeta_n. \quad (2.66)$$

In these the compressional wavenumber in the surrounding fluid is $k_1 = \omega/c_1$, $y_n(x)$ is the spherical Bessel function of the 2nd kind, and ζ_n and χ_n are the real and imaginary components of the coefficient α_n .

$$\zeta_n = \frac{-G_n^2}{G_n^2 + H_n^2}, \quad (2.67)$$

$$\chi_n = \frac{-G_n H_n}{G_n^2 + H_n^2}, \quad (2.68)$$

$$G_n = (L_n - n)j_n(k_1 a) + (k_1 a)j_{n+1}(k_1 a), \quad (2.69)$$

$$H_n = (L_n - n)y_n(k_1 a) + (k_1 a)y_{n+1}(k_1 a), \quad (2.70)$$

L_n is shown below for a fluid sphere:

$$L_n = \frac{\rho_1^{(0)}}{\rho_2^{(0)}} \frac{(k_2 a)[n j_n(k_2 a) - (k_2 a)j_{n+1}(k_2 a)]}{j_n(k_2 a)}, \quad (2.71)$$

where $\rho_2^{(0)}$ is the equilibrium density of the sphere material and k_2 is the compressional wavenumber in the sphere. For the case of a solid elastic sphere shear waves are created inside the sphere, and the function L_n is equal to

$$L_n = \frac{1}{2} \frac{\rho_1^{(0)}}{\rho_2^{(0)}} \frac{(K_2 a)^2 (T_n - U_n)}{(V_n - W_n)}, \quad (2.72)$$

in which

$$T_n = \frac{n j_n(k_2 a) - (k_2 a)j_{n+1}(k_2 a)}{(n-1)j_n(k_2 a) - (k_2 a)j_{n+1}(k_2 a)}, \quad (2.73)$$

$$U_n = \frac{2n(n+1)j_n(K_2 a)}{[2n^2 - (K_2 a)^2 - 2]j_n(K_2 a) + 2(K_2 a)j_{n+1}(K_2 a)}, \quad (2.74)$$

$$V_n = \frac{[(K_2a)^2/2 - n(n-1)]j_n(k_2a) - 2(k_2a)j_{n+1}(k_2a)}{(n-1)j_n(k_2a) - (k_2a)j_{n+1}(k_2a)}, \quad (2.75)$$

$$W_n = \frac{2n(n+1)[(1-n)j_n(K_2a) + (K_2a)j_{n+1}(K_2a)]}{[2n^2 - (K_2a)^2 - 2]j_n(K_2a) + 2(K_2a)j_{n+1}(K_2a)}. \quad (2.76)$$

In these equations the longitudinal and transverse wavenumbers in the sphere can be written as

$$k_2 = \frac{\omega}{c_2}, \quad K_2 = \frac{\omega}{C_2}, \quad (2.77)$$

where c_2 is the compressional wave speed in the sphere and C_2 is the shear wave speed in the sphere.

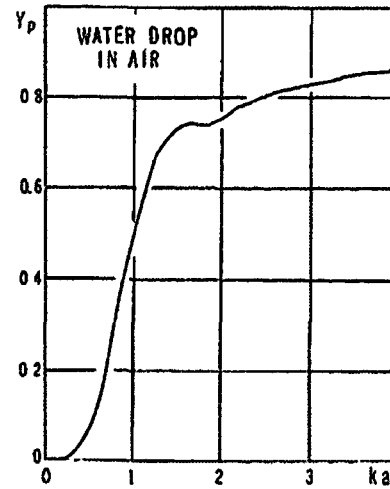
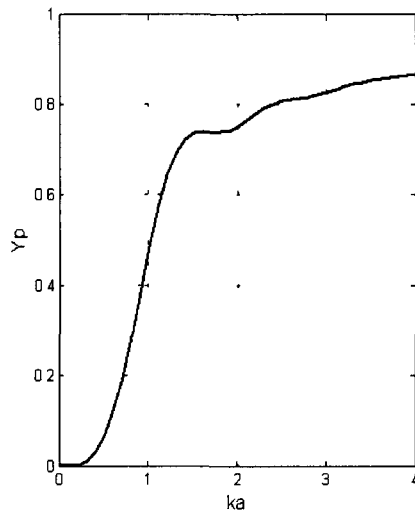
Numerical implementation of the inviscid equations was checked by direct comparison with plots published by Hasegawa [20], [21], [29]. We found that our plots of the radiation pressure function, Y_p , versus ka (where k is wavenumber in the surrounding fluid) match Hasegawa's plots very well. Figure 2.2 shows examples of these comparisons for a polyethylene (PE) sphere in water and for a fused silica sphere in water. It should be noted that the function Y_p is related to acoustic radiation force by the simple expression [20]:

$$Y_p = \frac{\langle \vec{F} \rangle}{\pi a^2 \bar{E}}, \quad (2.78)$$

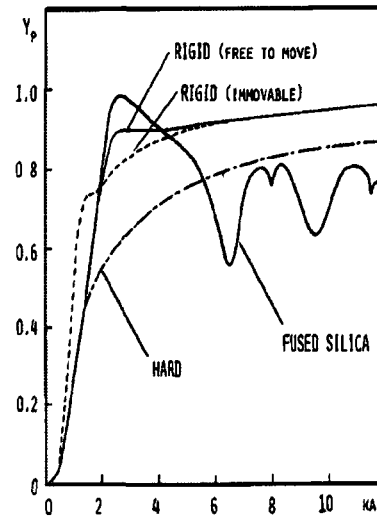
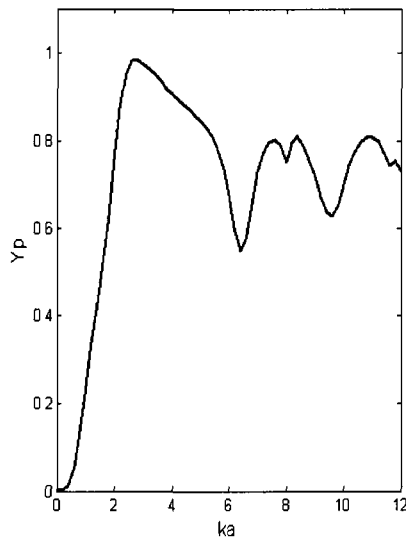
where the mean energy density is

$$\bar{E} = \frac{1}{2} \rho k^2 |\phi_0|^2, \quad (2.79)$$

where ϕ_0 is the amplitude of the incident wave (which we have set equal to 1).



(a) Matlab result for a water droplet in air. (b) Hasegawa's result for a water droplet in air.



(c) Matlab result for a fused silica sphere in water (d) Hasegawa's result for a fused silica sphere in water

Figure 2.2: Comparison between our results and Hasegawa's results, Y_p versus ka .

Table 2.2: Material Properties Used for Inviscid Model Comparison

Material	Density (g/cm^3)	Longitudinal Speed (cm/s)	Transverse Speed (cm/s)
Fused Silica	2.214	595,000	375,000
Water	1.0	150,000	–

[30], [31]

2.4 Viscous Model Code Verification and Convergence

As mentioned above, our code for plotting the inviscid model was checked against published plots that have been well verified in the literature. This comparison helped us establish confidence in our implementation of the inviscid model. However, there are currently no published plots, that we are aware of, using the viscous model. Radiation force versus ka was plotted using both models. In Figure 2.3, shear viscosity and bulk viscosity is decreased by one order of magnitude and then by two orders of magnitude. Figure 2.3 clearly shows that as viscosity goes to zero, the viscous model result yields the inviscid result. Furthermore, it was observed that certain material properties create resonance peaks in the radiation force plots. Resonant peaks are created because scattering resonances occur at eigenfrequencies of vibration of the scatterer [32]. Therefore, we expect that resonant positions will be similar for both models. When we plotted radiation force versus ka for the test case of a blood droplet in air we found that while the background behavior of radiation force differed for models 1 and 2, the resonance peaks occur at the same ka values, see Figure (2.4). Plotting the resonance peak positions of the inviscid model versus those of the

viscous model results in a correlation coefficient of $R^2 = 0.99996$. Additionally, as we incrementally changed the material properties we observed that the resonance peaks shifted the same amount in both models. Thus, by looking at the limiting case of letting viscosity go to zero and by comparing resonance peaks in the two models, we were able to establish confidence in our implementation of the viscous model.

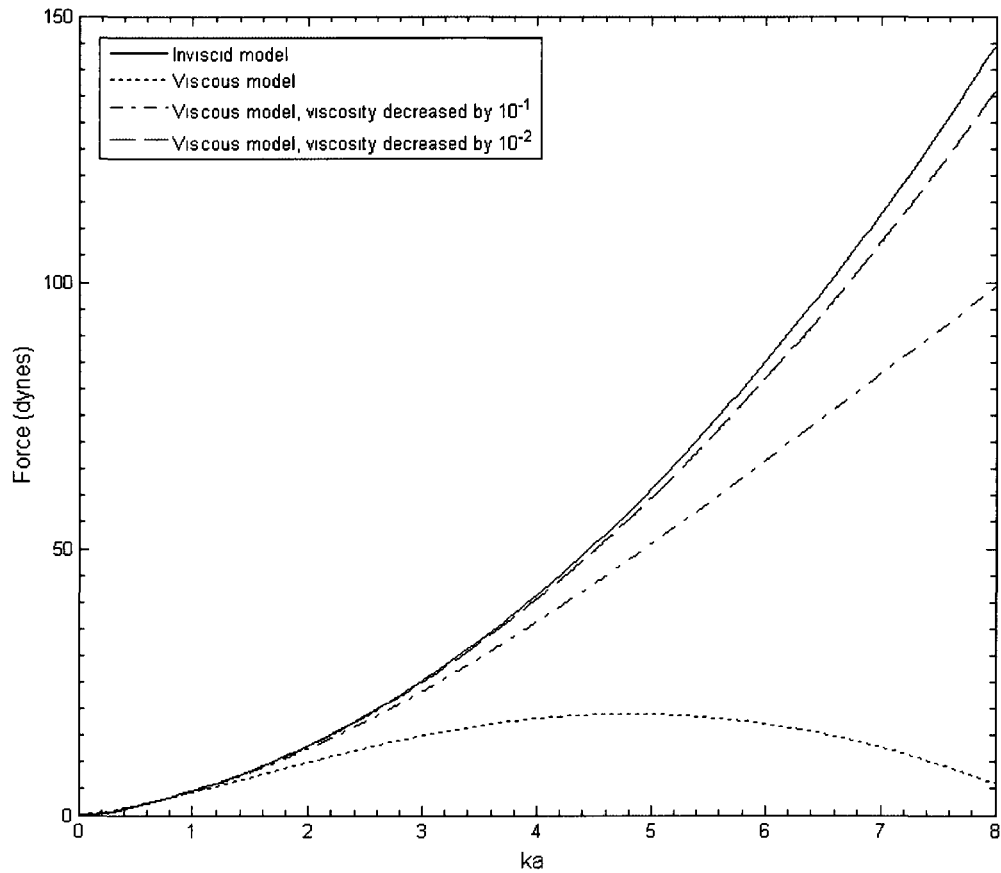


Figure 2.3: Radiation force versus ka (where k is longitudinal wavenumber of the surrounding media) for an air bubble in glycerol. As viscosity decreases, the viscous models tend toward the inviscid model result.

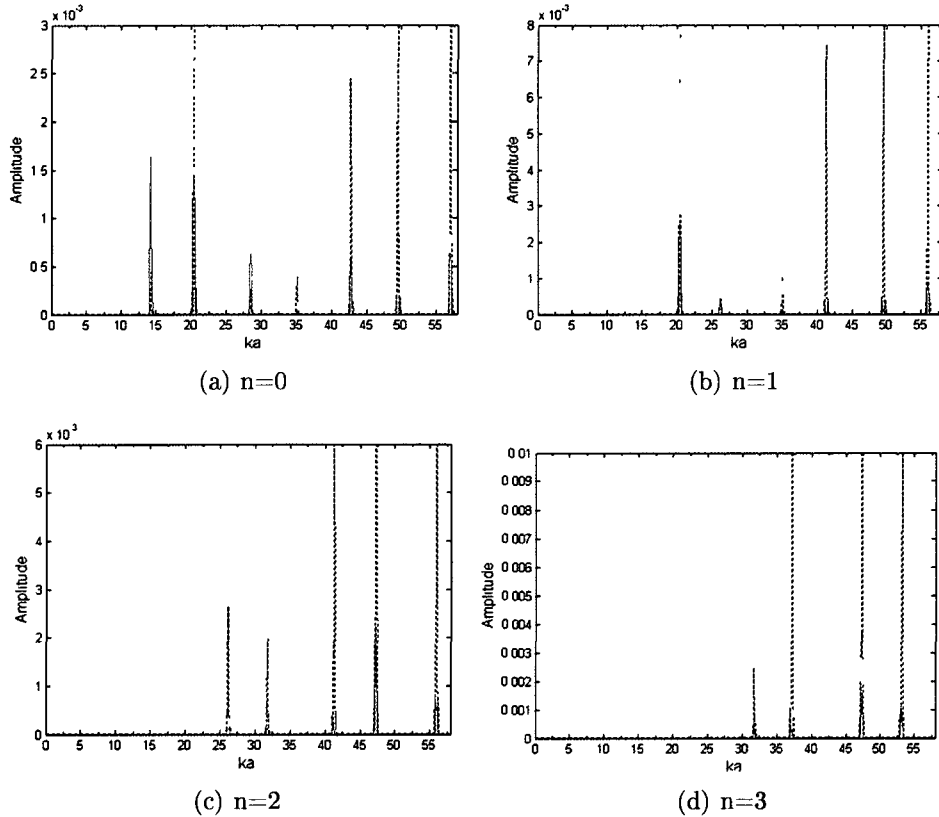


Figure 2.4: Blood droplet in air resonance peak positions for the inviscid model versus the viscous model. The dashed blue line is radiation force from the inviscid model and the solid magenta line is the result from the viscous model.

Implementation of the viscous model takes a significant amount of computational power. Numerical models were implemented with Matlab using the Typhoon cluster, part of the Sciclone computing cluster at the College of William and Mary. The cluster has 72 dual-processor, dual-core Dell SC1435 servers running at $2.6GHz$. The viscous model required over 3000 CPU hours in order to calculate radiation force for one material combination. The computation was accomplished in less wall-clock time by breaking the code into pieces and running up to 65 jobs at once. Due to the time required by the viscous model, the infinite summation in equations (2.62) and (2.49) was computed only to $n = 30$. The inviscid model can be numerically implemented

very quickly and takes only minutes to compute force for $n = 0 : 30$. Using the infinite sum rule from general scattering theory [33],

$$n_{end} = ka + 4(ka)^{(1/3)} + 10 \quad (2.80)$$

a summation of only $n = 0 : 30$ is only accurate to ka values of approximately $ka = 10$. We checked convergence of the inviscid model by extending the summation in the calculation of radiation force to larger n values. The viscous model, however requires large amounts of computing time as the summation over n is increased. Therefore, we checked convergence of the viscous model by calculating the n -dependent contribution to radiation force for larger n values, see Tables 2.3-2.4 for examples. We found that calculating the summation to $n = 30$ is indeed adequate for ka values up to 10.

Table 2.3: n Dependent Contribution to Acoustic Radiation Force, Progressive Wave: for n values of 40 to 48 at $ka = 10$

	Glycerol in Air $F_{total} = 0.142 \text{ dyn}$	Air in Glycerol $F_{total} = -15.1 \text{ dyn}$
n value	n dependent force contribution (dyn)	n dependent force contribution (dyn)
40	1.97×10^{-12}	2.26×10^{-8}
41	-1.80×10^{-12}	-5.88×10^{-8}
42	1.02×10^{-11}	7.71×10^{-8}
43	-5.70×10^{-13}	-4.68×10^{-8}
44	-9.58×10^{-12}	7.78×10^{-8}
45	4.39×10^{-12}	-4.09×10^{-8}
46	2.36×10^{-12}	2.02×10^{-7}
47	3.35×10^{-12}	1.43×10^{-7}
48	-1.74×10^{-11}	-4.22×10^{-8}

Table 2.4: n Dependent Contribution to Acoustic Radiation Force, Standing Wave: for n values of 40 to 48 at $ka = 10$ and $d = (1/8)\lambda$

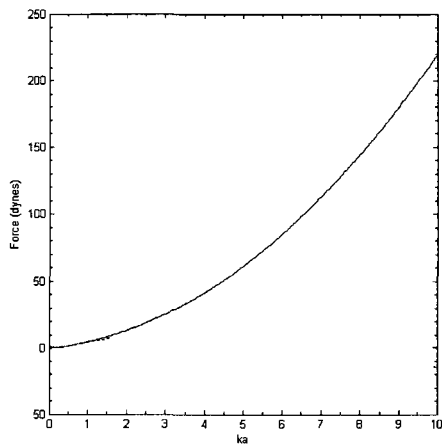
	Glycerol in Air $F_{total} = -7.80 \times 10^{-5} \text{ dyn}$	Air in Glycerol $F_{total} = 0.46 \text{ dyn}$
n value	n dependent force contribution (dyn)	n dependent force contribution (dyn)
40	-1.98×10^{-12}	-3.06×10^{-8}
41	-2.48×10^{-12}	5.32×10^{-8}
42	-7.18×10^{-13}	-4.40×10^{-8}
43	2.68×10^{-12}	-3.04×10^{-8}
44	-1.26×10^{-12}	-5.74×10^{-8}
45	-2.96×10^{-12}	7.46×10^{-8}
46	1.21×10^{-12}	5.96×10^{-8}
47	7.50×10^{-12}	2.14×10^{-7}
48	-5.34×10^{-12}	2.62×10^{-7}

2.5 Viscous Model Results

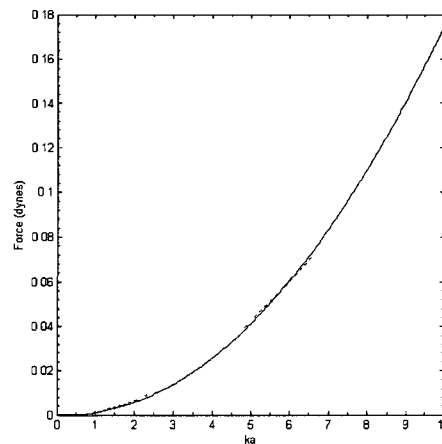
Figures 2.5 - 2.6 show radiation force for six cases: a gas bubble in a highly viscous fluid (air in glycerol), a gas bubble in a low viscosity fluid (air in water), a high viscosity liquid drop in a gas (glycerol in air), a low viscosity liquid drop in a gas (water in air), a high viscosity liquid drop in a low viscosity liquid (glycerol in water), a low viscosity liquid drop in a high viscosity liquid (ethanol in glycerol). These materials were chosen to show a variety of viscosity combinations between the surrounding fluid and the scatterer. The material combinations of air in glycerol, glycerol in air, and ethanol in glycerol are discussed briefly by Doinikov as limiting cases [22]. As predicted by Doinikov, our plots for these three cases show that force goes to zero as ka goes to zero. Furthermore, our results for all material combinations agree with the expected result that when $a \ll \lambda$ (very small ka), the viscous and inviscid models yield the same result. The material properties used in these plots are shown in Table 2.5 and the surface tension values are listed in the appendix.

The plots show that the two models do indeed yield differing results when viscosity of the scatterer and/or surrounding fluid is large. Figure 2.5 (b) shows that for a low viscosity scatterer in a low viscosity liquid the two models produce almost exactly the same result. In addition, Figure 2.5 (a) and Figure 2.6 show a negative force for some values of ka . This result supports Doinikov’s statement that in a viscous fluid the acoustic force on the scatterer due to a plane progressive wave can cause movement in a direction opposite from the incident sound wave.

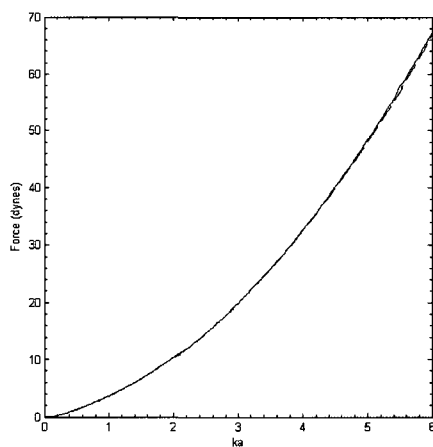
It should be noted that Figure 2.5 (c) and Figures 2.6 (a) - (c) are plotted to a smaller ka value because for these material combinations the numerical model yields non-numerical results (NaN) for larger ka values. This behavior is caused when spherical Bessel and spherical Hankel functions are calculated (in Matlab) for large imaginary arguments. The spherical Bessel functions go to $+$ or $-\infty$ (depending on order, n) and the spherical Hankel functions go to zero. For some of the material combinations shown below the transverse wavenumber reaches such values more quickly and causes the numerical results to “blow up”. As shown in equation (2.29), real and imaginary components for the transverse wavenumber are on the same order. This behavior shows a possible limitation to current numerical implementations of the viscous radiation force equations. Recent publications, such as [34] and [35], show that the behavior and numerical computation of Bessel functions with complex arguments is still an area of research. Furthermore, the result punctuates the need for experimental verification of the viscous acoustic force equations.



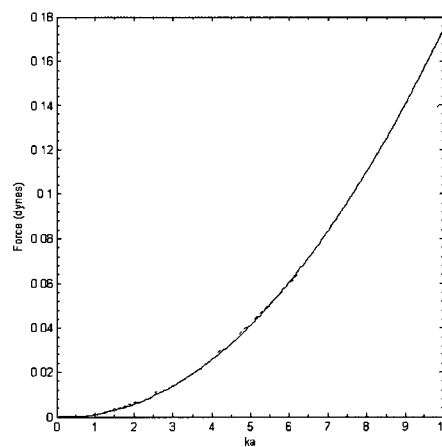
(a) Air in glycerol



(b) Glycerol in air

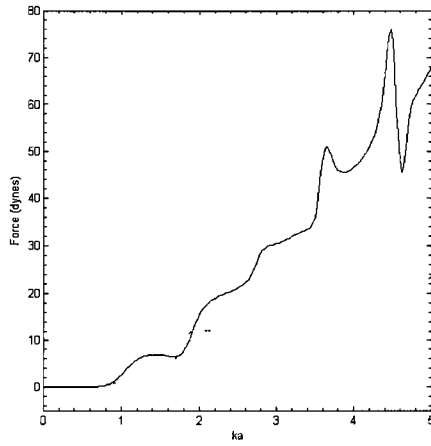


(c) Air in water

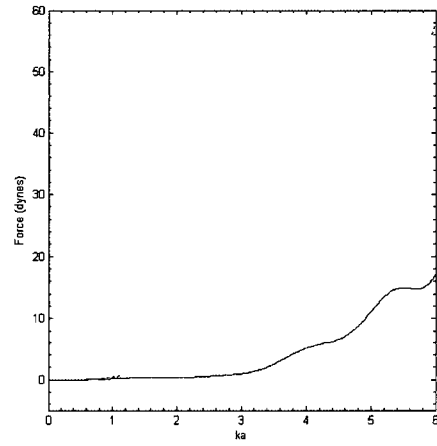


(d) Water in air

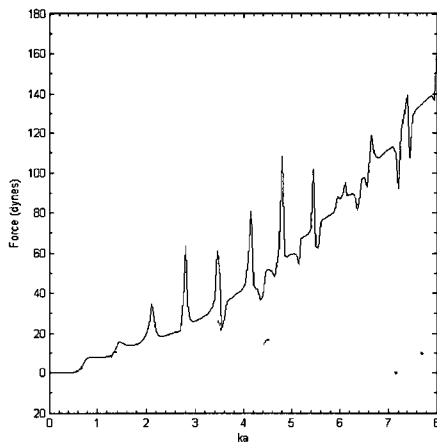
Figure 2.5: The solid line is radiation force from the inviscid model and the dashed line is the result from the viscous model.



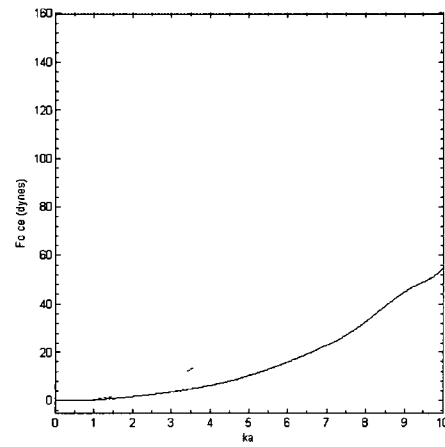
(a) Water in glycerol



(b) Glycerol in water



(c) Ethanol in glycerol



(d) Glycerol in ethanol

Figure 2.6: The solid line is radiation force from the inviscid model and the dashed line is the result from the viscous model.

Table 2.5: Material Properties

Material	Density (g/cm^3)	Speed of Sound (cm/s)	Viscosity (g/cms)	Bulk Viscosity (g/cms)
Air	0.0011745	34,800	0.000186	0.000180
Ethanol	0.789	114,400	0.012	0.010
Glycerol	1.261	190,400	15.0	10.0
Water	0.998	148,000	0.0101	0.02

[30], [31]

Chapter 3

Emboli Removal from Extracorporeal Circuits

3.1 Emboli in Cardiac Surgery

Emboli in the form of air bubbles and artery wall plaque can enter the blood stream during cardiac surgery. The relationship between increased embolic load to the brain and postoperative neurocognitive decline have been a concern for the past few decades [36]. During the past fifteen years numerous studies have been published linking neurocognitive decline to emboli [37], [38], [39], [40]. Reports have shown long-term postoperative neurocognitive impairment as high as 30% in coronary artery bypass graft surgery (CABG) patients [41]. Although recent reports clearly show that the direct relation between embolic load and cognitive impairment is still unresolved, removal of emboli from cardiopulmonary bypass (CPB) circuits appears at the present to be a valid precaution [36], [42], [43]. Arterial line filters are currently used to stop emboli in CPB circuits from passing back into the body during surgery. However, the pores of arterial line filters are only 25 to 40 μm in diameter [36], [44]. Emboli smaller

than the pore diameter can pass through the filters and make their way towards the brain. In addition, if the embolic load is high, larger emboli can pass through the filters [44]. It is important to monitor emboli load pre-filter because a warning of an increased load allows the medical team to eliminate emboli sources. Broadband ultrasound pulses can be used to detect and track emboli as well as to estimate the size of emboli using backscatter echoes [45], [46].

Via acoustic radiation force, ultrasound may also be used for thorough, real-time removal of gas and lipid emboli from extracorporeal circuits, including emboli smaller than $25\mu m$. Typical flow rates in CPB are around $30cm/s$, so emboli removal must be quick [45]. Gas bubble removal from CPB circuits using acoustic radiation force was proposed as early as 1992, but has yet to be implemented [47]. A lipid embolus is a good approximation of artery plaque composition which generally has a high-lipid content unless extreme calcification has occurred [48]. Removing emboli from the bloodstream will greatly decrease the risk of microemboli traveling to the brain. It is necessary to precisely know the behavior of radiation force as a function of ultrasound frequency in order to optimize the removal process. Acoustic radiation force is directly related to the material properties of the scatterer and the surrounding fluid. During cardiac surgery the material properties of blood will vary from patient to patient (as described in the next section). In this situation it is clearly not feasible to experimentally determine acoustic radiation force curves for each patient. An accurate mathematical model of acoustic radiation force is necessary to predict a reasonable range of potential values for the acoustic force upon emboli.

3.2 Results for Emboli in Blood

Figures 3.1 - 3.2 show radiation force versus k_a for the two material combinations that are relevant to emboli removal from CPB circuits: 1) an air bubble in blood, 2) a lipid embolus in blood. The properties associated with blood depend on temperature and blood thickness. Typically during bypass surgery the body is cooled to approximately $25^{\circ}C - 32^{\circ}C$ and the blood is thinned, with a target haematocrit (HCT) level around 27%, to prevent clotting [49]. A target haematocrit level is determined for each patient and blood thickness is monitored during surgery to maintain target levels.

Bulk viscosity values are overall unavailable in the literature. This lack of availability may be due to the fact that bulk viscosity is not required by the more simple and common models of scattering. Additionally, approximations for bulk viscosity in relation to shear viscosity are sometimes used when bulk viscosity is included. After extensive searching we were able to find approximate values for the materials presented in this chapter. A bulk viscosity value for lipid was the most difficult material property to find. The viscosity and bulk viscosity for lipid used in this work is from Disalvo and Simon [50]. The value for bulk viscosity that we found is surprisingly larger than the shear viscosity (when compared to the bulk/shear ratios of the other fluids listed). However, recent research has found that bulk viscosity can be larger than dynamic viscosity [23]. In fact, Dukhin concluded that there is no strong correlation between bulk viscosity values and other parameters such as dynamic viscosity. Clearly, more evidence of the precise material property values would increase the real-world accuracy of our modeling results. Since we must work with the material properties reported in the literature, we investigated the results of changes in material properties. We found that changes in bulk viscosity values of an order of magnitude and larger have little effect on the predicted radiation force. A longer discussion on

bulk viscosity can be found in section 3.3. Changes in the density of blood and in the shear viscosity of the lipid had the largest effect on radiation force. The lower and upper lines in Figures 3.1 and 3.2 represent the maximum range in radiation force due to the uncertainty in material properties. The material property ranges used for Figures 3.1 - 3.2 are shown in Table 3.1. The surface tension values are listed in the appendix. The viscosity of blood was calculated using $\eta = 0.015*(1+2.5*HCT)$ [51].

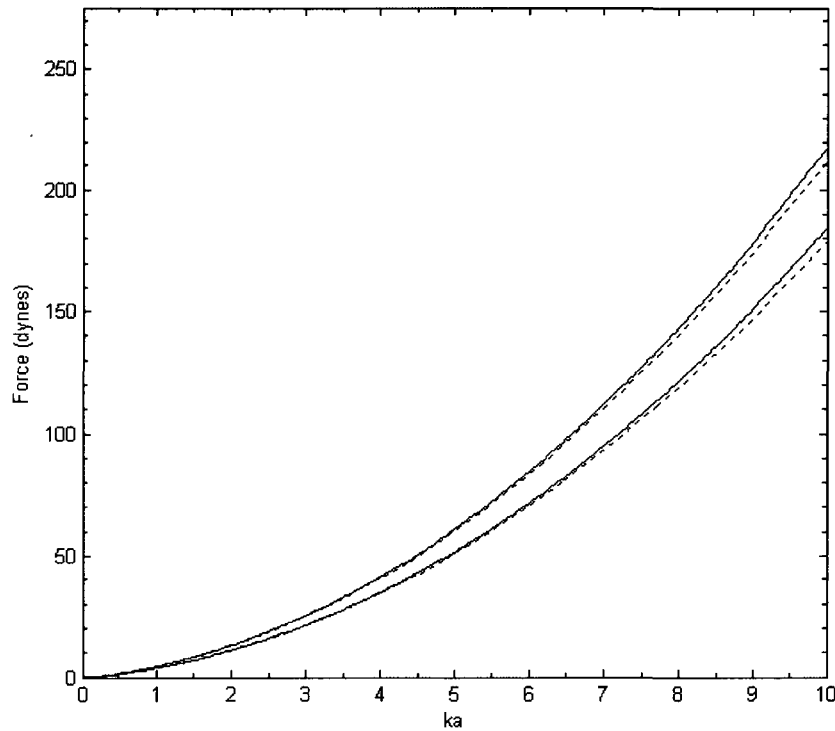


Figure 3.1: Radiation force versus ka for an air bubble in blood. The solid lines show the range of radiation force found using the inviscid model for the range of material properties listed in Table 3.1. The dashed lines show radiation force found using the viscous model for the range of material properties.

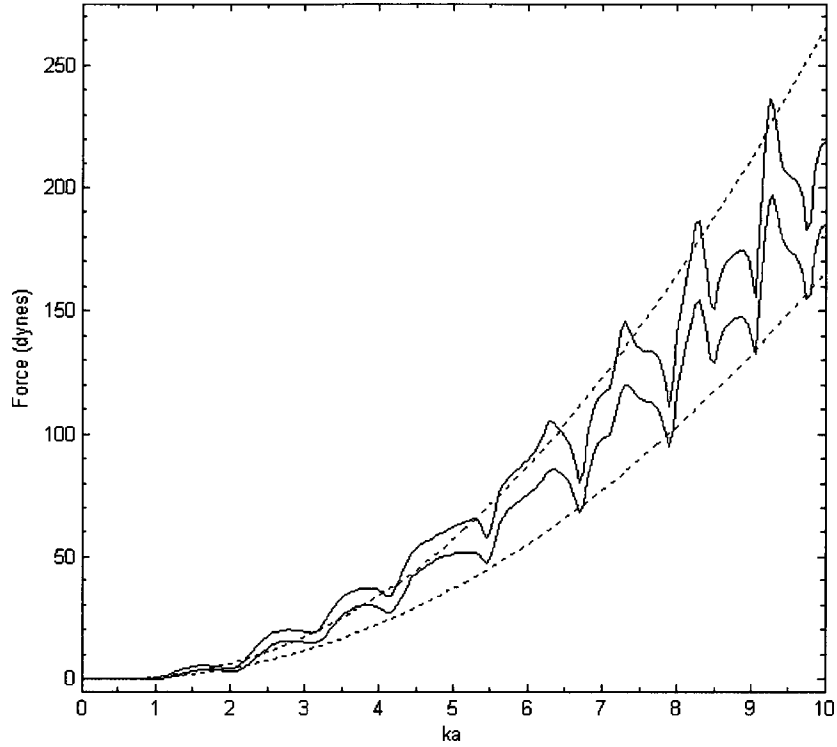


Figure 3.2: Radiation force versus ka for a lipid sphere in blood. The solid lines show the range of radiation force found using the inviscid model for the range of material properties listed in Table 3.1. The dashed lines show radiation force found using the viscous model for the range of material properties.

Table 3.1: CPB Material Properties Range

Material	Density (g/cm^3)	Speed of Sound (cm/s)	Viscosity ($g/cm.s$)	Bulk Viscosity ($g/cm.s$)
Air	0.001174 – 0.0013	32,100 – 35,000	0.00018482 – 0.00018673	0.00012 – 0.00019
Blood	1.060 – 1.2508	154,000 – 160,000	0.0225 – 0.0319	0.024 – 0.034
Lipid	0.89 – 0.924	143,000 – 147,000	1 – 16	$2.5 \cdot 10^6$ – $40 \cdot 10^6$

[52], [53], [54], [50], [55], [56]

3.2.1 Discussion of Results

Acoustic radiation force was plotted for air and lipid emboli in blood using the inviscid and viscous models. For an air bubble in blood the two models predict nearly the exact same behavior for force as a function of ka . For the case of a lipid embolus, the two models predict slightly different behavior, especially for large ka values. As shown in Figure 3.2, the viscous model predicts a smooth increase in force as ka increases while the inviscid model predicts maximas and minimas in force as a function of ka . Yet, the inviscid model predicts that force increases overall at an average rate similar to the viscous model. Both models yield the same order of magnitude for acoustic radiation force as a function of ka . For transducer frequencies in the low MHz range, small emboli (tens of microns) correspond to the low ka region ($ka < 1$) where the two models agree very well. Furthermore, when we take into account the inherent difficulties in finding precise material properties for individual patients and the computational time required by the viscous model, we conclude that the inviscid model is adequate for this application. As processing speeds increase and material properties become well known, the viscous model may become the preferred model.

Additionally, the results presented in section 3.2 show that there is no resonant peak behavior to take advantage of when choosing a transducer frequency for this application. The model results confirm that as emboli size decreases, higher frequencies are required to impart the same magnitude of force. The optimal transducer for emboli removal in extracorporeal circuits depends directly on the removal chamber setup, see Figure 3.3 for an example. If only a single transducer is used the optimal transducer will be broadbanded with a central frequency shifted towards that required to move small emboli. If an array of transducers is used, it would be best if each transducer has a different frequency that is intended for removal of a specific emboli size-range. Another option is to use a system like the *EDAC^(R) Quantifier*

(Emboli Detection and Classification, Luna Innovations, Roanoke VA) to predict what size emboli will be flowing through the removal chamber at a specific instant in time, and use a transducer that can be driven at various frequencies to adjust for the exact emboli sizes encountered. Note that another consideration in the removal chamber setup is the need for minimal heating. If a transducer is driven at high powers, heating can occur. In a medical application such as this, heating of the blood must be prevented. A cooling water bath between the transducer and the removal chamber could help decrease the possibility of heating.

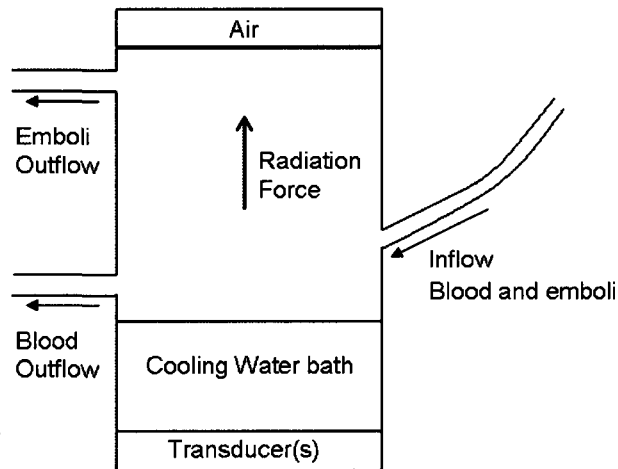


Figure 3.3: Example of a removal chamber setup - Blood and emboli flow into the removal chamber. Acoustic radiation force pushes air and lipid emboli towards the top of the removal chamber. Air bubbles either rise to the air pocket at the top or flow out of the emboli outflow tubing. Lipid emboli flow out through the emboli outflow tube.

3.3 Bulk Viscosity

As discussed above, very few experimental bulk viscosity values have been published. For an incompressible fluid, the second term in equation (2.7) goes to zero (definition of isochoric flow) [2]. Therefore, bulk viscosity is only important for compressible fluids. As described by Dukhin in a recent paper, bulk viscosity can be found experimentally through measurements of attenuation. At ultrasonic frequencies attenuation, α , is related to bulk viscosity, ξ , by [23]:

$$\alpha = \frac{\omega^2}{2\rho c^3} \left(\frac{4}{3}\eta + \xi \right) , \quad (3.1)$$

where ω is radial frequency, c is the speed of sound, and η is shear viscosity. Bulk viscosity, as described by Temkin, is related to the rotational and vibrational motion of the molecules in a fluid, while shear viscosity is related to translational motion [57].

Bulk viscosity enters the viscous equations through the longitudinal wavenumber, as shown in equation (2.29). The complicated nature of the viscous acoustic radiation force equations does not lead to a straightforward conclusion on how changes in bulk viscosity will affect the final value for acoustic force. Though, we can see from equation (2.29) that a very large bulk viscosity value leads to a small value for the corresponding longitudinal wavenumber. To further explore the effects of bulk viscosity on the value for force, we implemented the traveling wave viscous model for five points along the force versus ka curve (up to $ka = 10$). The model was not implemented for all ka values due to the large computational time required. The bulk viscosity for each material was varied between the maximum and minimum values shown in Table 3.1 (repeated in Table 3.2), while other material properties were held constant. For example, for the case of an air bubble in blood force was calculated for maximum and minimum bulk viscosity values for blood, thus affecting the longitudinal wavenumber

in the surrounding medium, while the material properties of air were held constant. The maximum percent difference in the acoustic radiation force due to changes in bulk viscosity for each material are shown in Table 3.2.

Table 3.2: Percent Difference in Force due to Changes in Bulk Viscosity
Air Bubble in Blood

Material	Minumum Bulk Viscosity (<i>g/cms</i>)	Maximum Bulk Viscosity (<i>g/cms</i>)	Maximum Percent Difference %
Blood	0.024	0.034	0.34
Air	0.00012	0.00019	0.14

Lipid in Blood

Material	Minumum Bulk Viscosity (<i>g/cms</i>)	Maximum Bulk Viscosity (<i>g/cms</i>)	Maximum Percent Difference %
Blood	0.024	0.034	0.34
Lipid	2.5×10^6	4.0×10^7	0.0028

As shown in the above table, changes in bulk viscosity had very little effect on the acoustic force. The largest change in acoustic radiation force due to changes in bulk viscosity was created by changing the bulk viscosity of blood. The bulk viscosity value found for lipid material is the most uncertain value in the table, yet changes of over an order of magnitude led to only small changes in acoustic force. However, it must be pointed out that a significantly smaller value for bulk viscosity of lipid would lead to more significant changes in acoustic force. As stated earlier, more certainty in the bulk viscosity would lead to more confidence for real-world modeling results.

Chapter 4

Acoustic Radiation Force: Plane Stationary Wave

4.1 Compressible Sphere in a Viscous Fluid

We will now discuss the equations that describe acoustic radiation force from incident standing waves. In 1962 L.P. Gor'kov derived the same result as Yosioka and Kawasima for standing wave acoustic radiation force. L. Crum, K. Higashitani and others have verified Yosioka and Kawasima's equations for acoustic radiation force on small spheres (where radius \ll wavelength) due to stationary waves [58], [59]. A.A. Doinikov later derived a standing wave expression for radiation force upon viscous compressible spheres in a viscous fluid. His derivation makes no restrictions on the scatterer size [22]. Results for acoustic radiation force upon a compressible sphere by an incident stationary wave is discussed below. For the inviscid case we follow the result of Yosioka and Kawasima. For the viscous fluid case we once again follow Doinikov.

For an incident standing wave, the force on a particle is directly related to its

distance from a nodal plane. A particle in a standing wave field will be pushed towards the nearest pressure node and away from pressure antinodes [60]. Thus, the force on a particle will change directions (and change signs) in both the inviscid and viscous models depending on the distance from a node, see Figure 4.1.

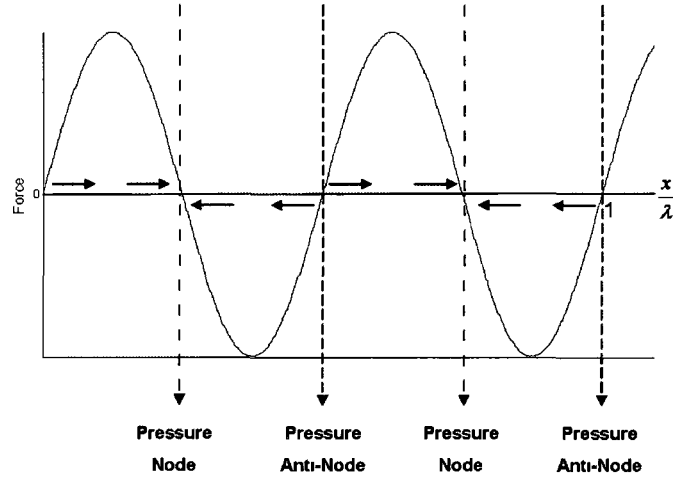


Figure 4.1: Radiation force in a standing wave field. Arrows show the direction of force on particles, pushing them to pressure nodes.

Equations (2.1) - (2.29) used in Chapter 2 still hold for the case of an incident standing wave. The wave solution, ϕ , however, is now a stationary wave and therefore must account for waves moving both to the left and right:

$$\begin{aligned} \phi_{inc} &= e^{ik(z+d)} + e^{-ik(z+d)} \\ &= \sum_{n=0}^{\infty} i^n (2n+1) j_n(kr) P_n(\cos \theta) [e^{ikd} + (-1)^n e^{-ikd}] \quad , \end{aligned} \quad (4.1)$$

where d is the distance from the center of the sphere to the nearest pressure node, see Figure 4.2.

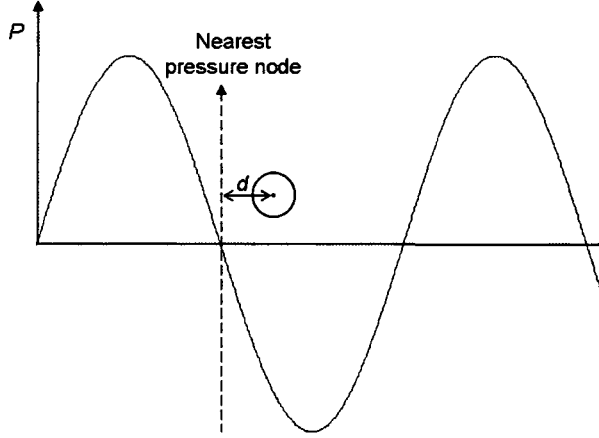


Figure 4.2: Distance, d , from the scatterer center to the nearest pressure node.

Accordingly, the scattered and transmitted wave functions are now described by

$$\begin{aligned}
\phi_{inc} &= \sum_{n=0}^{\infty} i^n (2n+1) j_n(k_1 r) P_n(\cos \theta) [e^{ik_1 d} + (-1)^n e^{-ik_1 d}] , \\
\phi_{scat} &= \sum_{n=0}^{\infty} i^n (2n+1) \alpha_n h_n(k_1 r) P_n(\cos \theta) [e^{ik_1 d} + (-1)^n e^{-ik_1 d}] , \\
\phi_{trans} &= \sum_{n=0}^{\infty} i^n (2n+1) \tilde{\alpha}_n j_n(k_2 r) P_n(\cos \theta) [e^{ik_2 d} + (-1)^n e^{-ik_2 d}] , \\
\psi_{scat} &= \sum_{n=1}^{\infty} i^n (2n+1) \beta_n h_n(K_1 r) P_n^{(1)}(\cos \theta) [e^{iK_1 d} + (-1)^n e^{-iK_1 d}] , \\
\psi_{trans} &= \sum_{n=1}^{\infty} i^n (2n+1) \tilde{\beta}_n j_n(K_2 r) P_n^{(1)}(\cos \theta) [e^{iK_2 d} + (-1)^n e^{-iK_2 d}] .
\end{aligned} \tag{4.2}$$

The second order streaming velocity is still expressed by equation (2.45), and $\langle \vec{v}_0^{(2)} \rangle$ is given by Doinikov as

$$\langle \vec{v}_0^{(2)} \rangle = \frac{i|k_1|^2}{8\omega} \left[(\vec{k}_1 - \vec{k}_1^*) \sin[(k_1 + k_1^*)(z+d)] - (\vec{k}_1 + \vec{k}_1^*) \sin[(k_1 - k_1^*)(z+d)] \right] . \tag{4.3}$$

The acoustic radiation force exerted by a plane standing wave is

$$\begin{aligned}
F = & \frac{3}{4}\pi\rho_1^{(0)} \sum_{n=0}^{\infty} (-1)^n (n+1) (D_n \sin(2k_1 d) + D_n^* \sin(2k_1^* d)) \\
& - \frac{3}{4}\pi\rho_1^{(0)} \frac{k_1 a k_1^* a}{K_1 a^2} \left[(k_1 a - k_1^* a) \sin(k_1 d + k_1^* d) \frac{\sin(k_1 a + k_1^* a)}{k_1 a + k_1^* a} \right. \\
& \left. - (k_1 a + k_1^* a) \sin(k_1 d - k_1^* d) \frac{\sin(k_1 a - k_1^* a)}{k_1 a - k_1^* a} \right] . \tag{4.4}
\end{aligned}$$

Equation (4.4) differs only slightly from (2.49), containing additional expressions that depend on the distance to a nodal plane. Calculating acoustic force due to a standing wave requires only simple changes to the Matlab code that was developed and tested for the plane progressive wave case.

4.2 Compressible Sphere in an Inviscid Fluid

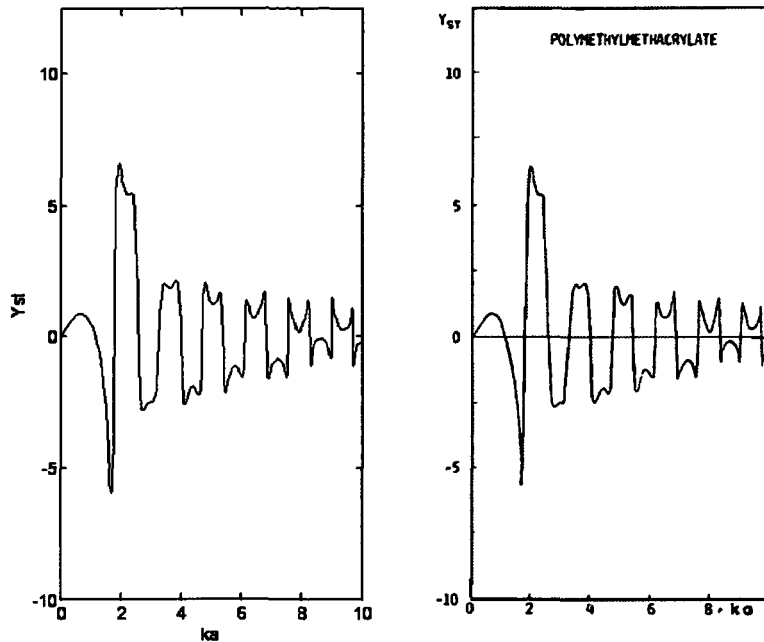
Again, in the inviscid case we only need incident and scattered scalar potential velocities. As shown in equation (4.2), the standing wave case differs from the progressive wave case by a factor of $[e^{ik_1 d} + (-1)^n e^{-ik_1 d}]$. Plugging velocity potential into equation (2.61), we get the following equation for the radiation force of an incident plane

standing wave in an inviscid fluid [61]

$$\begin{aligned}
F = & -4\pi\rho k_1 a^2 \sum_{n=0}^{\infty} (-1)^{(n+1)} (n+1) (U'_n U'_{n+1} + V'_n V'_{n+1}) \sin(2kd) \\
& + 4\pi\rho \sum_{n=0}^{\infty} (-1)^{(n+1)} n(n+1)(n+2) (U_n U_{n+1} + V_n V_{n+1}) \sin(2kd) \\
& + 4\pi\rho k_1 a \sum_{n=0}^{\infty} (-1)^{(n+1)} (n+1) [n(U_n U'_{n+1} + V_n V'_{n+1}) \\
& - (n+2)(U'_n U_{n+1} + V'_n V_{n+1})] \sin(2kd) \\
& - 4\pi\rho k_1 a^2 \sum_{n=0}^{\infty} (-1)^{(n+1)} (n+1) (U_n U_{n+1} + V_n V_{n+1}) \sin(2kd) ,
\end{aligned} \tag{4.5}$$

where U_n , U'_n , V_n and V'_n are defined as shown in section 2.3.

The inviscid standing wave code was verified by comparing results using our Matlab code with those published by Hasegawa. Figure 4.3 shows a comparison of results for a Polymethylmethacrylate sphere in water [61].



(a) Matlab result.

(b) Hasegawa's result.

Figure 4.3: Inviscid results for a polymethylmethacrylate sphere in water, showing the radiation force function, Y_{st} , versus ka .

4.3 Standing Wave Results

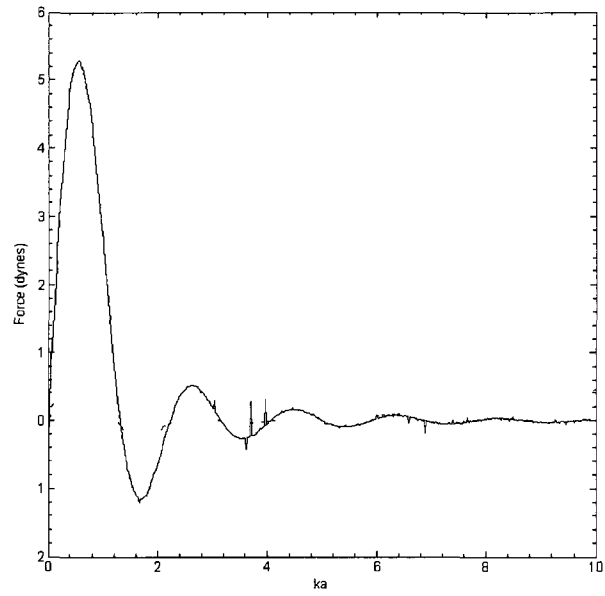
Figures 4.4-4.6 show radiation force results for various material combinations. As mentioned above, in the standing wave case acoustic radiation force upon an object depends on the distance between that object and the nearest node. This distance corresponds to the variable d that appears in standing wave force equations. The plots shown below in 4.4-4.7 are for $d = \lambda/8$. Figures 4.8-4.15 are 3D surface plots showing the dependence of radiation force on both ka and d . The y-axis is d in units of wavelength, i.e. a value of 0.5 is equal to $d = \lambda/2$. Note that the viscous and inviscid code results are plotted with the same axes limits and shading in order to aid

comparison. In seven of the eight cases the force falls to zero at pressure nodes and antinodes as expected (see the following paragraphs for discussion about the case of air in glycerol). For most of the cases the shape of the curve predicted by the viscous model mimics the behavior predicted by the inviscid model. In all cases the viscous model predicts force of a smaller amplitude than predicted by the inviscid model. The large decrease in amplitude is likely due to viscous attenuation. In section 2.5 we showed that for a plane progressive incident wave the viscous and inviscid models predict nearly the exact same result for some material combinations. This trend is no longer true in the standing wave case where viscosity had a significant effect on the force for all eight combinations.

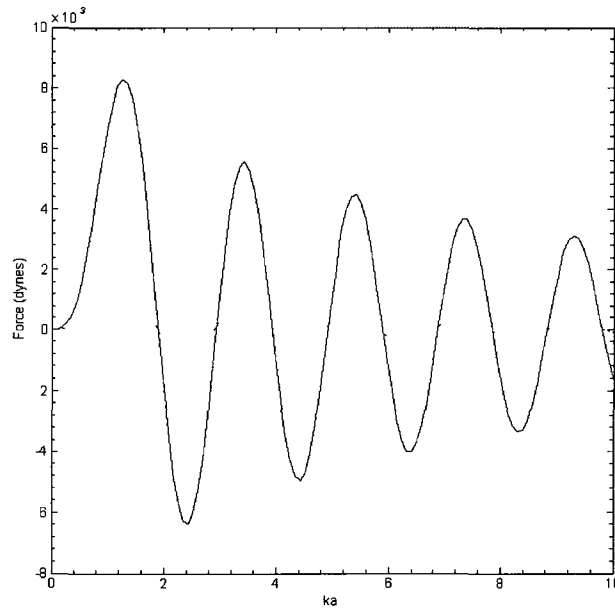
The sharp peaks that show up in the inviscid model for an air bubble in water and an air bubble in glycerol are not caused by numerical issues (such as too coarse of a step size in ka), but are physical resonances. Plotting the force with a finer step size in ka reveals the structure of the resonance peaks. Although it is difficult to see in the plots, due to the scale of the y-axis, these resonance peaks show up at the same ka positions for both the inviscid and viscous models, as expected.

One final result that must be discussed is the non-physical behavior shown in the surface plot for an air bubble in glycerol as ka increases. The force should drop to zero at pressure nodes and anti-nodes. The specific behavior is not caused by lack of convergence. Table 2.4 shows that for the case of an air bubble in glycerol the n -dependent force contribution for n -values larger than $n = 30$ is still six orders of magnitude smaller than the total force. Furthermore, we implemented the full case for this material combination out to $n = 40$ (which took 3250 CPU hours) and observed no change in results from those shown in Figure 4.4. The non-physical behavior for air in glycerol was investigated and is not caused by calculations of large complex arguments in the Bessel functions as discussed in section 2.5 (though that

issue also still affects the standing wave case). Yet, in a similar fashion, the behavior was created when the sine of a large complex number was calculated, resulting in $+/-\infty$. The first point where we can be sure that non-physical results show up in the surface plot is when the force does not fall to zero for all ka values as it should at $\frac{1}{4}\lambda$. The plot at $d = \lambda/8$ shows non-physical behavior as early as $ka = 5$ when resonance peaks disappear and the force begins steadily increasing. Note that the standing wave equation implementation also suffers from the issues created by large complex arguments in Bessel functions. As with the progressive wave models, we hope to see future work in the field that could provide experimental verification of the viscous model equations.

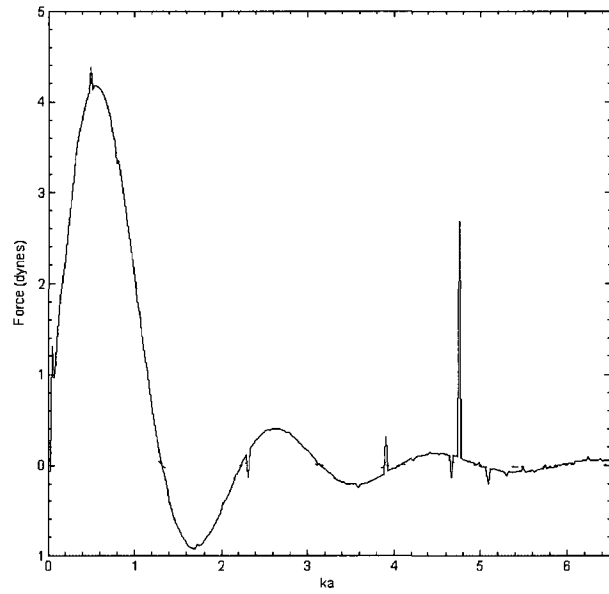


(a) Air in glycerol

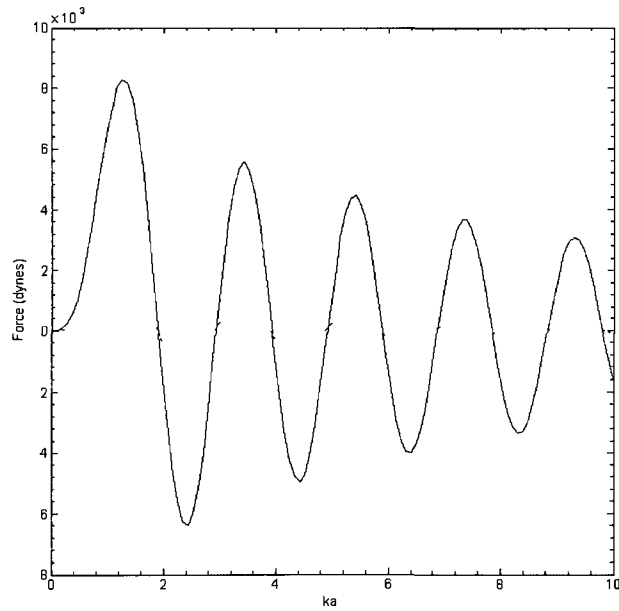


(b) Glycerol in air

Figure 4.4: The solid line is radiation force from the inviscid model and the dashed line is the result from the viscous model. All plots correspond to a nodal distance of $d = \lambda/8$.

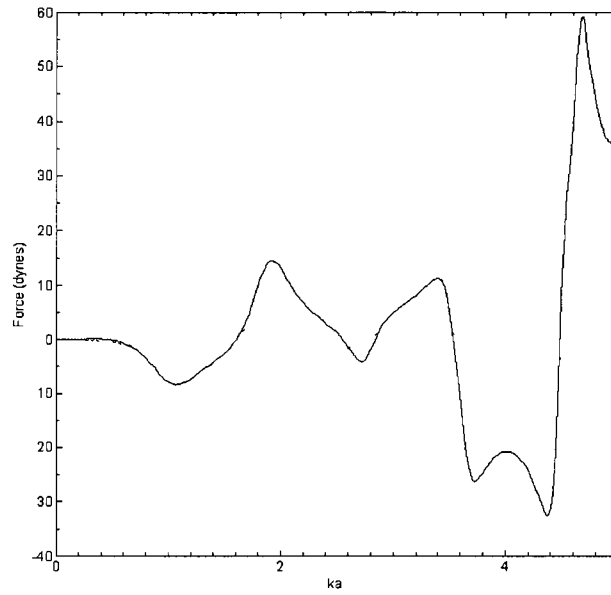


(a) Air in water

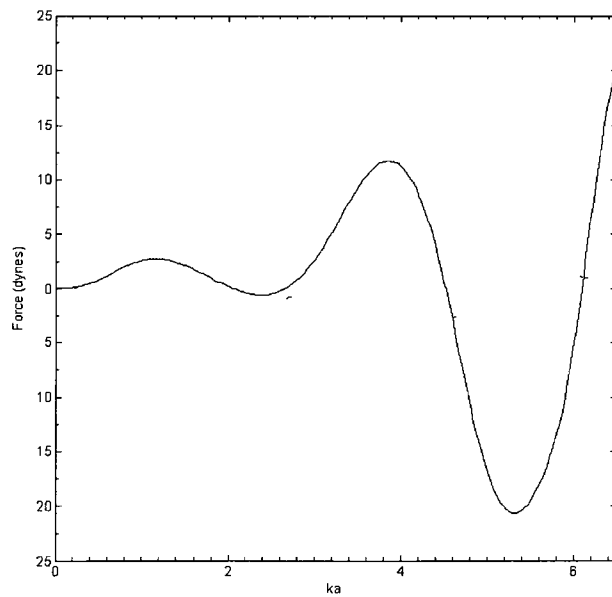


(b) Water in air

Figure 4.5: The solid line is radiation force from the inviscid model and the dashed line is the result from the viscous model. All plots correspond to a nodal distance of $d = \lambda/8$.

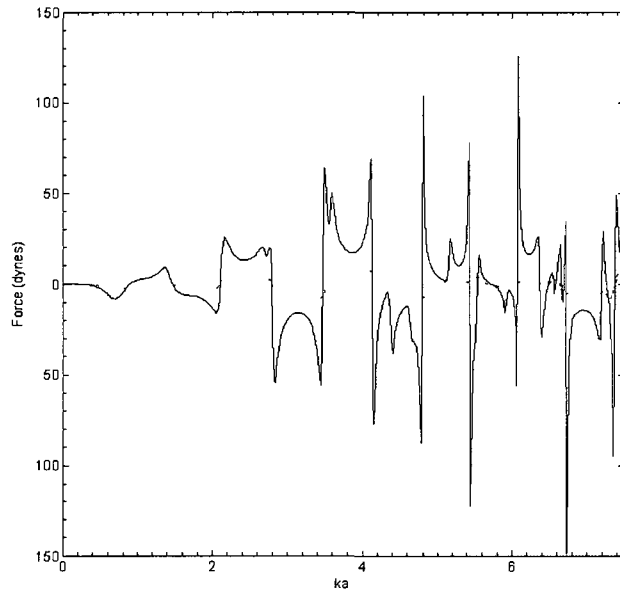


(a) Water in glycerol

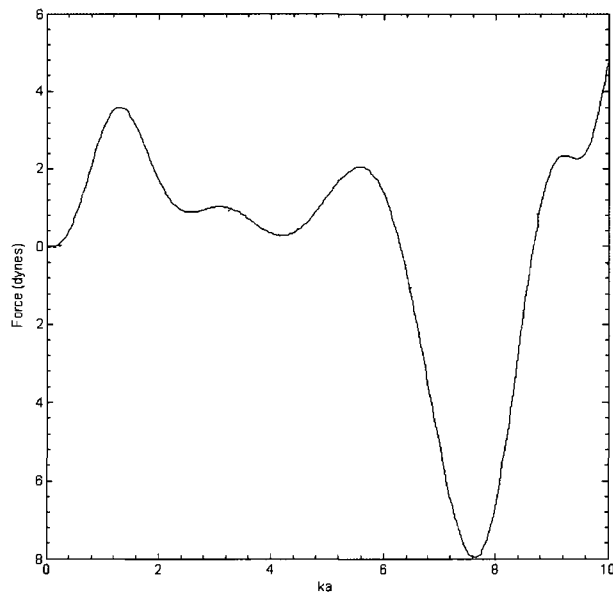


(b) Glycerol in water

Figure 4.6: The solid line is radiation force from the inviscid model and the dashed line is the result from the viscous model. All plots correspond to a nodal distance of $d = \lambda/8$.

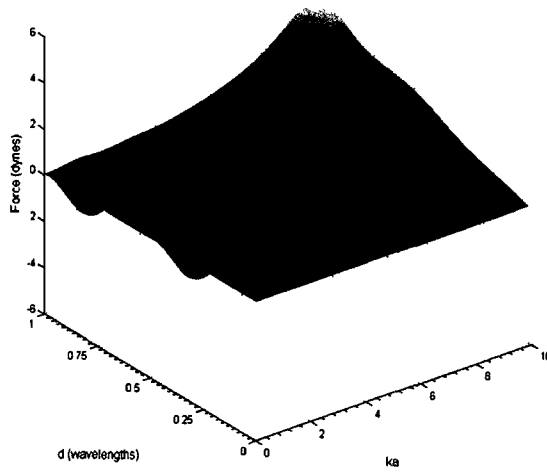


(a) Ethanol in glycerol

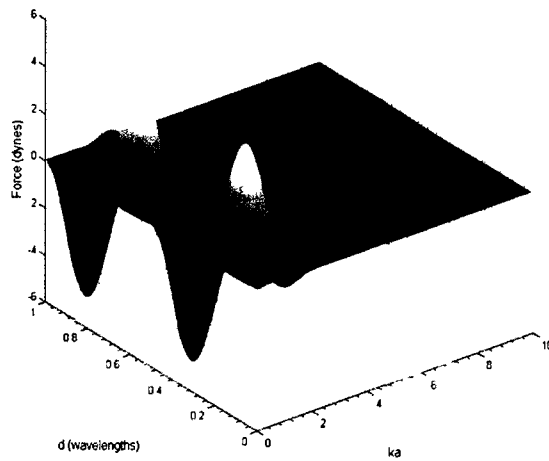


(b) Glycerol in ethanol

Figure 4.7: The solid line is radiation force from the inviscid model and the dashed line is the result from the viscous model. All plots correspond to a nodal distance of $d = \lambda/8$.

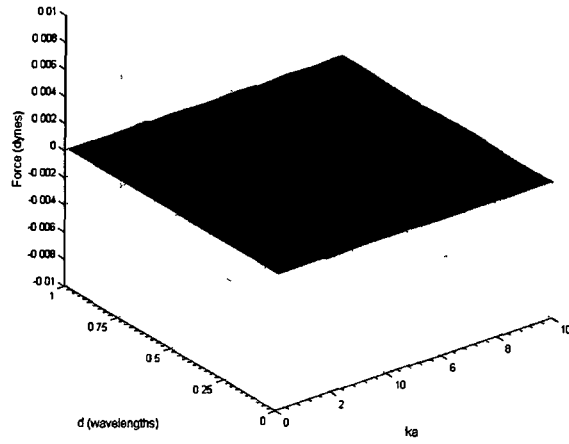


(a) Viscous code result.

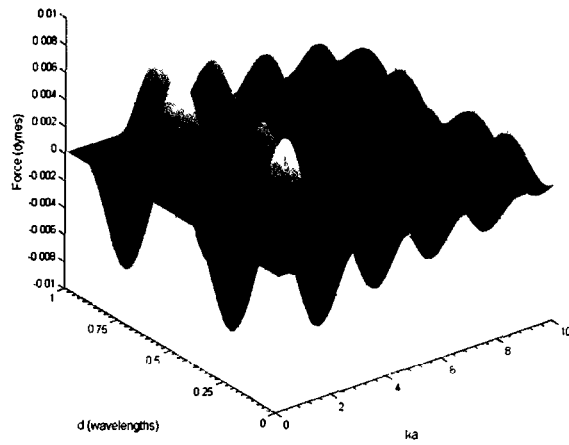


(b) Inviscid result.

Figure 4.8: Acoustic force result for an air bubble in glycerol.

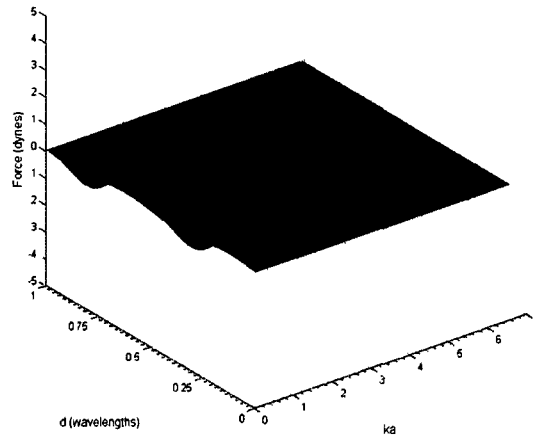


(a) Viscous code result.

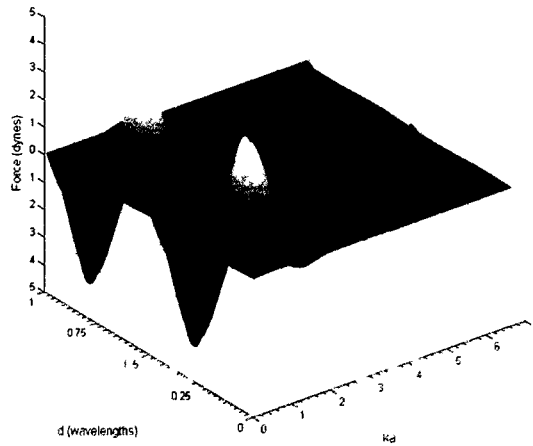


(b) Inviscid result.

Figure 4.9: Acoustic force result for a glycerol droplet in air.

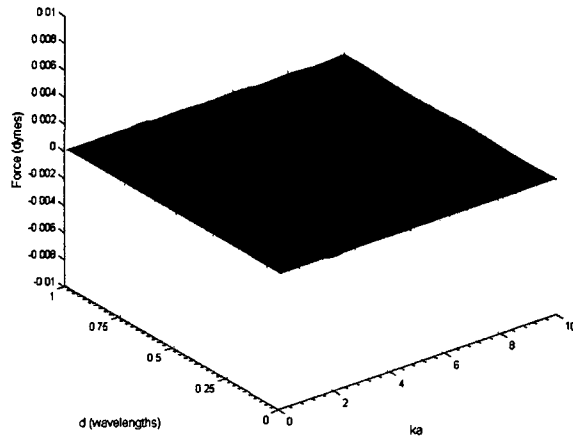


(a) Viscous code result.

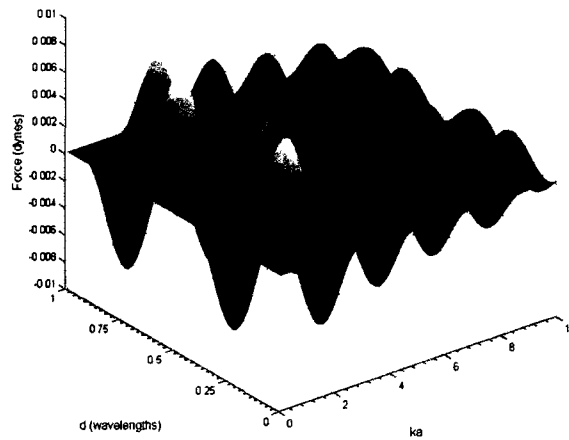


(b) Inviscid result.

Figure 4.10: Acoustic force result for an air bubble in water.

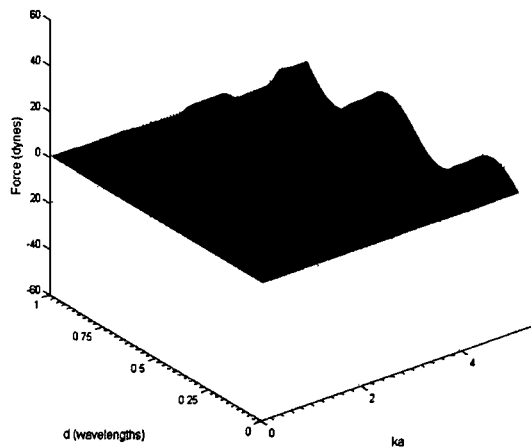


(a) Viscous code result.

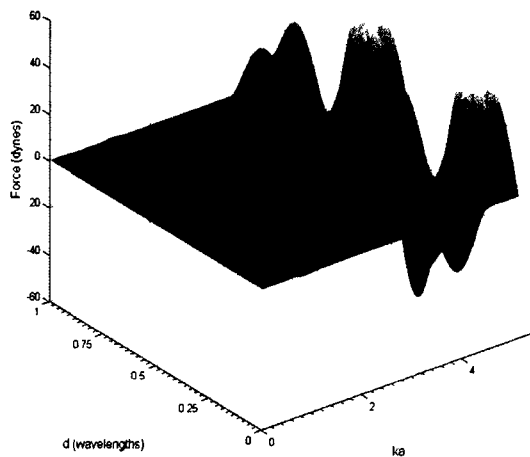


(b) Inviscid result.

Figure 4.11: Acoustic force result for a water droplet in air.

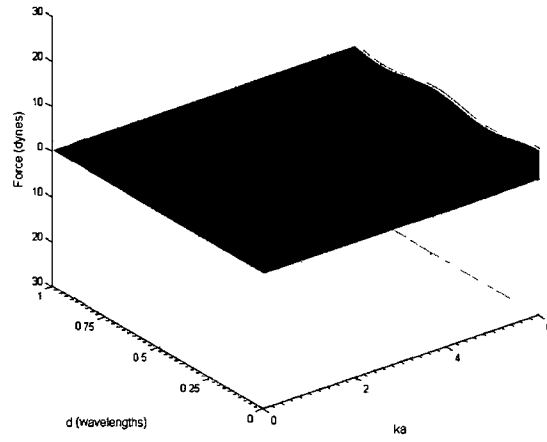


(a) Viscous code result.

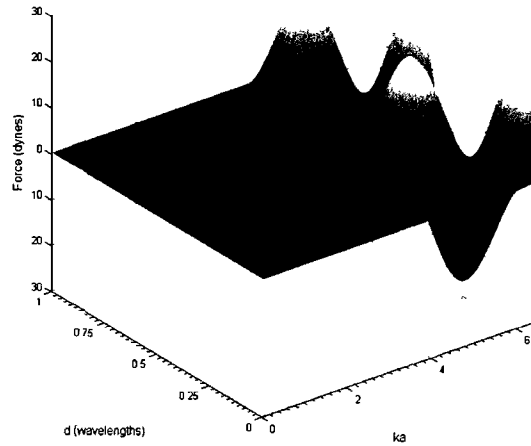


(b) Inviscid result

Figure 4.12: Acoustic force result for a water droplet in glycerol.

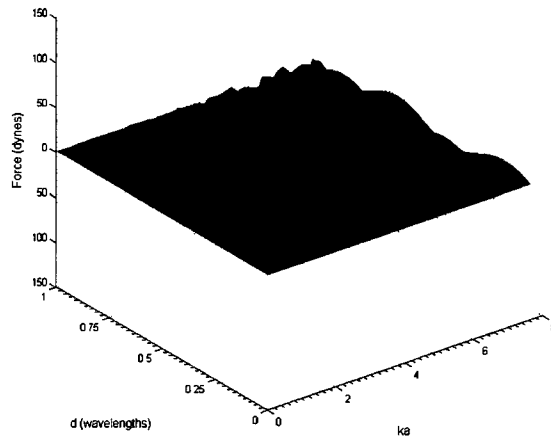


(a) Viscous code result.

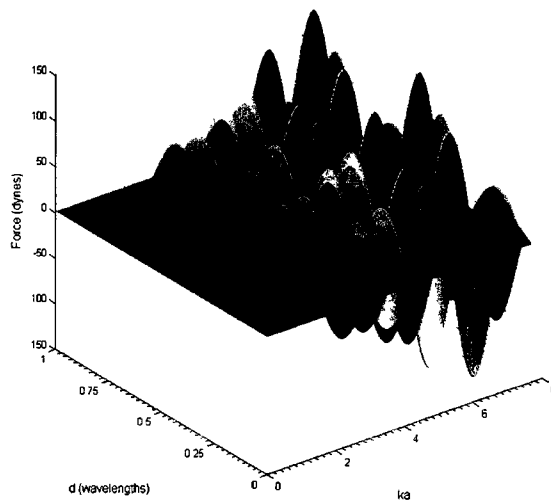


(b) Inviscid result.

Figure 4.13: Acoustic force result for a glycerol droplet in water.

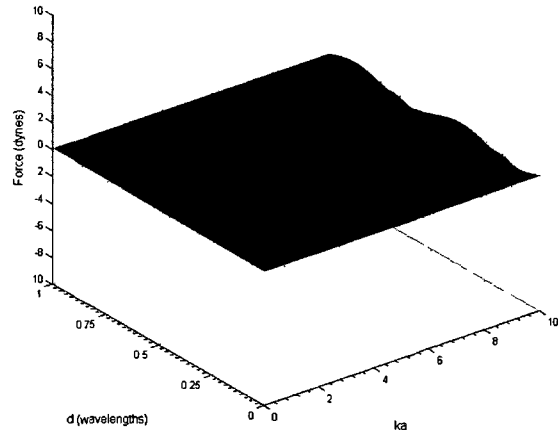


(a) Viscous code result.

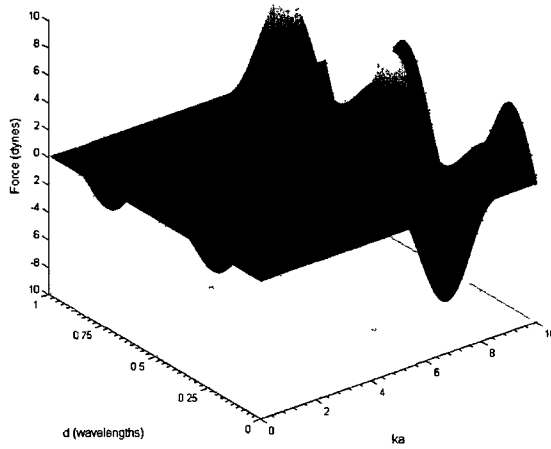


(b) Inviscid result.

Figure 4.14: Acoustic force result for an ethanol droplet in glycerol.



(a) Viscous code result.



(b) Inviscid result.

Figure 4.15: Acoustic force result for a glycerol droplet in ethanol.

Chapter 5

Acoustic Particle Separation for Microalgae Biofuels

5.1 Background

Particle separation via acoustic radiation force is an active field of study with numerous applications, such as ultrasound assisted sedimentation, enhanced biosensor sensitivity, and particle sorting [62], [63], [64]. Acoustic standing waves have also been used to manipulate liquid drops via acoustic levitation for microgravity material processing [65], [66]. Particles in a standing wave field are pushed towards nodes or anti-nodes depending on their acoustic properties. One method of acoustic particle separation uses standing waves to push particles to specific positions in the field where they can be sorted when particle columns are transported by wave envelopes or laminar flow to outlet channels [64], [67], [68]. The most common techniques require precise alignment of a transducer and reflector on either side of a channel of width $w = \frac{1}{4}n\lambda$ where, n is an integer and λ is wavelength, see Figure 5.1. There are less common techniques that do not require this precise alignment which rely on the

excitation of bending modes in a capillary containing the microparticles [69], [70].

Acoustic separation has benefits over traditional separation methods such as filtration and centrifugation because acoustic separation devices do not have the problems of filter clogging, mechanical issues with moving parts, or large space requirements [71], [62]. However, efficient particle separation via standing waves requires a precise knowledge of both acoustic radiation force and fluid dynamics. A transducer frequency must be chosen that results in adequate particle column separation distances (which affects processing times), while avoiding acoustic cavitation and acoustic streaming. Lower frequency transducers will result in larger distances between particle bands. Greater distances between bands will make particle collection easier. However, cavitation occurs more easily at lower frequencies. Cavitation is the creation of gas bubbles that can rapidly collapse, leading to large local pressure and temperature gradients, and is an unwanted event in acoustic particle separation because it breaks up particle banding. As frequency increases larger pressure amplitudes are required to induce cavitation, therefore, cavitation is less likely to occur during separation. Yet, a further complication is that at higher transducer frequencies acoustic streaming (discussed in section 5.1.4) occurs, which also disturbs particle bands [67]. Acoustic streaming can be prevented through sufficient transducer cooling, the use of tone bursts, and by maintaining a small free path length [72].

The use of stationary waves to collect particles at nodes or anti-nodes was experimentally investigated as early as 1874 by Kundt and Lehmann and in 1936 by Söllner and Bondy [73], [74]. Söllner and Bondy studied the use of acoustic radiation force to drive particles into groups at nodal positions, where increased particle coagulation then occurs due to inter-particle forces. Since these early experiments many authors have investigated the effects of acoustic stationary waves on particles immersed fluids. In the past three decades numerous authors in the field have focused on the use of 1-3

MHz frequency transducers to manipulate $1 - 50\mu m$ sized particles such as animal cells, erythrocytes, algal cells, polystyrene and latex spheres [62], [75], [76]. For very small particles where $ka \ll 1$ an acoustic force as small as $10^{-15} N$ ($10^{-10} dyn$) has been reported as adequate for particle concentration [77]. Acoustic particle manipulation techniques are discussed in detail in the sections 5.1.1 - 5.1.3.

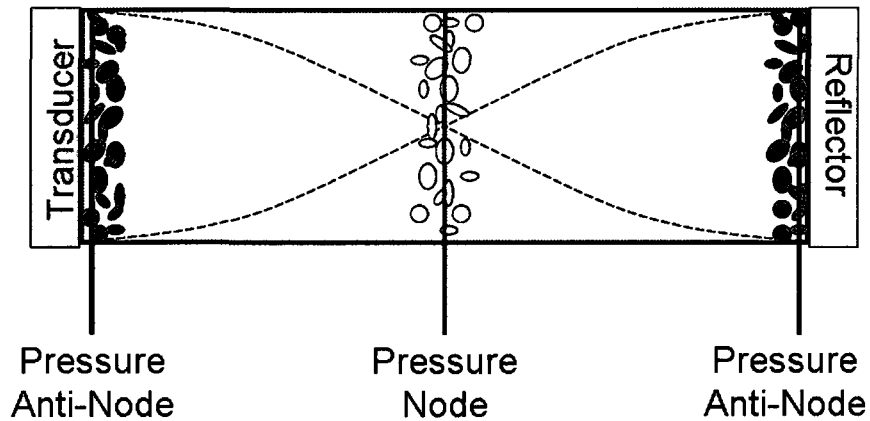


Figure 5.1: Acoustic particle separation via standing waves: particles move to pressure nodes or anti-nodes in a standing wave field depending on their acoustic properties (adapted from [78]).

5.1.1 Acoustic Sorting

In the early 1990s Feke and collaborators investigated the combination of acoustic standing wave particle banding and laminar flow based separators in order to collect particles based on their acoustic properties and size [79], [80]. Mandralis and Feke demonstrated that the acoustic contrast factor and size of a particle determines its response to acoustic radiation force. For a small compressible sphere in a standing wave (in an inviscid fluid) the acoustic contrast factor, C_F , is found by dropping higher order terms in equation (4.5), as described by Yosioka and Kawasima in their

derivation of acoustic radiation force in an inviscid fluid [19].

$$C_F = \frac{1}{3} \left[\frac{5\rho_p - 2\rho_f}{\rho_f + 2\rho_p} - \frac{\beta_p}{\beta_f} \right], \quad (5.1)$$

where ρ_p is the density of the particle, ρ_f is the density of the fluid, β_p is compressibility of the particle, and β_f is compressibility of the fluid. When a standing wave is applied to particles in a fluid some particles will move more quickly to nodal positions than others. Furthermore, particles with a negative acoustic contrast factor will move towards pressure antinodes while particles with a positive contrast factor will move towards nodes [81], [80]. This phenomenon can be used in combination with fluid flow to sort particles of a variety of sizes and contrast factors into different outgoing streams, see Figure 5.2, which is based on the flow path diagram by Mandralis and Feke [79]. Mandralis and Feke used a 722 *kHz* transducer at power levels up to 10 *W* to insonify 10^6 *particles/mL* in an acoustic chamber at acoustic intensities up to 76.5 *J/m³* to successfully separate particles based on size.

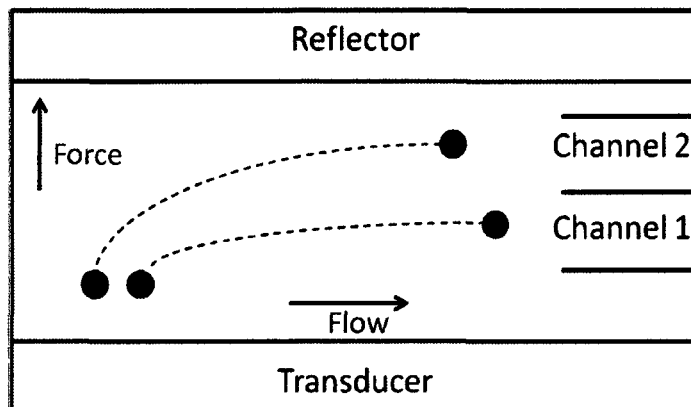


Figure 5.2: Flow path diagram showing two particles that move at different rates towards pressure nodal/antinodal positions due to standing waves. Introducing lateral movement, via laminar flow for example, can transport the particles into different outlet channels based on their acoustic properties (adapted from [79]).

Johnson and Feke also studied particle separation using standing waves. They created a half-wavelength wide flow-through chamber inside which they set up standing waves using a 250 *kHz* transducer at power levels of 4.8 to 20 *mW*. They successfully separated 100 μm from 170 μm polystyrene beads immersed in a fluid using three flow outlets: one for the carrier fluid, one for the small beads and one for the larger beads. The experiment yielded separation efficiencies up to 99.14% at flow rates of approximately 0.34 *L/hr*.

In recent years Nilsson, Petersson, and collaborators have used separation channels (350 μm wide channels) and standing waves to separate lipids from blood with the intention of removing lipid emboli during cardiac surgery [64], [81], [82]. Flow rates were chosen such that particles could fully make their way to nodal positions before sorting at outlet channels (see Figure 5.3). Suction was applied to the outlet channels to enhance outflow. The small separation channels were observed to operate most efficiently at flow rates around 0.012 *L/hr* [81].

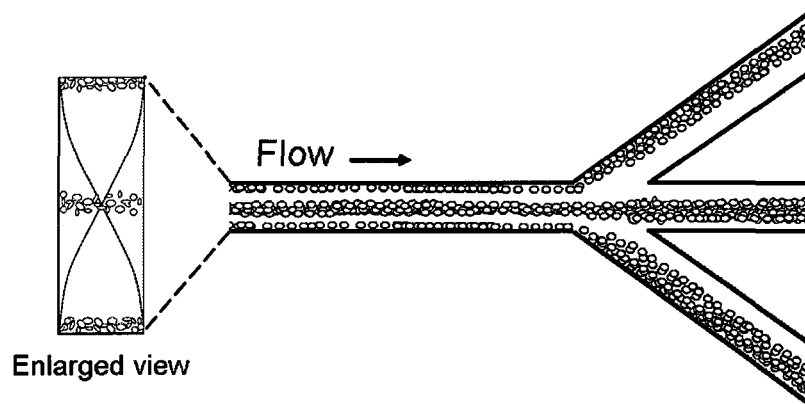


Figure 5.3: Particle separation combining acoustic standing waves and fluid flow through a separation chip. This figure shows the design used by Petersson and others [81], [83]. Other chip designs have been studied [84].

Similar methods of combining standing waves with flow separation devices have been studied by various authors [85], [71], [86]. The experimental setup from a selection of publications can be found in Table 5.1.

Other experimental techniques reported in the literature involve other methods for creating a standing wave field. Kozuka and colleagues set up standing wave micromanipulation experiments using a concave focused transducer [68]. Their results showed that a focused transducer allowed for precise manipulation of particles trapped at the focal point. Additionally, particles at the focal point could be transported laterally through frequency changes in the field. Another technique was investigated by Goddard and Kaduchak and does not rely on precise transducer-reflector alignment as required in the experiments discussed thus far [87]. Instead of using the type of setup shown in Figure 5.1, a cylindrical tube was driven at resonance at frequencies around 420 kHz . The acoustic excitation of the cylinder created a standing wave field inside the chamber. $10\text{ }\mu\text{m}$ polystyrene spheres were successfully concentrated in the center of the cylindrical chamber. Goddard and Kaduchak noted that this technique

allows for lower energy density in the chamber, decreasing the probability of acoustic cavitation.

A recent article reports further on the work performed by Greg Goddard and colleagues at Los Alamos National Laboratory [88]. LANL is part of the National Alliance for Advanced Biofuels and Bioproducts consortium and is continuing research in acoustic methods for processing algae for biofuels. They report that acoustic concentration via standing waves is an efficient way of separating biomass from water using “hundreds of times less power than centrifuges” [89]. The group is also investigating the use of acoustic cell lysing followed by acoustic oil fractionation (a method discussed in section 5.1.3).

5.1.2 Separation Via Acoustically Enhanced Sedimentation

Coakley, Whitworth, Gould and collaborators have studied the collection of micron sized particles at half wavelength intervals. They experimentally investigated the threshold pressure amplitudes for particle banding, the transport of particle groups via acoustic field modulation, and particle sedimentation [90], [91]. In ultrasound-assisted sedimentation particles are pushed into groups at nodes or anti-nodes. At nodal positions the particles that are a short distance from each other, approximately one particle diameter or less, may experience attractive interparticle forces. Interparticle forces can arise due to acoustic field scattering from neighboring scatterers [92]. Additionally, Bernoulli interactions due to pressure differences in the fluid can cause further agglomeration [93]. Furthermore, frequency modulation can be used to cause lateral particle movement which can assist particle clumping and transport [94]. Once the particles are grouped the acoustic field is turned off and particle clumps, which have a higher density than individual particles, sink to the bottom of the acoustic chamber where they can be collected. Gould and Coakley also studied the stability

of particle bands in the presence of acoustic streaming and cavitation [67]. Acoustic streaming is briefly discussed in section 5.1.4.

Studies in this field have primarily focused on small lab-scale experiments, with standing wave chambers that are typically around 100 *mL* in volume. The largest scale experiments to date, that we are aware of, were performed by Spengler and Jekel over 10 years ago. They set up both lab-scale and pilot-plant scale acoustic particle separators to remove particles from a suspension [72]. They used a 16-transducer array and a 20 cm x 24 cm x 24 cm acoustic chamber in the pilot-plant scale experiment to create standing waves. Spengler and Jekel found that dividing the free path length in the chamber with acoustically transparent films greatly decreased streaming effects, allowing them to achieve suspended solids separation efficiencies up to 94% (for 2 – 50 μm particles) at flow rates up to 150 L/hr yielding around 0.564 *g/L* of separated solids. Additionally, in the lab-scale experiment the team found that separation efficiency directly related to particle size, ranging from less than 50% for 2 μm particles to 98% for 50 μm particles.

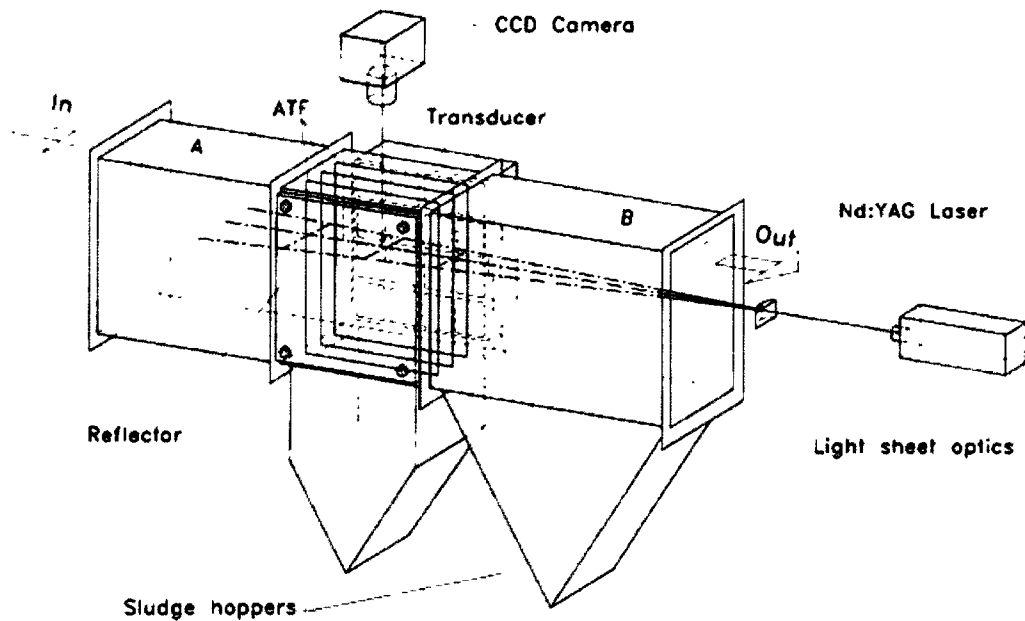


Figure 5.4: Experimental setup used by Spengler and Jekel. Acoustically transparent films (ATF) divide the acoustic chamber to reduce streaming. The ‘sludge hoppers’ collect sedimented particles. The CCD camera and YAG laser are used to view the particle behavior. Image from [72].

F. Trampler and colleagues also worked on developing larger acoustic particle separators. Their work focused on acoustic filtering and sedimentation for enhanced cell perfusion [95]. A commercially available acoustic separation device, the *BioSep*^(R) (Applikon Biotechnology, Schiedam, Netherlands), has been developed based on the work of Trampler et al. The largest *BioSep*^(R) devices work at flow rates around 41.6 L/hr [96].

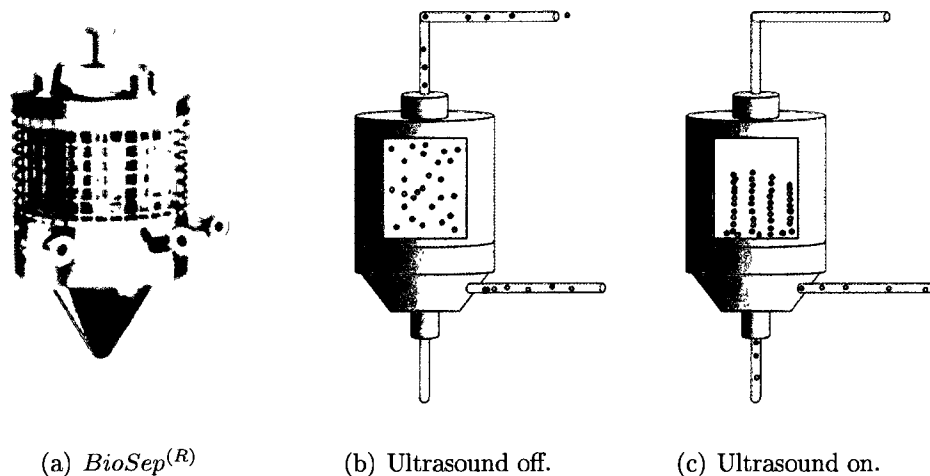


Figure 5.5: *BioSep*^(R) device used for enhanced sedimentation (Applikon Biotechnology, Schiedam, Netherlands). When the ultrasound is turned on the particles form groups and sink to the base of the container where they are removed from the suspension. Images from [96].

R. Bosma and collaborators recently demonstrated that methods of acoustic aggregation and enhanced sedimentation can be applied to harvest microalgae from water [62]. Bosma used a 2.1 *MHz* transducer at power levels up to 8 *W* to drive algae particles into clumps at nodal positions. The acoustic field was switched on for 60 to 300 *seconds* and then turned off for 3 *seconds* to allow particle settling. The acoustic chamber was a 4.5 cm x 1.25 cm x 1.25 cm *BioSep*^(R) chamber and contained algal cell densities ranging from 0.49×10^7 *cells/mL* to 43×10^7 *cells/mL*. At a cell density of 3×10^8 *cells/mL* with ingoing flow rates up to 6 *L/day* the group observed separation efficiencies above 90%. In addition, they found that efficiency levels dropped as the flow rate increased above 6.2 *L/day*. The biomass density was also observed to directly relate to separation efficiency. At low densities the small particle clumps did not lead to high efficiencies. Additionally, very high concentrations led to drops in efficiency because some cells could not be captured. Thus, a balance in cell

density and flow rate is required for high separation efficiencies. A cell concentration of 1×10^8 *cells/mL* is reported to correspond to 0.4 to 0.5 *g/L* dry weight. Thus, a separation efficiency of 90% presumably corresponds to approximately 0.45 *g/L* dry weight of separated biomass.

According to a recent report, two to five grams per liter (by dry weight) would be required for cost-effective biofuel production [88]. These numbers may be reached by further optimizing acoustic techniques.

It should be noted that in particle separation experiments a microscope or high resolution CCD camera combined with a light source is commonly used to observe particle behavior [85], [83], [97]. Additionally, commercially available particle counters such as a Coulter counter, can be used to monitor particle concentration and separation efficiencies [62].

Potential difficulties in acoustic particle manipulation, separation, and sorting techniques are acoustic streaming effects and sample and transducer heating. As mentioned above, acoustic streaming can be prevented through sufficient transducer cooling, using tone bursts, and by maintaining a small free path length [72]. Sample heating can be avoided through cooling techniques. In fact, with flow-through systems, the water flow itself through the acoustic chamber will help reduce heating.

5.1.3 Acoustic Separation of Liquid-Liquid Mixtures

The acoustic particle separation methods described above may also be used for separating immiscible liquid components. Acoustic standing waves can be used to collect liquid droplets of certain physical properties at a location in the acoustic chamber, separating the differing components of a liquid mixture [98], [99]. Peterson describes the use of 1 – 5 *MHz* pseudo-standing waves to concentrate components of immiscible fluids [98]. A specific example presented by Peterson uses a 2.2 *MHz* transducer

at an output power of 5 W/cm^2 to separate two immiscible fluids at a flow rate of 6 mL/min . The initial fluid content was water with an oil content of 22%. After the separation process less than 1 % of the oil remained in the water. Note that in this experimental setup the pseudo-standing wave moves through space at a non-zero group velocity, and therefore the separated droplets are carried through the chamber by the wave.

A similar liquid-liquid separation technique is described by Srinivas for a two phase system consisting of polyethylene glycol and potassium phosphate [100]. In this experiment, standing waves were not created. Acoustic waves were simply applied to increase droplet interaction and cause amalgamation of liquid droplets. The larger drops of one liquid then separate from the second liquid due to the buoyancy force. Srinivas used a transducer with a frequency of 1.2 MHz at a power level of 1.2 W/cm^2 to apply acoustic energy to the sample. A diagram of Srinivas' experimental setup is shown in Figure 5.6. When the experimental results were compared to simple demixing under gravity Srinivas concluded that the demixing times were cut in half, or more, by using acoustics to assist in separation. Srinivas and colleagues also investigated the effects of adding yeast cells to the two phase system. The group found that the addition of the microbial cells to the two phase system led to increases in demixing time. Therefore, particulate matter such as contaminants or cell debris could affect the efficiency of this method.

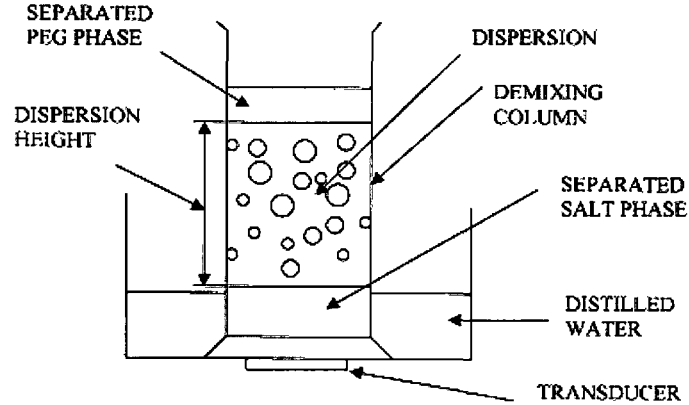


Figure 5.6: Srinivas experimental setup. Image from [100].

A third example of acoustic liquid-liquid separation is given by Varadaraj, who describes a method in which a water-in-oil emulsion is demulsified using ultrasound, without creating acoustic standing waves [99]. The emulsion is sonicated for approximately two minutes in a continuous pulse mode at frequencies between 15 to 20 MHz at 25 to 500 W/cm^2 , causing a separation of oil and water phases. The phase separation occurs when sonication “breaks the interfacial film in the emulsion” and the lower density liquid (oil in this case) rises to the surface. Varadaraj specifically describes the use of this method for crude oil emulsions and suggests that chemical demulsifiers can be added to the emulsion to aid in separation.

The acoustic specifications used in the experiments discussed in sections 5.1.1 - 5.1.3, as well as additional examples, are listed in Tables 5.1-5.2. Note that reported power levels may correspond to acoustic power or applied electrical power because in many cases in the literature the type of power is not specified, but only reported.

Table 5.1: Summary of Experimental Specifications in the Literature

Standing Wave Acoustic Particle Separation and Manipulation: Experimental Specifications								
Source	Sample Type	Particle Size	Transducer Frequency	Power	Chamber Volume	Particle Concentration	Maximum Flow Rate	Separation Efficiency
Mandralis 1993 [80]	Polystyrene spheres in water	2 to 30 μm	722 kHz	up to 10 W	0.035 mL	10^8 spheres/mL	20 mL/min (1.2 L/hr)	95%
Dobhoff-Dier 1994 [76]	Hybridoma cells in an RPMI medium	Not Specified (NS)	2.2 MHz	up to 50 W	up to 100 mL	8×10^5 cells/mL	13 L/hr	85% (13 L/hr)
Johnson 1995 [80]	Polystyrene spheres in water	100 and 170 μm	250 kHz	up to 20 mW	8.59 mL	NS	5.6 mL/min (0.34 L/hr)	99%
Yasuda 1995 [85]	Polystyrene spheres in water	1 to 10 μm	500 kHz	NS (180V)	0.045 mL	up to 3×10^6 spheres/mL	5 mm/s	90%
Hill 2000 [101]	Sand particles separated from water	60 μm	1 MHz	50 W	9.4 mL	NS	20 L/hr	97%
Hawkes 2001 [83]	Yeast cells and polystyrene spheres in water	5 to 25 μm	3 MHz		0.05 mL	4.5×10^7 particles/mL	0.72 L/hr	NS
Araz 2004 [69]	Polystyrene spheres in water	3 and 10 μm	up to 2 MHz	NS (10V)	0.00012 mL	NS	NA	NS
Petersson 2004 [81]	Polyamide spheres (blood phantom) and lipid particles in blood	5 μm	2 MHz	NS	7.2 mL	NS	0.3 mL/min (0.018 L/hr)	85%
Goddard 2005 [87]	Polystyrene spheres in water	10 μm	tube driven at 417 kHz to 462 kHz	tube driven at 1 W	11 mL	2.6×10^8 spheres/mL	25 mm/s	NA

Table 5.2: Summary of Experimental Specifications in the Literature

Pseudo-Standing Wave Acoustic Particle Separation and Manipulation: Experimental Specifications								
Source	Sample Type	Particle Size	Transducer Frequency	Power	Chamber Volume	Particle Concentration	Particle Transport Rate	Separation Efficiency
Whitworth 1991 [91]	Polystyrene spheres in water	9 μm	3.10 - 3.24 MHz	NS (80 V)	46 mL	NS	24 mm/s	93%
Kozuka 2000 [68] Saito 2002 [94]	Aluminum particles Euglena	16 μm 10x50 μm	4.5 - 7 MHz 2.1 - 3.9 MHz	NS (40 V) up to 20 mW/mm ² (2 W whole chamber)	NS 0.1 mL	NS NS	NS NS	NS 80% (trapping efficiency)
Standing Wave Acoustic Particle Sedimentation: Experimental Specifications								
Source	Sample Type	Particle Size	Transducer Frequency	Power	Chamber Volume	Particle Concentration	Flow Rate	Separation Efficiency
Trampler 1994 [95]	Hybridoma cells	NS	2.5 MHz	NS	32 mL	10 ⁶ cells/mL	1.0 L/hr	90%
Pui 1995 [102]	Hybridoma cells	NS	2.45 - 2.5 MHz	up to 180 W/L	75 mL	up to 9.1 x 10 ⁵ cells/mL	0.7 L/hr	90%
Spengler 2000 (plant scale) [72]	Oxidized iron and manganese	2 - 50 μm	3.3 MHz	200 W	up to 10 L	up to 600 mg/L (10 ⁷ to 10 ⁸ particles/L)	150 L/hr	94%
Spengler 2000 (lab scale) [72]	Oxidized iron and manganese	2 - 50 μm	3.3 MHz	45 W	up to 375 mL	up to 600 mg/L (10 ⁷ to 10 ⁸ particles/L)	12 L/hr	98%
Bosma 2003 [62]	Microalgae (Monodus subterraneus)	4 μm	2.1 MHz	up to 8 W	7 mL	10 ⁷ cells/mL	up to 18 L/day (0.75 L/hr)	90% at 6 L/day
Liquid-Liquid Separation: Experimental Specifications								
Source	Emulsion	-	Transducer Frequency	Power	Chamber Volume	-	Flow Rate	-
Peterson 1991 [98]	Oil in water	-	2.2 MHz	5 W/cm ²	15.6 mL	-	6 ml/min	-
Srinivas 2000 [100]	Polyethylene glycol/ potassium phosphate	-	1.2 MHz	1.2 W/cm ²	100 mL	-	Not Applicable (NA)	-
VaradaraJ 2004 [99]	Oil in water	-	20 kHz	50 to 350 W/cm ²	NS	-	NA	-

5.1.4 Acoustic Streaming

Acoustic streaming is a fluid flow effect that can occur in real fluids with or without the presence of a boundary and can be created in progressive and standing wave fields [103]. Acoustic streaming often takes the form of circular flow patterns. The circulatory stirring behavior of acoustic streaming can have a disruptive effect on standing wave fields. In the context of particle separation, using stationary waves, streaming is an unwanted event; it is a desirable phenomenon when utilized for acoustic mixing of microparticles [104]. We will briefly discuss three types of acoustic streaming, Schlichting, Rayleigh and Eckart (or 'quartz wind') streaming.

Both Rayleigh and Schlichting streaming occur due to the presence of a boundary, such as container walls or a scatterer. Acoustic energy is attenuated in the viscous boundary layer. Energy dissipation creates changes in momentum flux, leading to circulatory streaming patterns near the boundary, see Figure 5.7 (a) [105]. Rayleigh streaming is on the scale $ka \approx 1$, while Schlichting streaming is a smaller scale phenomenon associated with $ka \ll 1$ [106].

Eckart streaming occurs when acoustic energy is dissipated in the fluid itself due to viscosity. Acoustic energy attenuation creates differences in stress on each side of a fluid element see, Figure 5.7 [107]. The change in stress causes physical movement of the fluid particles. Eckart streaming is a macro-scale phenomenon (on a scale much larger than wavelength, $ka \gg 1$) that can pull particles from standing wave particle bands. Short fluid flow path lengths can help to prevent Eckart streaming, as discussed in section 5.1.2 [93].

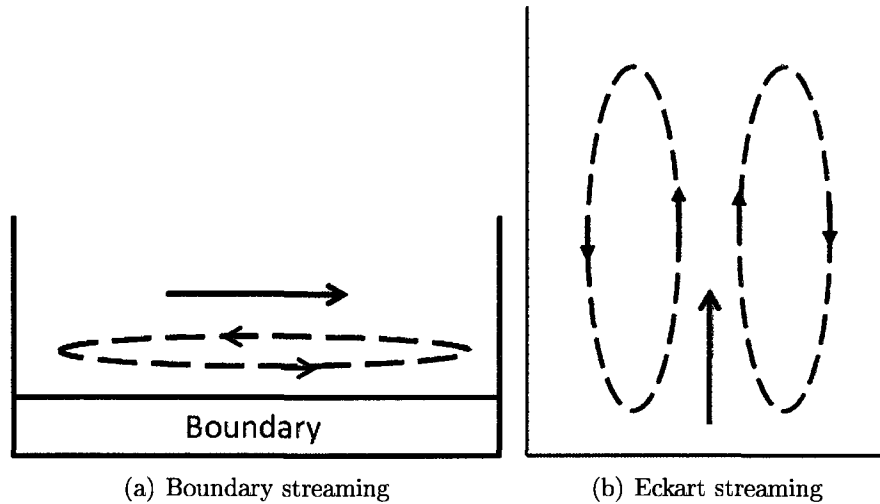


Figure 5.7: Examples of streaming patterns with direction of source wave propagation shown by the solid black arrow, (a) Boundary streaming [105], (b) Eckart streaming inside fluid-filled container [93].

5.2 Microalgae Biofuels

The global demand for energy has risen dramatically in recent years as the world population grows and as standards of living around the world increase [108]. These developments have led to a global realization that petroleum based fuel sources, which are being depleted, are unsustainable. At the same time, increased environmental awareness has led to a societal desire for both sustainable and environmentally friendly fuel sources. Biofuels, including corn-based and soybean-based ethanol and biodiesel, are presently used in order to slow down growth of petroleum demand. However, use of these biofuels impacts global food supplies. Furthermore, these crops require the use of large amounts of crop land for growth, which has led to ecological destruction around the world, such as the deforestation of the Amazon rain forest in Brazil to make room for soybean crops [109]. Recent reports have shown that the crop land

conversion required by these traditional biofuel sources actually means that overall, the use of these biofuels results in higher green house gas emissions than the use of petroleum [110]. Crop land is created by methods such as burning forests, plowing open fields, and draining wetlands. Not only do these methods release green house gases into the atmosphere, but this environmental degradation also removes vital CO_2 absorbers. Microalgae is an environmentally friendly alternative source for biofuels.

Microalgae is a term that commonly refers to diatoms, green algae, golden algae, (all eukaryotic microorganisms) and is occasionally used to refer to cyanobacteria (blue-green algae, prokaryotic) [111]. There are many environmental and social benefits to using microalgae as a biofuels source. Microalgae are not currently in demand as a world food source and can be used to make ethanol, biodiesel, biomethane, and biohydrogen. Additionally, microalgae have a much higher oil yield per square mile than other biodiesel sources, and therefore require much less land to produce significant fuel yields. For example, microalgae with 30% oil (by weight) in biomass produces approximately 340 times more oil per square mile than corn [112], and 15 times more oil per square mile than the current bio-oil producing leader, palm oil [113]. Furthermore, microalgae can be grown on non-arable land as well as in fresh and salt water. Since only approximately 13% of the Earth is arable land, decreasing the competition between biofuel and food crops is crucial. Microalgae grow quickly and have short harvesting cycles, and while traditional biofuel crops can be harvested only one to two times a year, microalgae can be harvested almost continuously [113].

Microalgae convert solar energy to chemical energy via photosynthesis. They require water, sunlight, carbon dioxide, and nutrients such as nitrogen and phosphorus for growth [112]. The nutrients and CO_2 needed to grow microalgae can be acquired from sources such as industrial plants, waste water, fresh water, and sea water. Microalgae are efficient CO_2 absorbers. Therefore, the growth of microalgae for biofuels

would have the added benefit of CO_2 sequestration without the output of greenhouse gases from crop land. As suggested by P.M. Schenk et al., the biomass that is not converted to fuel can be processed into agrichar/biochar chips - high carbon content chips that can be used to increase soil fertility [113].

Microalgae are commonly grown in raceways, man-made open ponds or in photobioreactors. Each growth method has pros and cons. Raceways and open ponds require large amounts of space and have high harvesting costs due to the unenclosed (less controllable) growth setup. Photobioreactors can be made in a way that requires much less space (for example, by a vertical tube alignment setup) and have low harvesting costs due to increased containment and species control. Raceways and ponds, however, have lower operating costs than photobioreactors which are a more complex system. Both systems may benefit from an improved harvesting system, which contributes up to 30% of the cost of dried algal biomass [114].



Figure 5.8: Raceway ponds used to grow microalgae at Earthrise Farms, CA, USA (aerial view). Image from www.ieagreen.org.uk.

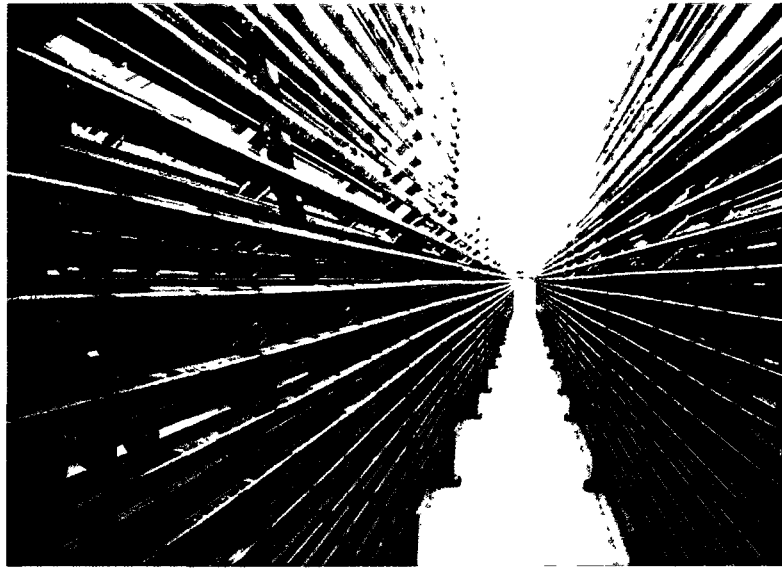


Figure 5.9: Photobioreactor used to grow microalgae (vertical tube alignment setup). Image from www.brae.calpoly.edu.

Microalgae grow naturally in waters all around the globe. Humans are leading to increases in the algal blooms that are caused by water eutrophication (an increase in nutrients). Eutrophication is caused by agricultural waste that contains fertilizers, water from sewage treatment plants, urban water runoff, and other human activities [115]. Although live microalgae absorb carbon dioxide and emit oxygen, oxygen is depleted when dead algae decompose. Thus, an increase in algal blooms also leads directly to hypoxic waters and dead zones where aquatic life cannot survive. Dead zones are expanding around the world, including in the Chesapeake Bay and the Gulf of Mexico. The spread of dead zones has an enormous impact on aquatic species and the fishing industry.

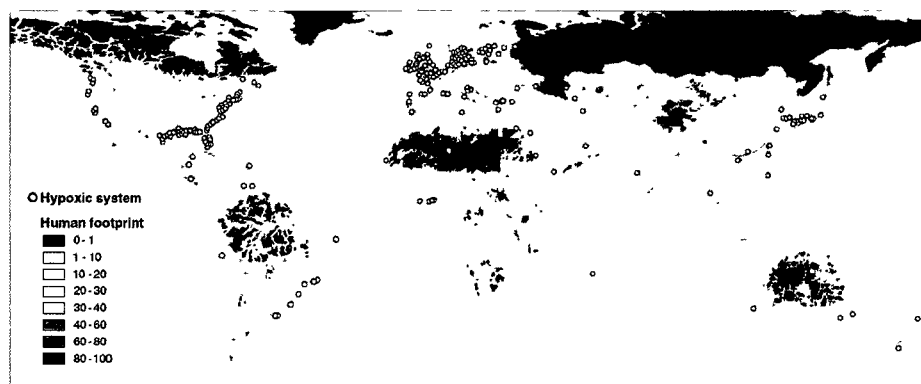


Figure 5.10: White circles represent ocean dead zones. Image from [116].

Microalgae biofuels can be made from wild growing algae that would be collected before decomposition leads to hypoxia. The concentration of free-floating algae in wild blooms is likely not high enough to conceive of efficient harvest size for economic biofuels. Currently researchers (such as collaborators in the Chesapeake Algae Project, ChAP [117]) are researching the possibility of growing wild algae in greater concentrations on man-made materials deployed into bay, river, or open seawaters. However, open water microalgae blooms can contain a single native species, closely related species, or very rarely, mixed class algae [118]. These blooms may include non-desirable alga, such as low lipid content algae. Therefore, it would be beneficial to sort the microalgae based on its content in order to successfully create fuels from wild microalgae. Farmed algae processes would also benefit from the ability to sort algae based on its content. Microalgae are primarily made up of lipids, carbohydrates, and proteins. Microalgae with high starch content are desirable for alcohol production (such as butanol), while algae with high lipid content can be used to make biodiesel. Algal sorting before chemical processing would have three important benefits: 1) high starch content algae can be sorted out to make ethanol, 2) low lipid content biomass leads to low quality biofuels, therefore, sorting out low lipid algae will increase the

quality of the produced biofuels [114], 3) processing costs can be reduced by converting only high oil content algae to diesel. Related work shows that high-lipid content algal cell isolation with wild algal strains is a current topic of interest in the algae biofuels field [119]. We will investigate the use of acoustic separation to harvest microalgae from water and the potential of sorting the algae based on its composition. The potential of acoustically dewatering the algae may lead to increased processing efficiency and lower costs [89].

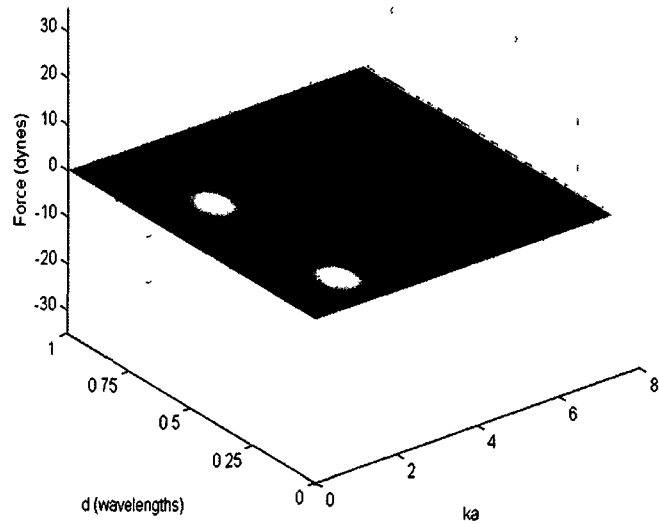
5.3 Modeling Results

We implemented the viscous and inviscid acoustic radiation force models for the cases of an algal cell in seawater and in freshwater. The results (Figures 5.11-5.14) show that the inviscid and viscous models yield very different results for force versus ka , as discussed further below. The material properties used for both cases are shown in Table 5.3. Salt and fresh water have similar material properties, leading to acoustic force results that are very close for the two cases. However, for the case of freshwater the viscous case yields NaN earlier, due to the reasons discussed in section 4.3. Note that the speed of sound and bulk viscosity values used for algae are based on material properties in the literature corresponding to lipids and oils. This approximation was necessary because acoustic properties of algae are largely unavailable in the literature. The density value used for the algal cell is based on a high lipid content algae as discussed by Barsanti and Gualtieri [120]. As with the emboli removal application, our modeling results would be even more appropriate for comparisons to experiment if the required material properties for algae were known more precisely.

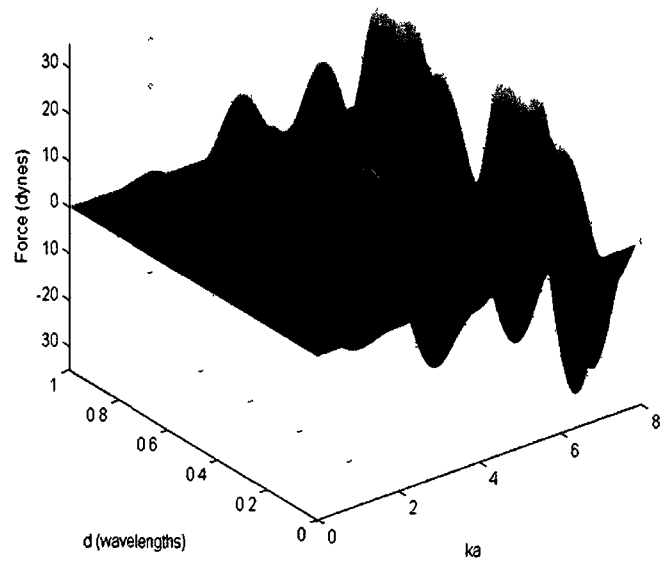
Table 5.3: Material Properties

Material	Density (g/cm^3)	Speed of Sound (cm/s)	Viscosity (g/cms)	Bulk Viscosity (g/cms)
Seawater	1.0268	153,300	0.012	0.03
Fresh water	0.998	148,000	0.0101	0.02
Algae	0.86	147,400	4.0	2×10^6

[120], [121]



(a) Viscous code result.



(b) Inviscid result.

Figure 5.11: Acoustic force result for an algal cell in seawater.

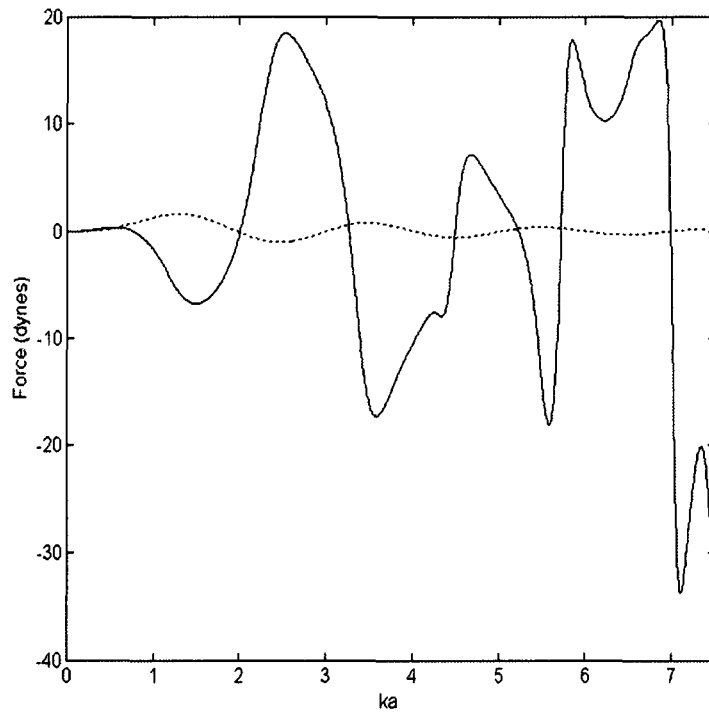
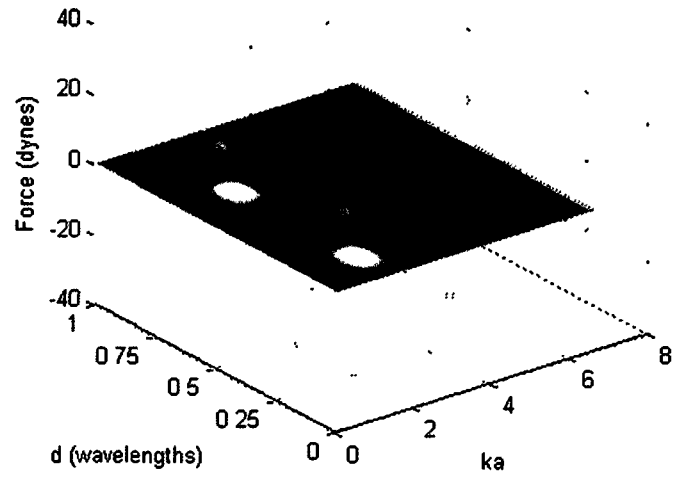
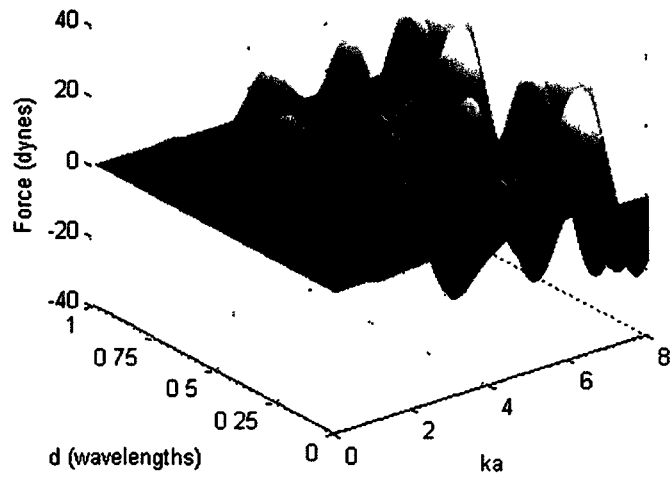


Figure 5.12: The plot shows the inviscid (solid line) and viscous (dotted line) results for an algal cell in seawater at a particle location of $d = \lambda/8$.



(a) Viscous code result



(b) Inviscid result

Figure 5.13: Acoustic force result for an algal cell in freshwater.

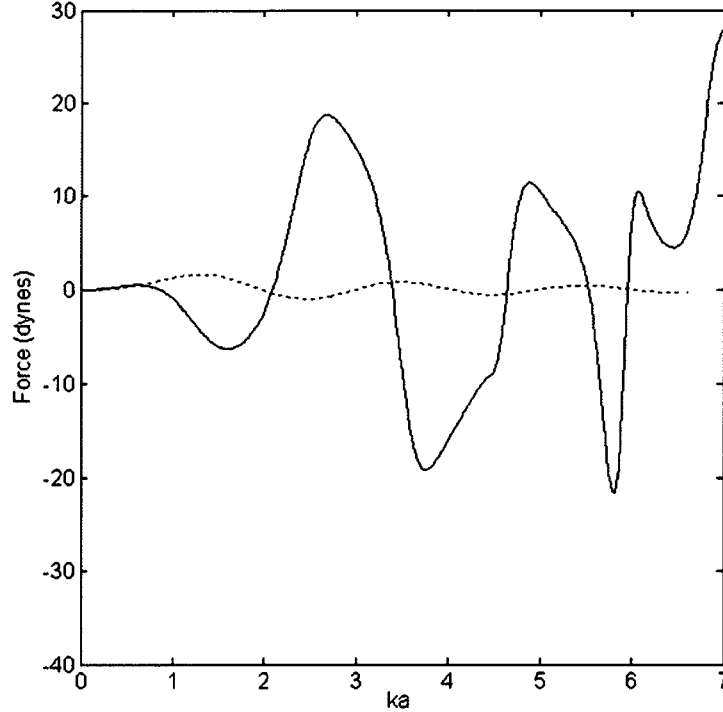


Figure 5.14: The plot shows the inviscid (solid line) and viscous (dotted line) results for an algal cell in freshwater at a particle location of $d = \lambda/8$.

5.3.1 Discussion of Algae Modeling Results

The results of the previous section show that the viscous model predicts a smaller magnitude of force upon the scatterer. This result means that in a real fluid it would take particles longer to move to nodal positions than in an ideal inviscid fluid. Very small algal cells (tens of microns) paired with low MHz range transducers correspond to the low ka region. The most important result from 5.11-5.14 is that the viscous model actually predicts force in a different direction from the inviscid model, even at low ka values. Most researchers in the field of acoustic micromanipulation reference the acoustic contrast factor given in equation (5.1) that is based on the inviscid fluid model. However, according to our results, for some material combinations viscosity

may cause the particles to move much differently than equation (5.1) predicts. Indeed, as suspected by Doinikov, these results help explain the strange movement of particles in a standing wave observed by Avetisyan [3], [122]. He observed the movement of steel particles in a standing wave field in glycerin and found that the particles moved to antinodes rather than nodes as predicted by the inviscid model.

The acoustic force models for a compressible sphere are a start towards understanding the force felt by algal cells in a standing wave field. The results clearly show the importance of viscosity for this material combination. However, the acoustic force model for a single compressible sphere immersed in a fluid is not sufficient for optimizing algal acoustic separation experiments. In order to optimize acoustic sorting methods, knowledge about multiple scattering from non-spherical algal cells in a standing wave field is needed, see Figure 5.15. The effect of increased biomass concentration on the standing wave field is of particular interest for optimizing experimental techniques. Authors such as Bosma have reported that separation efficiency is directly related to biomass concentration in the acoustic chamber [62]. In the following section we will use 3D acoustic standing wave simulations to investigate changes to the standing wave field as particle concentration increases.



Figure 5.15: Algal cells of various shapes. Berkeleya is a common algal species in the York River, VA.

5.4 3D Acoustic Finite Integration Simulations

There are numerous numerical methods for approximating the solutions to partial differential equations. Finite difference time domain (FDTD) is one common technique that has become familiar to many scientists since it was introduced in the 1960s for the purpose of numerically solving Maxwell's equations [123]. FDTD is a technique that turns differential equations into algebraic equations by approximating derivatives as differences [124]. Finite integration technique (FIT) differs slightly from FDTD in that the differential equations are integrated over a control volume (such as a cube in the case of Cartesian coordinates) and then the integrals are approximated [125], [126]. FIT has benefits over the more common FDTD techniques in that it naturally leads to a staggered grid with better stability [16]. Staggered grid FDTD techniques exist, but the staggered grid must be purposefully introduced [17]. FIT also leads to simpler implementation of boundary conditions [17], [126], [125]. Two other common numerical method techniques are Finite Element Method (FEM), which is available in various off-the-shelf software, and Boundary Element Method (BEM). FEM is a technique that approximates the exact solution to a differential equation over elements (subdomains) within the total space [127]. One benefit to FEM is that off-the-shelf software uses sophisticated meshers to break the simulation space into elements that can be non-rectangular, such as tetrahedra. Additionally the spatial step size of the mesh can be varied within a simulation space so that areas needing more detail have smaller elements. The meshers and solvers used in FEM software, however, are complicated and are not nearly as straightforward as FIT. The simplicity of FIT allows it to be implemented in various computer coding languages on any computer and provides full control over the equations involved.

In this chapter we have implemented three dimensional acoustic finite integration

technique (AFIT) simulations to simulate scattering from algal cells in a standing wave field. The AFIT simulation code was written and validated in our lab through comparisons to analytical solutions and experimental results [126]. We set up a standing wave with the AFIT code by specifying a simulation space length that is a multiple of the wavelength of the sinusoidal drive function. The AFIT equations are outlined in detail below. Note that the equations described below and the numerical AFIT simulations that we have performed do not take viscosity into account. The simulations are intended as a start to understanding multiple scattering in a standing wave field. Future work could include viscosity in the 3D AFIT simulations.

We begin by returning to the linearized Navier-Stokes equations in fluid, with pressure (M) and velocity (\vec{F}) source functions added to the right hand side [126], [128]:

$$\partial_t \rho = -\rho_0 \nabla \cdot \vec{v} + M \quad , \quad (5.2)$$

$$\rho_0 \partial_t \vec{v} = -\nabla p + \vec{F} \quad , \quad (5.3)$$

$$(5.4)$$

where we set the viscous terms in the stress tensor equal to zero, so that term one of the right hand side only depends on pressure. Using the equation of state

$$p = c^2 \rho \quad , \quad (5.5)$$

we can rewrite equation (5.2) in terms of pressure

$$\partial_t p = -\rho_0 c^2 \nabla \cdot \vec{v} + M \quad . \quad (5.6)$$

Next we integrate equations (5.6) and (5.3) over a control volume (a cube in this

case).

$$\int_V \partial_t p \, dV = \int_V (-\rho_0 c^2 \nabla \cdot \vec{v} + M) \, dV . \quad (5.7)$$

The first term on the right hand side can be turned into a surface integral using the divergence theorem, resulting in the following equation:

$$\int_V \partial_t p \, dV = - \oint_S \rho_0 c^2 (\vec{v} \cdot dS) + \int_V M \, dV , \quad (5.8)$$

where S is the boundary of volume V . We can treat equation (5.3) in a similar way, again using the divergence theorem,

$$\int_V \rho_0 \partial_t \vec{v} \, dV = - \oint_S p \, dS + \int_V \vec{F} \, dV . \quad (5.9)$$

We take the final step of approximating the integrals in (5.8) and (5.9) over a cubic control volume that is $\Delta x \times \Delta x \times \Delta x$, corresponding to a single grid cell in Figure 5.16, with the pressure and velocity components positioned on the grid as shown in the figure. A discussion of the importance of choosing an appropriate variable placement on the discrete grid can be found in [129]. We'll start with equation (5.8):

$$\partial_t p \Delta x^3 = -\rho_0 c^2 [(v_1^{1+} - v_1^{1-}) + (v_2^{2+} - v_2^{2-}) + (v_3^{3+} - v_3^{3-})] \Delta x^2 + M \Delta x^3 , \quad (5.10)$$

where $v = v_1 + v_2 + v_3$. As shown in Figure 5.16, we follow the notation used in [126]: v_1^{1-} corresponds to velocity in the negative x_1 direction from the center of the cell, and v_1^{1+} corresponds to velocity in the positive x_1 direction from the center of the cell. Similarly we get three equations for the velocity (expanded in three spatial

dimensions)

$$\begin{aligned}
\rho_0 \partial_t v_1 \Delta x^3 &= -(p^{1+} - p^{1-}) \Delta x^2 + F_1 \Delta x^3 , \\
\rho_0 \partial_t v_2 \Delta x^3 &= -(p^{2+} - p^{2-}) \Delta x^2 + F_2 \Delta x^3 , \\
\rho_0 \partial_t v_3 \Delta x^3 &= -(p^{3+} - p^{3-}) \Delta x^2 + F_3 \Delta x^3 .
\end{aligned} \tag{5.11}$$

Finally, we must solve equations (5.10) and (5.11) for pressure and velocity and approximate the time derivatives on the right hand side of each equation. In both cases we will use a difference to approximate the derivative. For $\partial_t p$ use a central-time difference to get

$$p^{(t+\Delta t/2)} = p^{(t-\Delta t/2)} + \dot{p}^{(t)} \Delta t . \tag{5.12}$$

Similarly, to approximate the velocity derivative we used an integer central-time difference,

$$v^{(t)} = v^{(t-\Delta t)} + \dot{v}^{(t-\Delta t/2)} \Delta t . \tag{5.13}$$

Thus, we arrive at a discrete set of equations for pressure and velocity that are staggered in space and time:

$$p^{t+\Delta t/2} = p^{t-\Delta t/2} - \rho_0 c^2 \frac{\Delta t}{\Delta x} [(v_1^{1+} - v_1^{1-}) + (v_2^{2+} - v_2^{2-}) + (v_3^{3+} - v_3^{3-})] + M \Delta t , \tag{5.14}$$

$$\begin{aligned}
v_1^t &= v_1^{t-\Delta t} - \frac{\Delta t}{\rho_0 \Delta x} - (p^{1+} - p^{1-}) + F_1 \frac{\Delta t}{\rho_0} , \\
v_2^t &= v_2^{t-\Delta t} - \frac{\Delta t}{\rho_0 \Delta x} - (p^{2+} - p^{2-}) + F_2 \frac{\Delta t}{\rho_0} , \\
v_3^t &= v_3^{t-\Delta t} - \frac{\Delta t}{\rho_0 \Delta x} - (p^{3+} - p^{3-}) + F_3 \frac{\Delta t}{\rho_0} .
\end{aligned} \tag{5.15}$$

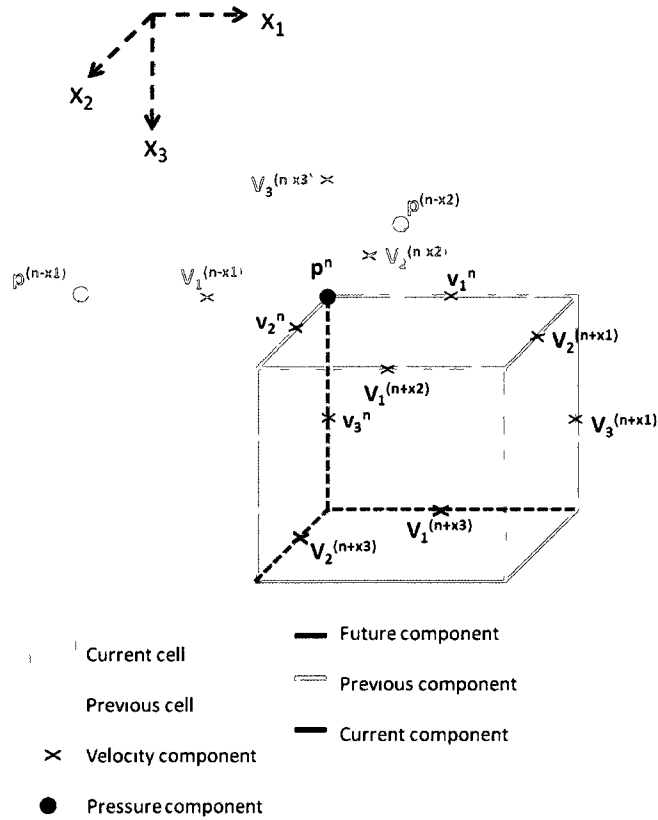


Figure 5.16: Velocity and pressure are staggered in the discrete spatial AFIT grid.

The number of grid cells in the simulation space is determined by assigning a minimum number of grid points to the shortest wavelength in the simulation. The required number of points per wavelength reported in the literature varies, ranging from $\lambda/8$ to $\lambda/15$ [130], [125]. The Courant condition is used to determine the time step size [125], [126]. The stability criteria for the discretization of the simulation are:

$$\Delta x \approx \frac{c_L}{bf_{max}}, \quad (5.16)$$

$$\Delta t \approx \frac{\Delta x}{c_L \sqrt{3}},$$

where c_L and f_{max} are the longitudinal speed of sound and maximum frequency in the surrounding fluid, and b is a constant with the criteria that $b \geq 8$.

The finite integration code was run in parallel on multiple CPUs on the SciClone computing cluster at William and Mary. Parallelization was accomplished by breaking up the simulation space onto a one-dimensional virtual topology, as shown in Figure 5.17. The virtual topology allows for the passing of required information between CPU processors (nodes) using Message Passing Interface (MPI). In the acoustic finite integration case, pressure must be sent to the neighboring node on the left side: $left = rank-1$ in the 1D virtual topology. Additionally, the velocity in the x_1 direction, v_1 , must be passed to the neighboring node to the right: $right=rank+1$. As discussed later in the Elastic Finite Integration section, passing of information can be more complicated than in the AFIT case. A 1D virtual topology is much more simple than creating a 2D virtual topology, but can be more limited in efficiency since values for the entire width of the simulation space must be passed to neighboring nodes. For very large simulation spaces a 2D virtual topology would be preferred [131]. Figure 5.18 is an example of the output created by the AFIT simulation for the case of a traveling wave scattering from a cylinder. The images represent the pressure output at a single point in time for two slices (horizontal and vertical) through the 3D simulation space. More complicated geometries of scatterers can easily be included in the AFIT simulation through direct changes to the C++ code.

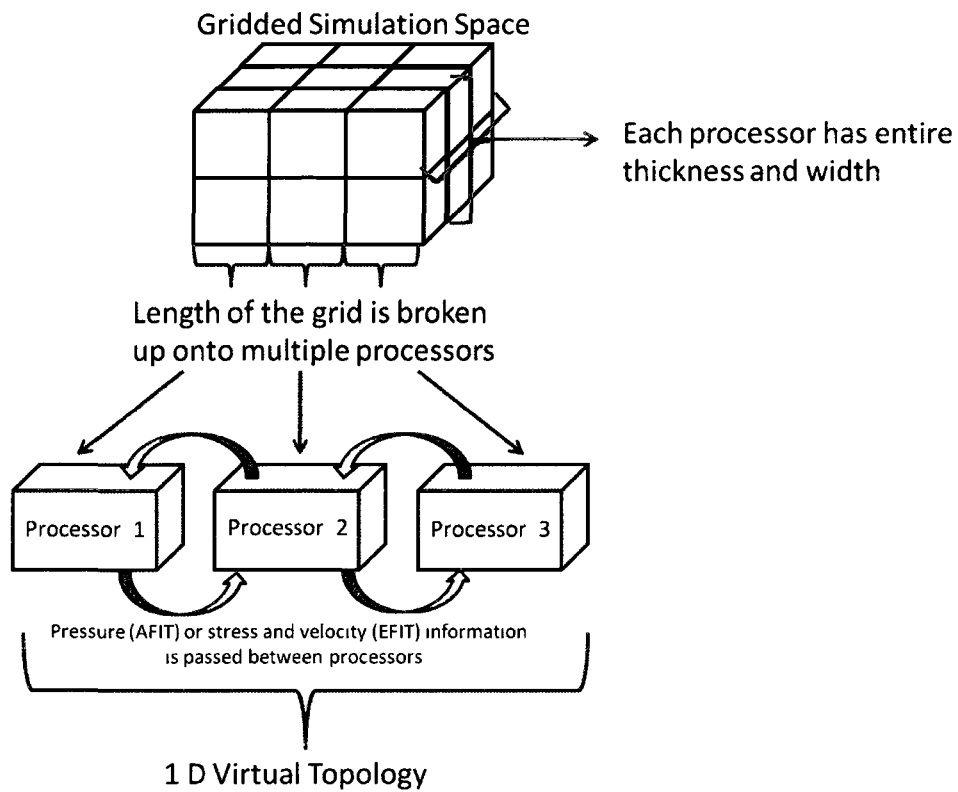


Figure 5.17: 1 dimensional virtual topology.

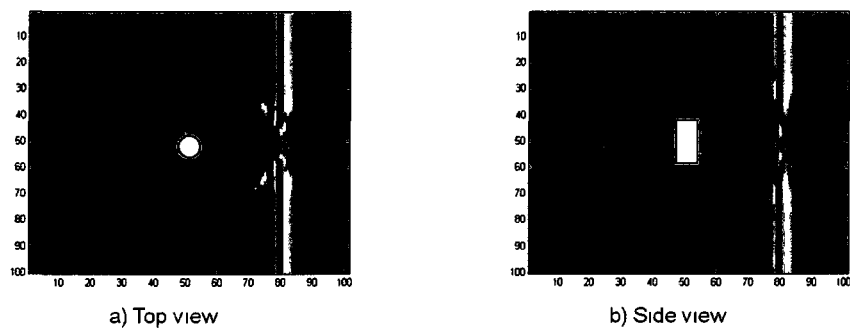


Figure 5.18: Example of AFIT results for a traveling wave scattering from a cylinder. Two spatial slices through the 3D simulation space are shown, a top view and a side view.

This type of 3D acoustic scattering code is useful for a variety of applications beyond the focus of this chapter. Acoustic security screening is one example application that requires knowledge of scattering from complex geometries. If a sound beam traveling through air interacts with an object, the resulting scattered signal can be analyzed to determine the geometries and materials that were encountered by the wave. In order for the beam to propagate long distances through air a parametric array can be used. The parametric array creates beam mixing that turns multiple higher frequency beams into a single lower frequency ($\approx 10 \text{ kHz}$) beam that is focused down to a small spot size at the target [132]. The beam can pass through clothing material to interact with weapons or other scatterers that may be hidden beneath. An incident beam of this type can be incorporated into AFIT. Figures 5.19-5.21 show AFIT scattering snapshots for the type of complex geometries required for security screening. The scattering images demonstrate that AFIT is well-suited for such applications.

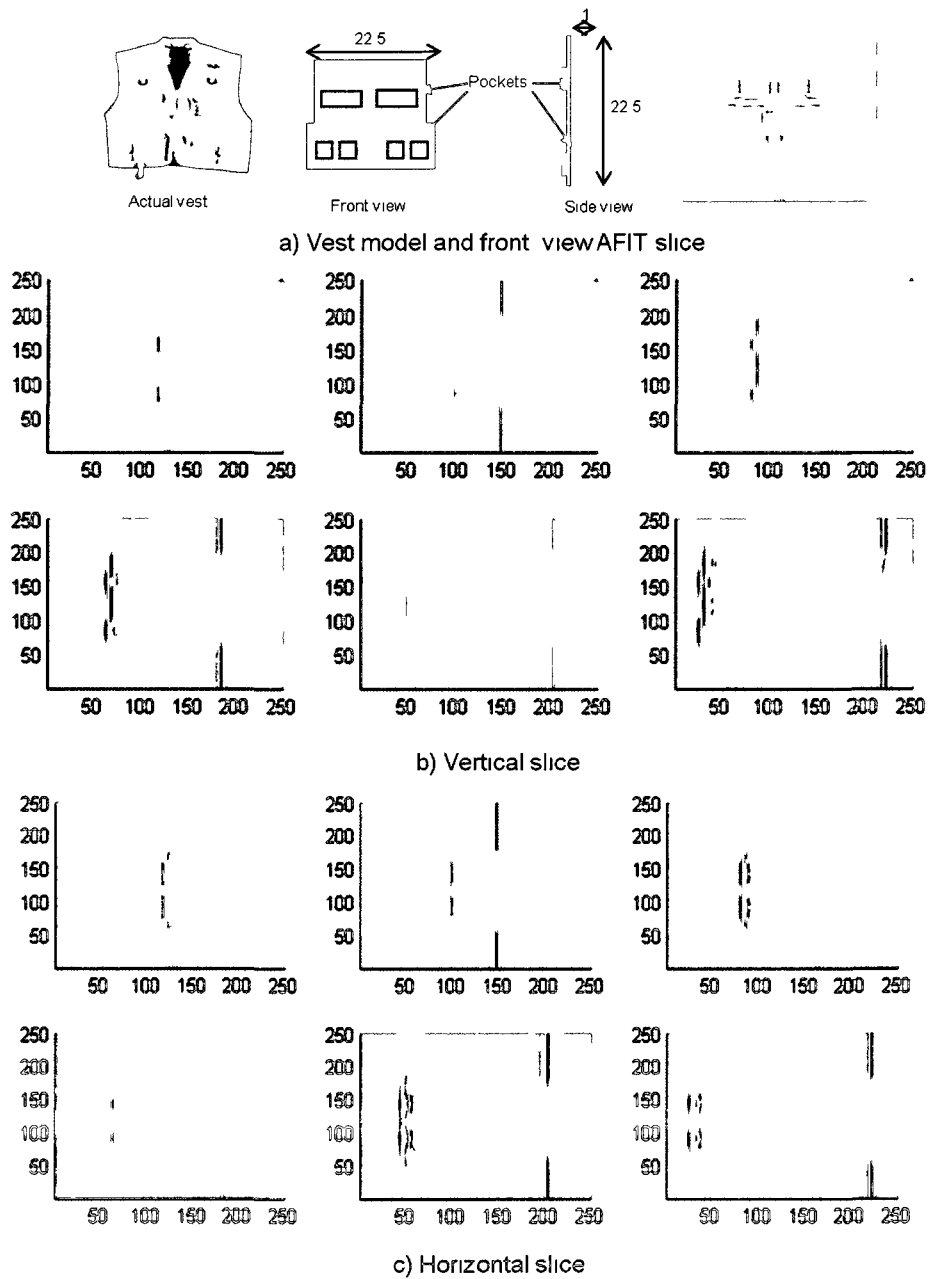
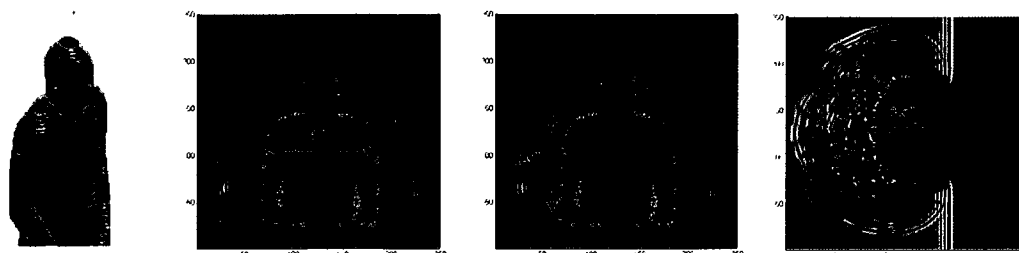
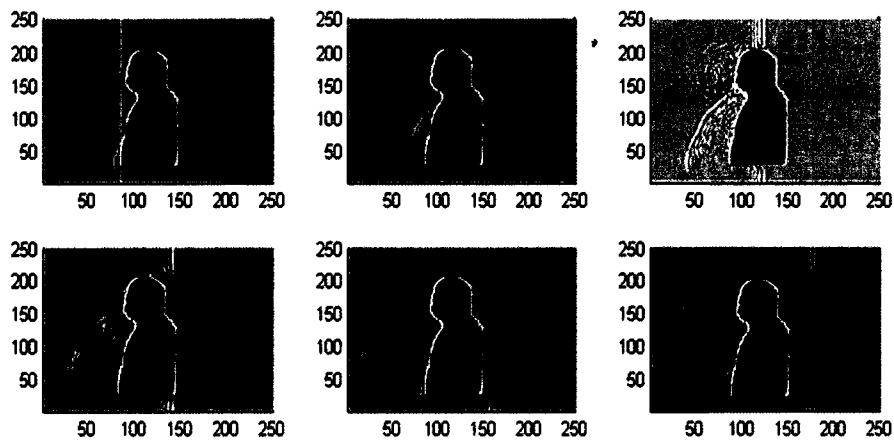


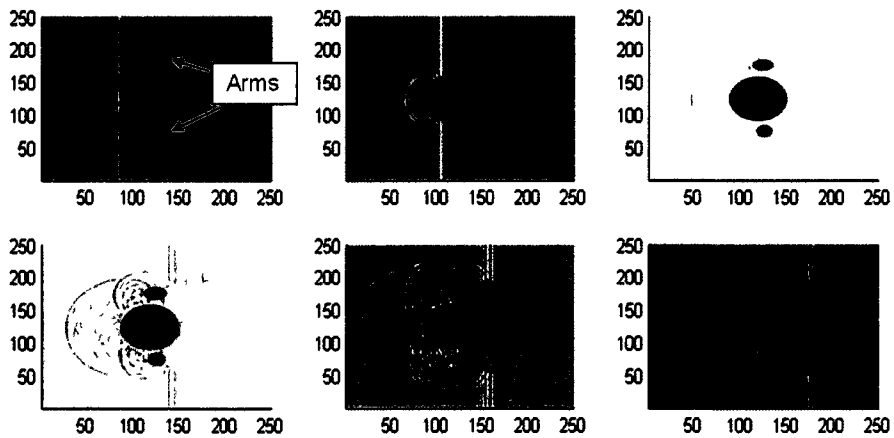
Figure 5 19: AFIT results for a series of snapshots in time showing wave scattering from a fishing vest



a) Human torso model and AFIT snapshots

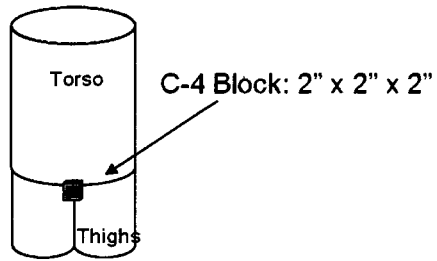


b) Vertical slice

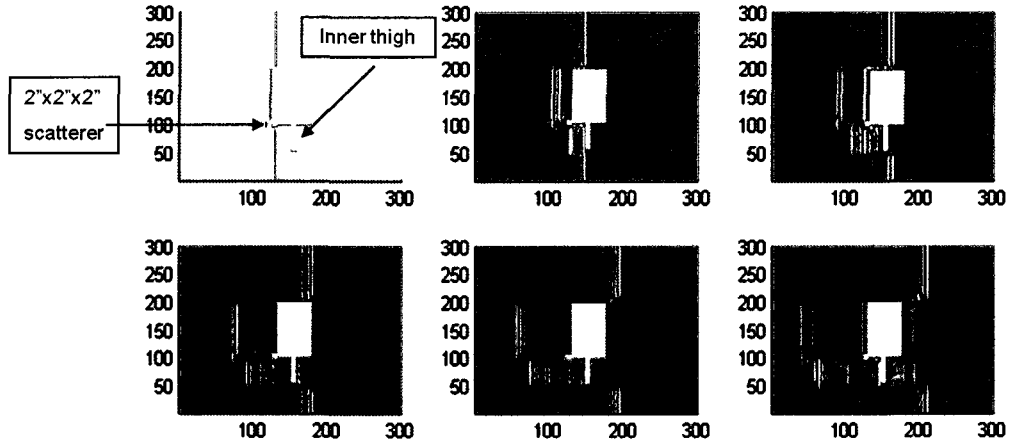


c) Horizontal slice

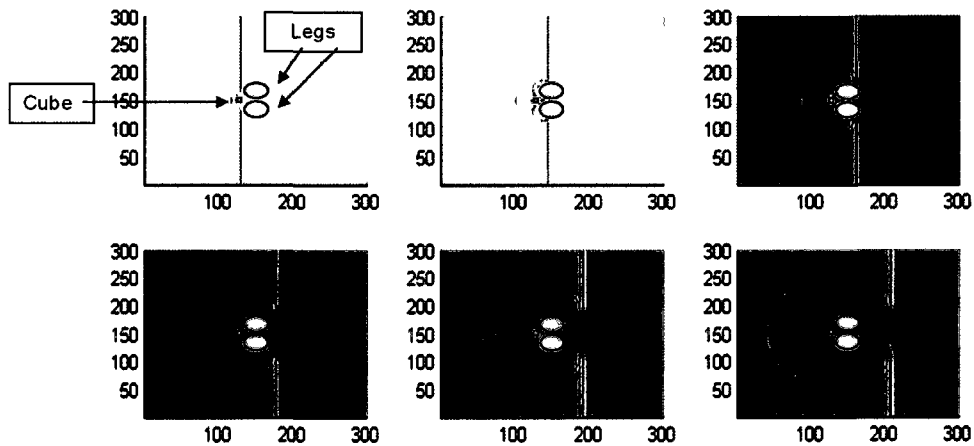
Figure 5.20: AFIT results for a series of snapshots in time showing scattering from a human torso.



a) Geometric model of torso and legs with C4



b) Vertical Slice



c) Horizontal Slice

Figure 5.21: AFIT results for a series of snapshots in time showing from C4 block located at the groin (modeled after the failed Northwest Airlines “underwear bomber”).

Running the code in parallel speeds up computational time significantly, and al-

lows the possibility of a smaller step size. In the algae scattering simulations we used up to 500 grid points per wavelength, leading to a spatial step size as small as $3 \mu m$. Such a small spatial step size was both necessary and feasible because we were investigating scattering from $30 \mu m$ algal cells within a total simulation space on the order of only $0.0002 mL$. It should be noted that output files from the 3D simulation space in the algae application were up to $30 GB$ per simulation.

5.5 AFIT Simulation Results

Based on the published experiments in acoustic micromanipulation (discussed in the previous section), we chose an incident wave frequency of $1 MHz$ for the AFIT multiple scattering simulations. Since AFIT does not account for viscosity, there is no attenuation of the incident wave. Therefore, we can set up and maintain a standing wave field by sending in a sine wave for n cycles in time (where n is a finite integer, $n = 2$ for the results shown below). The total length of the simulation space is set equal to one wavelength, which is $1.497 mm$ in the case of fresh water. The total simulation space volume was set to $0.0002 mL$. Figure 5.22 shows twelve plots of the wave amplitude for a 1D slice through the 3D simulation space for times $t_1 = 0.808 \mu s$ through $t_{12} = 2.84 \mu s$. The time increment between each plot is $\Delta t = 0.185 \mu s$. It takes approximately $1.99 \mu s$ to set up the standing wave in the simulation space (by t_8). The figure is intended to show the standing wave as it is created in the AFIT simulation space.

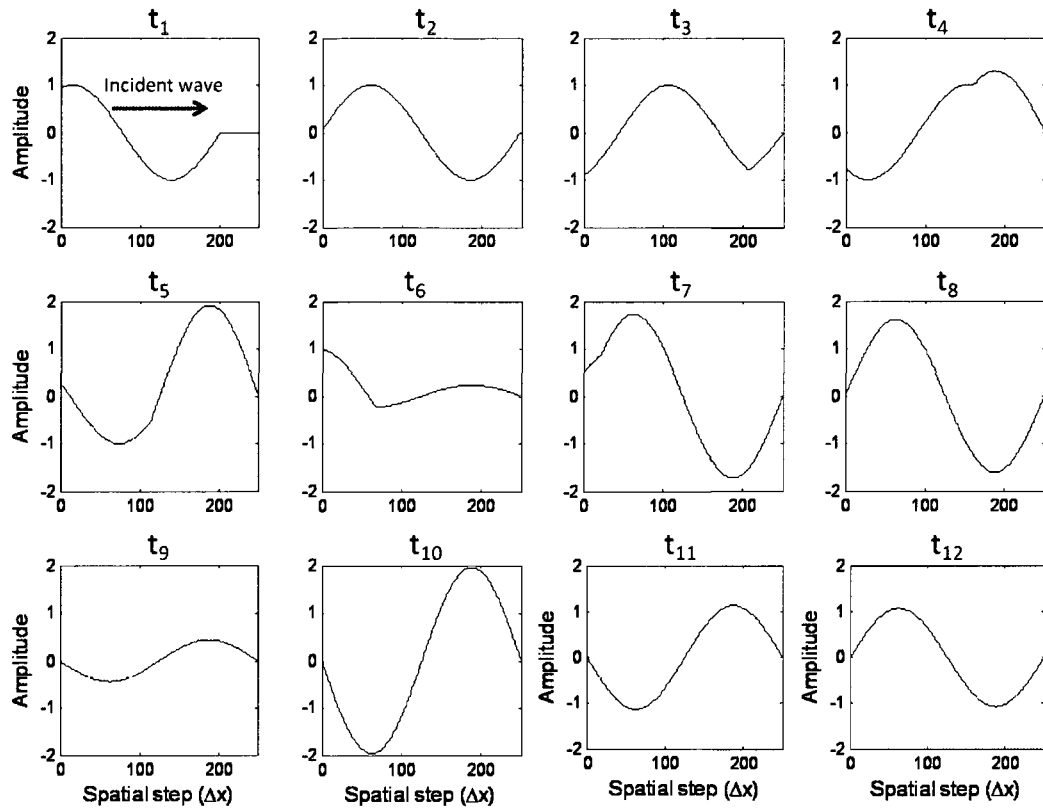


Figure 5.22: Snapshots in time of an incident wave propagating into the AFIT simulation space and creating a standing wave (1D slices through the 3D space).

Numerical rounding results in a small ripple that propagates back and forth along the standing wave, see Figures 5.23 and 5.24. The size of the ripple is less than $+/- 0.5$ percent of the maximum peak pressure amplitude. Experimental standing wave fields face similar issues due to the finite spread in frequency of real transducers (bandwidth), as well as other factors such as changes due to heating. In fact, the presence of a small wave propagating back and forth in an experimental standing wave field was reported in 1995 in a publication by H.M. Hertz. Hertz describes small propagating waves within the standing wave field that are on the order of 5

percent of the wave amplitude and observes that in a real fluid (with viscosity) these small fluctuations within the standing wave field can create acoustic streaming [133]. Acoustic streaming effects can be minimized experimentally through limited path lengths as discussed in section 5.1.4. More recently, Wiklund, Hertz, and Nilsson report acoustic intensity variations within an experimental standing wave field of ± 1.2 percent over the wave field cross-section [134]. For a standing wave acoustic intensity is related to pressure by

$$I_a = \frac{P^2}{2\rho c} , \quad (5.17)$$

where P is pressure, ρ is density, and c is longitudinal speed of sound. Thus, intensity is proportional to the square of the pressure amplitude. A variation of ± 1.2 percent in intensity is approximately equivalent to a pressure amplitude variation of ± 1.1 percent. The precision of an experimental standing wave field clearly depends on the technique used to create the field. Publications such as [135] and [77] discuss the complexity of creating precise standing wave fields for particle manipulation. With these reported experimental results in mind, we conclude that the precision of our simulated standing wave field is adequate for yielding information which may be useful for experimental procedures.

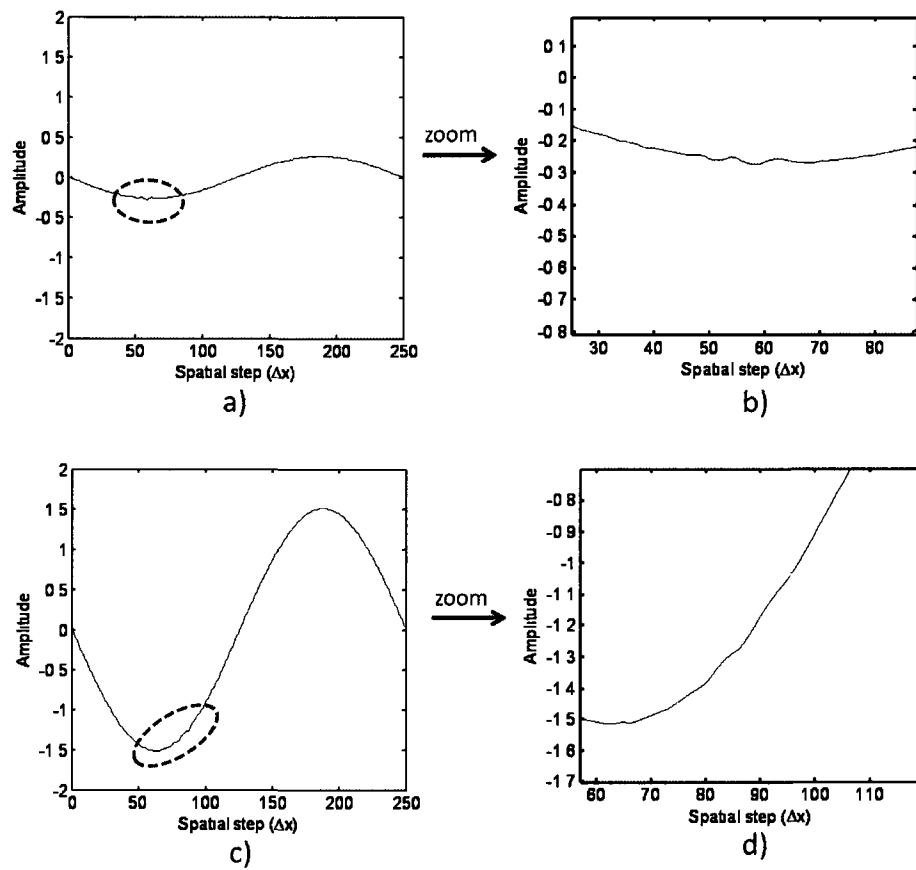


Figure 5.23: a) Standing wave at time= t_1 , b) zoomed in view of the circled region in (a), c) standing wave at time= t_2 , d) zoomed in view of the circled region in (c).

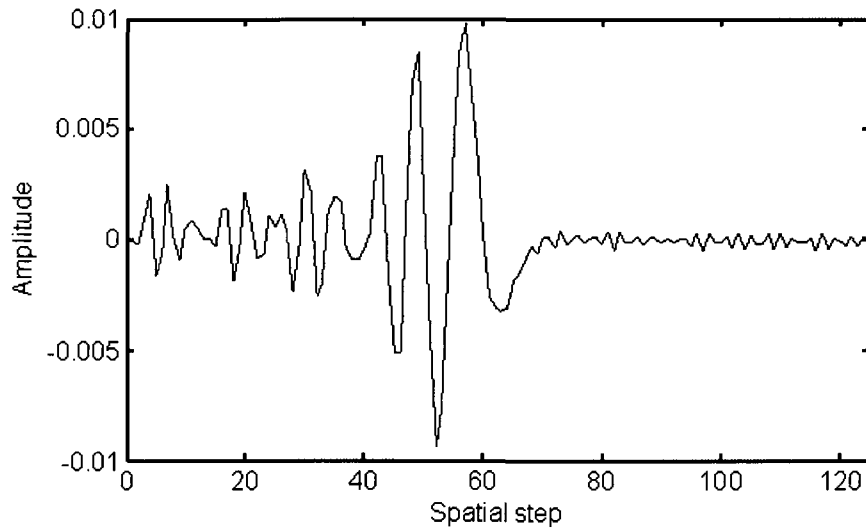
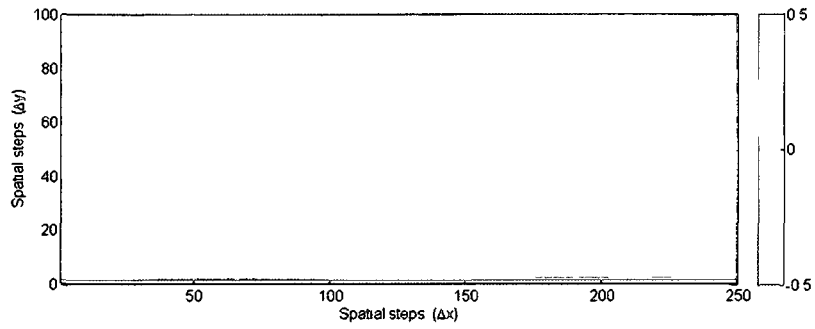


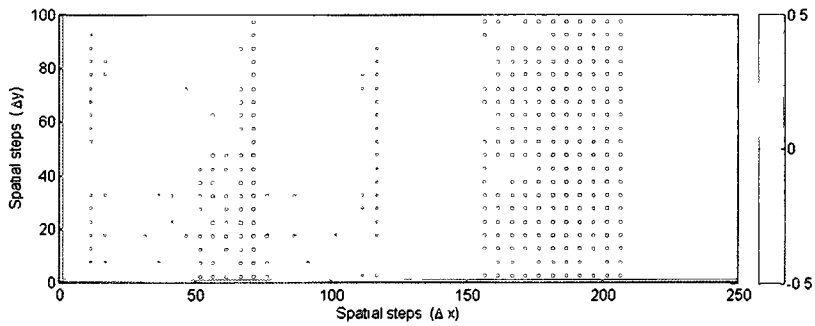
Figure 5.24: Standing wave ripple with the background subtracted.

The AFIT code allows us to place any number of scatterers of any shape into the simulation space. For investigations of scattering from algal cells we will use finite-length cylindrical scatterers, which are similar in shape to many types of algae, see section 5.3.1. In an early simulation 800 rigid cylindrical scatterers of diameter of $12\mu m$ and length of $30\mu m$ (a size similar to algal cells) were evenly dispersed in a single plane of the simulation space with fresh water as the surrounding fluid. This number of scatterers is equivalent to 2.2×10^3 particles per mm^2 since the scatterers were placed in a single plane. Note that we started with rigid scatterers because their positions can clearly be seen in the simulation output. The material properties used for algal cells in the simulation space are fairly similar to water, thus the positions of algal cells are not clearly visible in the images. The simulation was intended as a check that numerous scatterers could be correctly included in the simulation space. The result of this simulation not only verified the inclusion of numerous scatterers, but also yielded an interesting result. The small ripple is amplified by the presence

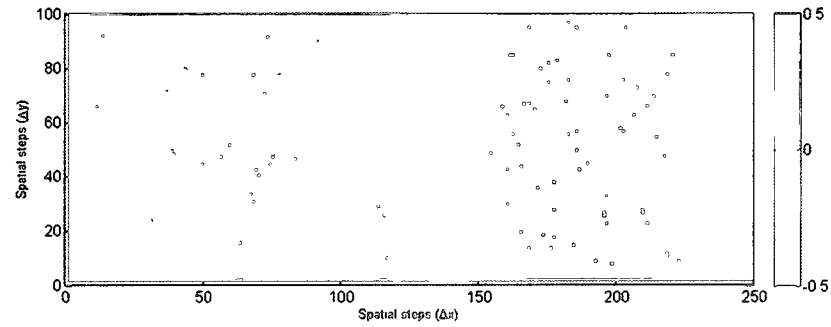
of the scatterers, as shown in Figures 5.25 and 5.26. Figure 5.26 is a color plot of the x-y plane, and corresponds to a 2D slice at a specified vertical position in the simulation space. The region between 50 and 100 Δx shows how the small ripple in the standing wave is amplified by the scatterers. Figure 5.25 shows an “A-line” plot corresponding to a single y position ($y = 72$). The change in amplitude of the ripple in the wave field is similar when the scatterers are evenly or randomly dispersed. Yet, the amplitude of the enhanced ripple for the random distribution case varies across the wave (y direction), as expected.



(a)



(b)



(c)

Figure 5.25: a) 2D slice of standing wave field at time $t=3.8 \mu s$ with no scatterers, b) 2D slice of standing wave field with 800 scatterers evenly distributed in a single plane c) 2D slice with 800 scatterers randomly distributed in a single plane. Scatterers are light green and viewed from above.

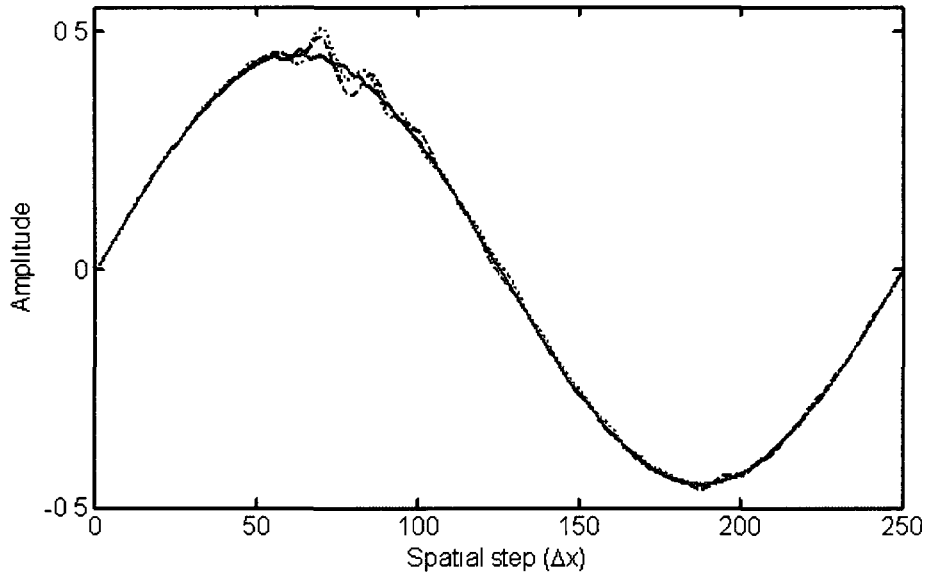
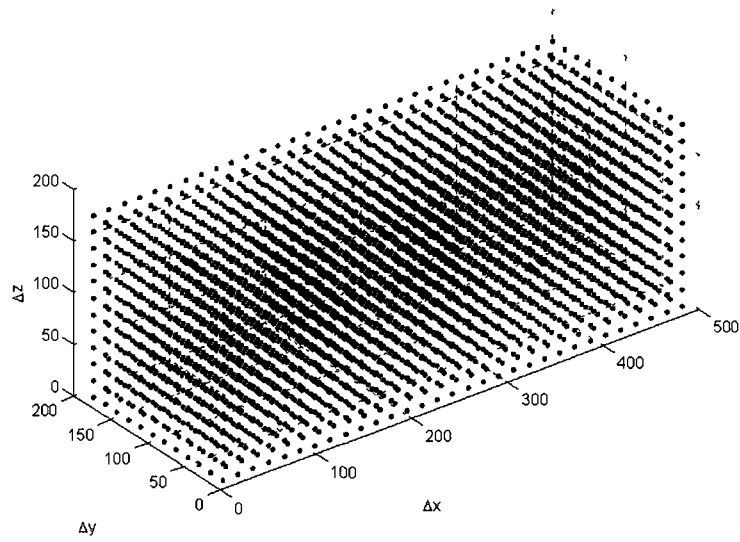
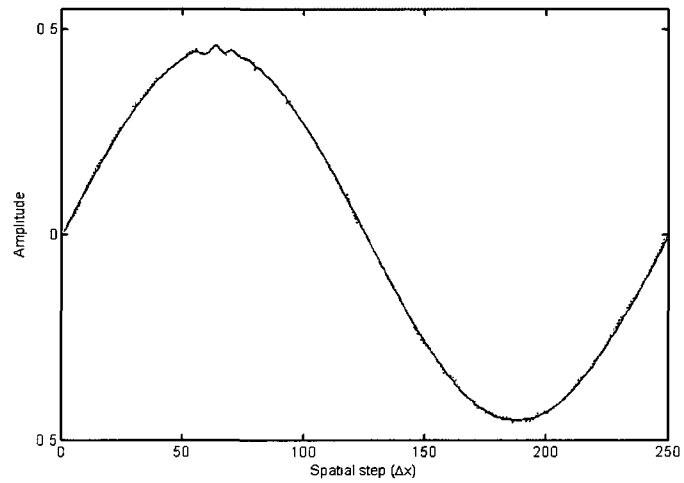


Figure 5.26: A-line plot at a single point in time ($t=3.8 \mu s$): standing wave with zero scatterers in the simulation space (solid black line), 800 evenly dispersed cylindrical rigid scatterers (red dotted line), and 800 randomly dispersed rigid scatterers (blue dashed line).

We increased the number of scatterers to 10^7 particles per mL and ran simulations with even and random dispersion throughout the simulation space (not just in a single plane). Figures 5.27 - 5.29 show results for rigid scatterers evenly distributed. The increase of scatterers leads to further changes in the standing wave field, however, the wave field is not significantly disrupted. Keeping in mind experimental reports of successful particle sorting at these particle concentration level, we would not have expected significant changes to the wave field due to 10^7 scatterers.

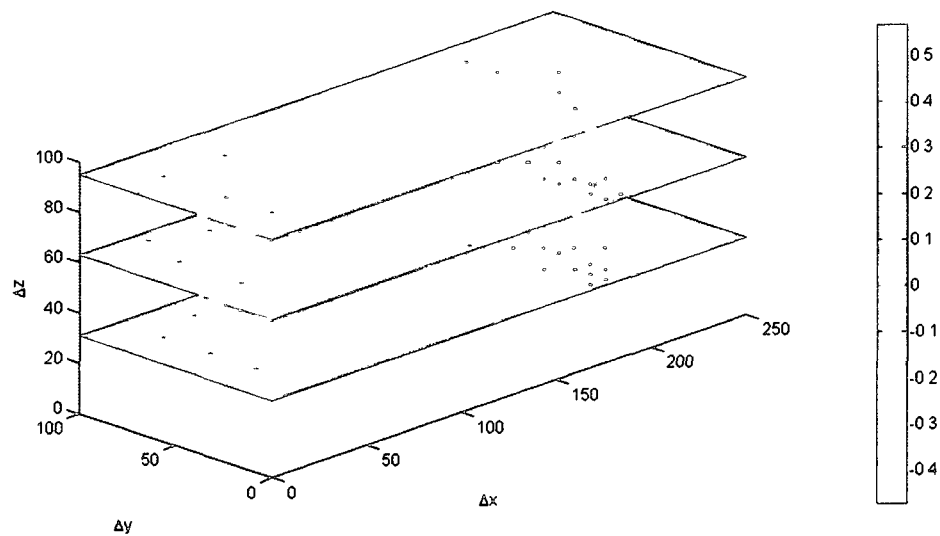


(a)

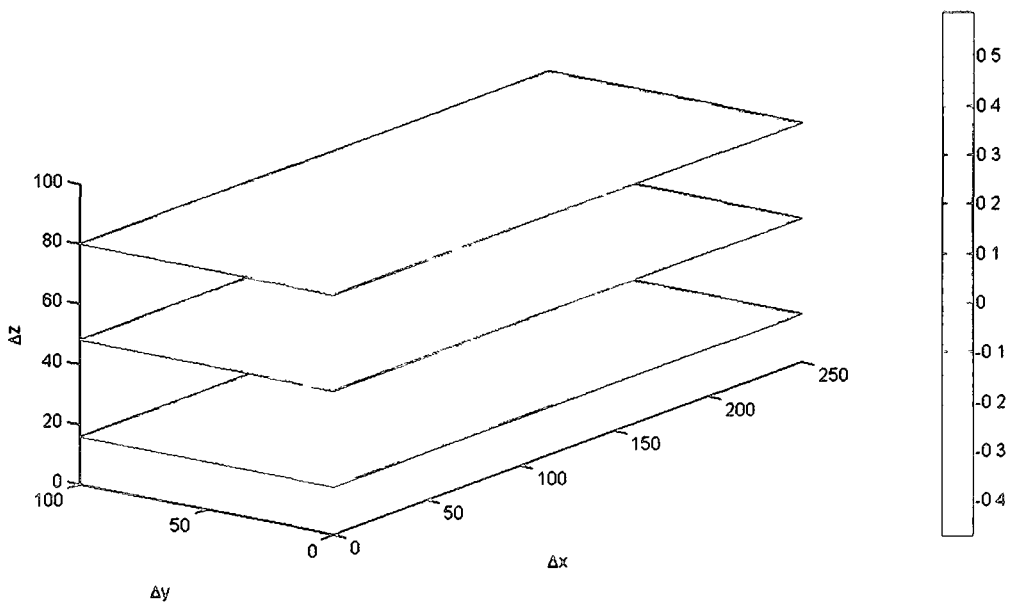


(b)

Figure 5.27: 2.2×10^7 particles per mL: a) Distribution of scatterers, b) A-line plot at a single point in time ($t=3.8 \mu s$): standing wave with zero scatterers in the simulation space (solid black line), 4464 evenly dispersed rigid cylindrical scatterers (red dotted line), equivalent to 2.2×10^7 particles per mL.



(a)



(b)

Figure 5.28: 2.2×10^7 particles per mL: a) Three 2D slices through the simulation space at the specified vertical positions, showing scatterers as viewed from above at time $t = 3.8\mu s$, b) 2D slices that do not show the scatterers.

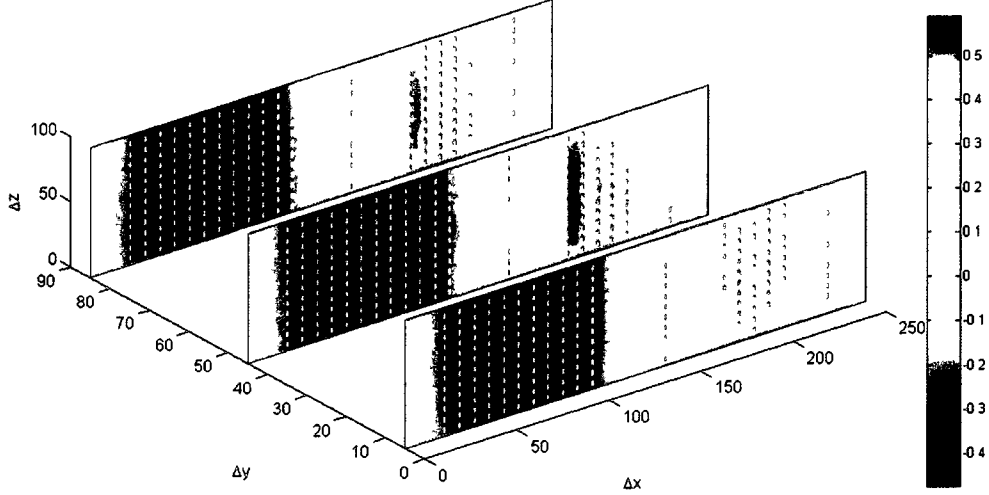


Figure 5.29: 2.2×10^7 particles per mL: 2D slices through the y-plane at time $t = 3.8 \mu s$ showing the length of the cylindrical scatterers.

Pressure is defined as force per unit area. Therefore, the force upon a scatterer can be approximated by multiplying the stress over a surface by the surface area, $F = \sigma A$. Since the finite integration simulations discussed above do not include viscous terms, the stress tensor is simply $\sigma = p$. We can use the change in pressure amplitude across a scatterer to approximate the force felt by a scatterer. Because the simulation space is a discrete space, we have pressure outputs corresponding to all grid points in the space for each time step. In order to approximate the total force upon a scatterer at a single point in time we sum the total pressure over the scatterer surface in each direction and calculate the change in pressure across the scatterer.

Many of the experiments listed in Table 5.1 report a particle concentration of around 10^6 to 10^7 cells/mL. Figure 5.31 shows the approximate force upon a single algal cell for the particle location described in figure 5.30, due to a standing wave field for particle concentrations of 8×10^5 algal cells per mL, 16×10^5 cells per mL, and 2.2×10^7 cells per mL. Interparticle forces and drag forces that exist in real

fluids (due to viscosity) are not taken into account in 5.31. The simulation space length for Figures 5.30 and 5.31 is one wavelength (1.497 mm), with a total volume of 0.0002 mL . The force was approximated from the AFIT simulation results as described above, and corresponds to the force upon an algal cell located as shown in Figure 5.30. Scatterer movement is not taken into account in Figure 5.31, so the figure represents force versus time felt by a fixed algal cell in the standing wave field. The material properties used in this simulation for the algal cell are a density of 0.86 g/cm^3 and a longitudinal speed of sound of $c_L = 1474\text{ m/s}$ (as given in Table 5.3). Each scatterer is cylindrical with a width of $12\mu\text{m}$ and a length of $30\mu\text{m}$.

The AFIT simulation predicts force upon the algal cell in the $+/-\hat{x}$ direction, with negligible force in the \hat{y} and \hat{z} directions, as expected based on experimental work in the literature, such as [62]. A negative force value in Figure 5.31 creates movement in the $-\hat{x}$ direction. The plots in Figure 5.31 show that as the concentration of scatterers increases, the changes to the standing wave field lead to changes in the force upon the scatterers. However, the change is relatively small. The largest change in force for a particle concentration increase from $8.0 \times 10^5\text{ cells/mL}$ to $2.2 \times 10^7\text{ cells/mL}$ leads to a percent difference in force of only 12%. It is also clear from the zoomed in plot in Figure 5.31 that as time progresses the changes to the standing wave field due to the scatterers increases.

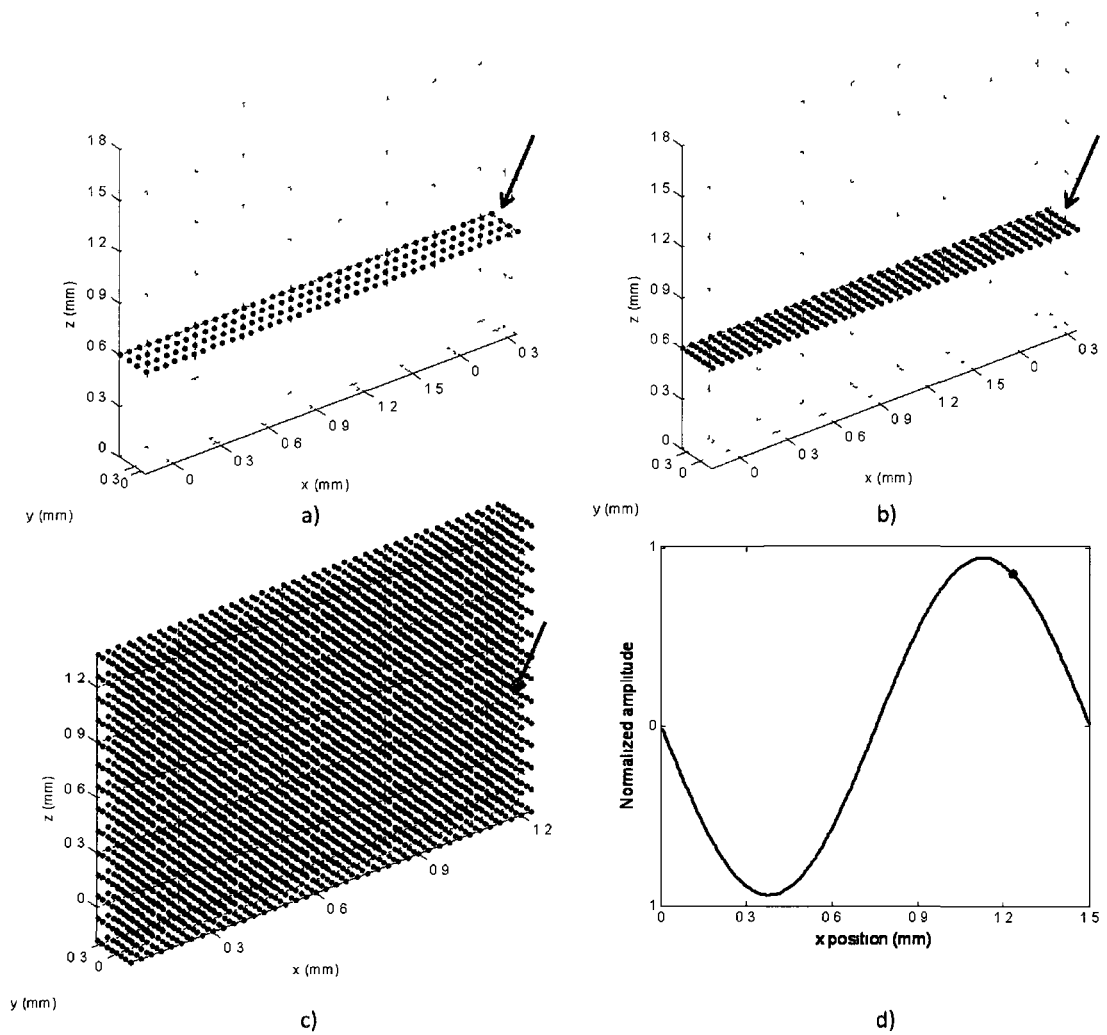
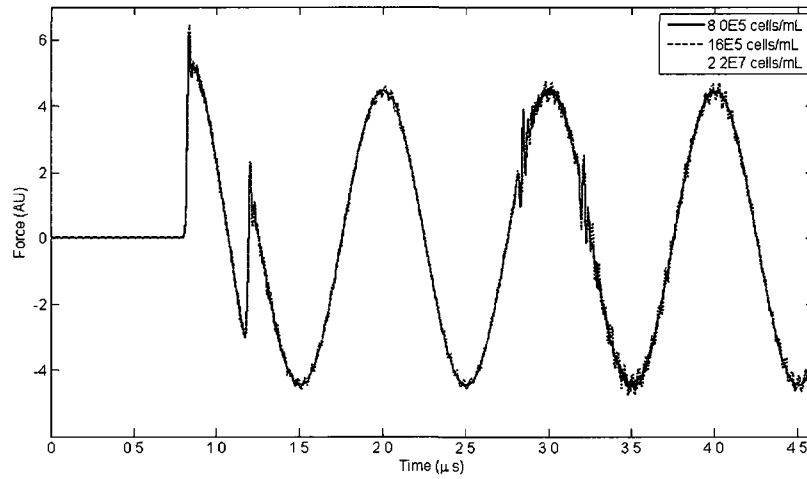
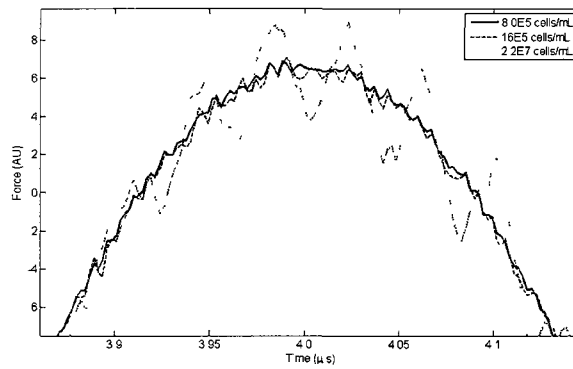


Figure 5.30: a)-c) show the arrangement of algal cell scatterers (represented here as blue spheres, though they were cylindrical in shape in the simulation) in the standing wave field for particle concentrations of 8×10^5 algal cells per mL, 16×10^5 cells per mL, and 2.2×10^7 cells per mL. The red dot represents the scatterer about which the force was calculated for Figure 5.31. d) shows the position of the red dot in the standing wave (near a pressure nodal position).



(a)

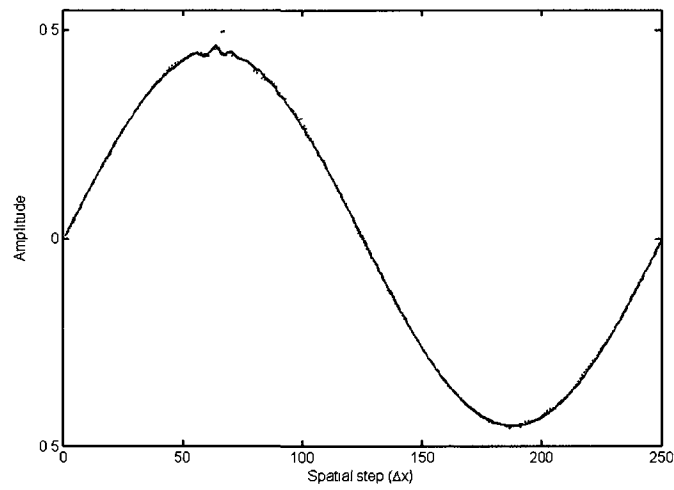


(b) A zoomed in view of a section of plot (a).

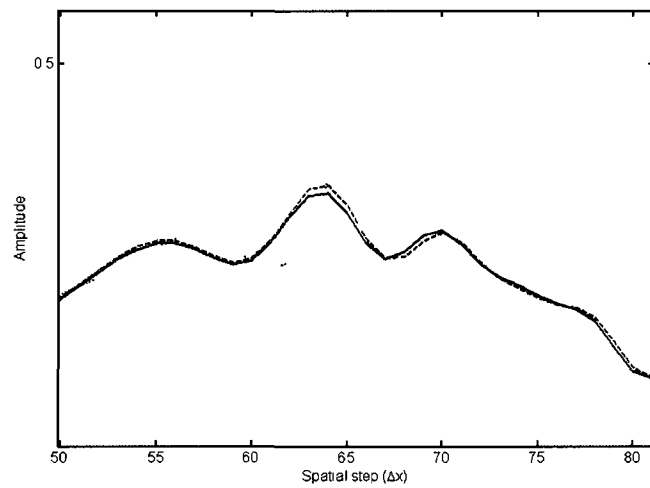
Figure 5.31: Approximate acoustic force (arbitrary units) upon evenly dispersed algal cells due to a standing wave field for various particle concentrations in the acoustic chamber (as shown in the legend). The plot does not account for scatterer movement, but rather shows the variation of force at a single location in the simulation space as time progresses. The standing wave field has been established by approximately $t = 2 \mu s$.

Figures 5.32 and 5.33 show results for rigid scatterers and for algal cells randomly dispersed in the space. The algal cells, which here have material properties fairly close to water (since viscosity is not included) have a much smaller effect on the stand-

ing wave field compared to the rigid scatterers, which allow no wave transmission. The results thus far show that although the scatterers are much smaller than the wavelength, particle distribution and the material properties of the scatterers are key factors leading to varied alterations in the standing wave field.



(a)



(b)

Figure 5.32: A-line plot at a single point in time ($t=3.8 \mu s$): a) No scatterers (black solid line), 10^7 rigid particles per mL randomly dispersed (red dotted line), 10^7 algal cells randomly dispersed (dashed blue line), b) Zoomed in view showing the slight difference between the field with no scatterers and with 10^7 algal cells.

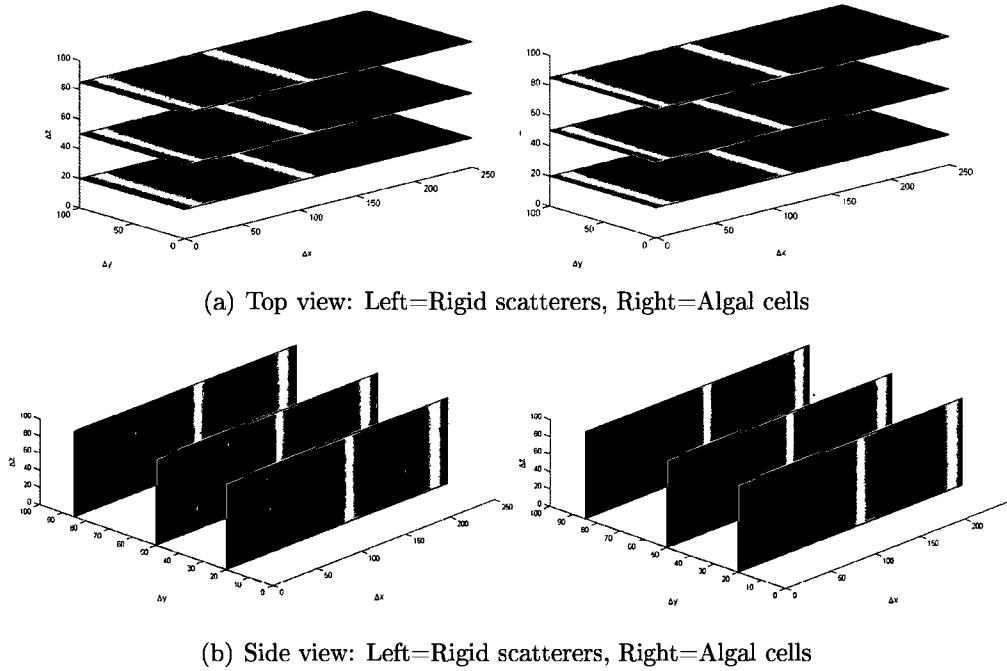
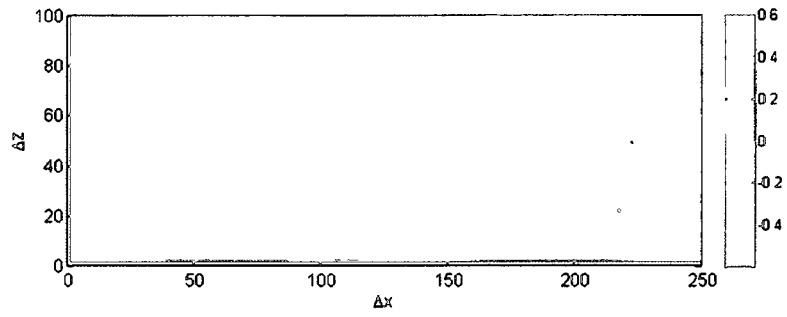
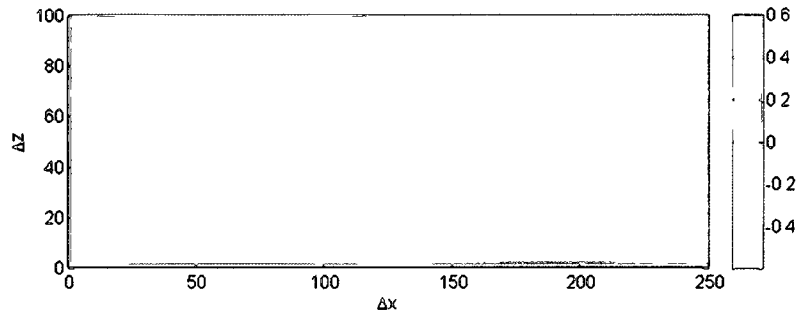


Figure 5.33: Standing wave field with 10^7 scatterers distributed randomly. a) Top view of rigid scatterers and algal cells, b) Side view of rigid scatterers and algal cells.

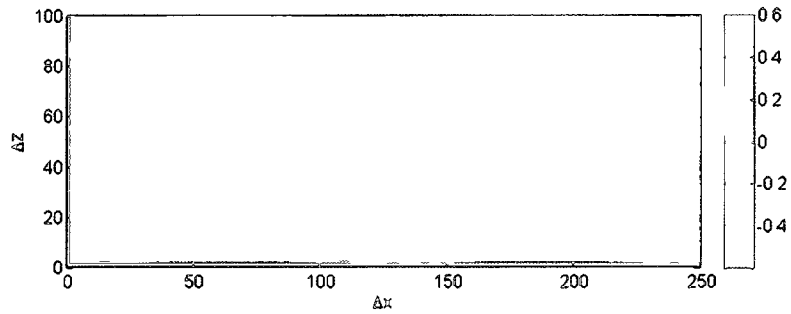
We further increased algal cell concentration incrementally from 5×10^7 to 5×10^9 particles per mL (randomly dispersed). Computational time for the highest particle concentration was approximately 155 CPU hours (9.7 hours of real-time running on 16 CPUs). Recall that the maximum particle concentration used in experiments reported in the literature (shown in Table 5.1) is 10^9 particles per mL. The AFIT results are shown in Figures 5.34 and 5.35. The increase in particle concentration from 5×10^7 to 5×10^9 particles per mL, created a change in pressure amplitude equivalent to a 23.5% difference (for the largest change). As shown in Figure 5.36, the change is large enough to significantly alter the force felt by the algal cells. The disturbance to the standing wave field increases as time progresses.



(a) 5×10^7 algal cells per mL



(b) 5×10^8 algal cells per mL



(c) 5×10^9 algal cells per mL

Figure 5.34: 2D color plots showing the wavefield at a single point in time ($t=3.8 \mu s$) for a slice at a single vertical position while the number of algal cells per mL was increased.

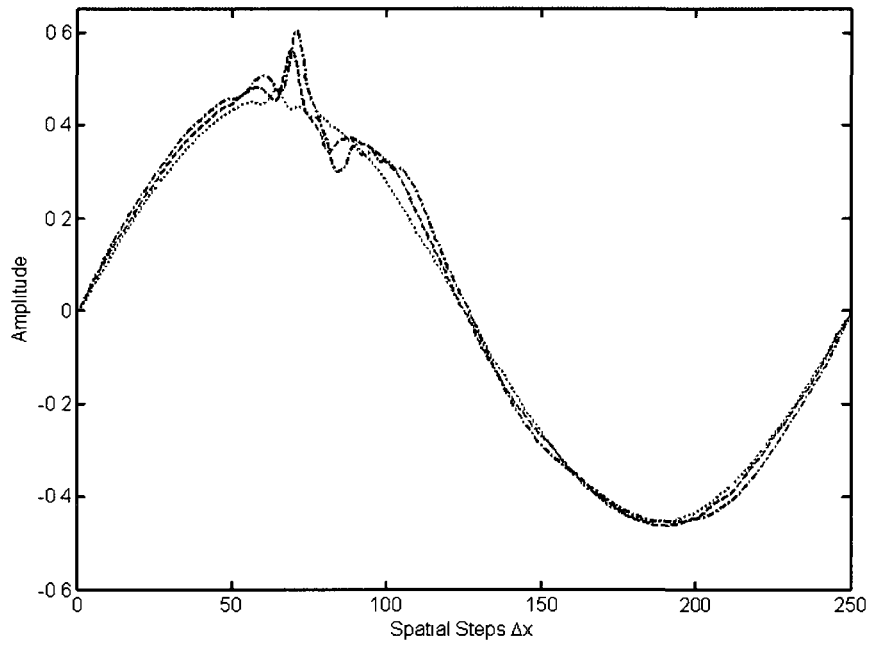


Figure 5.35: A-line result for three algal cell concentrations: 5×10^7 cells per mL (pink dotted line), 5×10^8 cells per mL (red dashed line), 5×10^9 cells per mL (blue dash-dotted line).

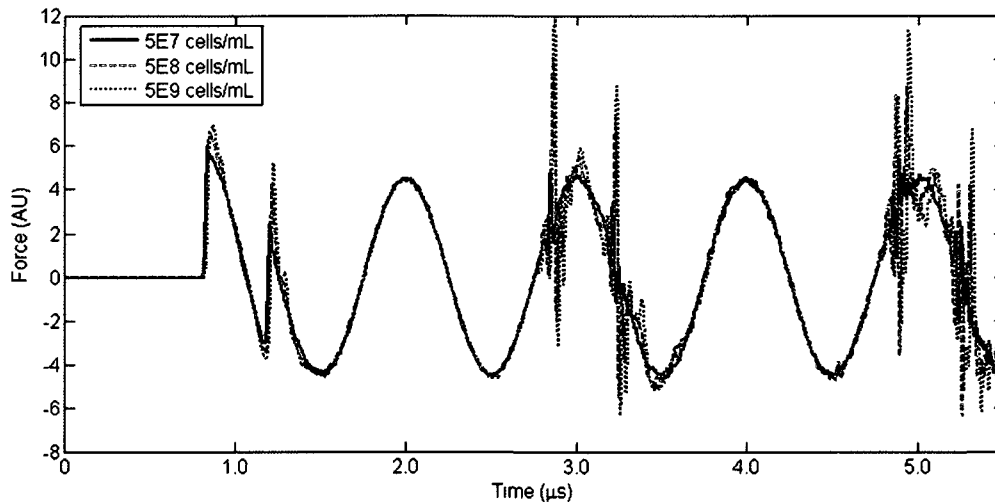


Figure 5.36: Approximate acoustic force (arbitrary units) upon randomly dispersed algal cells due to a standing wave field for various particle concentrations in the acoustic chamber (as shown in the legend). The plot does not account for scatterer movement, but rather shows the variation of force at a single location in the simulation space as time progresses. The standing wave field has been established by approximately $t = 2 \mu s$.

5.6 Discussion of AFIT Results

We have shown that AFIT simulation is a useful tool for investigating various multiple scattering effects in a standing wave field. Our results showed that the material properties of the scatterers are significant in determining the changes to the standing wave field. Our simulated standing wave field had a small propagating numerical ripple, comparable to experimental standing wave fields, which was amplified by the presence of scatterers. Increases in biomass concentration led to significant changes in force upon the algal cells. 3D standing wave simulations are a good start towards acoustic modeling that would help optimize the setup used in experimental manipulation of algal cells. However, as concluded from the modeling results in section 5.3,

viscosity should to be taken into account to capture the true behavior of the scatterers. In future work particle movement and drag forces could also be incorporated into simulations and force calculations for a more thorough investigation of the changes in force due to increases in particle concentration. These topics are discussed further in chapter 8.

Chapter 6

Ultrasonic Waves in Solid Media

The detection of flaws in metals, such as corrosion thinning, gouges, and cracks, is an important area of research in the field of nondestructive evaluation. Methods for efficient and accurate detection of flaws in aging aircraft, as well as in pipe/tank shaped structures, are particularly relevant for aeronautical and space vehicles where detection of flaws before failure is critical. Many publications have shown that guided ultrasonic waves are well suited for detecting flaws in plate-like structures. Guided Lamb waves can propagate long distances, up to tens of meters, potentially allowing large areas of a structure to be inspected quickly [136], [137]. Recent work in this field has shown that corrosion and thinning in aircraft structures can be detected through changes in Lamb wave mode arrival times due to the flaws [138]. Bingham showed that received guided wave signals are often very complex and can require sophisticated signal processing methods for automated interpretation. Furthermore, Bingham showed that numerical wave simulations can be critical in fully understanding experimental results.

We are interested in using numerical techniques to investigate detailed wave scattering behavior that is far too complicated for analytical models and that makes

experimental data difficult to interpret. Our work will focus on Lamb wave scattering from a void-type flaw in an aircraft-grade aluminum plate. We are specifically interested in flaws that not only cause changes in Lamb wave mode arrivals, but which create significant scattering of the modes.

6.1 3D Elastodynamic Wave Simulations

As computational power and availability continues to increase, the use of numerical techniques for modeling waves in acoustics, elastodynamics, and electromagnetics are becoming a common tool. Many numerical techniques are in use today, such as Finite Difference Time Domain (FDTD), Finite Element Methods (FEM), Boundary Element Methods (BEM), Finite Volume Time Domain (FVTD), and Finite Integration Technique (FIT) [16]. We will use FIT to model elastic wave scattering in materials.

FIT was developed by Weiland in 1977 for electromagnetic modeling [139]. A decade later Fellingner applied the technique to elastodynamics, creating the Elastodynamic Finite Integration Technique (EFIT) [140]. A thorough overview and history of FIT can be found in [16]. Marklein not only discusses acoustics, elastodynamics, and electromagnetics, but also describes coupled cases such as electromagnetic-ultrasonic FIT (EMUSFIT). Over the past decade EFIT has become a useful tool that has been used in a variety of applications. Schubert has reported a long line of work using EFIT to investigate nondestructive evaluation applications such as scattering from delaminations, cracks, and inclusions [141]. Early work by Schubert showed that EFIT can be used in conjunction with a thermoelastic source to model laser generated ultrasound [17]. EFIT has been used to simulate elastic wave propagation in an anisotropic heterogeneous media for applications ranging from wave scattering from surface breaking cracks in steel welds to wave propagation in concrete [142], [143].

Marklein and collaborators have used EFIT to investigate scattering from planar cracks in solids, such as the wheel shaft of a passenger train [144], [145]. Rudd et al developed a 3D cylindrical EFIT code that can properly model pipes with bends [146]. In 2010 Calvo and colleagues used a perfectly matching layer in EFIT simulations to study scattering from cylinders buried beneath sand at the ocean floor [147]. These are just a few examples of the applicability of EFIT in the field of nondestructive evaluation. Much of the work in the field, however, has been limited to 2D simulations. We will use the equations discussed below to create full 3-dimensional EFIT simulations.

EFIT is a numerical implementation of the elastodynamic equations that describe the propagation of elastic waves in solid isotropic media. In order to describe elastic wave propagation we begin by writing Cauchy's equation for momentum and Hooke's Law the isotropic form of the equations listed in section 1) [148]:

$$\rho \frac{\partial^2 u_j}{\partial t^2} = \frac{\partial T_{ij}}{\partial x_i} + f_j \quad , \quad (6.1)$$

$$T_{ij} = \lambda \epsilon_{kk} \delta_{ij} + 2\mu \epsilon_{ij} \quad , \quad (6.2)$$

where u_j is displacement, T_{ij} is the stress tensor, f_j is a source term, λ is Lamé's first parameter, μ is the shear modulus, ρ is density, and strain is defined by

$$\epsilon_{ij} = \frac{1}{2} \left(\frac{\partial u_i}{\partial x_j} + \frac{\partial u_j}{\partial x_i} \right) \quad . \quad (6.3)$$

The Lamé parameters are directly related to the longitudinal (c_L) and transverse (c_T)

speeds of sound:

$$\begin{aligned}c_L &= \sqrt{(\lambda + 2\mu)/\rho} \\c_T &= \sqrt{\mu/\rho} .\end{aligned}\tag{6.4}$$

Equations (6.1) and (6.2) are the linear equations of motions for elastic waves in solids (and can also be applied to viscous fluids [149]). Taking the time derivative of (6.2) and writing equations (6.1) and (6.2) in cartesian coordinates leads to nine equations of motion for elastic wave propagation. As with AFIT the equations are integrated over a control volume, and the integrals are approximated in a discrete form. To correctly transfer those equations into a discretized space, we place the stress and velocity components onto a discrete grid in the manner described by Fellingner and shown in Figure 6.1. Additionally, the material parameters μ , λ , and ρ are discretized to account for an inhomogeneous isotropic media, leading to equations (6.5) and (6.6) [150].

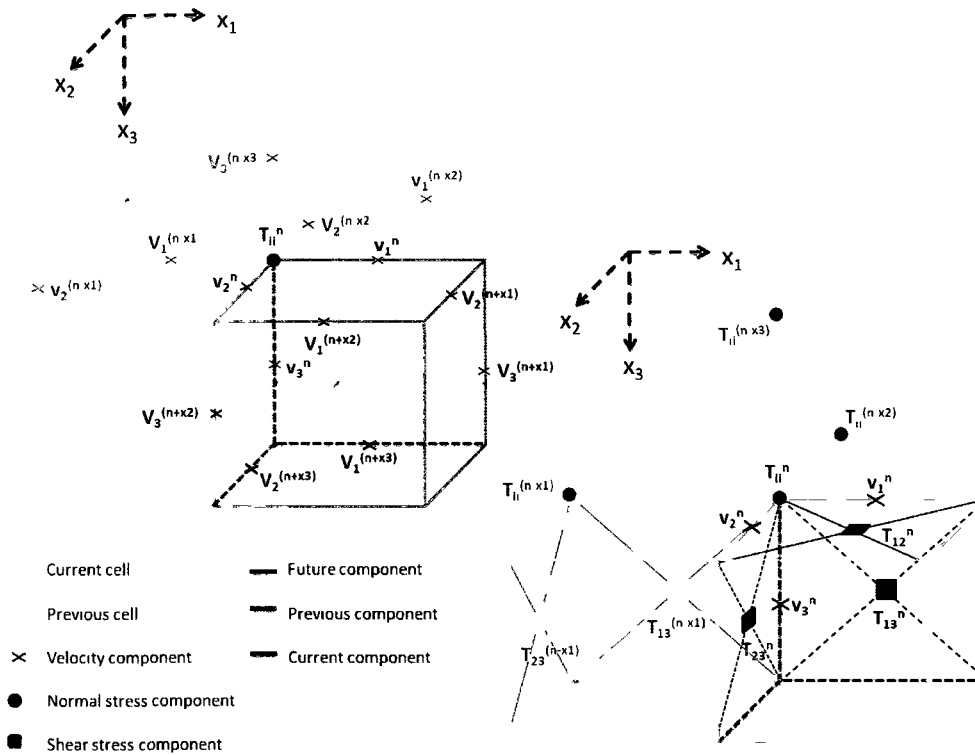


Figure 6.1: The two diagrams above show the 3D EFIT cartesian spatial grid. The image on the left shows the placement of velocity components on the spatial grid. The image on the right shows the stress components. Stress and velocity components are staggered in space (and time). T_{ii}^n represents T_{11} , T_{22} , and T_{33} for the current spatial step, n . The notation $v_2^{(n+x_3)}$ represents the v_2 velocity component for one step beyond the current cell in the \hat{x}_3 direction. As described in [150], the normal stress components fall on the grid cell corners, the shear stresses are on the faces of the grid cell, and the velocity components are along the edges. Color coding of cell type was not used with the shear stress components, instead the current shear stress components are displayed in three different colors to avoid confusion in the diagram.

Using this component placement, we can write nine equations describing wave propagation in a discrete form [151], [16].

$$\begin{aligned}
\dot{v}_1^{(n)}(t) &= \frac{1}{\Delta x} \frac{2}{\rho^{(n)} + \rho^{(n+\hat{x}_1)}} \left[(T_{11}^{(n+\hat{x}_1)}(t) - T_{11}^{(n)}(t)) + (T_{12}^{(n)}(t) - T_{12}^{(n-\hat{x}_2)}(t)) \right. \\
&\quad \left. + (T_{13}^{(n)}(t) - T_{13}^{(n-\hat{x}_3)}(t)) \right] , \\
\dot{v}_2^{(n)}(t) &= \frac{1}{\Delta x} \frac{2}{\rho^{(n)} + \rho^{(n+\hat{x}_2)}} \left[(T_{12}^{(n)}(t) - T_{12}^{(n-\hat{x}_1)}(t)) + (T_{22}^{(n+\hat{x}_2)}(t) - T_{22}^{(n)}(t)) \right. \\
&\quad \left. + (T_{23}^{(n)}(t) - T_{23}^{(n-\hat{x}_3)}(t)) \right] , \\
\dot{v}_3^{(n)}(t) &= \frac{1}{\Delta x} \frac{2}{\rho^{(n)} + \rho^{(n+\hat{x}_3)}} \left[(T_{13}^{(n)}(t) - T_{13}^{(n-\hat{x}_1)}(t)) + (T_{23}^{(n)}(t) - T_{23}^{(n-\hat{x}_2)}(t)) \right. \\
&\quad \left. + (T_{33}^{(n+\hat{x}_3)}(t) - T_{33}^{(n)}(t)) \right] ,
\end{aligned} \tag{6.5}$$

$$\begin{aligned}
\dot{T}_{11}^{(n)}(t) &= \frac{1}{\Delta x} \left[(\lambda^{(n)} + 2\mu^{(n)})(v_1^{(n)}(t) - v_1^{(n-\hat{x}_1)}(t)) + \lambda^{(n)}(v_2^{(n)}(t) - v_2^{(n-\hat{x}_2)}(t)) \right. \\
&\quad \left. + v_3^{(n)}(t) - v_3^{(n-\hat{x}_3)}(t) \right] , \\
\dot{T}_{22}^{(n)}(t) &= \frac{1}{\Delta x} \left[(\lambda^{(n)} + 2\mu^{(n)})(v_2^{(n)}(t) - v_2^{(n-\hat{x}_2)}(t)) + \lambda^{(n)}(v_1^{(n)}(t) - v_1^{(n-\hat{x}_1)}(t)) \right. \\
&\quad \left. + v_3^{(n)}(t) - v_3^{(n-\hat{x}_3)}(t) \right] , \\
\dot{T}_{33}^{(n)}(t) &= \frac{1}{\Delta x} \left[(\lambda^{(n)} + 2\mu^{(n)})(v_3^{(n)}(t) - v_3^{(n-\hat{x}_3)}(t)) + \lambda^{(n)}(v_1^{(n)}(t) - v_1^{(n-\hat{x}_1)}(t)) \right. \\
&\quad \left. + v_2^{(n)}(t) - v_2^{(n-\hat{x}_2)}(t) \right] , \\
\dot{T}_{12}^{(n)}(t) &= \frac{1}{\Delta x} \frac{4}{\frac{1}{\mu^{(n)}} + \frac{1}{\mu^{(n+\hat{x}_1)}} + \frac{1}{\mu^{(n+\hat{x}_2)}} + \frac{1}{\mu^{(n+\hat{x}_1+\hat{x}_2)}}} \left[(v_1^{(n+\hat{x}_2)} - v_1^{(n)}) \right. \\
&\quad \left. + (v_2^{(n+\hat{x}_1)} - v_2^{(n)}) \right] , \\
\dot{T}_{13}^{(n)}(t) &= \frac{1}{\Delta x} \frac{4}{\frac{1}{\mu^{(n)}} + \frac{1}{\mu^{(n+\hat{x}_1)}} + \frac{1}{\mu^{(n+\hat{x}_3)}} + \frac{1}{\mu^{(n+\hat{x}_1+\hat{x}_3)}}} \left[(v_1^{(n+\hat{x}_3)} - v_1^{(n)}) \right. \\
&\quad \left. + (v_3^{(n+\hat{x}_1)} - v_3^{(n)}) \right] , \\
\dot{T}_{23}^{(n)}(t) &= \frac{1}{\Delta x} \frac{4}{\frac{1}{\mu^{(n)}} + \frac{1}{\mu^{(n+\hat{x}_2)}} + \frac{1}{\mu^{(n+\hat{x}_3)}} + \frac{1}{\mu^{(n+\hat{x}_2+\hat{x}_3)}}} \left[(v_2^{(n+\hat{x}_3)} - v_2^{(n)}) \right. \\
&\quad \left. + (v_3^{(n+\hat{x}_2)} - v_3^{(n)}) \right] ,
\end{aligned} \tag{6.6}$$

The equations are discretized in time using central differences, which results in the velocity and stress components being staggered in time by $\Delta t/2$ [152].

$$v_i^{(t)} = v_i^{(t-\Delta t)} + \dot{v}_i^{(t-\Delta t/2)} \Delta t , \tag{6.7}$$

$$T_{ij}^{(t+\Delta t/2)} = T_{ij}^{(t-\Delta t/2)} + \dot{T}_{ij}^{(t)} \Delta t , \tag{6.8}$$

where t and $t + / - \Delta \frac{1}{2}$ are full and half time steps. For each time step equations (6.5) and (6.6) are solved at all points in the simulation space. Using equations (6.5) through (6.8) the simulation proceeds forward in time in a ‘leap frogging’ manner as

described in detail below [153]. At each time step the velocity values for the entire grid volume are updated, then the stress values for the entire grid are updated.

Time step t=1:

- 1) Initial condition at time step $t = 1$ means that $T^{(1/2)}$ is known
- 2) Using $T^{(1/2)}$ and (6.5), $\dot{v}^{(1/2)}$ can be found
- 3) $\dot{v}^{(1/2)}$ can be used with (6.7) to find $v^{(1)}$ (where for the initial time step, $t = 1$, $v^{(t-1)} = 0$)
- 4) With $v^{(1)}$, (6.6) can be used to find $\dot{T}^{(1)}$
- 5) $\dot{T}^{(1)}$ is used with (6.8) to find $T^{(1+1/2)}$

Time step t=2:

- 1) At $t = 2$, $T^{(1+1/2)}$ is known from the previous time step
- 2) Find $\dot{v}^{(2-1/2)}$ using (6.5)
- .
- .
- etc. as in time step 1.

Stability conditions require minimum time and spatial step sizes. We will use the same size spatial step in all directions since our discretized space is broken up into cubes. The reported number of points per wavelength in the literature varies, ranging from $\lambda/8$ to $\lambda/15$ [17], [125]. The Courant-Friedrichs-Levy condition is used to determine the time step size [125], [152]. The stability criteria for the discretization of the simulation are (assuming $\Delta x_1 = \Delta x_2 = \Delta x_3 = \Delta x$):

$$\begin{aligned} \Delta x &\approx \frac{c_{min}}{bf_{max}} \ , \\ \Delta t &\approx \frac{\Delta x}{c_{max}\sqrt{3}} \ , \end{aligned} \tag{6.9}$$

where c_{max} and c_{min} are the maximum and minimum wavespeed, f_{max} is the maximum frequency, and b is a constant with the criteria that $b \geq 8$. The minimum wavespeed will correspond to a transverse wave and the maximum wavespeed will correspond to a longitudinal wave, since $c_{transverse} \approx \frac{1}{2}c_{longitudinal}$.

6.2 Stress-free Boundary Conditions

For a material specimen in air (solid-air interface), we will apply stress-free boundary conditions on the surface of material so that the boundaries are traction free. Stress free boundary conditions are implemented by setting the shear stresses and normal stress components equal to zero at the boundaries. The shear components are on the surface so we simply set them equal to zero [151]. To make the normal stresses equal to zero we set $T_{ii}^{(n)} = -T_{ii}^{(n+\hat{x}_i)}$ on lower boundaries and $T_{ii}^{(n+\hat{x}_i)} = -T_{ii}^{(n)}$ on upper boundaries [17], [154]. Applying the boundary conditions at an upper boundary we get

$$\dot{v}_i^{(n)}(t) = \frac{-2T_{ii}^{(n)}(t)}{\rho^{(n)}\Delta x}, \quad (6.10)$$

and at a lower boundary

$$\dot{v}_i^{(n)}(t) = \frac{2T_{ii}^{(n+\hat{x}_i)}(t)}{\rho^{(n)}\Delta x}. \quad (6.11)$$

6.3 Parallel Processing

As with the acoustic finite integration simulations discussed in section 5.4, we ran the code in parallel on multiple CPUs. We used the simple 1D virtual topology described earlier, but the passing of required components is slightly more complicated than the AFIT case. We are breaking up the simulation space in the x_1 direction, and therefore all equations that require stress or velocity values in the $+/-\hat{x}_1$ direction

must have those values passed across node boundaries (from one computer processor to its neighbors), see Figure 6.2. For the 1D virtual topology the EFIT equations require that T_{13} , T_{12} , and v_1 be passed to the right (rank+1), and that T_{11} , v_2 , and v_3 be passed to the left (rank-1) across processor boundaries. For example, since $T_{13}^{(n-x_1)}$ is required by $\dot{v}_1^{(n)}$, it must be passed to the right neighboring processor in order to calculate $\dot{v}_1^{(n)}$.

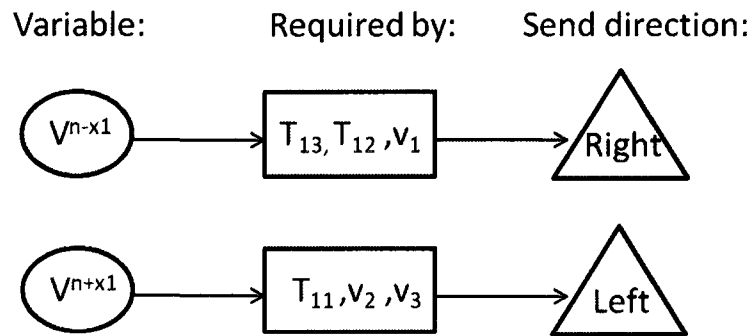


Figure 6.2: Direction of variable passing required by EFIT with a 1D virtual topology.

6.4 EFIT Code Verification

In section 5.4 it was not necessary to verify the AFIT code because it was previously verified through comparisons to experimental results [126]. For the algae application we did not need to change the velocity and stress equations or the parallelization (message passing) part of the code. The EFIT code, however, has been significantly changed from the cylindrical elastodynamic finite integration (CEFIT) code on which it is based. Therefore, we must benchmark the code by comparing simulation results to basic scattering cases. EFIT simulations for this work were run on one of three available computing resources: the typhoon sub-cluster of the SciClone Computing

Cluster at the College of William and Mary (72 dual-processor, dual-core Dell SC1435 CPUs at 2.6 GHz), a new HP DL785 multicore machine (8 6-core cpus at 2.4 GHz) in the NESB Branch at NASA Langley Research Center, or the K-Cluster at NASA Langley (252 8-core Intel Xeon 5355 CPUS. at 2.66 GHz).

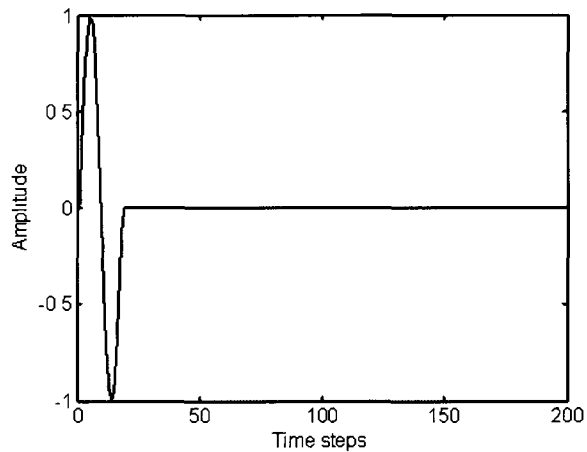
The first step we took to benchmark the EFIT code was to run simulations of wave scattering from boundaries at various angles in order to verify the overall large-scale (geometrical/ray scattering scale) behavior of the EFIT code. These simple cases allowed us to check for the presence of mode conversion and to check reflection and transmission angles. Figure 6.4 shows one example result for an incident longitudinal elastic wave created by a circular transducer on the top a steel block containing an angled stress-free boundary. The transducer drive function and frequency content of the incident beam are shown in Figure 6.3. Note that the x and y axes labels correspond to the number of simulation steps, where step size multiplied by the number of steps equals distance. The total simulation space in this case is equal to $5.54 m^3$, and the 2D slice represents $3.13 m^2$ since the step size in Figure 6.4 is $\Delta x = 0.0118 m$. The angle of wave incidence in this case is $\theta_{inc} = 20 \text{ degrees}$. The material parameters used for steel are a density of $\rho = 7820 \text{ kg/m}^3$ and longitudinal and shear wave speeds of $c_L = 5900 \text{ m/s}$ and $c_T = 3200 \text{ m/s}$.

The images clearly show mode conversion as a result of scattering from the angled boundary. Using Snell's Law we can calculate the expected angle of reflection for the scattered longitudinal and shear waves (θ_{scatt}^L and θ_{scatt}^S),

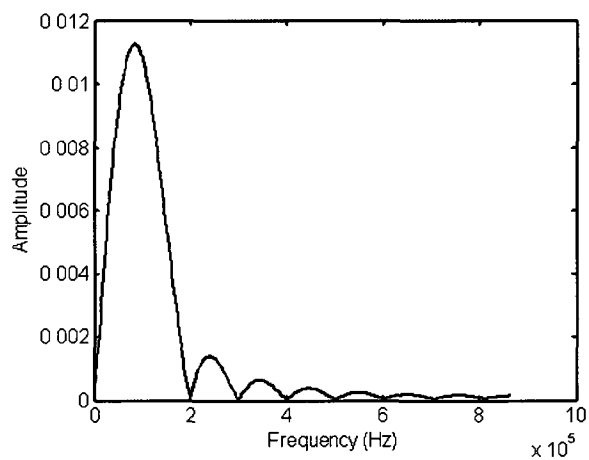
$$\frac{\sin(\theta_{inc}^L)}{c_L} = \frac{\sin(\theta_{scatt}^L)}{c_L} = \frac{\sin(\theta_{scatt}^S)}{c_T} . \quad (6.12)$$

For an angle of incidence of 20° , the reflected angles should be $\theta_{scatt}^L = 20^\circ$ and $\theta_{scatt}^S = 10.7^\circ$. Black lines in images f) and g) have been placed at the expected

scattering angles for the longitudinal and shear waves. The reflected angles in the EFIT simulation match those calculated by Snell's Law. Additionally, we see that the incident longitudinal wave has traveled approximately 1.36 m ($\Delta x \cdot 115\text{ steps}$) in $231\text{ }\mu\text{s}$, which is what we expect based on the wave speed. Figures 6.5 and 6.6 show 2D and 3D images of EFIT simulation results for elastic waves created by a circular transducer on top of a steel block containing a wedge of brass at an angle of 30° . The drive function for this simulation is the same as shown in Figure 6.3. The expected angle of the transmitted longitudinal wave (shown in the Figure 6.5) was calculated using a longitudinal wave speed in brass of $c_L = 4687\text{ m/s}$. The expected angle matches well with the transmitted wave from the EFIT simulation. Note that the shear wave appears later in time (as in Figure 6.4), but was difficult to distinguish from edge reflections of the longitudinal wave.



(a) Steel block: drive function.



(b) Steel block: transducer frequency.

Figure 6.3: Drive function used for Figures 6.4 - 6.6.

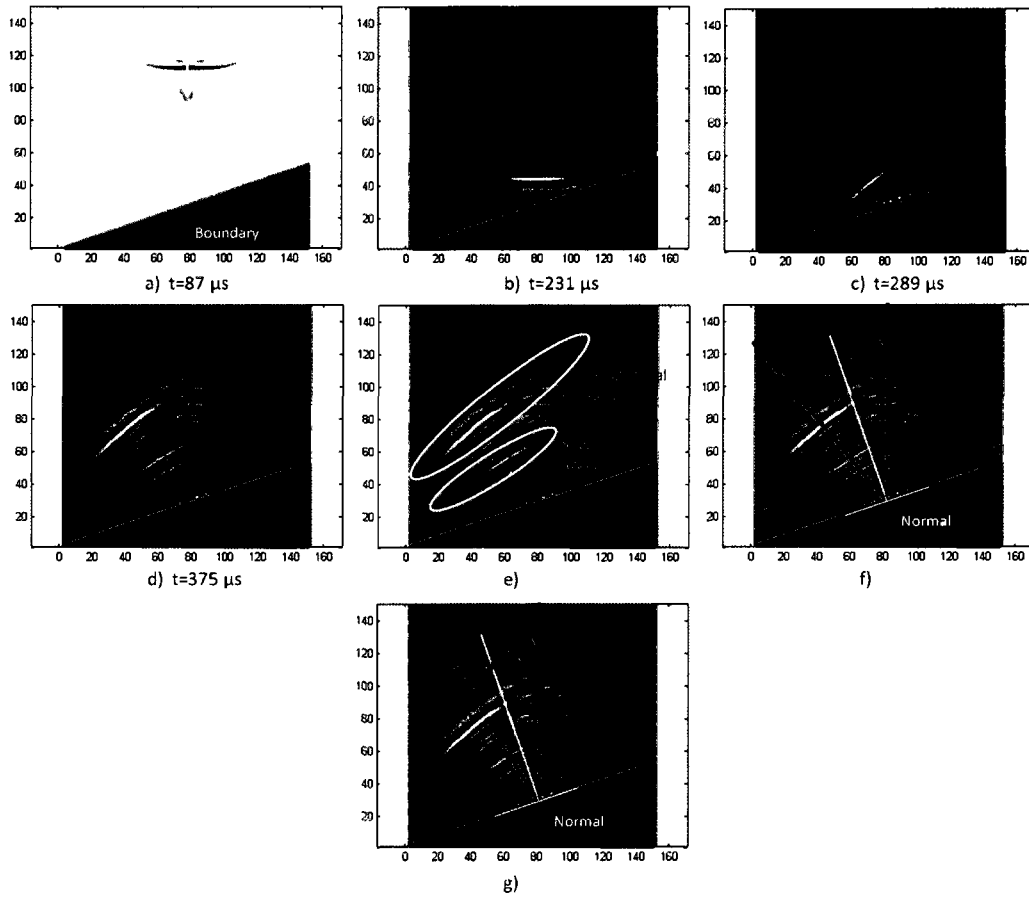


Figure 6.4: Elastic wave in a steel block scattering from an angled free surface at 20° . Both axes represent the number of spatial steps. The circular transducer is on the top surface of the block. Image a) shows a 2D vertical slice through the 3D simulation space of the wave at time $t = 87\mu\text{s}$, b) - d) show additional snapshots of wave propagation, e) longitudinal and shear waves after reflection and mode conversion, f) calculated angle of reflection for longitudinal wave, g) calculated angle of reflection for the shear wave.

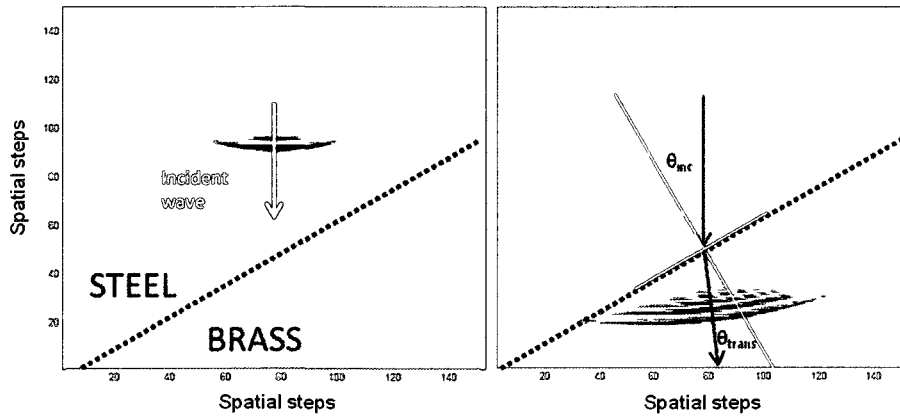


Figure 6.5: Elastic wave in a steel block incident upon brass wedge angled at 30° . A dotted black line shows the location of the steel-brass boundary. The left image shows a 2D vertical slice through the 3D simulation space of the wave at time $t = 127 \mu s$, the image on the right shows the behavior of the scattered and transmitted longitudinal waves at $t = 282 \mu s$. The white lines in the right image show the surface normal at the steel-brass boundary. The calculated longitudinal transmitted angle is shown.

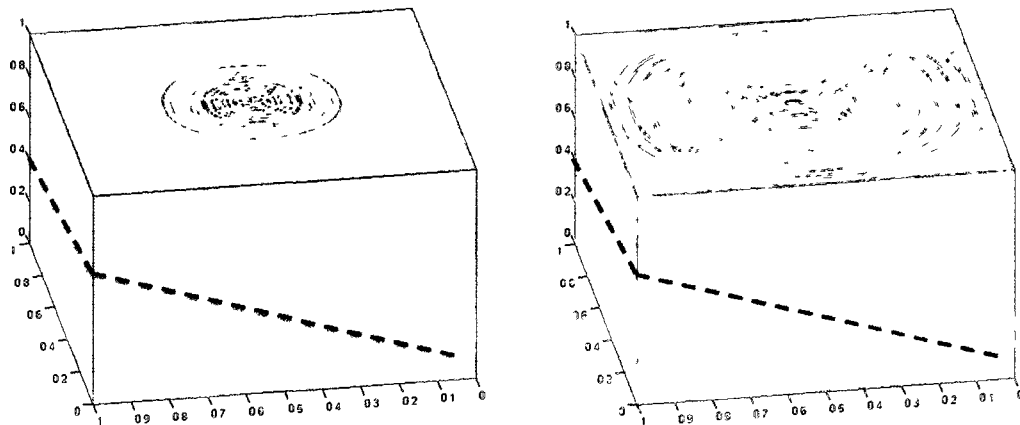


Figure 6.6: Elastic wave in a steel block incident upon brass wedge angled at 30° . The axes represent distance in arbitrary units. The images show wave propagation in the 3D block at two snapshots in time, left: $t = 127 \mu s$ and right: $t = 346 \mu s$. The black dashed line represents the steel-brass boundary.

In order to verify the detailed behavior in the EFIT simulations we compared sim-

ulation output to the analytical result for the canonical case of elastic wave scattering from an elastic sphere. We compared simulation results with the equations derived by Hinders that describe the behavior of a longitudinal plane wave incident upon an immovable elastic sphere embedded in an elastic medium [155]. In section 6.1 we jumped straight from equations 6.1 - 6.3 to discretized equations of motion. If we were instead to plug equations 6.2 and 6.3 into equation 6.1 with no source term, we would get the time harmonic equation of motion for an isotropic medium:

$$\rho \frac{\partial^2 \vec{u}}{\partial t^2} - \mu \nabla^2 \vec{u} - (\mu + \lambda) \nabla(\nabla \cdot \vec{u}) = 0 . \quad (6.13)$$

We can use a Helmholtz decomposition to separate displacement into scalar and vector potentials (longitudinal and transverse parts)

$$\begin{aligned} \vec{u} &= \vec{u}_L + \vec{u}_T , \\ &= -\frac{1}{k^2} \nabla \phi + \nabla \times r \vec{\psi} , \end{aligned} \quad (6.14)$$

where we are following the notation used by Hinders. We assume harmonic variation in time. For the linear case where transverse and longitudinal waves are not coupled, plug (6.14) into (6.13) to get transverse and longitudinal wave equations

$$\left(\nabla^2 + \frac{\omega^2}{c_{long}^2} \right) \vec{u}_L = 0 , \quad \left(\nabla^2 + \frac{\omega^2}{c_{trans}^2} \right) \vec{u}_T = 0 , \quad (6.15)$$

which are satisfied by a plane wave solution. The incident, scattered, and transmitted potentials for shear horizontal and longitudinal waves due to an incident longitudinal wave are listed below [155]. For an incident longitudinal wave there is no shear

horizontal wave.

$$\begin{aligned}
r\phi_L^{inc} &= \sum_{n=0}^{\infty} i^{n+1}(2n+1)\psi_n(k_1r)P_n(\cos\theta) \\
r\phi_L^{scat} &= \sum_{n=0}^{\infty} i^{n+1}(2n+1)\left(\frac{\Delta_1}{\Delta_0}\right)\zeta_n(k_1r)P_n(\cos\theta) \\
r\phi_L^{trans} &= \sum_{n=0}^{\infty} i^{n+1}(2n+1)\left(\frac{\Delta_2}{\Delta_0}\right)\psi_n(k_2r)P_n(\cos\theta) \\
r\psi_{SV}^{scat} &= \sum_{n=0}^{\infty} i^{n+1}(2n+1)\left(\frac{\Delta_3}{\Delta_0}\right)\zeta_n(K_1r)P_n^{(1)}(\cos\theta) \\
r\psi_{SV}^{trans} &= \sum_{n=0}^{\infty} i^{n+1}(2n+1)\left(\frac{\Delta_4}{\Delta_0}\right)\psi_n(K_2r)P_n^{(1)}(\cos\theta).
\end{aligned} \tag{6.16}$$

where r is the distance from the center of the sphere, and the Riccati-Bessel and -Hankel functions are defined as

$$\psi_n(x) = xj_n(x) = \sqrt{\frac{x\pi}{2}}J_{n+1/2}(x) \quad \zeta_n(x) = xh_n(x) = \sqrt{\frac{x\pi}{2}}H_{n+1/2}^{(1)}(x) \tag{6.17}$$

in which $J_{n+1/2}(x)$ and $H_{n+1/2}(x)$ are half-order Bessel and Hankel functions and $j_n(x)$ and $h_n(x)$ are spherical Bessel and Hankel functions. Subscript 1 refers to material properties of the surrounding fluid and subscript 2 refers to the material of the scatterer. The modal coefficients $\Delta_0 - \Delta_4$ are determined from boundary conditions. The boundary conditions require that shear and normal displacement and stress are continuous across the boundary. Only the scattered longitudinal potential was required for the comparison to simulations results since no shear wave is created for $\theta = \pi$ (backscattering), therefore only Δ_0 and Δ_1 are listed in appendix 8.2.2. Longitudinal displacement and velocity in the \hat{r} direction are

$$\vec{u}_L = -\frac{1}{k^2}\nabla\phi_L\hat{r}, \tag{6.18}$$

$$\vec{v}_L = -i\omega\vec{u}_L\hat{r} \ , \quad (6.19)$$

where k is the longitudinal wavenumber. The full form of the equations derived by Hinders are so complicated that it was necessary to check results of the Matlab code implementing the analytic equations against plots available in the literature. Figure 6.7 shows a comparison between our Matlab code and results of far-field backscattering amplitude published by Brill and Gaunaud for an epoxy sphere in steel [156]. The material parameters for the sphere are $\rho_{epoxy} = 1.18g/cm^3$, $c_L = 2.54 \cdot 10^5 cm/s$, $c_T = 1.16 \cdot 10^5 cm/s$ and for the surrounding media are $\rho_{steel} = 7.54g/cm^3$, $c_L = 5.80 \cdot 10^5 cm/s$, $c_T = 3.10 \cdot 10^5 cm/s$.

The differences between the Matlab code results and the plots published by Brill are due to differences in the step size of ka and the computational precision available today versus in 1987 (for example, our code displays more resonance peak behavior). Furthermore, the equations derived by Hinders makes no approximations that the backscattered amplitude is in the far-field. The comparison shown in Figure 6.7 gives us confidence in our implementation of the complicated analytic scattering equations since our code yields results that match well with published plots. For comparisons to EFIT simulations the infinite summation in 6.16 was calculated to $n = 50$, which guarantees convergence up to frequencies of 1 *MHz* [17]. The highest frequency used for our analytical comparisons was only approximately 30 *kHz*

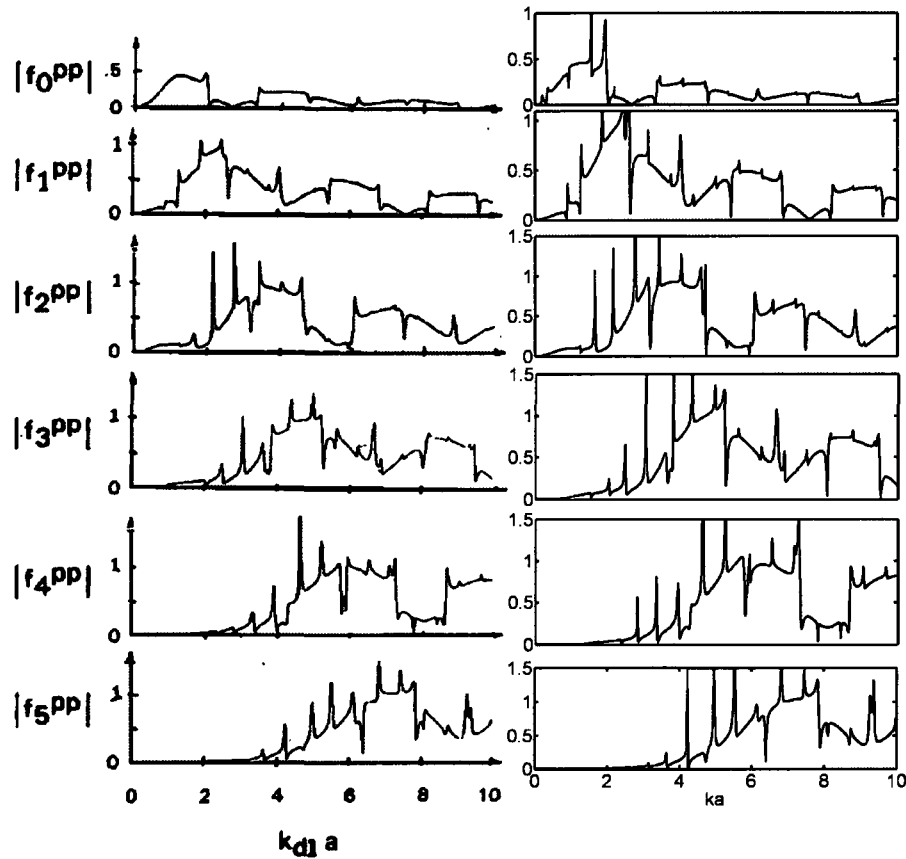


Figure 6.7: Backscattered amplitude for an epoxy sphere in steel for n values of 0 to 5. Comparison of Brill's results (left column) to our Matlab result(right column) [156].

6.4.1 Analytical Solution Comparison

Before comparing EFIT results to the analytical solution we first isolate the backscattering behavior in the simulation by subtracting EFIT results with the sphere present from EFIT results with no sphere. This step is necessary because the incident wave is extended in time and the backscattering is not easily separated from incident wave propagation. In order to compare EFIT time domain results to the frequency domain analytical model we take the Fourier transform (FFT in Matlab) of the EFIT

backscattering result. Next the Fourier transform of the incident wave used in the EFIT simulation is multiplied by the analytical frequency domain result (equivalent to convolution in time domain). In all cases we have normalized the amplitudes to fall within the interval $[0,1]$.

It is important to note that we are dealing with discrete signals, which requires that we choose appropriate sampling rates to avoid aliasing. We made sure that our sampling rate (samples per unit time) for the EFIT backscattered signal satisfies the Nyquist-Shannon sampling theorem, which states that for proper sampling of a signal the sampling frequency must be greater than twice the bandwidth [157]:

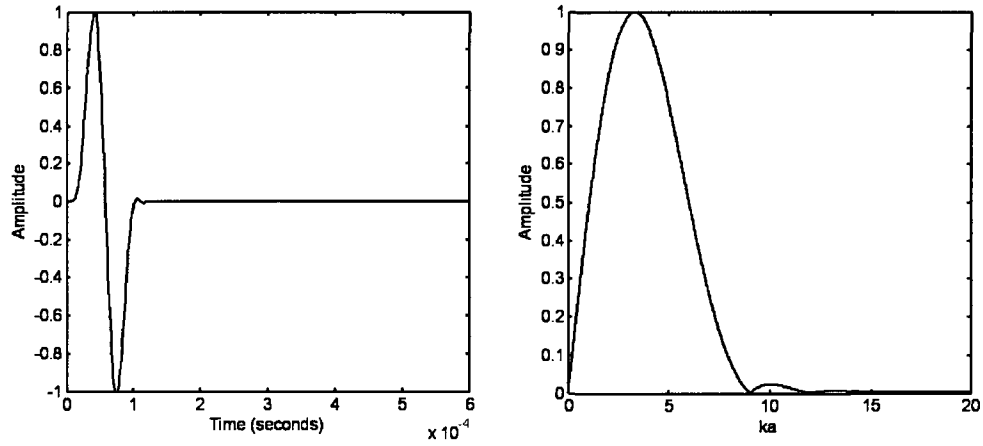
$$f_s > 2B \tag{6.20}$$

where B is the bandwidth and f_s is samples per unit time. Furthermore, in order to obtain sufficient sampling for the Fourier transformed signal of the EFIT result we used zero-padding to increase the length of the time signal, which increases the resolution of its FFT. Zero-padding does not add any frequency content to a time signal, it simply consists of adding zeros to the beginning or end of the signal and is an accepted technique in digital signal processing for gaining resolution in the FFT of a signal [157].

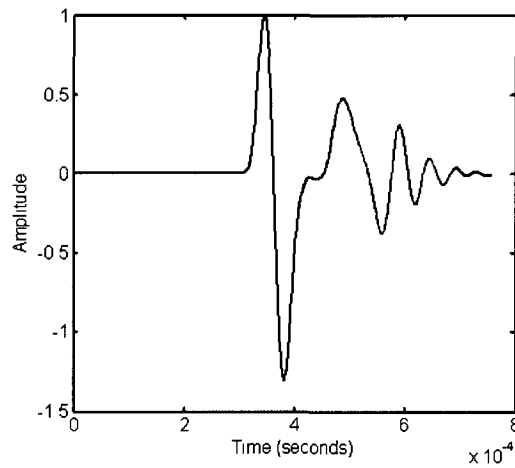
The discrete nature of the simulations can inherently create differences between the EFIT simulations and the analytical model. The finite grid spacing leads to numerical dispersion, which is non-physical and does not occur in the analytical model. Numerical issues are decreased by using a smaller step size. Yet, a smaller step size leads to a larger simulation space which means more computational time and large data output. Furthermore, the smoothness of the discretized sphere depends on the step size and affects the scattering results. Another issue that appears in the simu-

lations is the necessity of time gating (recording the backscattered signal only up to a certain point in time). In our EFIT code the scattered waves from the sphere will eventually reflect off of the walls of the simulation space (corresponding to the edge of the material in which the sphere is embedded). We must, therefore gate out the wall reflections in time domain since the analytical model we are comparing to does not include such reflections. Gating can lead to a loss of information since it inevitably removes part of the scattered wave from our simulation results.

Figures 6.8 and 6.9 show an example of the results of different time gatings of the EFIT result for an aluminum sphere of radius $a = 21 \text{ cm}$ embedded in brass for a spatial step size of 8.3 mm . The spatial step size in this case has not been optimized and corresponds to approximately $\lambda_{smallest}/5$, which does not satisfy equation (6.9). Figure 6.10 shows the poor spatial discretization. The density and longitudinal and transverse velocities used for aluminum are $\rho = 2761 \text{ kg/m}^3$, $c_L = 6363 \text{ m/s}$, $c_T = 3161 \text{ m/s}$ and for brass are $\rho = 8400 \text{ kg/m}^3$, $c_L = 4400 \text{ m/s}$, $c_T = 2200 \text{ m/s}$. The wavenumber is $k = \omega/c$, where ω is radial frequency ($\omega = 2\pi f$). The incident waves used for our comparisons were created using a sine wave filtered by a Tukey window (tapered cosine window) in Matlab. The simulation space size can be increased to reduce the effects of gating; however, we also need to use small spatial step sizes to avoid a poor sphere approximation, aliasing, and numerical dispersion. Therefore, in order to run the simulation in a reasonable amount of time, we must come to a compromise between step size and the total simulation space size.

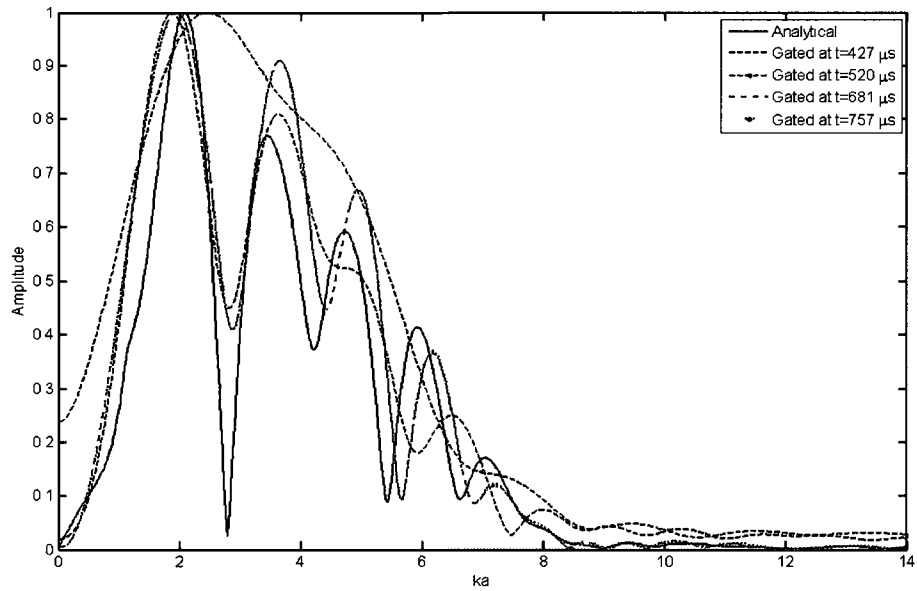


(a) EFIT incident wave in time domain (left) and frequency domain (right). The frequency domain shows normalized amplitude versus ka where $k = \frac{2\pi f}{c}$ and a is radius.

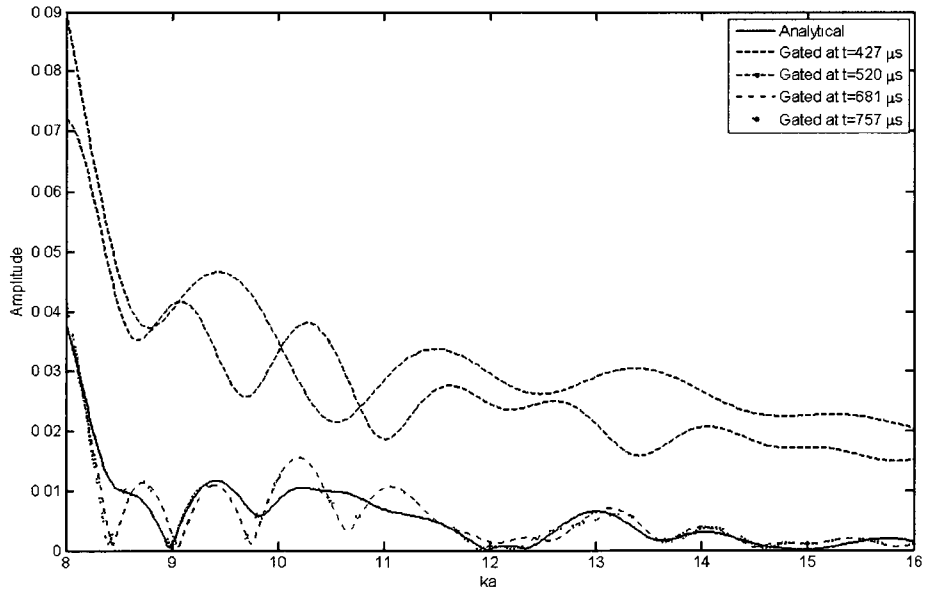


(b) EFIT backscattered amplitude for an aluminum sphere in brass with three gating times indicated: Green= $427 \mu s$, Blue= $520 \mu s$, Pink= $681 \mu s$, Purple= $757 \mu s$.

Figure 6.8: Incident wave and backscattering.

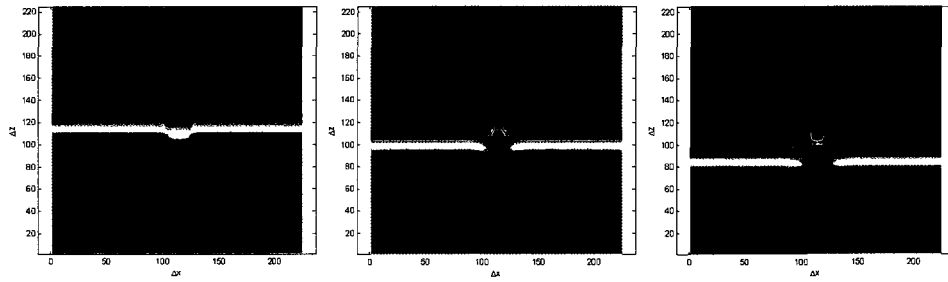


(a) EFIT frequency domain result (normalized magnitude of the displacement) compared to the analytical result for backscattering from an aluminum sphere of radius 21 cm embedded in brass. The plot shows EFIT results for a single step size, $\Delta s = 8.3 \text{ mm}$ for three different gates in time. The longest time gating clearly matches best with the analytical result. A smaller step size would create even better agreement.

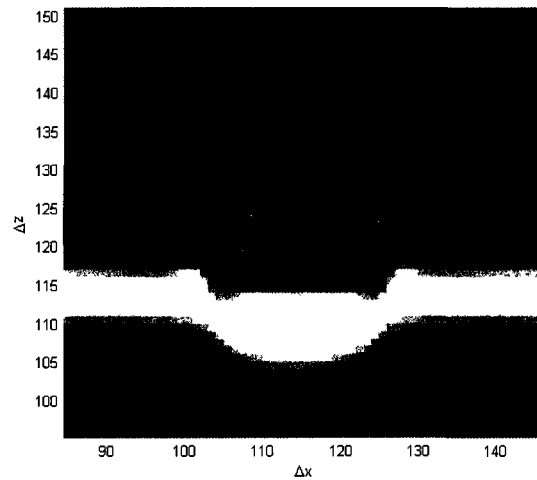


(b) EFIT frequency domain result showing the effects of gating, zoomed in view of results for large ka values

Figure 6.9: Gating results.



(a) Three 2D snapshots in time (earliest on the far left) of EFIT simulation results for scattering from an aluminum sphere in brass. The wave enters the sphere and speeds up, as expected. Part of the wave is scattered from the back side of the sphere and part is transmitted through.

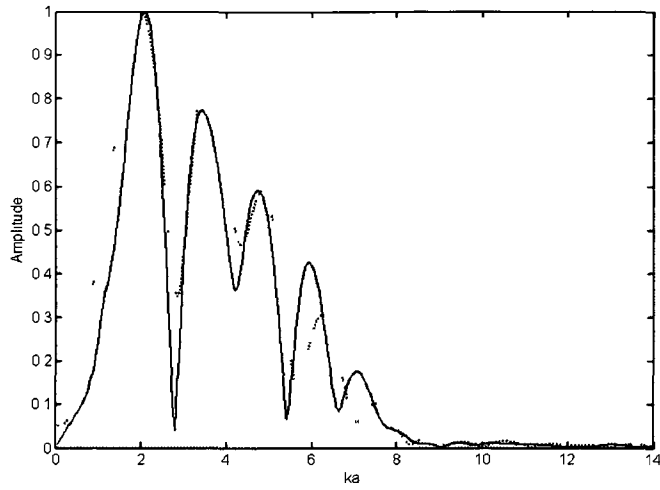


(b) Zoomed in view of the image on the far left showing poor discretization of the sphere (spatial step size $\Delta s = 8.3$ mm).

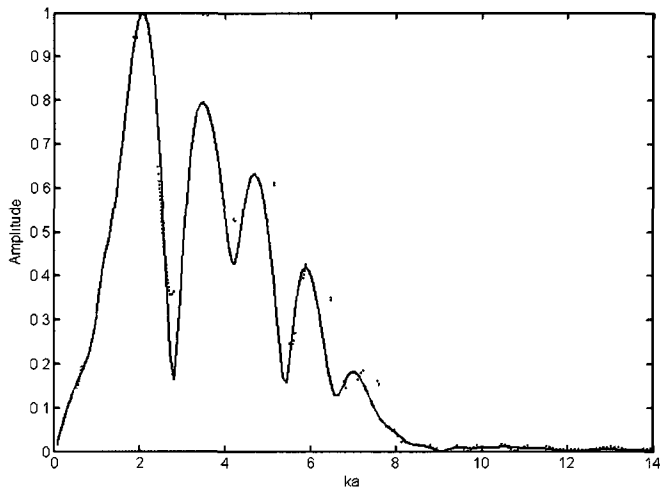
Figure 6.10: Scattering from an aluminum sphere in brass.

It is clear that the step size leads to a rough discretization of the sphere and scattering effects, which leads to the differences in EFIT backscattering results compared to the analytical solution. Figure 6.11 shows backscattering results for a smaller step

sizes of $\lambda/14 = 3.1 \text{ mm}$ and $\lambda/20 = 2.2 \text{ mm}$. Although we are only comparing backscattering (which does not require 3D code), we are testing the code in full 3D form to make sure that not only are the 3D governing equations implemented correctly, but that the message passing and output parts of the code are also working correctly. The smallest step size corresponded to a simulation space 800 X 800 X 800 steps (512 million matrix elements for each time step totaling around 0.8TB of data) and took approximately 50 hours of runtime on 32 processors (1600 CPU hours). Unfortunately, the simulation space size was not large enough for the step size (and resulting sphere radius), and resulted in gating issues. The first plot in 6.11 with a $\lambda/15$ step size and longer gating shows the first peak shifting towards the analytical result. The later peaks also shift slightly towards the analytical result. The plot for step size $\lambda/20$ shows a better match for peak and null positions, though gating has resulted in larger amplitude differences and peak shifting for larger ka values. We are confident that with better gating EFIT results would match even better with the analytical solution. However, the computing cluster is a shared resource, so we did not push the simulation size any further.



(a) $\Delta s = \lambda/14$ (3.1 mm)



(b) $\Delta s = \lambda/20$ (2.2 mm)

Figure 6.11: EFIT backscattering result (dotted line) compared to analytical result (solid line) for two step sizes. Both EFIT results suffer from gating issues.

6.4.2 Discussion of Results

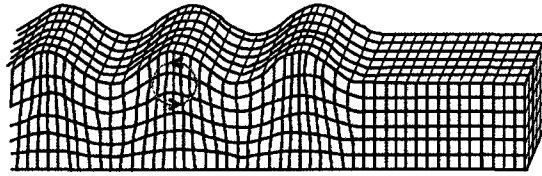
In 1998 Schubert and colleagues published the first comparisons between heterogeneous EFIT results and analytical models [17]. They compared 2-dimensional cylindrical elastodynamic finite integration (CEFIT) simulation results to the Ying model for scattering from a sphere [158]. The Ying and Truell model is a special case of the general equations derived by Hinders that we discussed above. Schubert found that a step size of $\lambda/13$ led to nearly perfect agreement for scattering from an elastic sphere in an elastic solid. Our analytical comparison results show that the Cartesian version of EFIT requires very small step sizes to be well-suited for spherical/curved shapes. Other researchers in the field have noted the difficulty in implementing circular shapes using cartesian EFIT [159]. Verifying the EFIT code using the case of backscattering from a sphere was chosen for the simplicity of the analytical solution. Cylindrical elastodynamic finite integration technique (CEFIT) appears to be better suited for accurately modeling scattering from a single sphere. However, from the results presented in section 6.4.1 we are confident in our implementation of the 3D EFIT equations.

Chapter 7

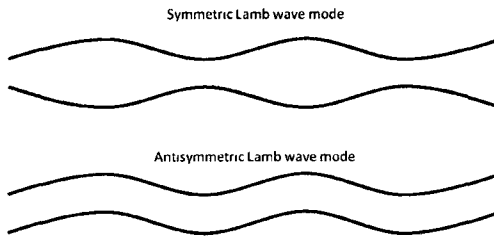
Lamb Wave Scattering

7.1 Guided Waves

Guided waves occur when waves propagate at stress-free boundaries or at boundaries between two differing media. Guided waves and bulk waves are described using the same partial differential equations, but guided waves behave differently from waves in a bulk material. Mode conversion and wave interference due to the boundaries can lead to an infinite number of guided wave modes (wavepackets) [8]. This means that not only do longitudinal and shear (vertical and horizontal) waves propagate in the plate, but any number of other modes as well. Surface (Rayleigh) waves and plate (Lamb) waves are two examples of commonly used guided waves that occur due to stress-free boundaries, see Figure 7.1.



(a) Rayleigh wave [160].



(b) Lamb wave.

Figure 7.1: Examples of guided waves.

More extensive information about guided waves can be found in [8], [10]. This chapter focuses on guided Lamb waves which are created in a plate with stress-free boundaries on upper and lower surfaces. As shown in Figure 7.1, antisymmetric and symmetric lamb wave modes can be created in a plate made of isotropic material (as is the case in our application), and correspond to either a flexing or bulging of the plate material. Lamb wave modes have group and phase velocities that are determined by a frequency-thickness product: the frequency of the driving wave multiplied by the thickness of the plate. When phase and group velocities are not equal, frequency dependent wave speed behavior arises and is referred to as dispersion. An example EFIT simulation result that clearly shows Lamb wave mode propagation in a plate is shown in Figure 7.2. Dispersion curves corresponding to an aluminum plate are shown in section 7.2.

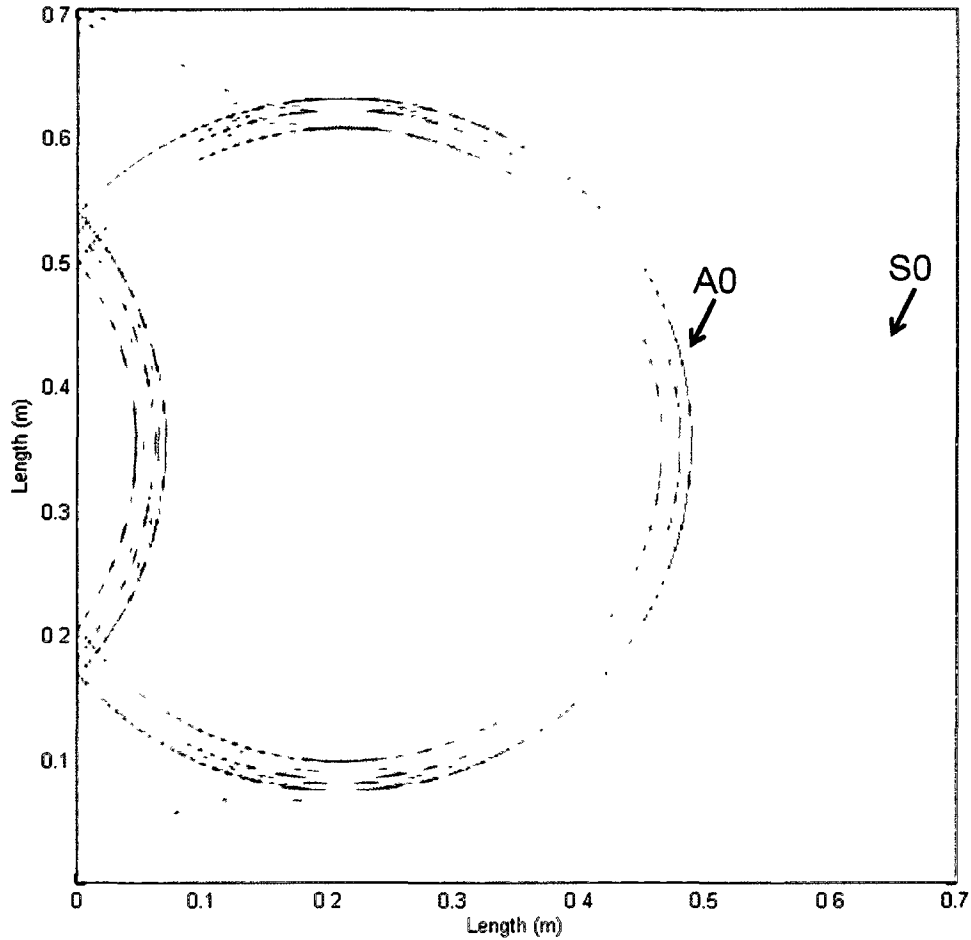


Figure 7.2: 2D slice from an EFIT simulation with a circular transducer on an aluminum plate ($70\text{ cm} \times 70\text{ cm} \times 0.35\text{ cm}$) of frequency-thickness of $1.56\text{ mm} \cdot \text{MHz}$ (see Figure 7.5 for dispersion curves). S0 and A0 Lamb wave modes are indicated, propagating in the plate at their expected group velocities. Waves reflected off of plate boundaries can also be seen in the image (unlabeled).

7.2 EFIT Simulation Results

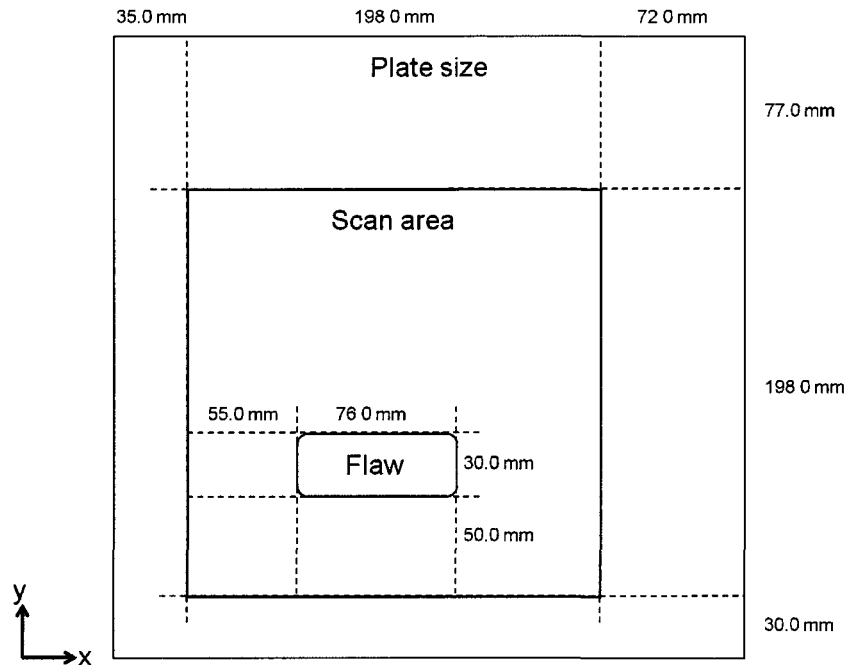
We will look at scattering from a void cut into a $305\text{ mm} \times 305\text{ mm} \times 3.154\text{ mm}$ aluminum 2024 alloy plate as the void depth increases. Previous work in the field showed

that for frequency-thickness values where modes are spread apart, mode arrival times can be extracted from experimental data and correlated with flaw thickness using group velocity dispersion curves [138]. If modes can be identified in experimental signals using signal processing techniques, then changes in mode arrival times should allow a determination of void depth. Also, even when flaw depth cannot be determined based on mode arrivals, the flaw shape and position can often be determined based on experimental data with tomographic reconstruction methods [161]. We will use EFIT simulations to investigate complicated scattering situations for the specific experimental setup discussed below.

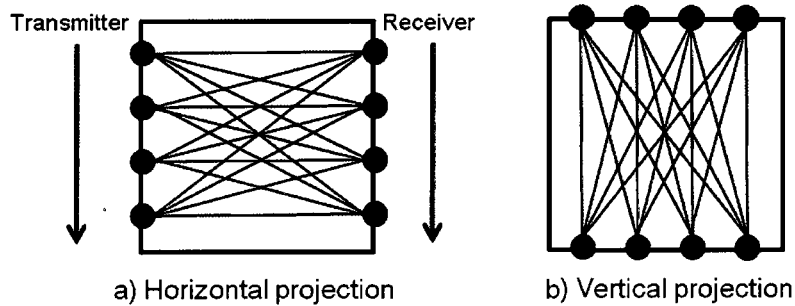
Al 2024 contains approximately 4% copper and 1.5% magnesium and is a common material used in aircraft structures. The void shape considered here is a rounded rectangle, as shown in Figures 7.3 and 7.4. A 1/4" end mill bit was used to machine the void into the plate, leading to a rounded rectangle 76 *mm* in length and 30 *mm* in width with rounded corners corresponding to a circle of radius 3.18 *mm*. Experimental data was taken with a circular 6.35 *mm* (0.25*inch*) diameter transducer with a center frequency of about 2.15 *MHz*. The transducer frequency is sufficient for detecting changes in thickness due to the flaw since the wavelength (approximately 3 *mm*) is on the same order as the plate thickness. An 11.5 *mm* long cylindrical acrylic delay line of diameter 7 *mm* was attached to the transducer. Glycerin was used as a couplant between the delay line and the plate surface. The transducers stepped through 100 locations spaced by 2 *mm* increments. Figure 7.3 (b) shows an example of transmitter and receiver locations and the ray paths between transducers.

Dispersion curves for the group and phase velocities of lamb wave modes for Al 2024 are shown in Figures 7.5 and 7.6, with the frequency-thickness for the full thickness of the aluminum plate specified by the orange line. As the phase velocity of a mode goes towards $+\infty$ (an asymptote), the group velocity goes to zero due to of

the creation of standing waves across the plate thickness [8]. In an isotropic plate the waves separate into symmetric and antisymmetric modes, as shown in the figure [8].



(a) Flaw placement on the plate. The dark black square outlines the transducer placement on the plate.



(b) Example of transmitter and receiver placement and movement for collecting experimental data. The ray paths of the waves are shown between transmitter and receiver positions.

Figure 7.3: Experimental setup.



Figure 7.4: Experimental setup in William and Mary NDE lab (scanning in the vertical projection).

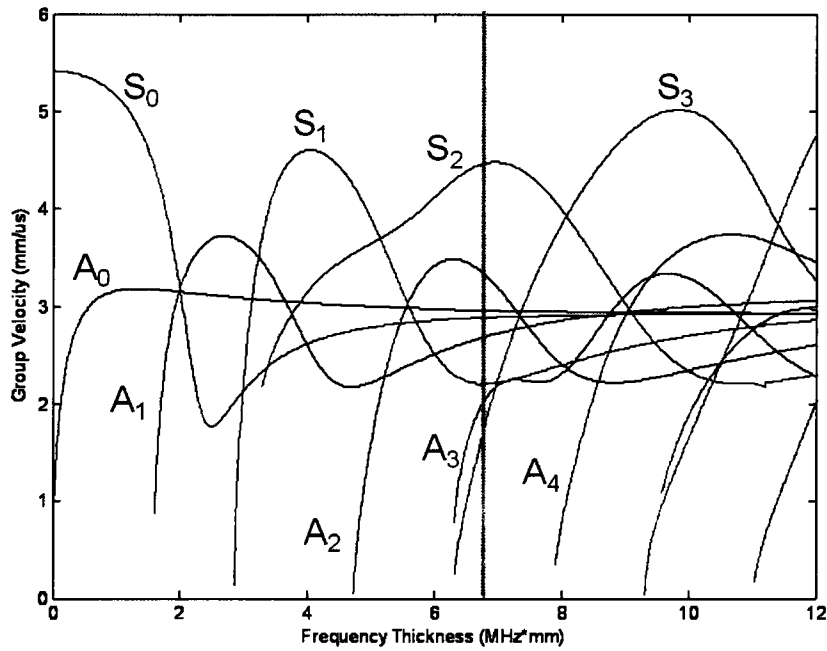


Figure 7.5: Group velocity dispersion curves for Al 2024: The frequency-thickness corresponding to 2.15 MHz and 3.154 mm is specified by the orange line. Symmetric modes are shown in red and antisymmetric modes are blue.

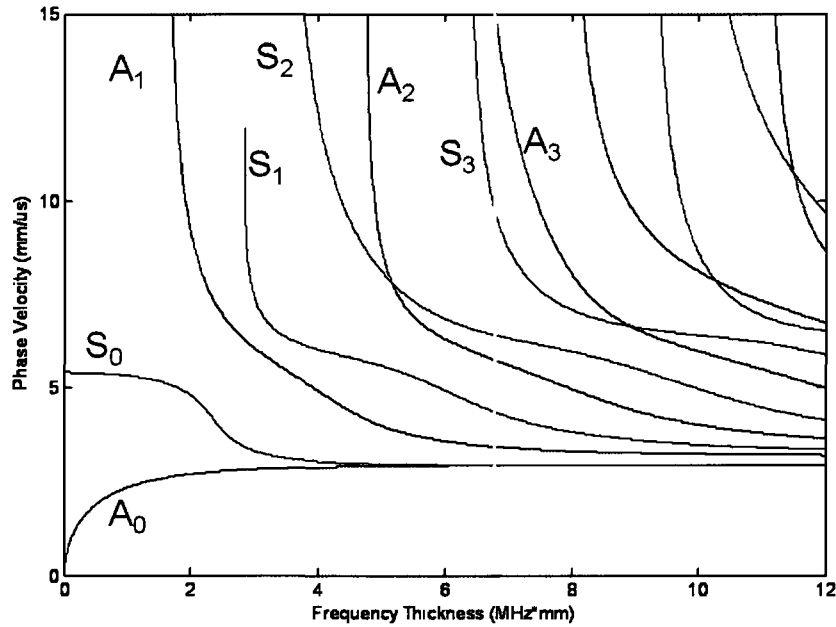


Figure 7.6: Phase velocity dispersion curves for Al 2024: The frequency-thickness corresponding to 2.15 MHz and 3.154 mm is specified by the orange line. Symmetric modes are shown in red and antisymmetric modes are blue.

Experimental data was taken for all transducer locations as the flaw was incrementally milled deeper. Table 7.1 shows the experimental flaw depths. The transducer was excited using a Matec TB1000 tone-burst plug-in card with a voltage range of $200 - 300 \text{ V}$. The generated incident wave in the experiment was a 5-cycle sine wave tone burst with a center frequency of 2.15 MHz . The transmitting transducer converts electrical energy into mechanical energy, creating sound waves which propagate through the material. The waves are then detected at another position on the plate using a second transducer, which now converts the mechanical sound wave energy back into electrical energy. This transmitter/receiver setup is known as a pitch-catch method. The signal is sampled using an analog to digital (A/D) converter at a specified sampling frequency.

Table 7.1: Void Depth

Remaining Material Thickness (<i>mm</i>)	Percent Thickness Loss (%)
3.154	0
3.147	0.7
3.039	3.6
2.995	5.4
2.922	7.3
2.818	10.7
2.584	18.1
2.490	21.3
2.215	29.9
2.008	36.3
1.811	42.6
1.556	50.6
1.289	59.1
0.983	68.8
0.681	78.4
0.456	85.5
0.000	100

As shown in equations (6.5) and (6.6) the EFIT simulation tracks nine variables at each position and time. From these simulations we output v_3 for comparisons to experiment. This choice was made because the transducers used in the experiment receive longitudinal waves and are normal to the plate surface (corresponding to the \hat{x}_3 direction). We used the delay line diameter when sending the transducer drive function into the simulation. The EFIT drive function was a 5 cycle sine wave at a 2.15 *MHz* (thus lasting 2.33 μs), as used in the experiment. The properties used in the simulation for the aluminum plate were a density of $\rho = 2780 \text{ kg/m}^3$ and longitudinal and transverse wavespeeds of $c_L = 6235 \text{ m/s}$ and $c_T = 3139 \text{ m/s}$. A step size of 0.097 *mm* ($\lambda_{mn}/15$) was used in the EFIT simulations.

The void-type flaw is incorporated into the simulation by creating stress-free boundary conditions at the flaw location. We can vary the thickness of the void by

changing the depth where the stress-free boundary conditions begin. We were able to incorporate a void of the same shape as the experimental flaw, although discretization leads to an approximation of the rounded corner curves. Each EFIT simulation of the experimental plate for a single transmitter location and void depth took around 1400 CPU hours. The simulations were completed in less wall-clock time (45 hours) by running the parallel code on 32 processors. We anticipate that at some point the void will be so deep that the wave packets will be significantly scattered, and Lamb wave modes will not propagate strongly through the thinned region. For such a void depth, and beyond, it is likely that flaw depth cannot be determined based on mode arrival times.

From the group velocity dispersion curves shown in Figure 7.5 we see that most of the Lamb wave modes at the frequency-thickness of the flawless plate ($6.78 \text{ mm} \cdot \text{MHz}$) have group velocities that are very close together. EFIT simulations may be particularly helpful for cases such as this, where the existence and overlap of multiple modes will make experimental data much more difficult to analyze. One symmetric mode, the S2 mode, has a higher velocity than the other modes. Therefore, based simply on the dispersion curves we would expect to be able to distinguish that mode propagating out front of the rest in the simulation and in experimental data. However, as shown in Figures 7.7 and 7.8, the amplitude of the S2 mode is very low. The colormap in both figures had to be altered to show the S2 mode. The simulation result confirms why the S2 mode was not detected experimentally. At the expected arrival time for the S2 mode no waves were detected above the amplitude of noise in the raw experimental data, see Figure 7.9. The figure indicates approximate expected mode arrival times and shows the raw experimental data, denoised experimental data, and the EFIT result. The delay lines introduce a shift around $8 \mu\text{s}$ to the right (later in time) in the experimental data. The EFIT result shown in the figure has been

shifted by $8 \mu s$ for comparison to experimental data. The marked arrival times for the experimental results are only an approximation because instrumentation delays can introduce further shifting of an unknown amount.

The filtered raw data was denoised using the Matlab 'cmddenoise' function, which is a wavelet decomposition of the signal. A 'coif3' mother wavelet was used with 5 levels of decomposition. All denoised experimental waveforms in this chapter were filtered using this function. Although the figure shows experimental data and the EFIT result, a direct comparison is not intended for EFIT simulation verification. That type of comparison would be misleading because the experimental waveforms are affected not only by shifting in time, but also by the frequency response of the transmitting and receiving transducers. For example, the transmitter is not sending only a 2.15 MHz wave, but has a finite bandwidth. The figure is rather intended to point out the low amplitude of the S2 mode in both experiment and simulation.

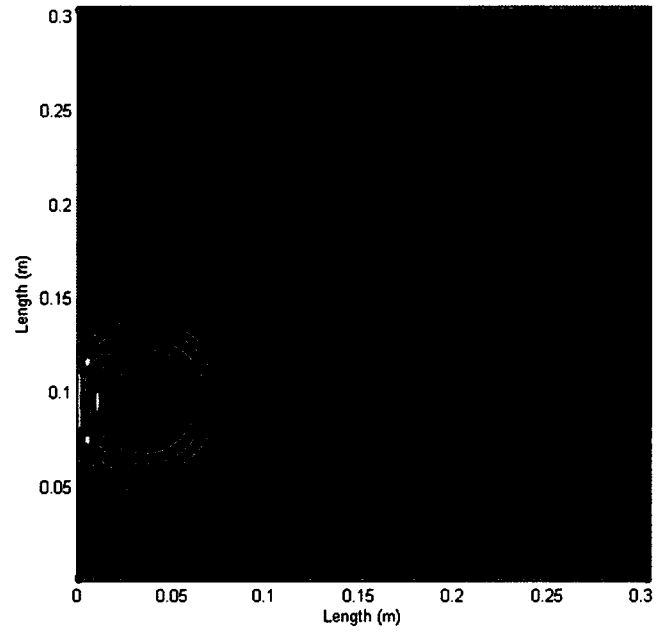


Figure 7.7: 2D image (top view) of EFIT wave propagation in the Al 2024 plate with no flaw for a single snapshot in time. The colormap has been chosen to show the presence of the S2 mode, which has a very low amplitude.

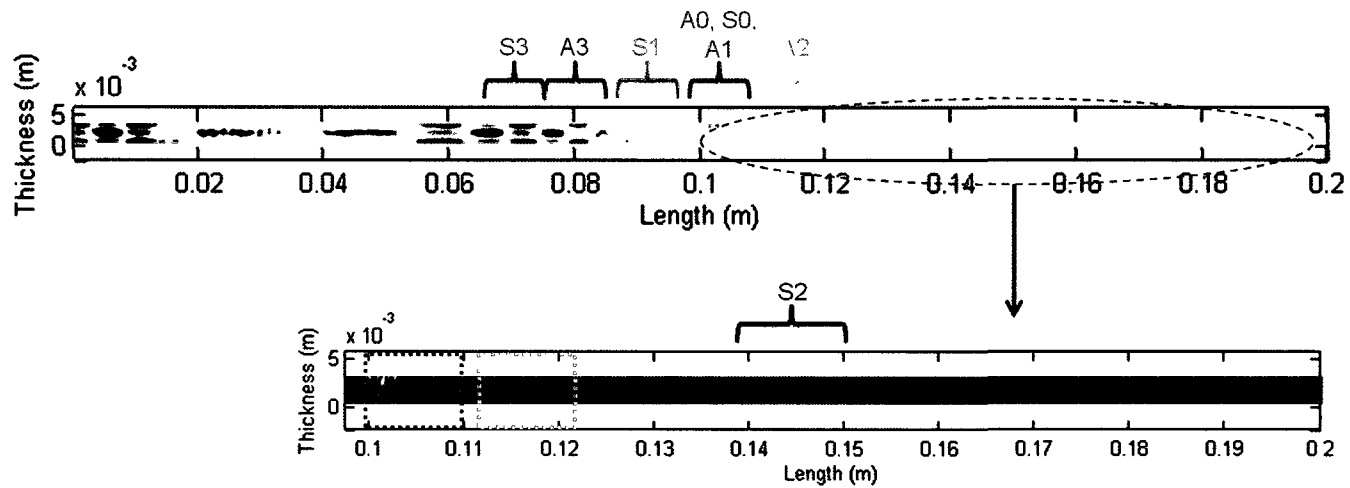


Figure 7.8: 2D slice at $y = 0.095 \text{ m}$, for a single snapshot in time, showing wave modes through the plate thickness. Expected mode propagation distances are marked (top image). A zoomed in view of a section of the plate is shown with the colormap chosen to show the presence of the S2 mode which has a very low amplitude (bottom image). A2 and A0, S0, A1 mode positions are marked in the bottom image by the colored boxes.

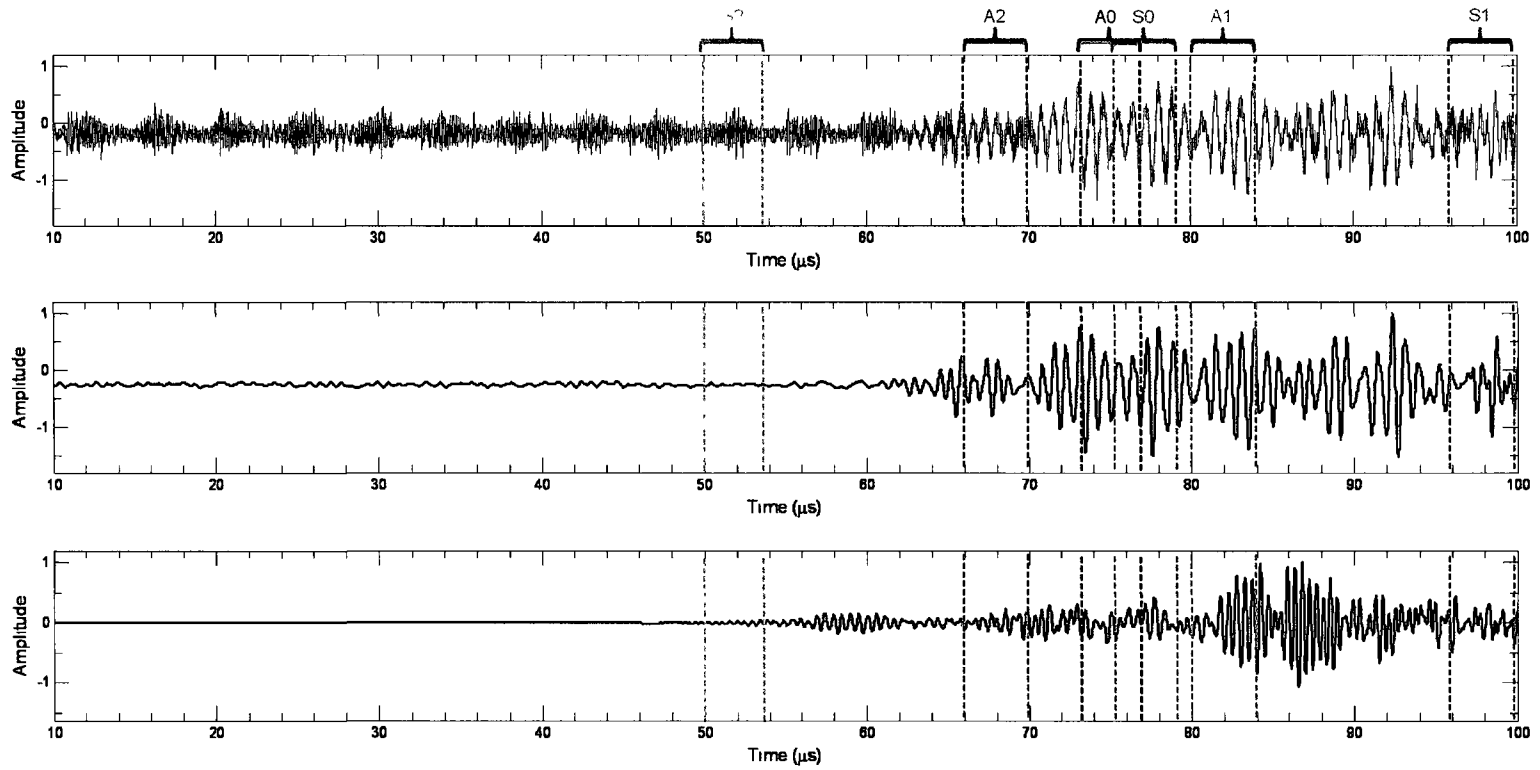


Figure 7.9: Top: Raw experimental data for the plate with no flaw and the transmitter and receiver directly across from each other in the horizontal projection (shortest possible path). The approximate mode arrival times are marked. As early as $84 \mu\text{s}$ low amplitude reflections from the right plate edge enter the signal. After $105 \mu\text{s}$ very large peaks are created due to higher amplitude reflections from the plate edge (gated out above). Middle: Denoised experimental signal after a wavelet filter was applied. Bottom: EFIT result (with $8 \mu\text{s}$ shift for comparison with raw data).

Because the 3D EFIT simulations are computationally demanding, we will limit simulations to four transmitter positions that have been chosen to explore a variety of different scattering situations. As waves enter the thinned region the modes are expected to behave according to the phase and group velocity dispersion curves. Phase velocity changes with thickness make it more difficult to see group velocity mode changes in the EFIT simulation images. A helpful way of viewing the mode propagation is to take the short time Fourier transform in the spatial domain for a single A-line slice through the space (single depth and y -position). This technique is performed easily via the “spectrogram” function in Matlab with one over the spatial step size ($1/\Delta s$) used as the sampling frequency. For the remainder of this chapter we will simply use the term spectrogram when referring to the “spatial spectrogram”. The result of taking the spectrogram in spatial domain is a plot of position versus wavenumber (here defined without the 2π , $k = f/c_{phase}$, in Matlab’s FFT computation), with amplitude represented by the colormap (Matlab’s caxis). All spectrograms shown in this chapter are plotted using the same amplitude colormap. Note that the position axis of the spectrogram result is altered slightly due to window overlap. In our case the overlap leads to a position axis of length 0.29 m instead of the original 0.305 m . This type of analysis on experimental data is not possible with the pitch-catch experimental setup where the displacement at each point in time is known only at the receiver location in the x - y plane at the top surface of the plate.

Since the Lamb wave modes change speed and phase corresponding to thickness, plotting the wavenumber versus position helps separate out mode behavior as the waves propagate. As expected, for the case of no flaw we see wavepackets propagating at the same wavenumbers as time progresses, see Figure 7.10. By this we mean that there are no new or missing modes as the waves propagate. The colormap used in Figure 7.10 will be used for all spectrograms in this chapter and is provided as

a comparison of relative amplitude within each plot. Notice that the spectrogram figures clearly show wave modes separating out as they propagate, due to differences in group velocity. Waves propagating in the plate that do not create Lamb wave modes also show up in the spectrogram. The high amplitude wave packets at the bottom of the spectrogram plots represent very low wavenumbers (high phase velocities), and are at least partly made up of S3 and A3 modes.

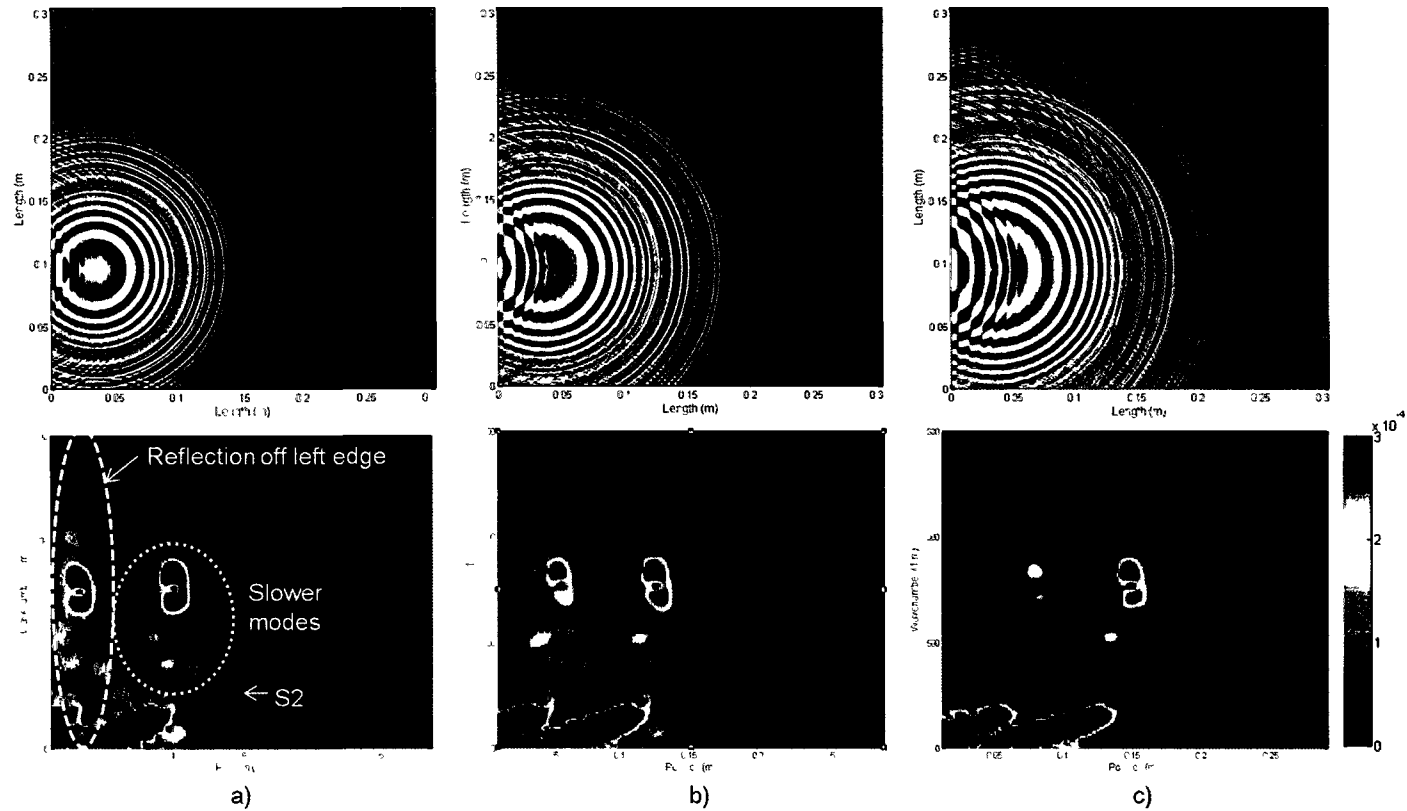


Figure 7.10: Top: EFIT images (2D slice along the top of the plate), Bottom: spectrogram results for the plate with no flaw corresponding to an A-line at $y = 0.095$ m, for times a) $t = 27.0 \mu$ s, b) $t = 36.1 \mu$ s, c) $t = 45.1 \mu$ s. The colormap represents amplitude.

We introduce a void of depth of approximately 0.33 mm (corresponding to 10% material loss) and place the transducer in a position directly in line with the center of the void (shown in Figure 7.11). The frequency-thickness product for this material loss level is $6.06 \text{ mm} \cdot \text{MHz}$ and leads only to small changes in the phase and group velocities. Figure 7.12 shows the EFIT result (2D slice taken directly beneath the void) and spectrograms at two points in time. In this chapter the same colormap is used for all EFIT gray scale slices showing the x - y plane, except Figures 7.10 and 7.13. The spectrogram shows the S2 mode group velocity decreasing slightly as it enters the thinned region, as expected. Later modes are difficult to distinguish individually. The figure corresponding to time $t = 32.5 \mu\text{s}$ shows a wave packet moving to the left as it scatters from the location of the flaw edge, yet from the figures it is clear that the modes still propagate into the thinned region.

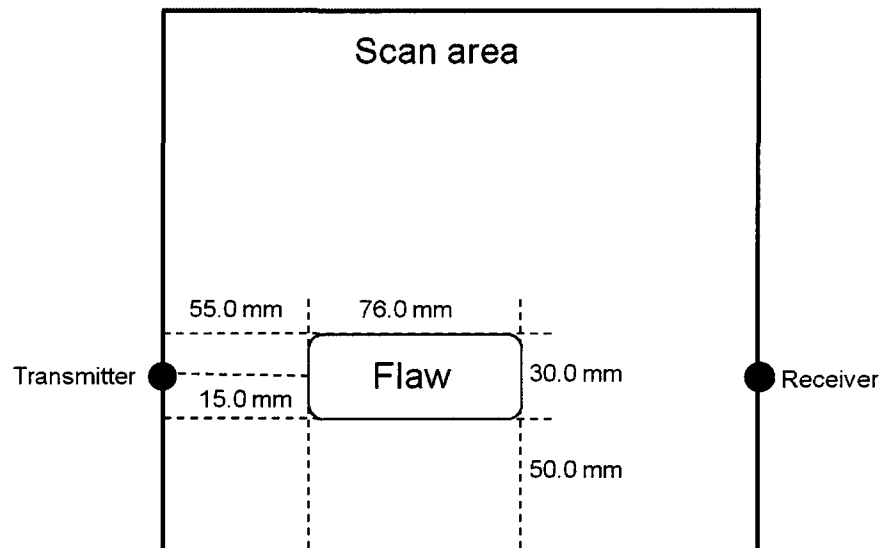


Figure 7.11: Transducer location 1 is represented by the black circle.

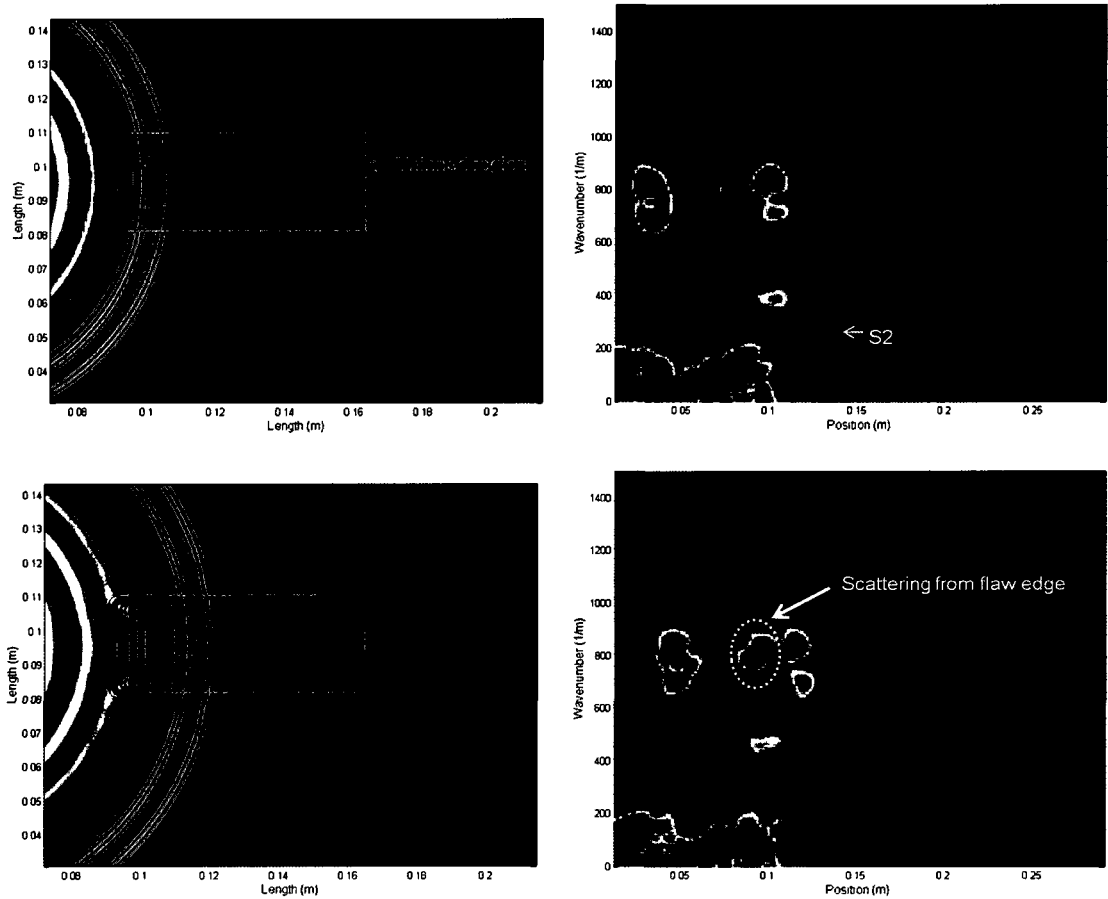


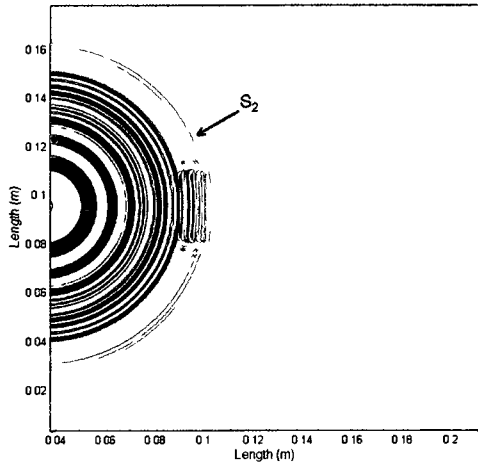
Figure 7.12: Top left: EFIT result for 10% material loss at time $t = 27.0 \mu s$ for a 2D slice taken directly beneath the void, top right: corresponding spectrogram for an A-line at $y = 0.095 m$, bottom left: EFIT result at time $t = 32.5 \mu s$, bottom right: corresponding spectrogram for an A-line at $y = 0.095 m$. The thinned region extends from approximately 0.09 m to 0.16 m.

We increase the void depth to 1.85 mm (corresponding to 59.1% material loss) where the frequency-thickness product is $2.77 mm \cdot MHz$. At this frequency-thickness the only existing modes are S0, A0, A1, and perhaps S1 (which is on the verge of nonexistence and has a larger phase velocity). Figure 7.13 shows the S2 mode entering the flaw region. The colormap has been enhanced to display the S2 mode

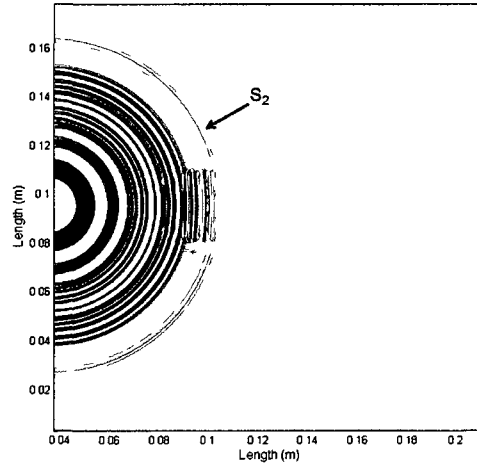
clearly (which saturates following modes). Unlike Figure 7.12, modes can no longer be tracked visually as they enter the thinned area due to larger changes in phase velocity. Mode conversion leads to complicated wave behavior. Figure 7.14 shows 2D slices of the EFIT result at four later points in time with the colormap chosen to show scattering effects within the thinned region.

Figure 7.15 shows spectrogram plots for this void depth. Looking at the simulation results in this way allows us to see the Lamb wave modes that exist inside the thinned region. The plots show S0, A0, and A1 modes appearing as the waves propagate beneath the void and spreading out in time due to differing group velocities. We also see what is most likely the S1 mode propagating in the thinned region, though the labeled wave packet seems to have a group velocity that would be higher than expected for S1. As the modes leave the thinned region we see the reappearance of the modes that exist at $6.78 \text{ mm} \cdot \text{MHz}$.

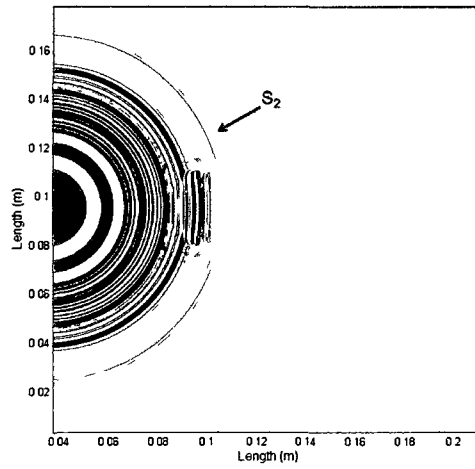
From the spectrogram plots we expect to see all eight Lamb wave modes in the experimental signal. The receiver position is around 0.233 m in the spectrogram plots. Figure 7.16 shows experimental data for this void depth and ray path compared to the same ray path for the clean plate (plate with no flaw). Expected arrival times of Lamb wave modes are indicated in the figure, and are based on the time of re-emergence in the spectrogram plots and the mode group velocities. Most arrival times fall too close to each other to distinguish individual modes. The expected times appear to match well with the experimental signal. Therefore, for this void depth it may still be possible to determine flaw depth experimentally based on mode arrival time shifts, though the calculation would be slightly more complicated to account for mode conversion.



(a) Time $t = 15.5 \mu s$.

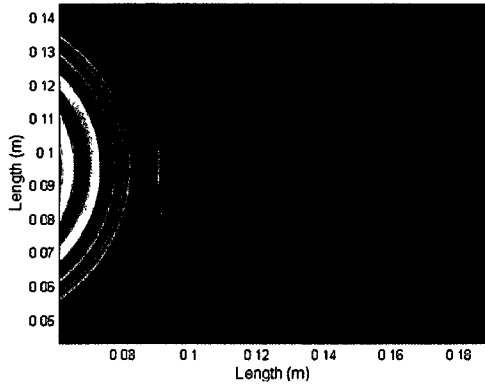


(b) $t = 15.9 \mu s$.

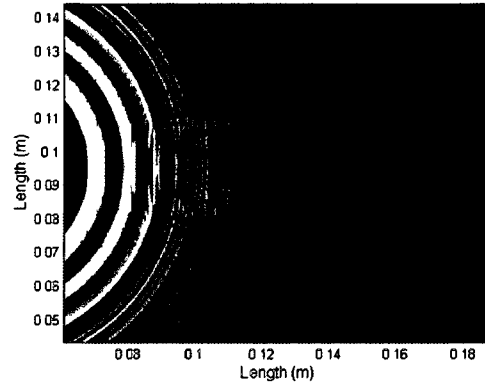


(c) $t = 16.2 \mu s$.

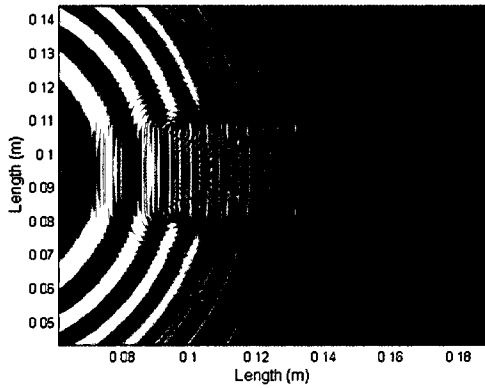
Figure 7.13: Plate with 1.85 mm void (59% material loss): 2D slices directly beneath the flaw. The S2 mode is indicated outside the flaw.



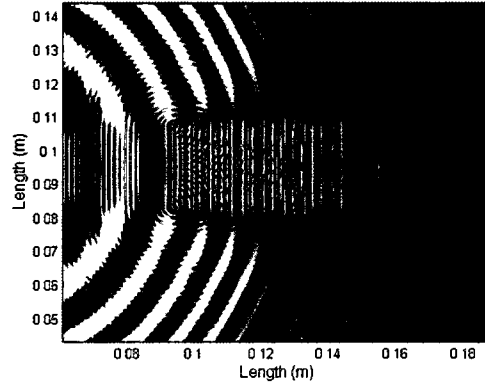
(a) Time $t = 18.0 \mu s$.



(b) $t = 27.0 \mu s$.



(c) $t = 36.1 \mu s$.



(d) $t = 45.1 \mu s$.

Figure 7.14: Plate with 1.85 mm void (59% material loss): 2D slices directly beneath the flaw. The colormap is chosen to show scattering inside the thinned region.

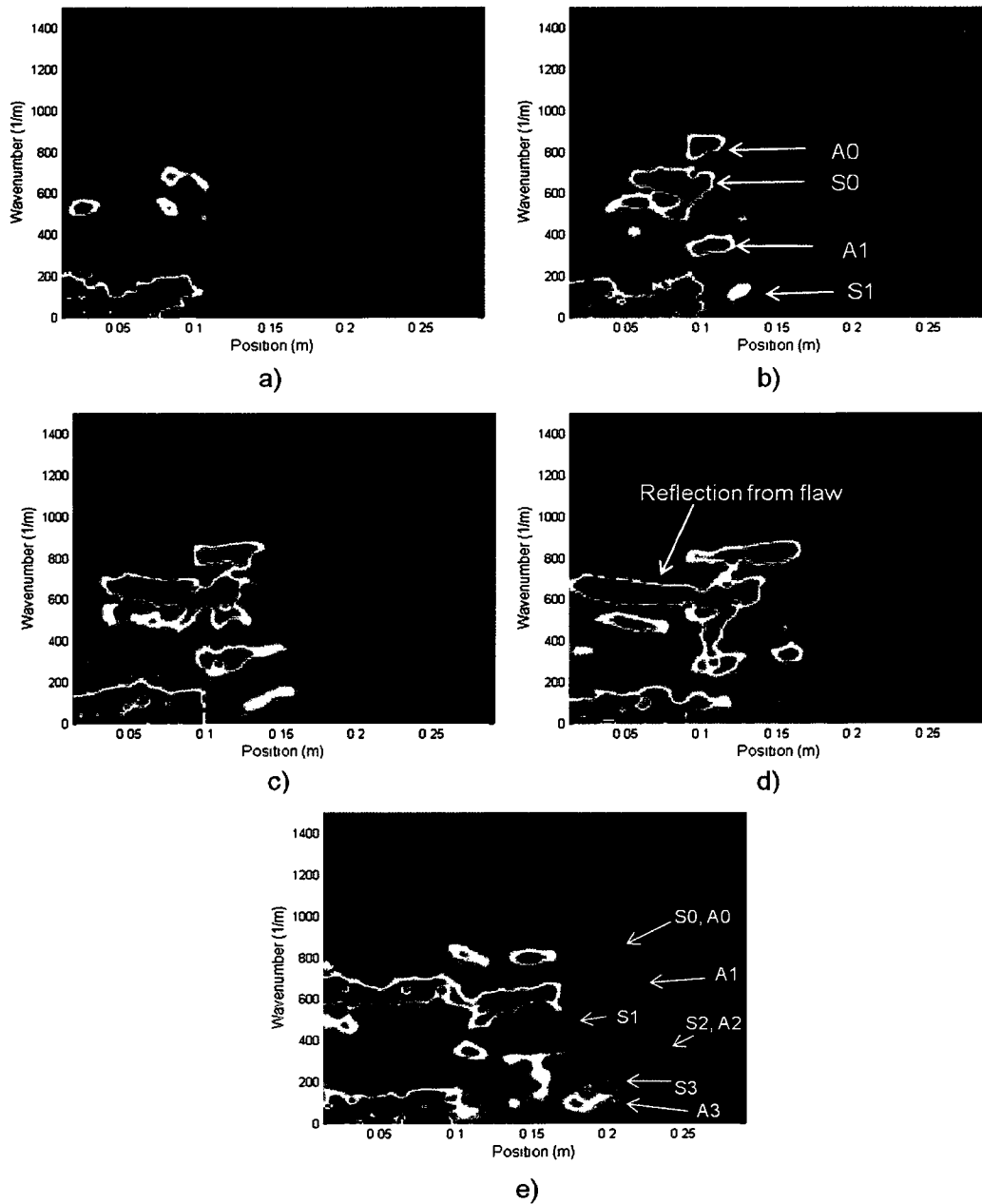


Figure 7.15: Spectrogram plots for 59% material loss for an A-line directly beneath the void at $y = 0.095 \text{ m}$: a) time $t = 27.0 \mu\text{s}$, b) $t = 36.1 \mu\text{s}$, c) $45.1 \mu\text{s}$, d) $t = 54.1 \mu\text{s}$, e) $71.9 \mu\text{s}$. The thinned region extends from approximately 0.09 m to 0.16 m . The colormap shows amplitude (red=highest, blue=lowest).

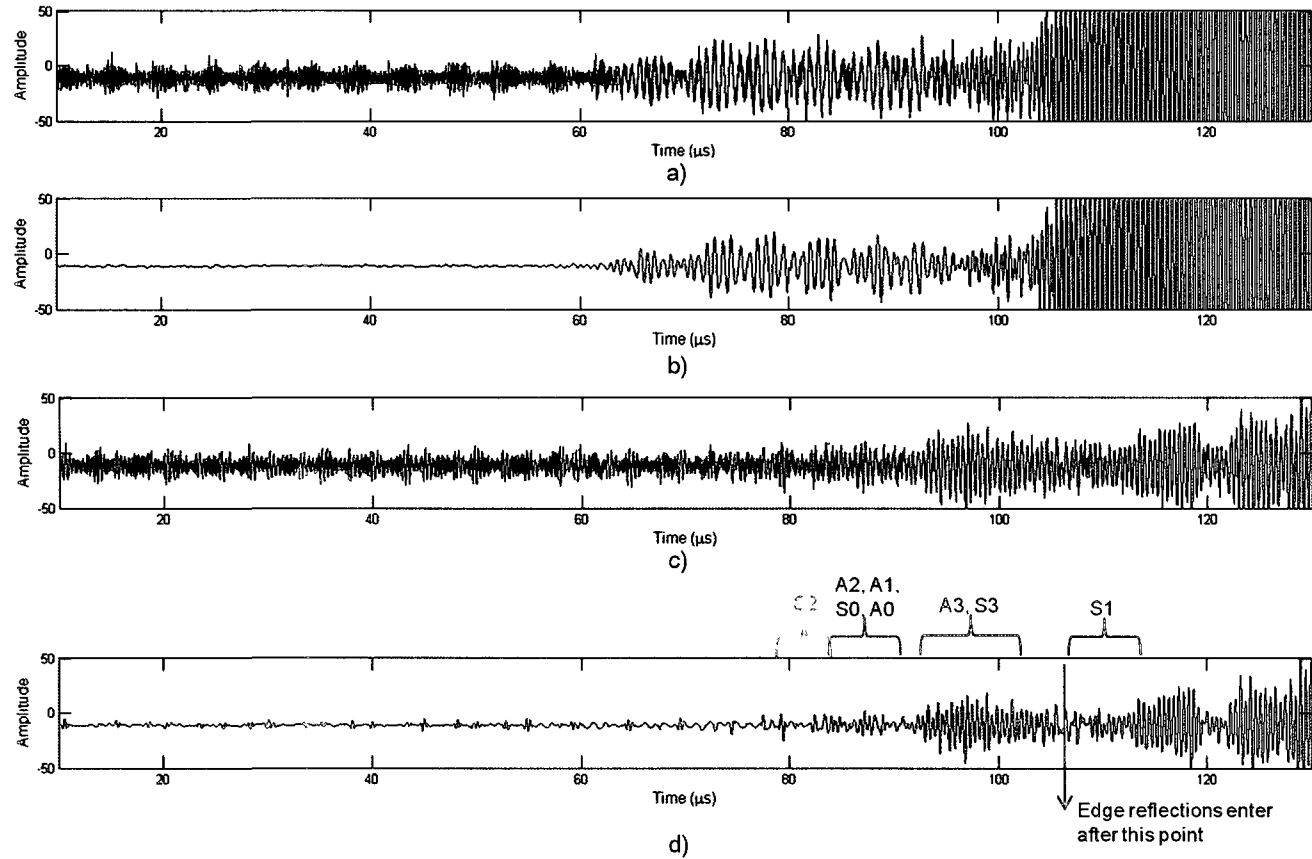


Figure 7.16: Experimental waveforms for the clean plate and 59% material loss for transducer position 1: a) A-line data for the clean plate for the ray path specified in 7.11, b) denoised clean plate waveform, c) raw experimental data for the flawed plate and the ray path specified in 7.11, d) denoised experimental waveform for the flawed plate. Lamb wave mode arrival times based on spectrograms are indicated.

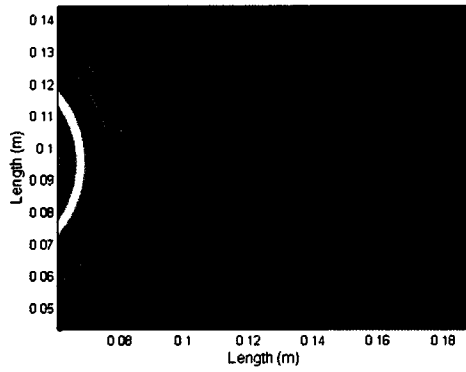
By 85% material loss the EFIT output shows much more significant scattering due to the flaw, see Figure 7.17. Compared to Figure 7.14, we see that for 85% material loss the circular waves traveling into the flaw are more distorted due to scattered waves traveling to the left from the void edge. In the thinned region the wave fronts are extremely fractionated due to diffraction at the void corners and wave interference effects. Such a result can only be observed using three dimensional simulations. The frequency-thickness product for this material loss is around $0.98 \text{ mm} \cdot \text{MHz}$. From the dispersion curves we expect to see two Lamb wave modes, A0 and S0, in spectrogram plots around $k = 925 \text{ m}^{-1}$ and $k = 402 \text{ m}^{-1}$. Inside the thinned region we see what is likely the A0 mode (indicated in the figure), though it has a low amplitude and seems to be disrupted as it propagates beneath the void. We also see what may be an extremely low amplitude S0 mode at time $t = 27 \text{ } \mu\text{s}$. However, if this is the S0 mode it has been significantly affected by scattering due to flaw depth, and/or deconstructive interference due to the flaw shape and dimensions.

The spectrogram plots show the creation of high amplitude waves at much slower phase velocities (around $k = 1200 \text{ m}^{-1}$) that reflect back and forth within the thinned region. At time $t = 54.1 \text{ } \mu\text{s}$ these slow phase velocity waves extend over the full length of the thinned region, making the extent of the region easy to see. As the waves leave the thinned region we see the reappearance of six of the eight expected modes. A1 and S3 modes are missing after the thinned region. What we identify in the figure as S0 and A0 modes after the flaw are shifted to slightly higher wavenumbers than expected and are extended spatially. Later parts of the S0/A0 wavepacket have higher amplitude than other re-emerged modes. In fact, these post-flaw S0 and A0 modes have a higher amplitude than they did at 59% material loss. The exact dimensions of the thinned region seems to have created constructive interference that affected the S0 and A0 modes in this manner. Interestingly, after the thinned region we can

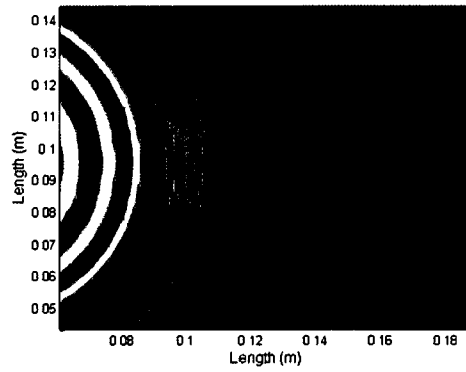
clearly see the S3 mode, which was indistinguishable prior to the flaw, emerge with a large amplitude. The spectrogram plots show the creation of high amplitude waves at much slower phase velocities (around $k = 1200m^{-1}$) that reflect back and forth within the thinned region. At time $t = 54.1 \mu s$ these slow phase velocity waves extend over the full length of the thinned region, making the extent of the region easy to see. As the waves leave the thinned region we see the reappearance of six of the eight expected modes. A1 and S3 modes are missing after the thinned region. What we identify in the figure as S0 and A0 modes after the flaw are shifted to slightly higher wavenumbers than expected and are extended spatially. Later parts of the S0/A0 wavepacket have higher amplitude than other re-emerged modes. In fact, these post-flaw S0 and A0 modes have a higher amplitude than they did at 59% material loss. The exact dimensions of the thinned region seems to have created constructive interference that affected the S0 and A0 modes in this manner. Interestingly, after the thinned region we can clearly see the S3 mode, which was indistinguishable prior to the flaw, emerge with a large amplitude.

The emergence of high amplitude wavepackets is quite surprising. Figure 7.19 shows experimental signals for this void depth and ray path compared the clean plate signal for this ray path. We indeed see very high amplitude wavepackets before large edge reflections enter the signal. Without the EFIT simulations these features in the experimental signal would be very difficult to explain since it is rather unexpected. The figure also indicates expected arrival times for the Lamb wave modes based on the spectrogram plots. Most arrival times fall too close to distinguish individual modes. The receiver position is around $0.233 m$ in the spectrogram plots. The S2 mode (a low amplitude mode) should be the first detected mode, occurring around $71 \mu s$ when the experimental delay is included. S2 is detected at nearly the same time as the leading lower amplitude A0 and S0 modes. Later modes are indicated in

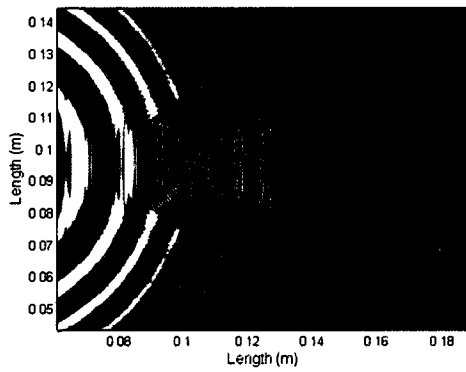
the figure, along with the higher amplitude S0/A0 modes that emerge from the flaw.



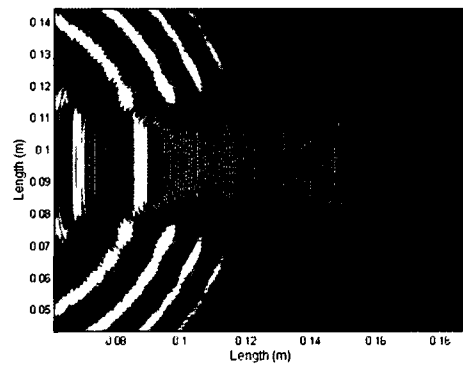
(a) Time $t = 18.0 \mu s$.



(b) $t = 27.0 \mu s$.



(c) $t = 36.1 \mu s$.



(d) $t = 45.1 \mu s$.

Figure 7.17: Plate with 2.69 mm void (85% material loss): 2D slices directly beneath the flaw.

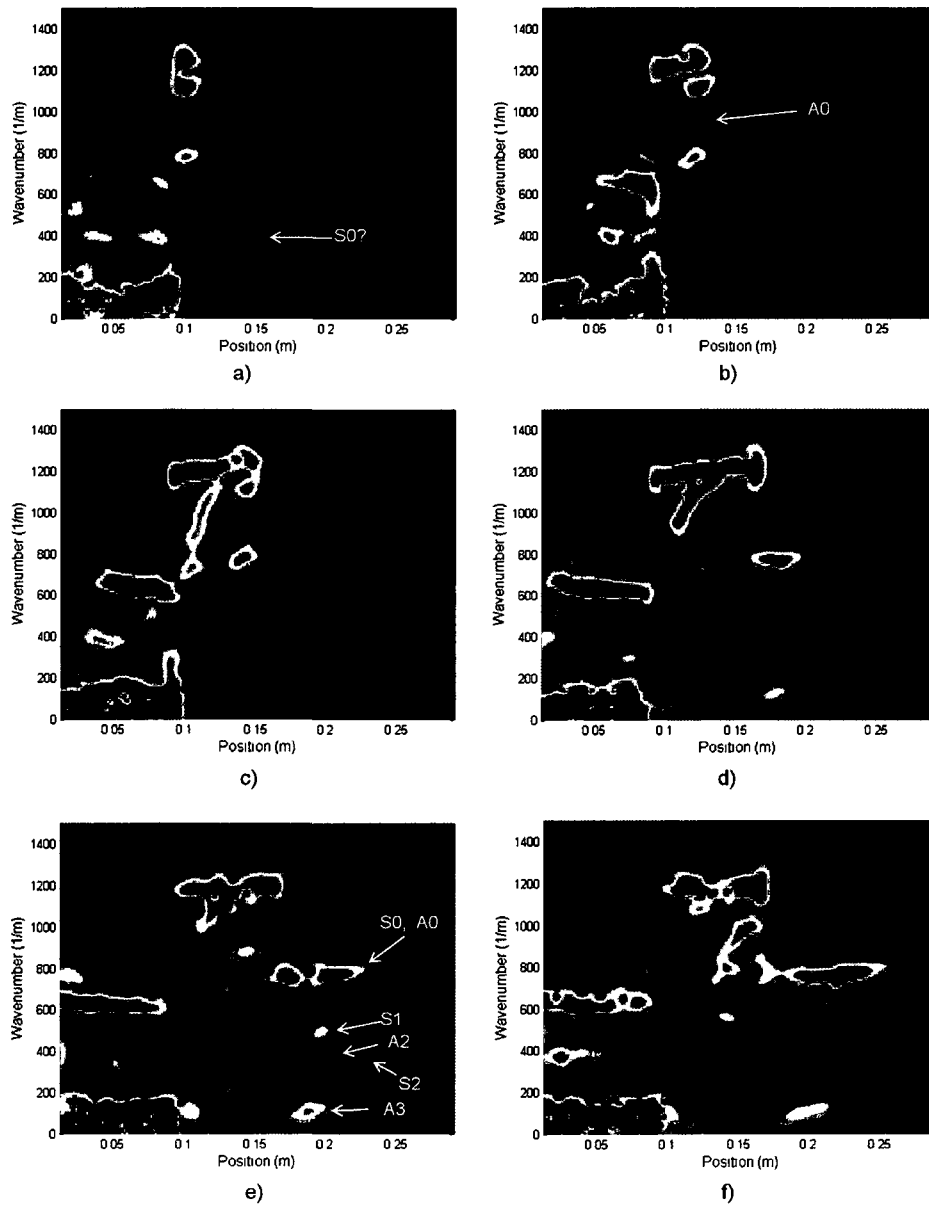


Figure 7.18: Spectrogram plots for 85% material loss for an A-line directly beneath the void at $y = 0.095 \text{ m}$: a) time $t = 27.0 \mu\text{s}$, b) $t = 36.1 \mu\text{s}$, c) $45.1 \mu\text{s}$, d) $t = 54.1 \mu\text{s}$, e) $t = 63.1 \mu\text{s}$, f) $t = 71.2 \mu\text{s}$. The thinned region extends from approximately 0.09 m to 0.16 m . The colormap shows amplitude (red=highest, blue=lowest).

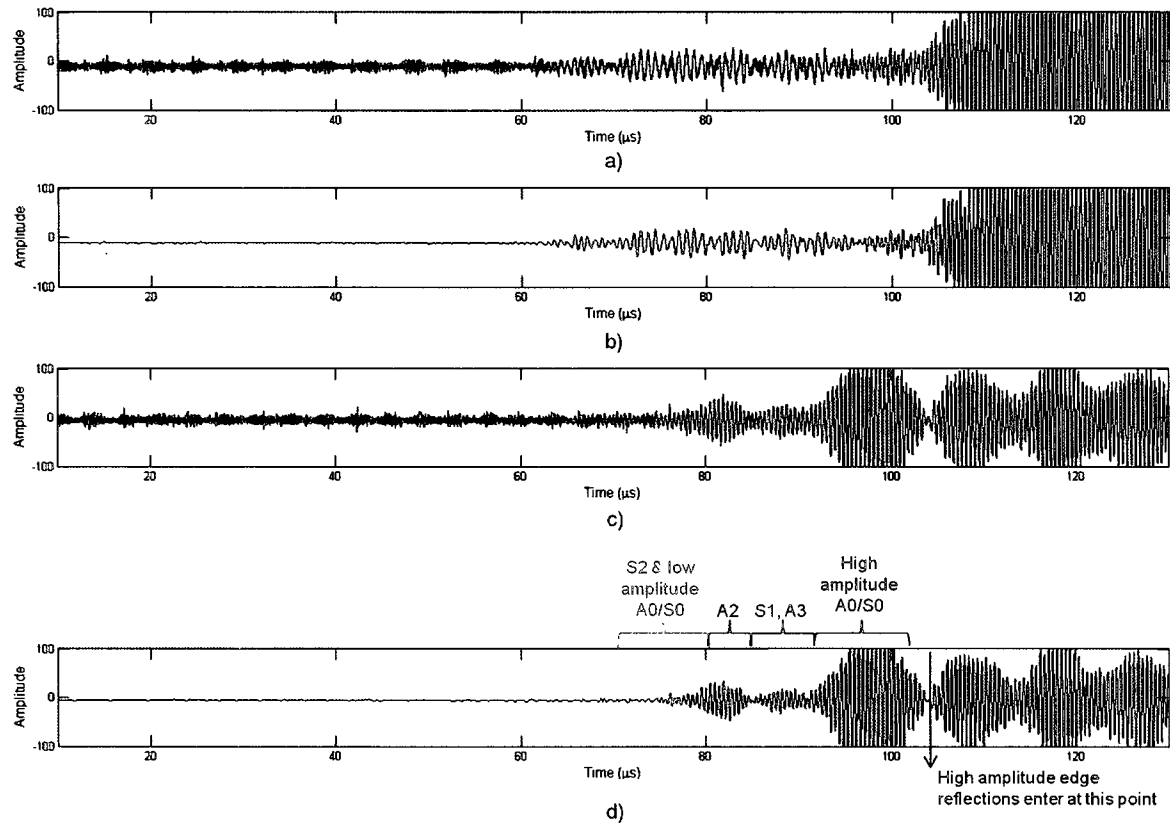


Figure 7.19: Experimental waveforms for the clean plate and 85% material loss for transducer position 1: a) A-line data for the clean plate for the ray path specified in 7.11, b) denoised clean plate waveform, c) raw experimental data for the flawed plate at the ray path specified in 7.11, d) denoised flawed plate experimental waveform. Lamb wave mode arrival times based on spectrograms are indicated. Note the larger y-axis compared to all other experimental signal plots in this chapter.

If more severe scattering from the left edge of the flaw is the primary cause of the near (perhaps total) disappearance of S0 we should be able to see significant changes in the reflected field in 2D EFIT slices taken through the plate thickness. However, Figures 7.20 and 7.21 show only small changes due to waves reflected to the left as void depth increases from 59% to 85% material loss. By $t = 36 \mu s$ we do see reflected waves affecting the incoming waves at both flaw thicknesses. The scattered waves moving to the left disturb incoming wavepackets making them appear as close groups of small circles instead of the solid pancake shapes seen at $27 \mu s$. Since we still see the emergence of all eight expected Lamb wave modes for 59% material loss, these disturbances must not be significant enough to disrupt/destroy the modes. Because the flaw region is too thin to examine scattering via thickness slices, we must rely on the 2D $x-y$ plane images to examine interference effects there. Therefore, based on the small changes in thickness plots and the strong interference patterns in Figure 7.17, we conclude that the most likely cause of such significant changes to modes in the thinned region is due to wave interference created by the void shape and size.

The results discussed above show that by 85% material loss the Lamb wave modes inside the thinned region are considerably affected by scattering. Most of the Lamb wave modes that are re-created outside thinned region are more disrupted than they are at smaller void depths, and one mode fails to reappear at all. Identification of void depth based on arrival times would be much more difficult for this material loss level, and perhaps impossible for greater void depths.

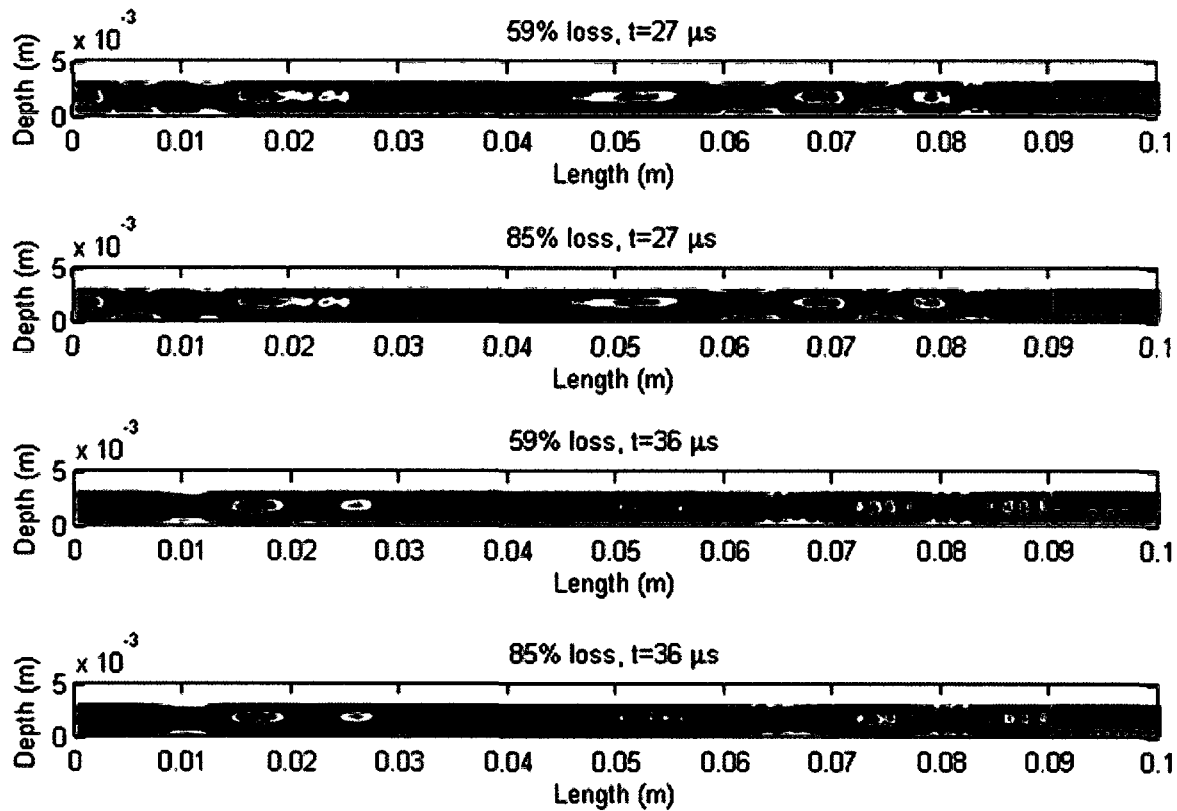


Figure 7.20: 2D slices of EFIT results showing the full thickness of the left half of the plate for $y = 0.083 \text{ m}$ (along to the bottom edge of the flaw) for 59% and 85% material loss at two points in time (indicated above figures). The amplitude colormap is the same for all images. The void region is shown in solid black.

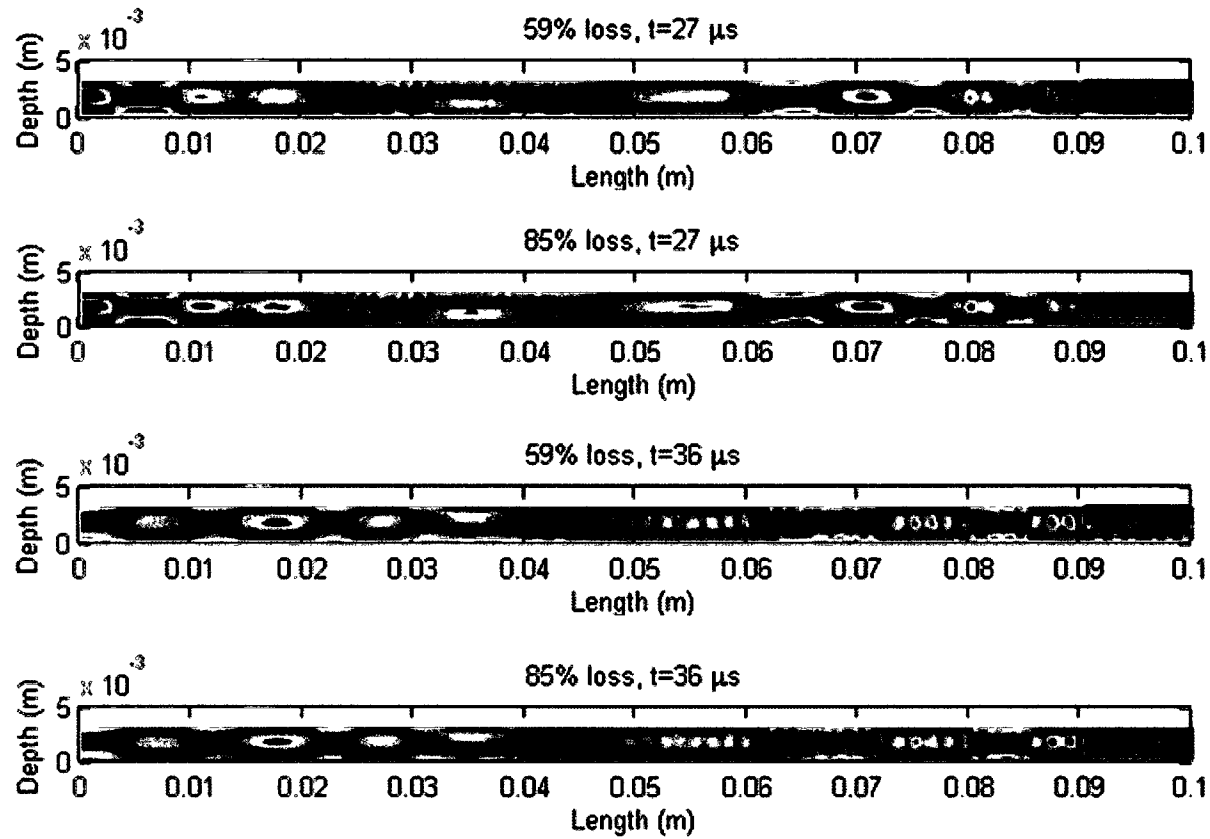


Figure 7.21: 2D slices of EFIT results showing the full thickness of the left half of the plate for $y = 0.095 \text{ m}$ (through the center of the flaw) for 59% and 85% material loss at two points in time (indicated above figures). The amplitude colormap is the same for all images. The void region is shown in solid black.

Next we consider Lamb wave behavior for a second transmitter position, shown in Figure 7.22. This transducer position will lead to different scattering from the flaw, especially from the void corner. For spectrogram plots we will assume the ray path associated with the receiver location shown in the figure. Figure 7.23 shows the chosen ray path overlaid upon the x - y plane of EFIT output. The starting and ending position of the ray path represents transmitter and receiver locations. The thinned region will fall between $0.06 m$ and $0.13 m$ in spectrogram plots. As expected, the spectrogram corresponding to this ray path for the case of no flaw in the plate yields the same result as shown earlier in Figure 7.10, and is not repeated here.

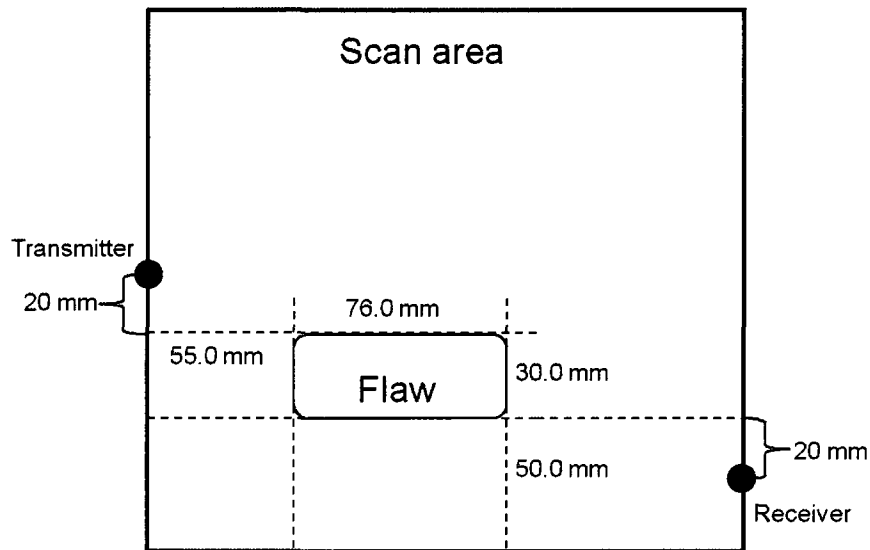


Figure 7.22: Transmitter location 2 is represented by the black circle. Receiver location used for spatial spectrogram plots is indicated.

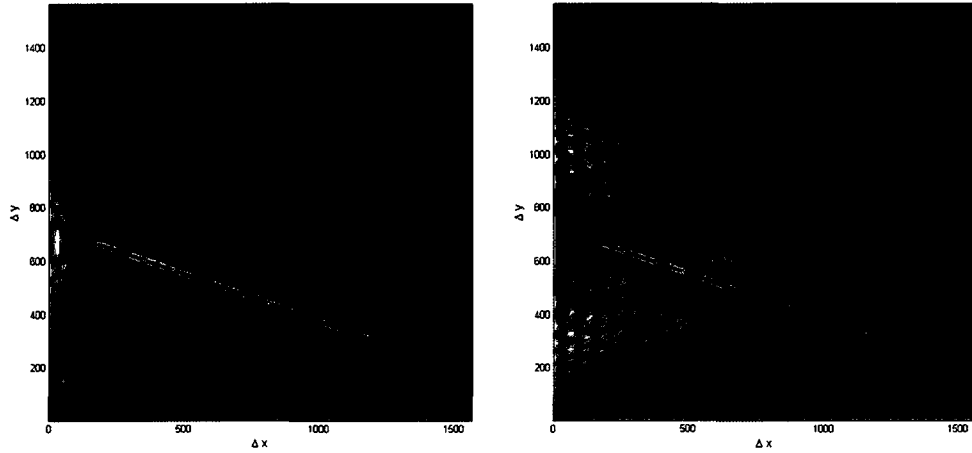


Figure 7.23: The spectrogram ray path used for transducer position 2 is shown in red, with flaw position represented by the green rectangle.

At this transmitter position the EFIT simulation results for various depths show significant scattering from the flaw corner. In fact, the EFIT simulation images show that waves along ray paths which do not go through the flaw are affected by the flaw presence. At 59% material loss the A0 mode was difficult to identify in the spectrogram thinned region, but appeared with the other expected modes. By 68% material loss ($2.11 \text{ mm} \cdot \text{MHz}$) the A0 mode ($k = 790 \text{ m}^{-1}$) briefly appears in the thinned region but disappears by $t = 36.1 \mu\text{s}$ (see 7.24 and 7.25). Additionally, what we have identified as potentially the A1 mode is disrupted by time $t = 72 \mu\text{s}$. Again, the spectrogram plots show the creation of high wavenumber waves within the thinned region. Also notice that the spectrograms show no strong reflection of waves from the void corner, like we saw at the void edge for the previous transducer location.

Once the waves have propagated through the thinned region we only see the re-emergence of a low amplitude wave packet at the wavenumber corresponding to S0 and A0 modes, which are grouped closely both in phase and group velocities. Thus, along this specific ray path the Lamb wave modes are significantly disrupted

and/or destroyed. Figure 7.26 shows experimental data corresponding to this ray path compared to data for the clean plate. Low amplitude waves reflected from the right plate edge would enter experimental signal by approximately $t = 88 \mu s$ (when the experimental delay lines are included). Additionally, in the EFIT images we see reflections from the bottom plate edge approaching the receiver position at $72 \mu s$. Edge reflections at higher amplitudes will enter the signal at a later time, as is clearly seen in the clean plate signal.

Based on the spectrograms, the re-emerged S0 and A0 modes should reach the receiver around $88 \mu s$ ($\approx 96 \mu s$ with delay lines). The receiver is located around $0.2 m$ in the spectrogram plots. The re-emerged S0 and A0 modes would be somewhat mixed in with reflected waves from the right and bottom edges of the plate. In the experimental data we do see a peak occurring around $96 \mu s$, which may be the detection of S0 and A0 modes. An earlier peak around $90 \mu s$ is most likely edge reflections. Later peaks in the signal are likely to be edge reflections as well. In the figure we see that nearly all peaks prior to reflection from the plate edge have disappeared in the experimental signal corresponding to this ray path. This result matches well with the EFIT simulations results. As before we expect that the disappearance of Lamb wave modes is caused by the interference of waves in the thinned region due to the shape and size of the flaw region. The 2D slice showing the $x-y$ plane EFIT result certainly shows extreme wave interference in the thinned region.

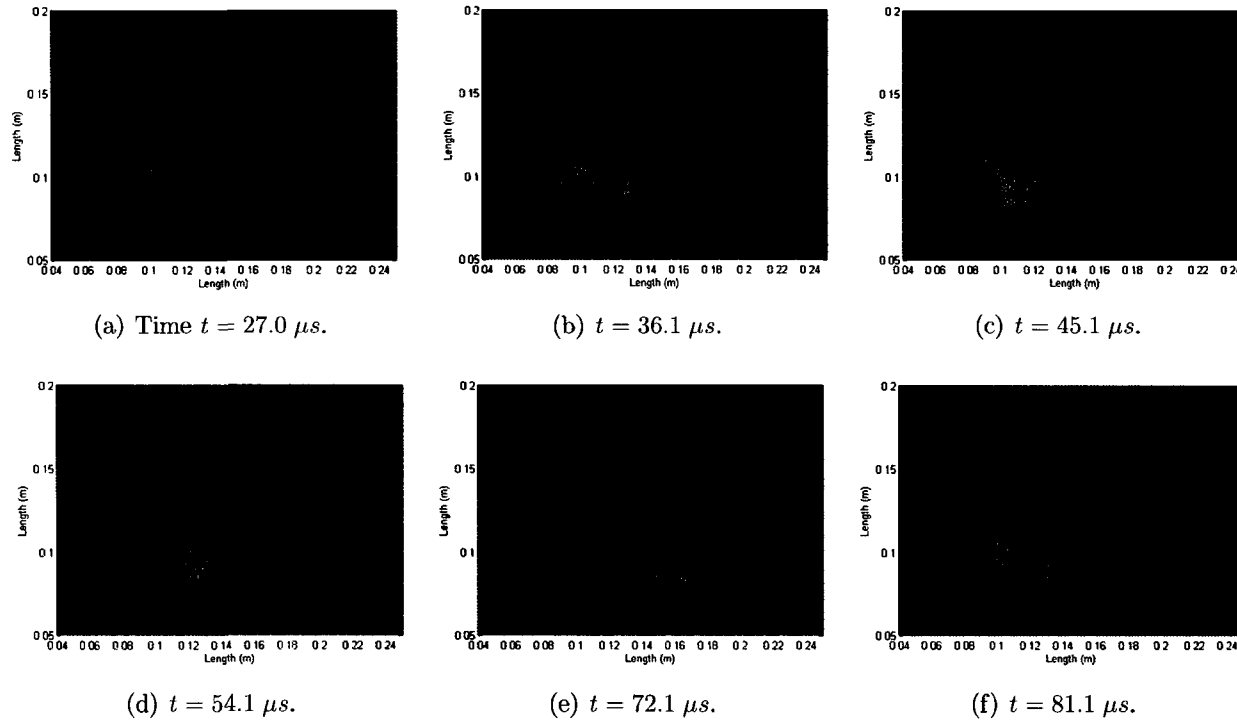


Figure 7.24: Plate with 2.171 mm void (68% material loss): 2D slices directly beneath the flaw.

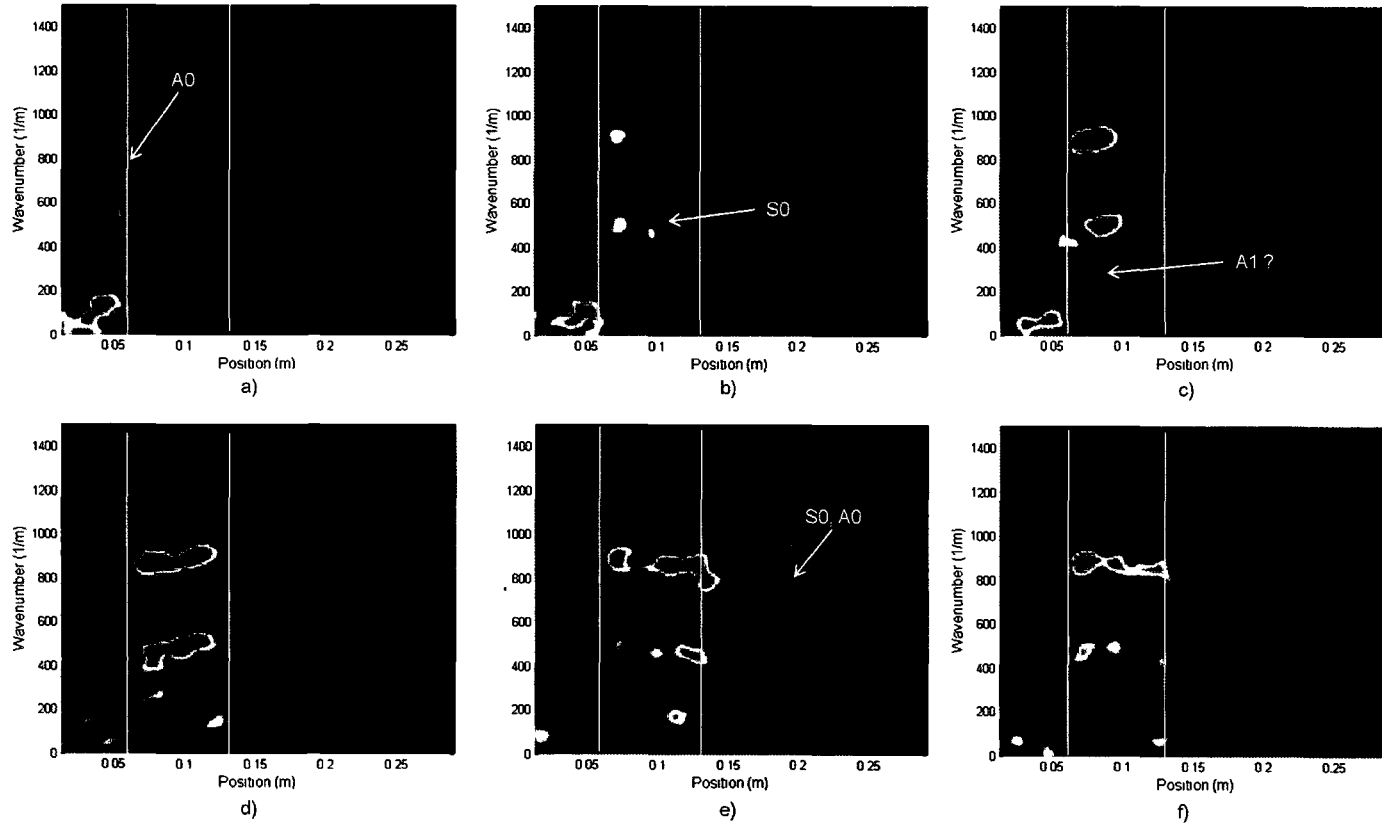


Figure 7.25: Spectrogram for 68% material loss and transducer position 2: a) time $t = 27.0 \mu s$, b) $t = 36.1 \mu s$, c) $45.1 \mu s$, d) $t = 54.1 \mu s$, e) $t = 72.1 \mu s$, f) $t = 81.1 \mu s$. The thinned region is outlined by the white lines.

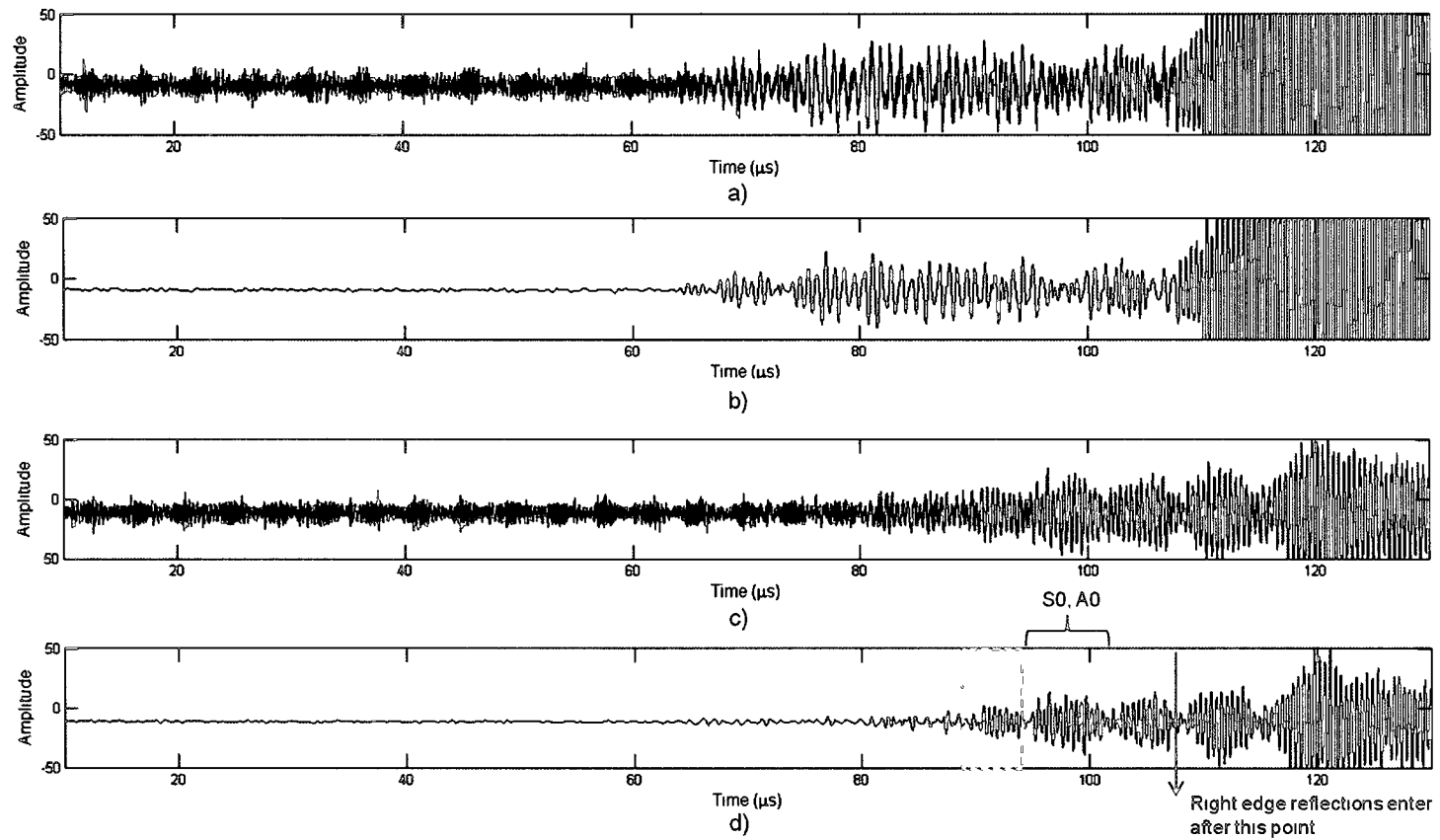


Figure 7.26: Experimental waveforms for 68% material loss for transducer position 2: a) A-line data for the clean plate for the ray path specified in 7.22, b) denoised clean plate waveform, c) raw experimental data for the flawed plate, d) denoised flawed plate experimental waveform with the earliest reflections from the plate edge indicated in orange and the potential detection of the re-emerged S0 and A0 modes around $t = 96 \mu\text{s}$ indicated in purple.

In Figure 7.27 we compare the scattering from the void edge (a corner in this case) to a void depth where expected modes clearly appeared in the thinned region, 29% material loss. The thickness plots are taken along the same ray path used for the spectrograms. We see increased scattering in the thickness plots at 68% material loss. The scattering is what leads to the changes circled in white. This scattering appears to slightly disrupt incoming wavepackets. However, in Figure 7.20 we saw this type of mode disturbance, but still observed the creation of expected Lamb wave modes in the thinned region. Note that the region circled in red shows disturbances due to reflections from the left edge of the plate. There are no significant changes in amplitude due to interactions of scattered waves with incoming waves. Therefore, in this case we also conclude that the largest effect on the Lamb wave modes is due to interference created by the void shape and size.

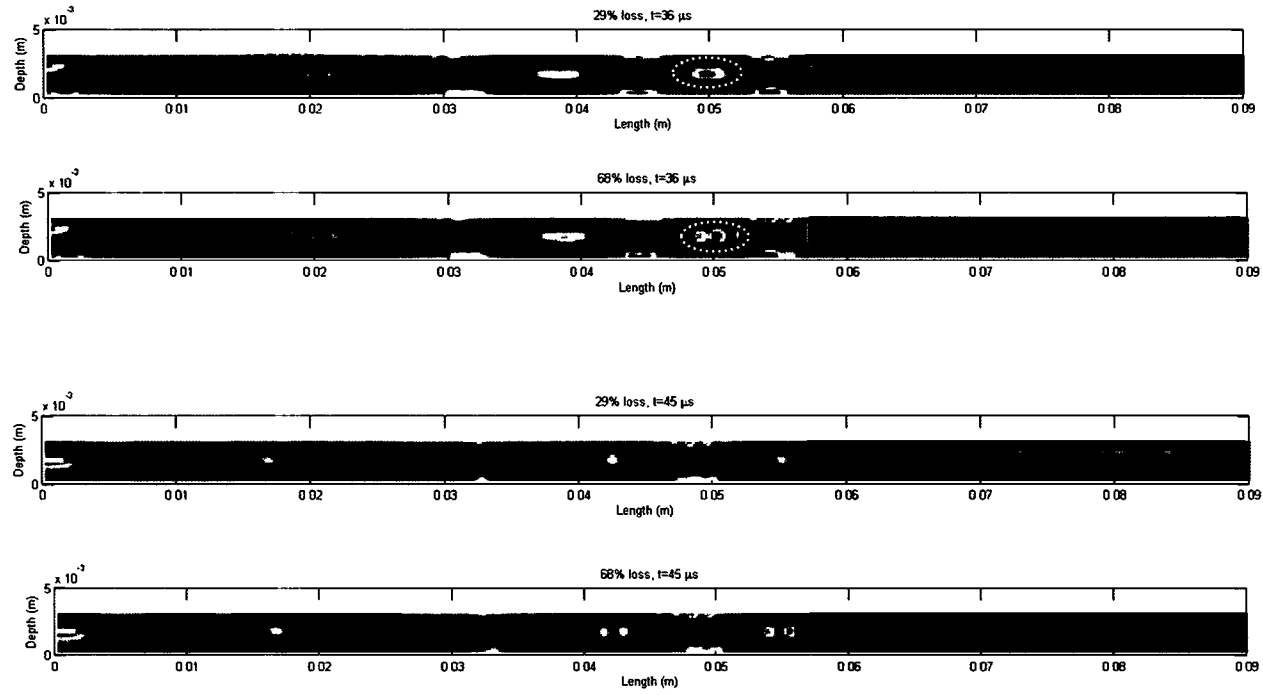


Figure 7.27: 2D slices of EFIT results showing the full thickness of the plate for the ray path shown in 7.23 for 29% and 68% material loss at two points in time (indicated above figures). The amplitude colormap is the same for all images. The void region is shown in solid black. The white dotted circles indicate a region affected by scattering at greater material loss. The red dashed region shows a region affected by scattering from the left edge of the plate.

A third transmitter position that is of particular interest is with the transducer in line with a corner and edge of the void, see Figure 7.28. The ray path corresponding to the indicated receiver location will be taken immediately above the flaw region. This path will be used to investigate the effects of waves scattered from the void on modes that do not pass through the flaw. Figure 7.29 shows 2D slices of EFIT results for 59% material loss. Note that by $72.1 \mu s$ scattering from the bottom and left edges of the plate enters into the images. Figure 7.30 shows thickness slices taken along $y = 0.111 m$ at six points in time. The thinned region extends to $y = 0.11 m$. By $t = 36 \mu s$ scattering from the void region has started affecting wavepackets traveling to the right. As seen in earlier figures, the scattering disrupts the solid pancake shape of the waves. By $54 \mu s$ reflections from the left plate edge also disrupt wavepackets.

The corresponding spectrogram plots, 7.31 and 7.32, show reflections from the void edge. The spectrograms in Figure 7.31 were created using an A-line at a depth directly beneath the flaw and the spectrograms in Figure 7.32 were created using an A-line along the top surface of the plate. The plots at both depths lack Lamb wave modes that would correspond to the full plate thickness. When compared to 7.10, it is clear that ray paths which do not pass through the thinned region are still affected by the void.

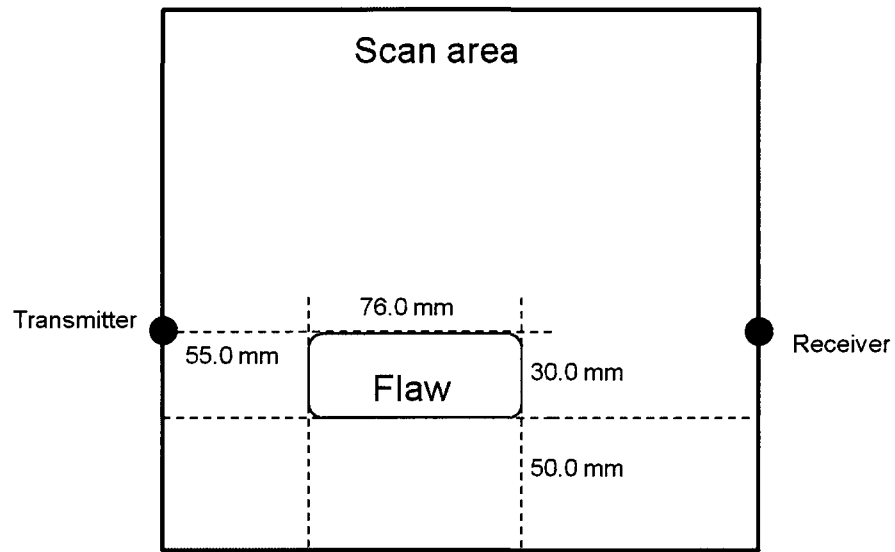


Figure 7.28: Transmitter location 3 is represented by the black circle. Receiver location used for spatial spectrogram plots is indicated.

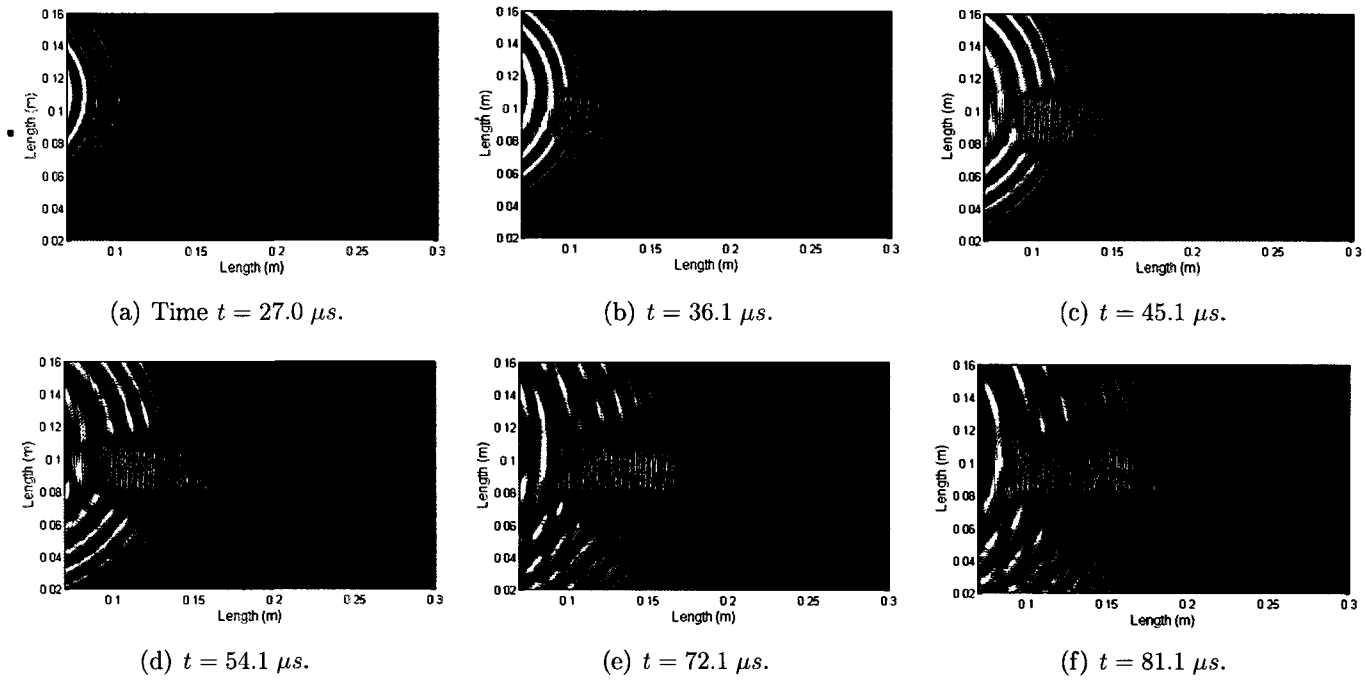


Figure 7.29: Plate with 1.85 mm void (59% material loss): 2D slices directly beneath the flaw.

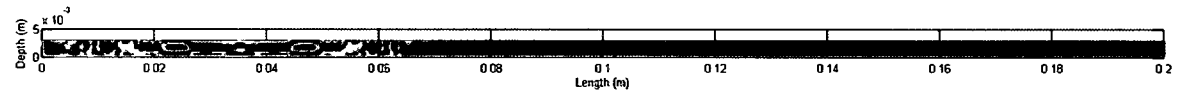
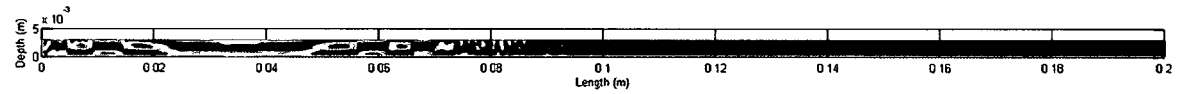
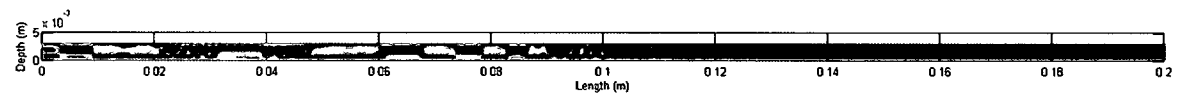
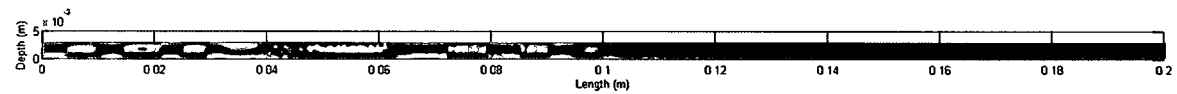
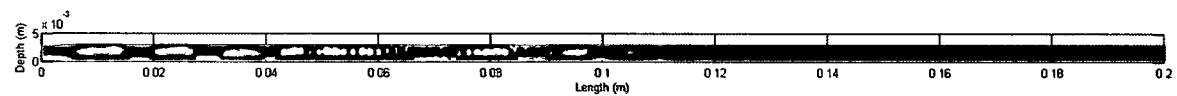
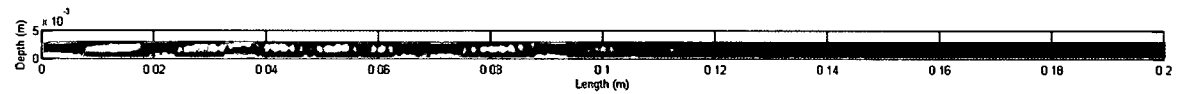
(a) Time $t = 9.0 \mu\text{s}$.(b) $t = 18.0 \mu\text{s}$.(c) $t = 27.0 \mu\text{s}$.(d) $t = 36.1 \mu\text{s}$.(e) $t = 45.1 \mu\text{s}$.(f) $t = 54.1 \mu\text{s}$.

Figure 7.30: Plate with 1.85 mm void (59% material loss): thickness slices at $y = 0.111 \text{ m}$, corresponding to the ray path in 7.28.

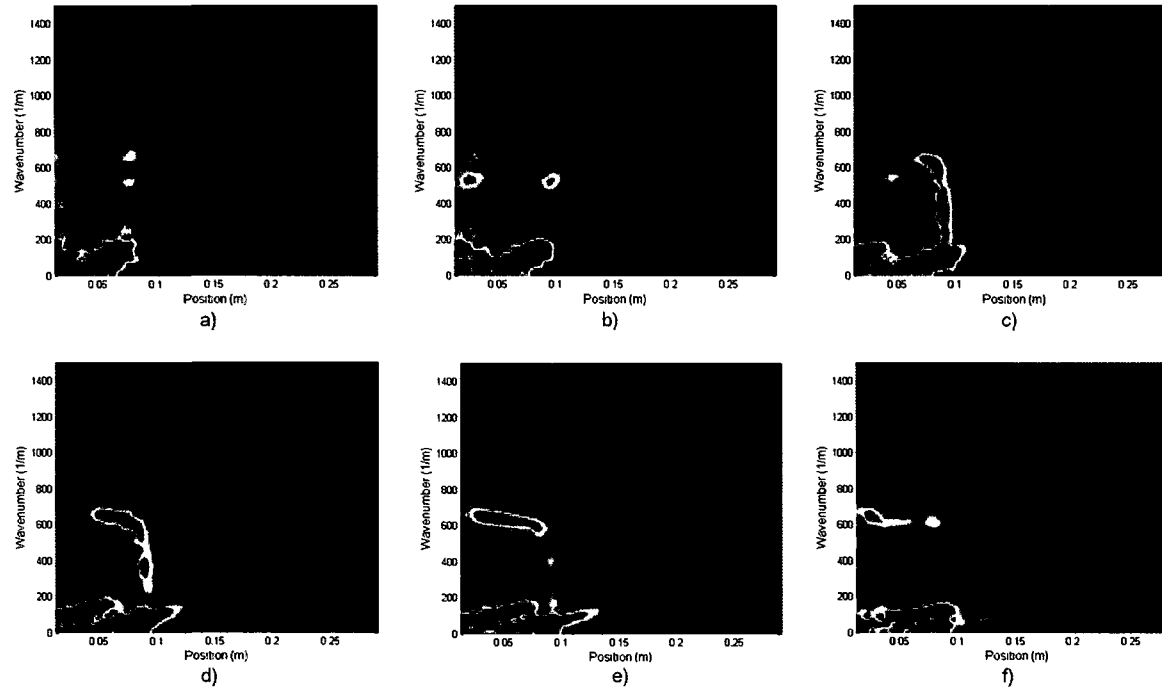


Figure 7.31: Spectrogram for 59% material loss and transducer position 3 taken along $y = 0.111 m$ at a depth directly beneath the void: a) time $t = 18.0 \mu s$, b) $t = 27.0 \mu s$, c) $36.1 \mu s$, d) $t = 45.1 \mu s$, e) $t = 54.1 \mu s$, f) $t = 72.1 \mu s$. The region from approximately $0.09 m$ to $0.16 m$ is parallel to the thinned region.

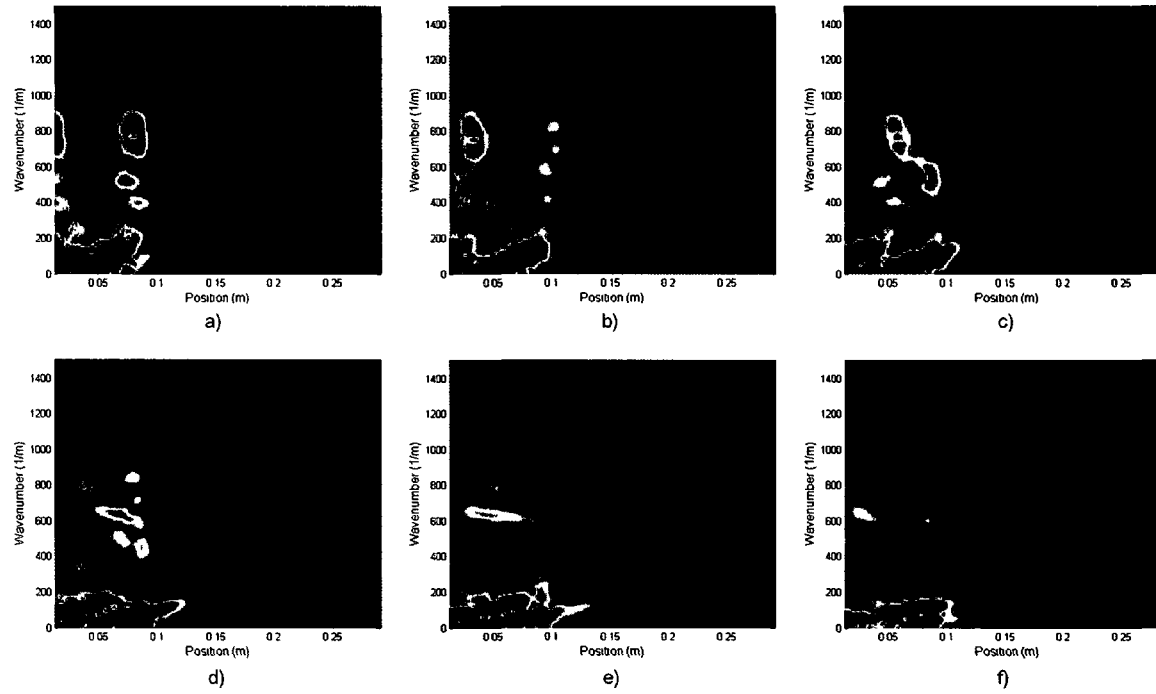


Figure 7.32: Spectrogram for 59% material loss and transducer position 3 taken along $y = 0.111$ m on the top surface of the plate: a) time $t = 18.0 \mu s$, b) $t = 27.0 \mu s$, c) $36.1 \mu s$, d) $t = 45.1 \mu s$, e) $t = 54.1 \mu s$, f) $t = 72.1 \mu s$. The region from approximately 0.09 m to 0.16 m is parallel to the thinned region.

Figure 7.33 shows experimental waveforms corresponding to the transmitter and receiver locations for this ray path compared the experimental waveform clean plate along this ray path. The experimental results clearly show that although this ray path does not pass through the thinned region it is significantly affected by the presence of the void. Peaks that show up above noise level in the data for the clean plate disappear in experimental data this ray path. In fact, the experimental signal shows no waves with significant amplitude detected until edge reflections enter the signal. As mentioned earlier, tomographic reconstructions of flaws using straight ray path methods are sometimes used with experimental data to find flaw locations and size [161]. These results explain why straight ray reconstruction methods can predict flaws larger than the actual size. Figure 7.34 shows predicted flaw enlargement in a tomographic ray path reconstruction of the rounded rectangle void with 59% material loss created using experimental data. The predicted thinned region is the bright white area in the image. The image was created assuming straight ray paths and is a slowness plot. Overlapping ray paths with slower speeds create the white area representing the flaw.

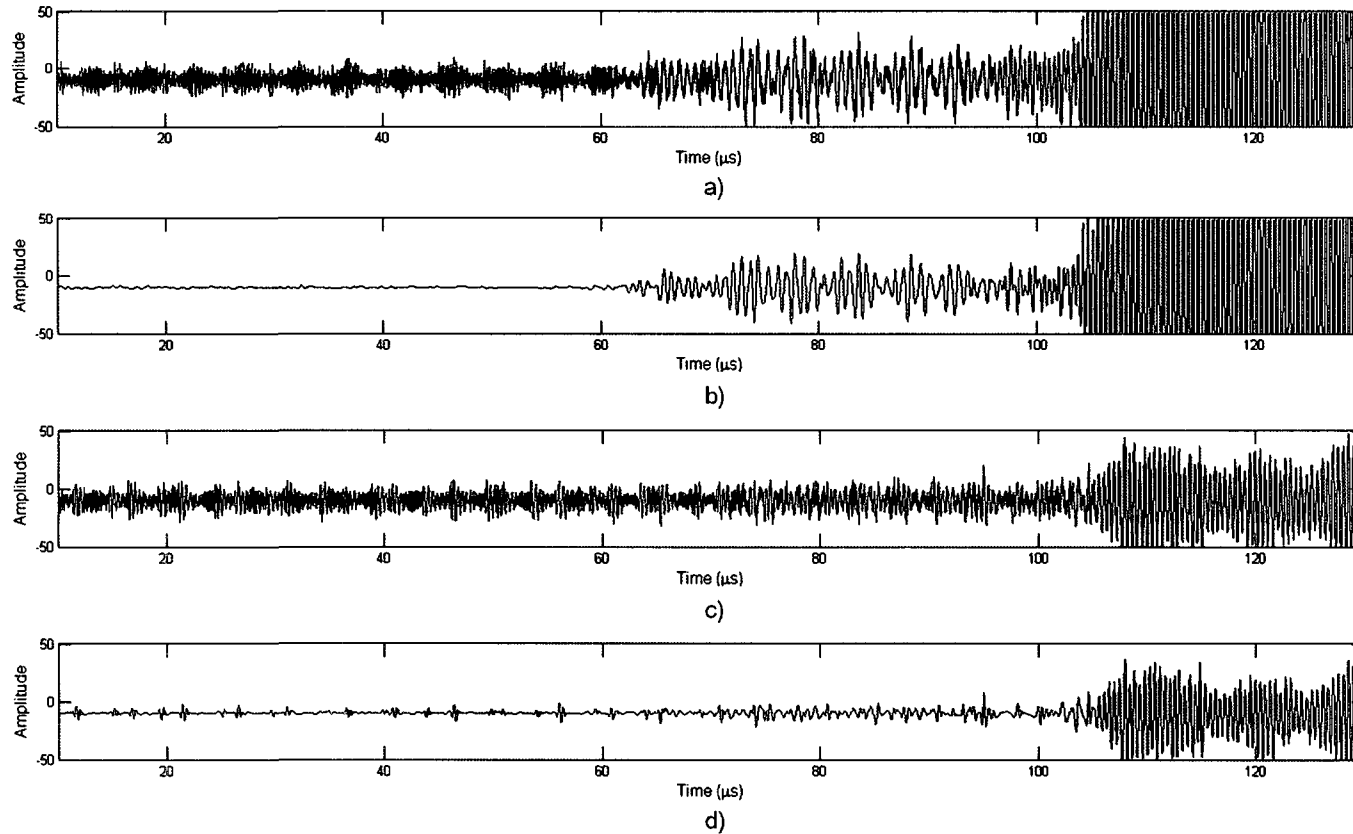


Figure 7.33: Experimental waveforms for the clean plate and 59% material loss for transducer position 3: a) A-line data for the plate with no flaw for the ray path specified in 7.28, b) denoised clean plate waveform, c) raw experimental data for the ray path specified in 7.28, d) denoised experimental waveform. Edge reflections enter the signal around $t = 105 \mu\text{s}$.

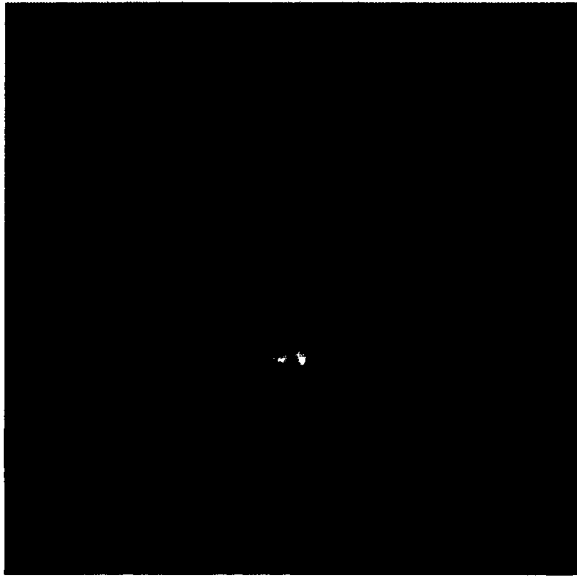


Figure 7.34: Tomographic flaw reconstruction created with experimental data for 59% material loss. The actual flaw size is indicated with the red box. The predicted flaw region is the bright white area and is enlarged due to scattering interactions on ray paths that do not pass through the thinned region. [Provided by W&M student Corey Miller]

By plotting spectrograms at increasing y values we can find the limit of scattering effects on ray paths above the flaw. We will plot spectrograms along straight lines parallel to the top edge of the flaw, as in Figure 7.31. Figures 7.36 and 7.37 show spectrograms and thickness plots for the ray paths shown in Figure 7.35 at time $t = 54 \mu s$. Reflections at the void location show up in the spectrograms and reflected wave effects can be seen in the thickness plots. By $y = 0.1363 m$ scattering from the flaw has little effect on the modes.

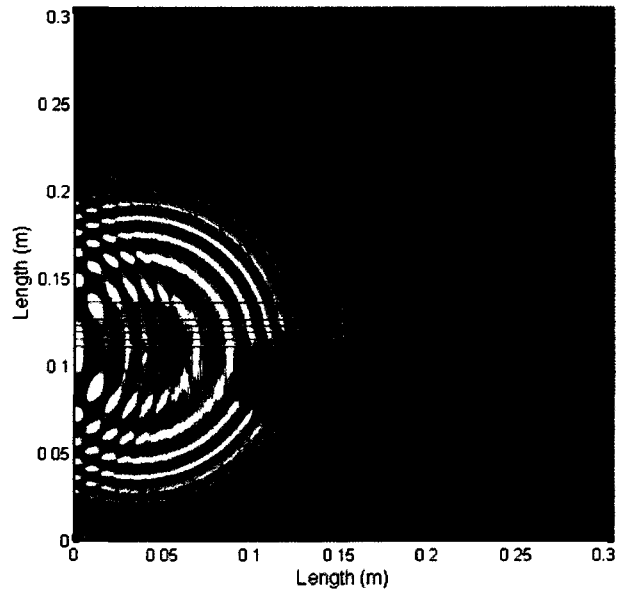
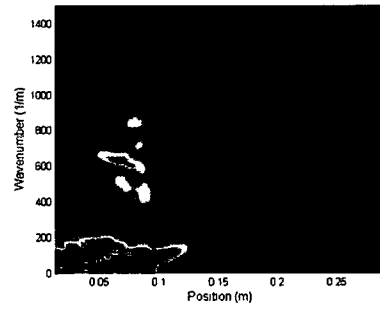
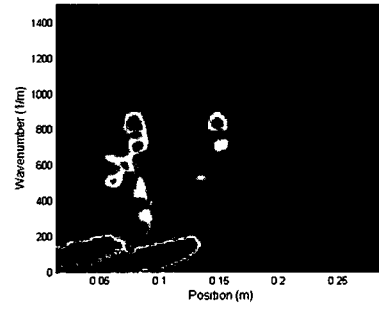


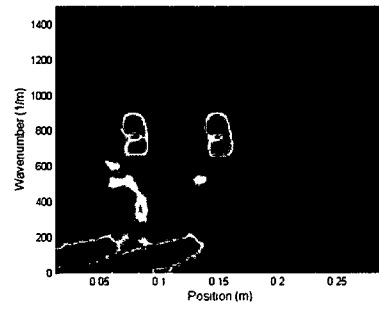
Figure 7.35: EFIT 2D slice on the top of the plate at time $t = 54 \mu s$ with red lines showing the A-line positions used for Figure 7.36.



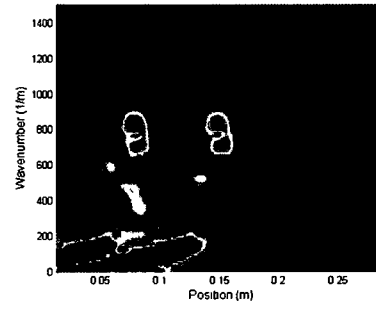
(a) $y = 0.1110 \text{ m}$.



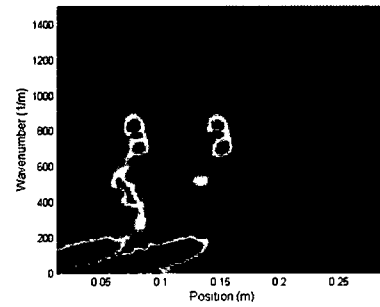
(b) $y = 0.1149 \text{ m}$.



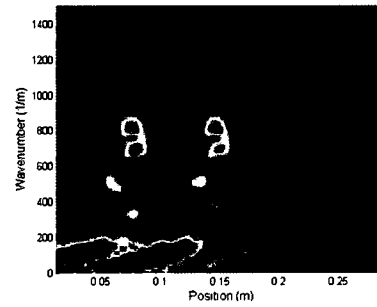
(c) $y = 0.1197 \text{ m}$.



(d) $y = 0.1226 \text{ m}$.



(e) $y = 0.1265 \text{ m}$.



(f) $y = 0.1363 \text{ m}$.

Figure 7.36: 59% material loss: spectrograms at time $t = 54 \mu\text{s}$ for A-lines at the specified y values. The region from approximately 0.09 m to 0.16 m is parallel to the thinned region.

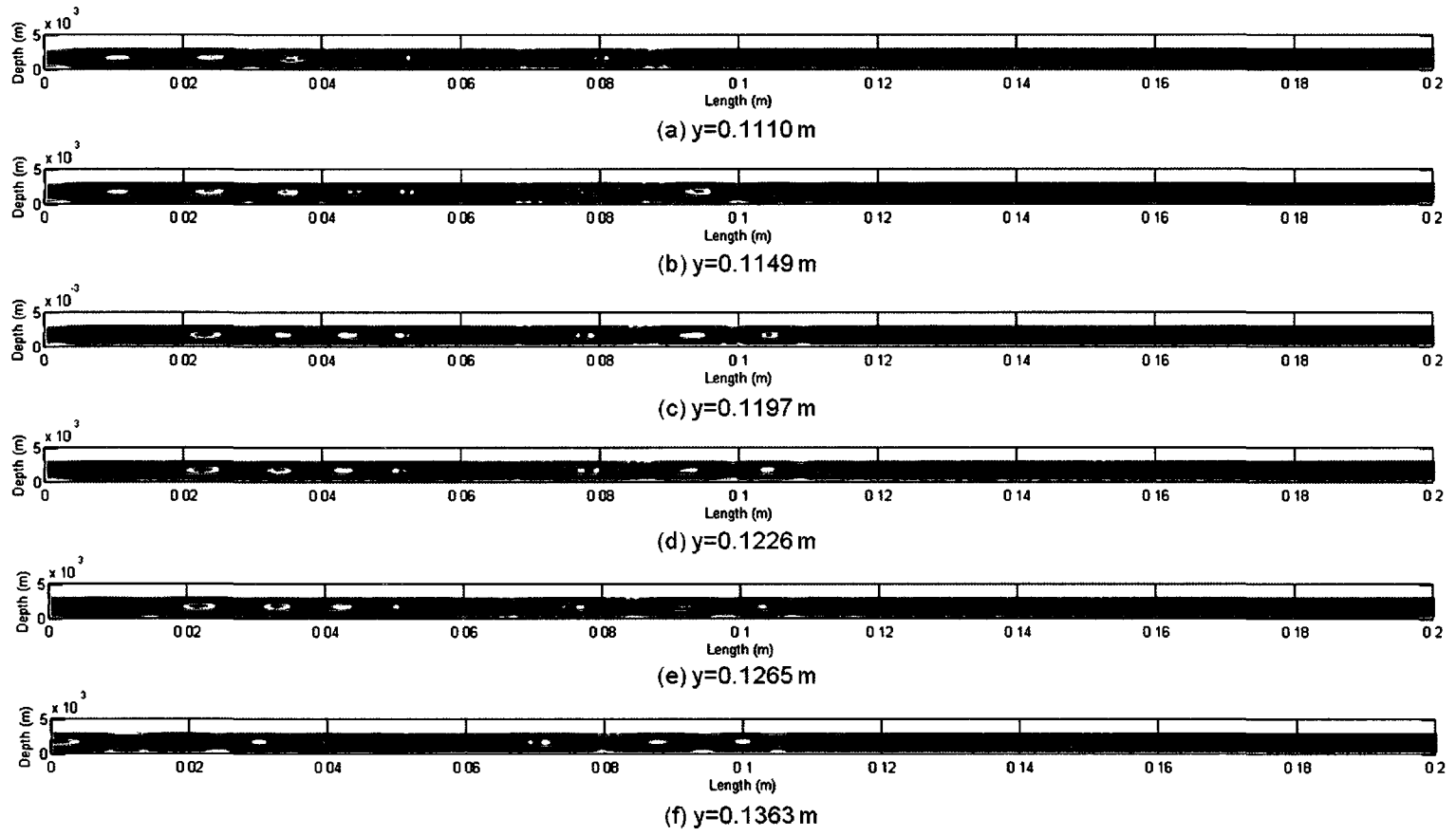


Figure 7.37: Thickness plots at time $t = 54 \mu s$ for specified y values.

The final transmitter position that we will explore in this chapter is shown in Figure 7.38. At this location the transducer is again in line with a straight edge of the flaw, however, the distance between the transmitter and void region is double that for transducer position 1 (Figure 7.11). Therefore, we expect the Lamb wave modes to have more time to separate out spatially before reaching the thinned region. Additionally, the flaw length in the direction of wave propagation is only 0.03 m instead of 0.076 m which will lead to different wave interference effects in the thinned region.

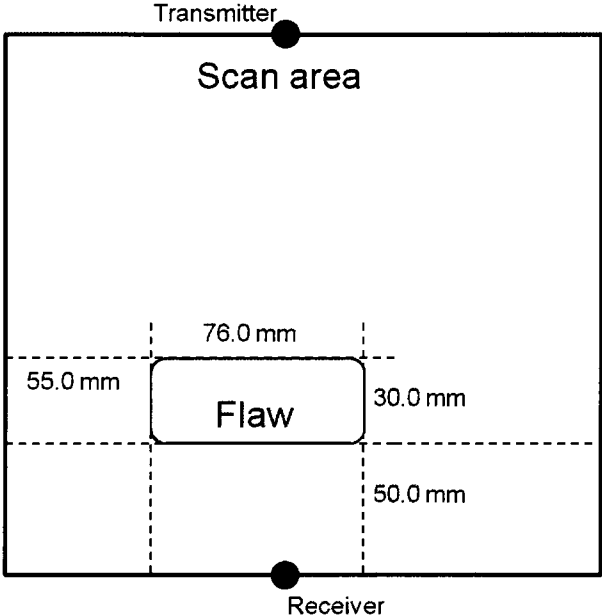


Figure 7.38: Transmitter location 4 is represented by the black circle. Receiver location used for spatial spectrogram plots is indicated.

Figures 7.39 - 7.41 show EFIT results at 59% material loss. At 18 μs we see all expected modes in the unthinned plate. By time $t = 26 \mu s$ S2 should enter the flawed region (based on its group velocity). In the spectrograms S2 is barely visible,

with a very low amplitude at the depth directly beneath the flaw. By approximately $t = 58 \mu s$ nearly all initial Lamb wave modes have passed into the flaw region. The S3 mode is the slowest mode, entering the thinned region around $67 \mu s$. But, we expect the S3 mode to be low amplitude since it is reaching its asymptotic limits in phase and group velocity. Note that what appear to be low wavenumber A3 and S3 modes in the spectrograms have not been identified as such because the packets move at group velocities too fast to be A3 and S3. At $t = 54 \mu s$ we only see two expected Lamb wave modes in the thinned region, A0 and S0. Lamb wave modes that should exist at $2.77 \text{ mm} \cdot \text{MHz}$ are A0 ($k = 769 \text{ m}^{-1}$), S0 ($k = 615 \text{ m}^{-1}$), A1 ($k = 337 \text{ m}^{-1}$) and perhaps S1 ($k = 180 \text{ m}^{-1}$). As time progresses, however, we see the emergence of A1, S1 and S0. When the spectrograms are compared to the EFIT 2D x - y plane slices we see that A1 and S1 emerge as higher amplitude waves enter the thinned region, at a time after all Lamb wave modes have passed through the region. We expect that these later waves are not Lamb wave modes, but simply other waves traveling in the plate. We do not see the re-emergence of the A0 mode in the thinned region at these later times, but we do see higher wavenumber modes inside the thinned region as in the other cases. After $81 \mu s$ we see Lamb wave modes emerge beyond the flaw as these later waves leave the thinned region.

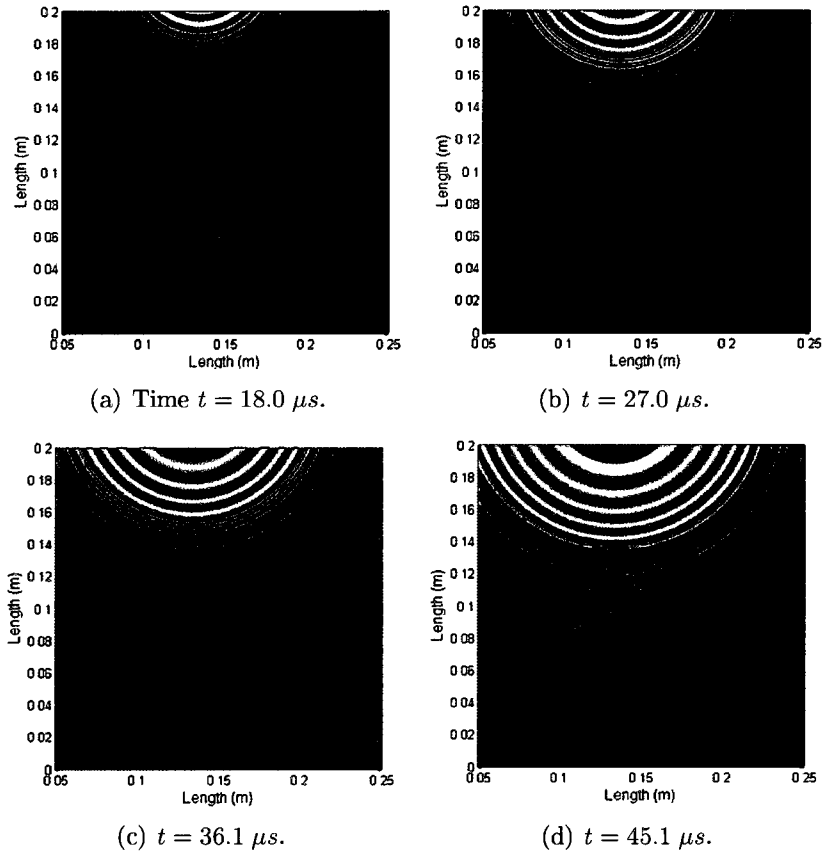


Figure 7.39: 59% material loss: 2D EFIT slices at specified times with transducer position 4.

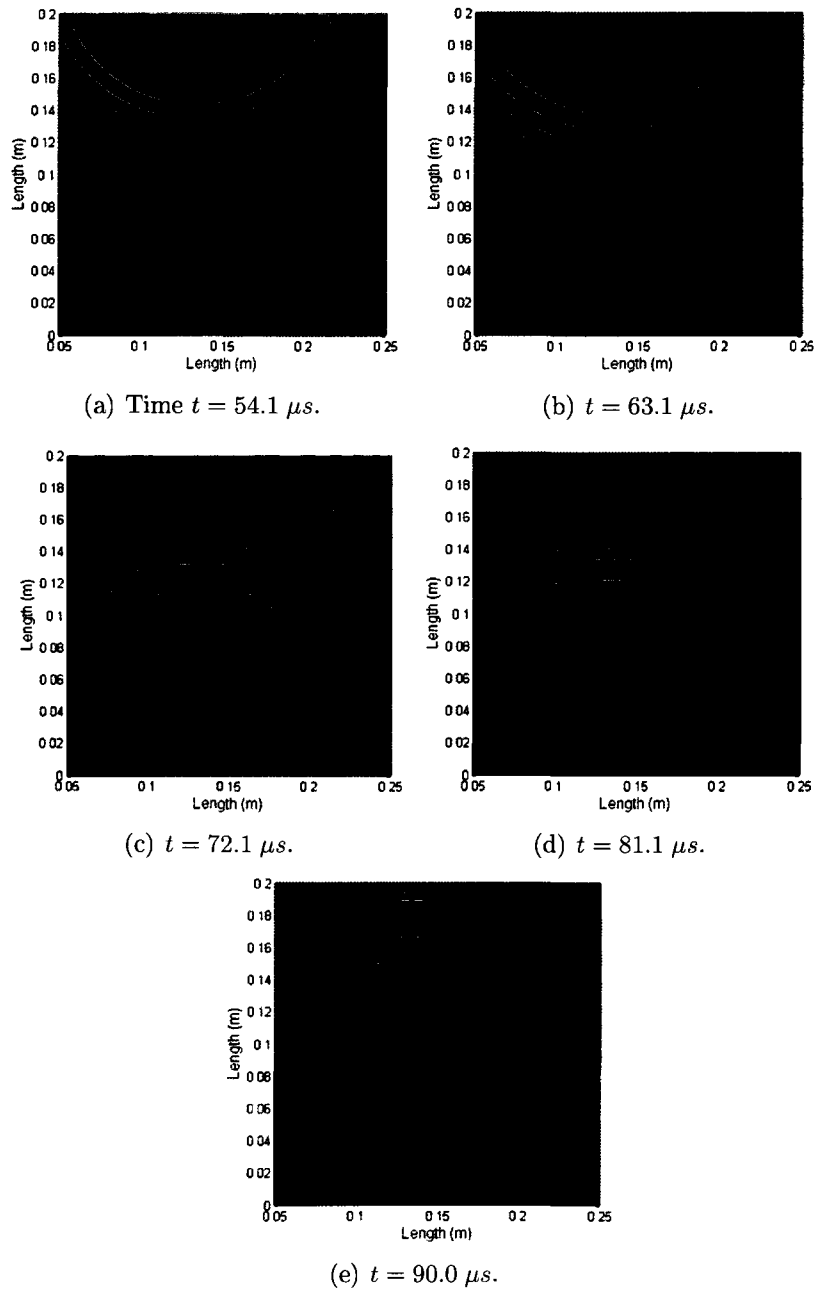


Figure 7.40: 59% material loss: 2D EFIT slices at specified times with transducer position 4.

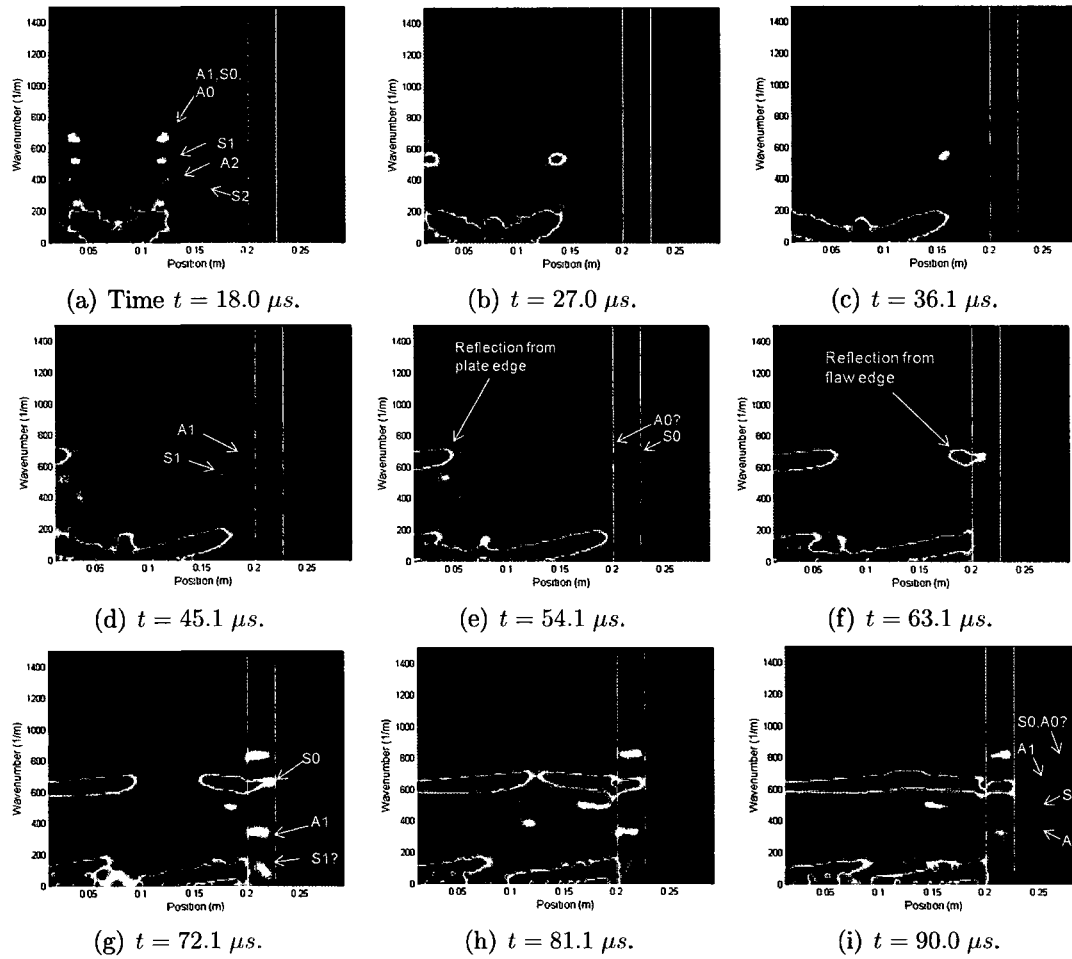


Figure 7.41: 59% material loss: spectrograms at specified times with transducer position 4. The thinned region extends from approximately 0.2 m to 0.226 m.

Figure 7.42 shows experimental signals for this ray path for the clean plate and for a void depth corresponding to 59% material loss. Based on the EFIT simulation results we would expect that the first waveforms of significant amplitude would be detected between 80 and 90 μs . This is indeed what we see in the experimental signal. The receiver position falls around 0.275 m in the spectrogram plots shown above. Low amplitude reflections from the bottom plate edge enter the signal around $t = 90 \mu s$. Higher amplitude reflections enter around 105 μs . The figure indicates the potential detection of the re-emerged Lamb wave modes. Although S0, A0 and A1 have a slower group velocity than A2, we expect to detect these modes earlier because they reappear at an earlier time from the thinned region in the spectrogram plots. A2 and S1 modes re-emerge slightly later from the thinned region. The faster A2 mode would be detected first followed by the slower S1 mode, as indicated in the figure.

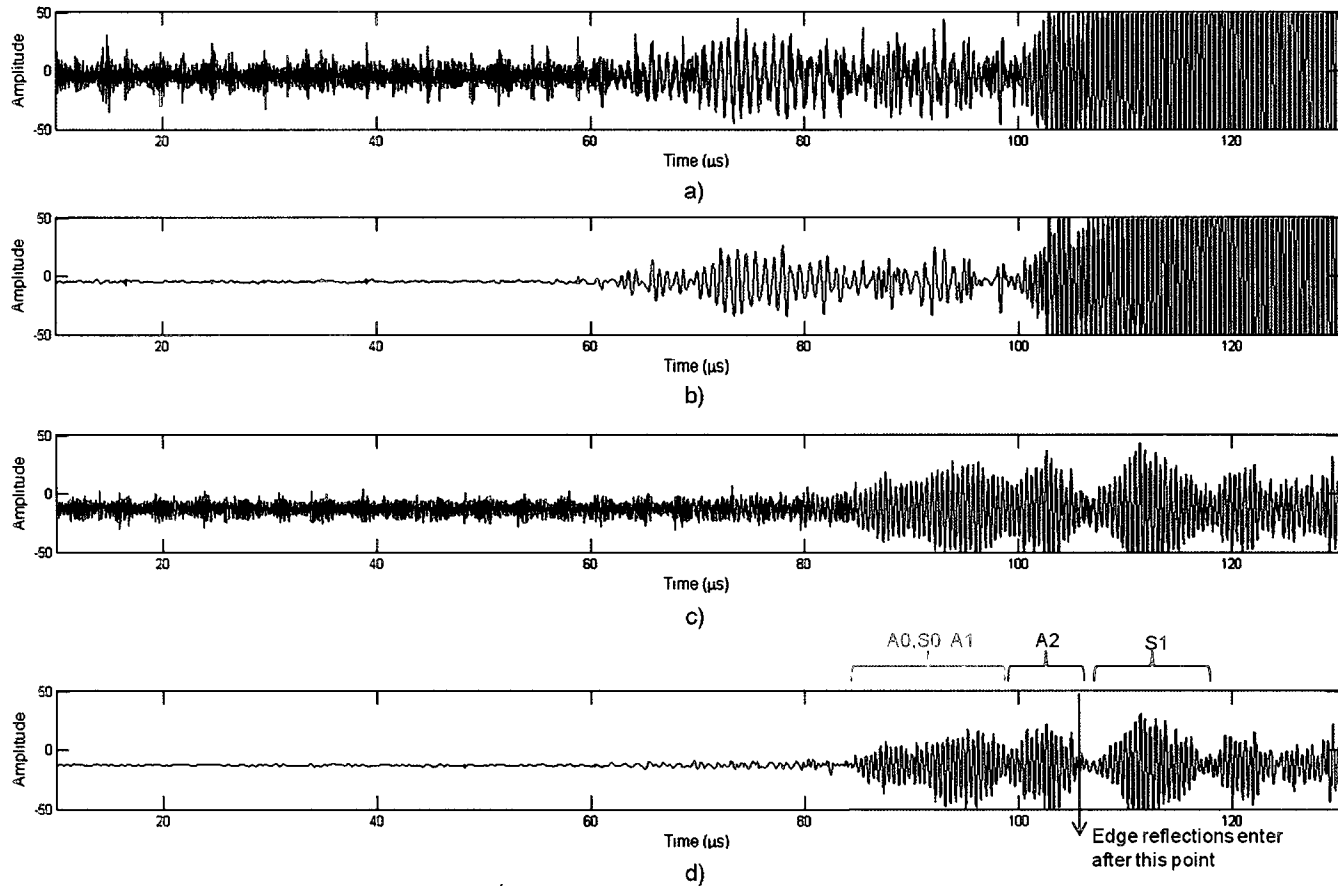


Figure 7.42: Experimental waveforms for the clean plate and 59% material loss for transducer position 4: a) A-line data for the clean plate for the ray path specified in 7.38, b) denoised clean plate waveform, c) raw experimental data for the flawed plate, d) denoised flawed plate experimental waveform. Lamb wave mode arrival times based on spectrograms are indicated.

7.2.1 Discussion of Results

We have used 3D EFIT simulations to investigate scattering situations corresponding to a well-controlled experimental case. The frequency-thickness of the clean plate leads to the creation of eight Lamb wave modes which propagate and interact with the rounded rectangle flaw. The EFIT simulation output was used in a way which provided insight into mode behavior before, during, and after the thinned region. We found that the flaw shape and size led to significant scattering and wave interference effects in the thinned region. In some cases the scattering led to the disappearance expected of Lamb modes. The transmitter position was found to have a large effect on scattering behavior, as we would expect. The same void depths for some transducer positions led to more scattering than for other locations. Additionally, ray paths that pass near but not through the flaw were significantly affected by the void.

We saw some unexpected behavior due to the flaw, such as the creation of high wavenumber waves inside the thinned region for all transducer locations and void depths that were investigated. We also observed unexpected effects of constructive interference. In all cases we found features in the experimental waveforms that seem to correspond to those predicted by the EFIT simulations. Finally, our results show that 2D simulations would not be sufficient to gain an understanding of the complex scattering behavior of Lamb wave modes. The 3D EFIT simulations helped us to gain an understanding of Lamb wave scattering behavior on a level that would not be available otherwise.

Chapter 8

Conclusions and Future Work

8.1 Acoustic Force Models

We have investigated wave scattering using methods that, when implemented for real-world problems, bring us up against the limits of available cluster computing resources. Our studies have found that the numerical implementation of complicated analytic solutions is made more practical using computing clusters. The specific analytic formulations that we implemented for acoustic force on spheres in a viscous fluid were applied to two real-world applications of current interest. The lack of availability of viscous material properties and massive computational demands of the viscous model means that the inviscid model is today more useful. However, it would be necessary to use the viscous formulation in situations where viscous effects are large enough to have a significant impact on the specific application. These chapters illustrated that for any application, the level of detail chosen for an analytic solution must be weighed against the complexity of the resulting equations and the availability of required material properties.

Experimental verification of the viscous model would be an important area of

future work on this topic. An experiment that creates air bubbles in a readily available and well-characterized high viscosity liquid such as glycerol would be ideal for such a measurement. A clear acoustic chamber containing the liquid could be created with a micropipette tube inserted at the bottom to allow for the input of air bubbles. As the air bubbles rise in the solution due to their buoyancy, a transducer on the container face, normal to the upward air bubble path, could be switched on to impart lateral acoustic force. Very precise optical tracking of horizontal bubble motion could be used to find the acoustic force upon the bubbles. Stokes drag forces would of course need to be taken into account.

The standing wave models for acoustic micromanipulation can be applied to microgravity containerless material processing. Acoustic manipulation has been of interest to NASA since the 1970's [162], [65]. This early work suggested the use of acoustic standing waves to levitate solid or fluid materials for containerless crystal growth, the measurement of surface tension, and containerless melting. At that time, it was expected that industrial scale low gravity material processing would someday take place on an orbital space station like the ISS. In a low gravity situation low field strengths could avoid unwanted heating or other effects caused by acoustic cavitation. Additionally, acoustic levitation experiments in microgravity that were performed aboard the NASA operated KC-135 aircraft show that particle disbanding is less likely to occur in low gravity situations [163]. Furthermore, the research aboard KC-135 shows that smaller particles can be manipulated in microgravity than at 1 g due to decreased convection. Generally frequencies on the order of $20 - 100 \text{ kHz}$ (λ on the order of 1 cm) are used in acoustic levitation studies where the $\approx \text{mm}$ (or smaller) size sample is levitated in air [162], [164].

Various high viscosity experiments have been performed in ground-based acoustic levitation experiments. Containerless melting and solidification experiments have

been performed using materials such as tin and indium, which, in liquid form, have viscosities slightly above ethanol [65], [165]. Surface tension measurements of high viscosity drops require knowledge of the acoustic pressure and equilibrium drop shape [65]. More recent work in the field suggests that containerless processing of chemical and biochemical materials would be ideal for avoiding contamination from container walls [164].

In approximately the past year an acoustic levitation device named “SpaceDRUMS” (Space Dynamically Responding Ultrasonic Matrix Systems) has been a new addition to scientific devices aboard the International Space Station [166]. The device uses 20 acoustic beams to position base-ball sized samples. The current goal for SpaceDRUMS, as reported by NASA, is the creation of exotic advanced materials such as metal-ceramic composites, bioceramics, and intermetallics [167], [168]. The viscous acoustic force model could be useful for providing insight into cases involving high viscosity materials. For example, a measurement of certain material properties of newly created materials could require precise knowledge of the acoustic force upon the material. In fact, the more complex model derived by Doinikov which includes thermal effects could be implemented if needed; although based on the work mentioned above, we expect that in microgravity thermal effects would be negligible in most cases [4].

8.2 Numerical Scattering Simulations

8.2.1 AFIT

We also investigated wave scattering using a numerical method called Finite Integration Technique. Since a model of a single spherical scatterer in a standing wave field is merely a very basic start to understanding algal cell manipulation via standing

waves, we used 3D AFIT code to investigate multiple scattering. We found that an increase in particle concentration in an acoustic chamber can significantly disrupt the standing wave field and change the force felt by algal cells. Additionally, the material properties of scatterers changed the effects on the field. Future work on multiple scattering in standing wave fields should incorporate viscosity, the motion of the scatterers due to the field, drag forces, and interparticle forces.

A model of viscosity could be introduced by including the full stress term in the first order Navier-Stokes equations. This would lead to

$$\begin{aligned}\partial_t p &= -\rho_0 \nabla \cdot \vec{v} + M \ , \\ \rho_0 \partial_t \vec{v} &= -\nabla p + \frac{1}{3} \eta \nabla (\nabla \cdot \vec{v}) + \xi \nabla (\nabla \cdot \vec{v}) + \eta \nabla^2 \vec{v} + \vec{F} \ .\end{aligned}\tag{8.1}$$

Reducing this equation to its finite integration form is more complicated than its inviscid form due to the second order derivatives. Via the divergence theorem and a vector identity it is nevertheless straightforward to write

$$\int \partial_t p dV = - \int \rho_0 \vec{v} \cdot dS + \int M dV \ ,\tag{8.2}$$

$$\begin{aligned}\int \rho_0 \partial_t \vec{v} dV &= - \int p dS + \frac{1}{3} \int \eta \nabla \vec{v} \cdot dS + \int \xi \nabla \vec{v} \cdot dS + \int \eta \nabla \vec{v} \cdot dS \\ &+ \int \eta \nabla \times (\nabla \times \vec{v}) dV + \int \vec{F} dV \ .\end{aligned}\tag{8.3}$$

Correctly discretizing these equations presents a challenge because of the gradient and curl terms that are involved.

A more direct method for including viscosity in the finite integration simulations may be to use the EFIT code with a few changes. In 1991 Hinders described how

to apply the elastodynamic wave formulation to scattering from spheres in viscous fluids [149]. Both elastic media and viscous fluids support shear and longitudinal waves, so it is natural to look for a link between the formulations. Hinders describes frequency domain equations for scattering in a viscous fluid by first defining the transverse and longitudinal wavenumbers and speeds according to the Kelvin-Voight model:

$$\begin{aligned} K &= \omega/c_T \quad , & k &= \omega/c_L \quad , \\ c_T^2 &= -i\omega\eta/\rho \quad , & c_L^2 &= \left(\frac{1}{\kappa} - 2i\omega\eta\right) \quad , \end{aligned} \tag{8.4}$$

where κ is fluid compressibility and η is shear viscosity. The complex wavenumbers account for attenuation due to viscosity. The result differs from the elastodynamic equations only by the material properties that are included. This implies that a simple change of variables in the EFIT equations may be a reasonable approach for approximating scattering in a viscous fluid.

The inclusion of particle movement could also be introduced into the simulations. Once the force upon a scatterer is calculated at a specific point in time, the acceleration, velocity, and new position of the scatterer in the simulation space could be found using the following simple kinematic equations:

$$\begin{aligned} a_i &= \frac{F_i}{\rho V} \quad , \\ v_i &= v_0 + a_i\Delta t \quad , \\ x_i &= x_0 + v_0\Delta t + \frac{1}{2}a_i(\Delta t)^2 \quad , \end{aligned} \tag{8.5}$$

where a_i is acceleration in the \hat{i} direction (and is considered constant for a single time step), V is scatterer volume, ρ is density, v_i is velocity, x_i is the new position of the scatterer due to the force, x_0 is initial position, v_0 is initial velocity, and Δt is the

change in time. Computationally this process would be accomplished by running the AFIT simulation for a single time step, calculating the force, acceleration, velocity and new position from the AFIT output, then inputting the new initial position into the AFIT simulation.

Stokes drag forces for a spherical scatterer would be included in force calculations using [2]:

$$F = 6\pi\eta Rv \quad (8.6)$$

where η is the viscosity of the surrounding fluid, R is the scatterer radius, and v is the scatterer velocity. Additionally, in a real-world experiment an increased particle concentration would lead to particle agglomeration due to inter-particle forces [87]. For spherical particles in a standing wave field in the limit that $ka \ll 1$, the attractive/repulsive forces between neighboring spheres, due to variations in the pressure field from the presence of the spheres, is described by [77]:

$$F(x) = 4\pi a^6 \left(\frac{(\rho_0 - \rho)^2 (3 \cos^2 \theta - 1)}{6\rho d^4} v^2(x) - \frac{\omega^2 \rho (\beta_0 - \beta)^2}{9d^2} p^2(x) \right) , \quad (8.7)$$

where, as stated by Groschl, d is the distance between sphere centers, β_0 is compressibility of the particle, β is compressibility of the surrounding fluid, θ is the angle between the two particles' centerline and the incident wave propagation direction, $p(x)$ and $v(x)$ are pressure and velocity at the particle position for the unperturbed field.

These types of advanced models could be beneficial to NASA since it is currently involved in algae biofuels research through the development of off-shore algae nurseries [169]. The OMEGA (Offshore Membrane Enclosure for Growing Algae) project plans to grow specific algal strains inside plastic bags floating in the ocean. Partial dewatering is accomplished through the bag material via forward-osmosis, but an

acoustic dewatering method may help in further reducing the water content of the harvest. Furthermore, future research may involve wild algal cell strains and growth methods that could benefit from acoustic algal cell sorting.

8.2.2 EFIT

In the final sections of this work we applied FIT to scattering in solids. An important step in using numerical models with confidence is verification of the code. We benchmarked our 3D EFIT code through comparisons to the simplest 3D geometry for which the exact analytical solution is known. The parallel EFIT code is computationally demanding, requiring cluster computing resources to simulate 3D scattering problems. We found that the 3-dimensional wave modeling provides an understanding of scattering that is not available with 2D models, although the EFIT simulations create very large amounts of data which must be dealt with in a way that allows the extraction of useful information. For complicated scattering applications, the difficulties of working with parallel EFIT code are outweighed by the insight that can be provided to experimental techniques.

One area of immediate future work is to apply EFIT simulations to crack-type flaws for investigating aircraft related damage. As mentioned earlier, one benefit of the EFIT code is that it easily allows for the incorporation of nearly any 3-dimensional flaw shape. Therefore, placing a realistic crack shape into the simulation space is straightforward. Formulations of waves scattering from cracks generally come in two forms: analytic solutions that make assumptions about the crack shape and angle of incidence, and numerical approximations. Analytic solutions are often based on Kirchhoff theory which assumes a single scatterer and is usually applied to planar cracks in a half-space. In general the Kirchhoff approximation says that the scattered field for an arbitrary scatterer is described by the summation of scattering due

to planar waves upon planar scatterers (that together approximate the actual scatterer). The scattered field for an arbitrary incident wave can then be described by the convolution of the actual incident field with the impulse response function (Green's function) for the approximated scatterer. The Kirchhoff method also assumes small wavelengths (compared to the scale of the flaw), which served the radar scattering community well but is not necessarily appropriate for non-destructive evaluation applications. The analytic approach leads to complicated integral equations and accurately describes scattering for only certain scatterer shapes [170], [171], [1], [172]. Numerical methods that can be applied to cracks include those mentioned earlier in this work, FEM, BEM, FIT. In fact, EFIT has been applied to cracks in 2 dimensions in both isotropic and anisotropic media [142], [145]. 3D EFIT simulations could be very useful in finding experimental setups where cracks at various angles with respect to transmitter/receiver locations can be detected and for optimizing aircraft structural health monitoring systems where the number of sensors must be minimized.

EFIT can also be applied to complicated situations such as wave propagation in porous media. Porous ceramic materials are of particular interest to NASA because they can operate at higher temperatures than metals. Aircraft engines are more efficient when they can operate at high temperature, thus, heat tolerant materials are very important. Additionally, the use of ultra-high temperature ceramics (melting at $> 3000^{\circ}C$) are ideal for hypersonic air-breathing or reentry vehicles which fly at speeds above Mach 5 and must deal with high temperature flow [173]. In order for these high temperature materials to gain wide use, questions such as how best to detect and quantitatively characterize flaws must be answered.

3D EFIT analysis has recently been applied to porous concrete materials and compared to experimental results by Algernon and Schubert [143], [174]. Algernon and colleagues were investigating scattering from large objects over long distances,

and therefore used frequencies less than 100 kHz (wavelength $\approx 2\text{ cm}$). Furthermore, since they were not interested in scattering from small features they did not include porosity in the 3D EFIT simulations. For this case the group found good agreement between EFIT and experimental results. Schubert accounted for the heterogeneity of concrete by directly including porosity in 2D EFIT simulations. However, the pore sizes were on the order of 0.3 to 2 mm . Ceramic materials often contain pores of various sizes and shapes, although methods do exist to create uniform porosity in a ceramic [175]. In Tang’s work pore sizes on the order of 1 μm were created.

EFIT could be implemented with small voids representing pores in ceramic material. However, this type of approach would allow for only small simulation sizes due to the small step size required to create micron sized pores. This approach may be ideal for simulating small flaws over a small area, however, the detection of flaws in larger sample sizes would be very useful for this application. On a larger scale, porous material will lead to an overall wave attenuation. One analytic approach to account for elastic wave attenuation is the Kelvin-Voight viscoelastic model, which defines stress with a “viscous” damping term [8]. This model creates complex longitudinal and transverse wavenumbers,

$$\begin{aligned} k &= \frac{\omega}{c_L} + \frac{i\eta_L\omega}{2\pi} , \\ K &= \frac{\omega}{c_T} + \frac{i\eta_T\omega}{2\pi} , \end{aligned} \tag{8.8}$$

where η_L and η_T are damping terms. Viscoelastic EFIT simulations is one approach to numerically modeling elastic waves with attenuation in ceramic material. In fact, viscoelastic EFIT simulations have been applied to concrete by Marklein [176]. Following the analytic method, adding viscoelastic effects into the isotropic EFIT equations

requires changing the definition of the stress tensor to include a damping term:

$$T_{ij} = \lambda \epsilon_{kk} \delta_{ij} + 2\mu \epsilon_{ij} + \left(\eta_T - \frac{2}{3} \eta_L \right) \epsilon_{kk} \delta_{ij} + 2\eta_T \epsilon_{ij} . \quad (8.9)$$

The effects of porosity on acoustic waves in larger ceramic samples could be achieved by finding the attenuation terms versus frequency for specified pore sizes and materials. Attenuation directly depends on frequency, so this relationship must be found. This task could be accomplished by running a series of EFIT simulations on smaller scale samples where porosity is directly included, and observing the average wave attenuation by the end of the propagation path. By incorporating this attenuation directly into the viscoelastic EFIT equations, fairly accurate simulations over larger porous samples with realistic flaws could be achieved.

Appendices

Appendix A: Surface Tension Values

Table 8.1: Surface Tension

Scatterer	Surface tension (dyn/cm)
Ethanol	22
Glycerol	64
Lipid	33
Water	72

[53], [177], [178]

Table 8.2: Surface Tension

Material Combination	Surface tension (dyn/cm)
Air in blood	57
Air in glycerol	64
Air in water	72

[53], [177], [178]

Appendix B: Viscous Fluid Equations

α_n and β_n for equation (2.50) are:

For $n = 0$

$$\alpha_0 = \frac{xj_1(k_1a) - gj_0(k_1a)}{gh_0(k_1a) - k_1ah_1(k_1a)}, \quad \beta_0 = 0$$

$$g = k_2aj_1(k_2a) \left(\frac{\rho_2^{(0)}}{\rho_1^{(0)}} j_0(k_2a) + 2k_2aj_1(k_2a) \left(\frac{2(1 - \frac{\eta_2}{\eta_1})}{(K_1a)^2} - \frac{\sigma_{ST}}{\rho_1^{(0)}\omega^2a^3} \right) \right)^{-1}$$

where σ_{ST} is the surface tension. For $n \geq 1$

$$\alpha_n = -\frac{j_n(k_1a)}{h_n(k_1a)} \left(\frac{\Delta_1}{\Delta_0} \right)$$

$$\beta_n = -\frac{j_n(k_1a)}{h_n(K_1a)} \left(\frac{\Delta_2}{\Delta_0} \right)$$

$$\begin{aligned} \Delta_0 = & \left(\frac{(k_1a)h'_n(k_1a)}{h_n(k_1a)} \left(1 + \frac{(K_1a)h'_n(K_1a)}{h_n(K_1a)} \right) - n(n+1) \right) (M_{33}M_{44} - M_{34}M_{43}) \\ & - M_{33} \left(\frac{(k_1a)h'_n(k_1a)}{h_n(k_1a)} \left(1 + \frac{(K_2a)j'_n(K_2a)}{j_n(K_2a)} \right) - n(n+1) \right) \\ & - M_{44} \left(\frac{(k_2a)j'_n(k_2a)}{j_n(k_2a)} \left(1 + \frac{(K_2a)h'_n(K_2a)}{h_n(K_2a)} \right) - n(n+1) \right) \\ & + \left(\frac{(k_2a)j'_n(k_2a)}{j_n(k_2a)} \left(1 + \frac{(K_2a)j'_n(K_2a)}{j_n(K_2a)} \right) - n(n+1) \right) \\ & + M_{34} \left(\frac{(k_1a)h'_n(k_1a)}{h_n(k_1a)} - \frac{(k_2a)j'_n(k_2a)}{j_n(k_2a)} \right) \\ & + n(n+1)M_{43} \left(\frac{(K_1a)h'_n(K_1a)}{h_n(K_1a)} - \frac{(K_2a)j'_n(K_2a)}{j_n(K_2a)} \right) \end{aligned}$$

$$\begin{aligned}
\Delta_1 = & \left(\frac{(k_1 a) j'_n(k_1 a)}{j_n(k_1 a)} \left(1 + \frac{(K_1 a) h'_n(K_1 a)}{h_n(K_1 a)} \right) - n(n+1) \right) (M_{33} M_{44} - M_{34} M_{43}) \\
& - M_{33} \left(\frac{(k_1 a) j'_n(k_1 a)}{j_n(k_1 a)} \left(1 + \frac{(K_2 a) j'_n(K_2 a)}{j_n(K_2 a)} \right) - n(n+1) \right) \\
& - M_{44} \left(\frac{(k_2 a) j'_n(k_2 a)}{j_n(k_2 a)} \left(1 + \frac{(K_2 a) h'_n(K_2 a)}{h_n(K_2 a)} \right) - n(n+1) \right) \\
& + \left(\frac{(k_2 a) j'_n(k_2 a)}{j_n(k_2 a)} \left(1 + \frac{(K_2 a) j'_n(K_2 a)}{j_n(K_2 a)} \right) - n(n+1) \right) \\
& + M_{34} \left(\frac{(k_1 a) j'_n(k_1 a)}{j_n(k_1 a)} - \frac{(k_2 a) j'_n(k_2 a)}{j_n(k_2 a)} \right) \\
& + n(n+1) M_{43} \left(\frac{(K_1 a) h'_n(K_1 a)}{h_n(K_1 a)} - \frac{(K_2 a) j'_n(K_2 a)}{j_n(K_2 a)} \right) \\
\Delta_2 = & \left(\frac{(k_1 a) h'_n(k_1 a)}{h_n(k_1 a)} - \frac{(k_1 a) j'_n(k_1 a)}{j_n(k_1 a)} \right) ((M_{33} M_{44} - M_{34} M_{43}) - M_{44} \\
& + \left(1 + \frac{(K_2 a) j'_n(K_2 a)}{j_n(K_2 a)} \right) M_{43})
\end{aligned}$$

$$\begin{aligned}
M_{33} = & \frac{\rho_2^{(0)}}{\rho_1^{(0)}} \left(1 - \left(\frac{2(1 - \frac{\eta_1}{\eta_2})}{(K_2 a)^2} \right) [n(n+1) - 2 \frac{(k_2 a) j'_n(k_2 a)}{j_n(k_2 a)}] \right. \\
& \left. + \left(\frac{\sigma_{ST} \rho_2^{(0)} a}{(\eta_2)^2} \right) \frac{(n-1)(n+2)}{(K_2 a)^4} \frac{(k_2 a) j'_n(k_2 a)}{j_n(k_2 a)} \right)
\end{aligned}$$

$$M_{34} = n(n+1) \frac{\rho_2^{(0)}}{\rho_1^{(0)}} \left(\left(\frac{2(1 - \frac{\eta_1}{\eta_2})}{(K_2 a)^2} \right) \left[1 - \frac{(K_2 a) j'_n(K_2 a)}{j_n(K_2 a)} \right] + \left(\frac{\sigma_{ST} \rho_2^{(0)} a}{(\eta_2)^2} \right) \frac{(n-1)(n+2)}{(K_2 a)^4} \right)$$

$$M_{43} = \frac{2\rho_2^{(0)}}{\rho_1^{(0)} (K_2 a)^2} \left((1-n) + \left(n - \frac{(k_2 a) j'_n(k_2 a)}{j_n(k_2 a)} \right) \right)$$

$$M_{44} = \frac{\rho_2^{(0)}}{\rho_1^{(0)}} \left(1 - \left(\frac{2(1 - \frac{\eta_1}{\eta_2})}{(K_2 a)^2} \right) \left((n^2 - 1) + \left(n - \frac{(K_2 a) j'_n(K_2 a)}{j_n(K_2 a)} \right) \right) \right)$$

The S_n functions in equation (2.50) are:

$$\begin{aligned}
S_{1n} = & \frac{1}{2}((n+2)(k_1a)^2 - n(k_1^*a)^2)(H_{nn+1}^{(0)}(k_1a, k_1a) - H_{nn+1}^{(2)}(k_1a, k_1a)) \\
& - k_1ak_1^*a(H_{n+1n}^{(0)}(k_1a, k_1a) - H_{n+1n}^{(2)}(k_1a, k_1a)) \\
& + \frac{((k_1a)^2 - (k_1^*a)^2)}{(K_1a)^2} [nk_1^*aH_{nn}^{(1)}(k_1a, k_1a) \\
& + (n+2)k_1aH_{n+1n+1}^{(1)}(k_1a, k_1a) - k_1ak_1^*aH_{n+1n}^{(0)}(k_1a, k_1a)] \\
& + (k_1ak_1^*a/(K_1a)^2)G_n^{(2)}(k_1a)
\end{aligned}$$

$$\begin{aligned}
S_{2n} = & n(n+2)\{K_1aK_1^*a(H_{n+1n}^{(0)}(K_1a, K_1a) - H_{n+1n}^{(2)}(K_1a, K_1a)) \\
& - (n+1)(K_1a)^2(H_{nn+1}^{(0)}(K_1a, K_1a) - H_{nn+1}^{(2)}(K_1a, K_1a)) \\
& - (n+1)[h_n^{(1)}(K_1a)(h_n^{(2)}(K_1^*a))' + (h_{n+1}^{(1)}(K_1a))'h_{n+1}^{(2)}(K_1^*a)]\}
\end{aligned}$$

$$\begin{aligned}
S_{3n} = & (n+2) \left[\frac{1}{2}(n(K_1^*a)^2 - (n+1)(k_1a)^2)(H_{nn+1}^{(0)}(k_1a, K_1a) - H_{nn+1}^{(2)}(k_1a, K_1a)) \right. \\
& - k_1aK_1^*a(H_{n+1n}^{(0)}(k_1a, K_1a) - H_{n+1n}^{(2)}(k_1a, K_1a)) + \frac{(k_1a)^2K_1^*a}{2}(H_{nn}^{(-1)}(k_1a, K_1a) \\
& - H_{nn}^{(1)}(k_1a, K_1a)) + \frac{k_1a(K_1a)^2}{2}(H_{n+1n+1}^{(-1)}(k_1a, K_1a) - H_{n+1n+1}^{(1)}(k_1a, K_1a)) \\
& \left. + \frac{(k_1a)^2}{(K_1a)^2}(nK_1^*aH_{nn}^{(1)}(k_1a, K_1a) - (n+1)k_1aH_{n+1n+1}^{(1)}(k_1a, K_1a)) - L_n^{(1)}(k_1a, K_1a) \right]
\end{aligned}$$

⋮

$$\begin{aligned}
S_{4n} = & n \left[\frac{1}{2} ((n+2)(K_1a)^2 - (n+1)(k_1^*a)^2) (H_{nn+1}^{(0)}(K_1a, k_1a) - H_{nn+1}^{(2)}(K_1a, k_1a)) \right. \\
& + k_1^*a K_1a (H_{n+1n}^{(0)}(K_1a, k_1a) - H_{n+1n}^{(2)}(K_1a, k_1a)) \\
& - \frac{k_1^*a (K_1a)^2}{2} (H_{nn}^{(-1)}(K_1a, k_1a) - H_{nn}^{(1)}(K_1a, k_1a)) - H_{nn}^{(1)}(K_1a, k_1a) \\
& + \frac{(k_1^*a)^2 K_1a}{2} (H_{n+1n+1}^{(-1)}(K_1a, k_1a) - H_{n+1n+1}^{(1)}(K_1a, k_1a)) \\
& - \frac{(k_1^*a)^2}{(K_1a)^2} ((n+1)k_1^*a H_{nn}^{(1)}(K_1a, k_1a) - (n+2)K_1a H_{n+1n+1}^{(1)}(K_1a, k_1a)) \\
& \left. + K_n^{(2)}(k_1a, K_1a) \right]
\end{aligned}$$

$$\begin{aligned}
S_{5n} = & \frac{1}{2} ((n+2)(k_1a)^2 - n(k_1^*a)^2) (J_{nn+1}^{(0)}(k_1a, k_1a) - J_{nn+1}^{(2)}(k_1a, k_1a)) \\
& - k_1a k_1^*a (J_{n+1n}^{(0)}(k_1a, k_1a) - J_{n+1n}^{(2)}(k_1a, k_1a)) \\
& + \frac{((k_1a)^2 - (k_1^*a)^2)}{(K_1a)^2} [n k_1^*a J_{nn}^{(1)}(k_1a, k_1a) \\
& + (n+2)k_1a J_{n+1n+1}^{(1)}(k_1a, k_1a) - k_1a k_1^*a J_{n+1n}^{(0)}(k_1a, k_1a)] \\
& + (k_1a k_1^*a / (K_1a)^2) (G_n^{(1)}(k_1a) + G_n^{(2)}(k_1a))
\end{aligned}$$

$$\begin{aligned}
S_{6n} = & \frac{1}{2} ((n+2)(k_1a)^2 - n(k_1^*a)^2) (J_{n+1n}^{(0)}(k_1a, k_1a) - J_{n+1n}^{(2)}(k_1a, k_1a))^* \\
& - k_1a k_1^*a (J_{nn+1}^{(0)}(k_1a, k_1a) - J_{nn+1}^{(2)}(k_1a, k_1a))^* \\
& + \frac{((k_1a)^2 - (k_1^*a)^2)}{(K_1a)^2} [n k_1^*a J_{nn}^{(1)}(k_1a, k_1a) \\
& + (n+2)k_1a J_{n+1n+1}^{(1)}(k_1a, k_1a) - k_1a k_1^*a J_{nn+1}^{(0)}(k_1a, k_1a)]^* \\
& + (k_1a k_1^*a / (K_1a)^2) (G_n^{(1)*}(k_1^*a) + G_n^{(2)}(k_1a))
\end{aligned}$$

$$\begin{aligned}
S_{7n} = & n \left[\frac{1}{2} ((n+2)(K_1a)^2 - (n+1)(k_1^*a)^2) (J_{nn+1}^{(0)}(K_1a, k_1a) - J_{nn+1}^{(2)}(K_1a, k_1a)) \right. \\
& + k_1^*a K_1a (J_{n+1n}^{(0)}(K_1a, k_1a) - J_{n+1n}^{(2)}(K_1a, k_1a)) \\
& - \frac{k_1^*a(K_1a)^2}{2} (J_{nn}^{(-1)}(K_1a, k_1a) - J_{nn}^{(1)}(K_1a, k_1a)) \\
& + \frac{(k_1^*a)^2 K_1a}{2} (J_{n+1n+1}^{(-1)}(K_1a, k_1a) - J_{n+1n+1}^{(1)}(K_1a, k_1a)) \\
& - \frac{(k_1^*a)^2}{(K_1a)^2} ((n+1)k_1^*a J_{nn}^{(1)}(K_1a, k_1a) - (n+2)K_1a J_{n+1n+1}^{(1)}(K_1a, k_1a)) \\
& \left. + \frac{1}{2} (K_n^{(1)}(k_1a, K_1a) + K_n^{(2)}(k_1a, K_1a)) \right]
\end{aligned}$$

$$\begin{aligned}
S_{8n} = & (n+2) \left[\frac{1}{2} (n(K_1^*a)^2 - (n+1)(k_1a)^2) (J_{n+1n}^{(0)}(K_1a, k_1a) - J_{n+1n}^{(2)}(K_1a, k_1a))^* \right. \\
& - k_1a K_1^*a (J_{nn+1}^{(0)}(K_1a, k_1a) - J_{nn+1}^{(2)}(K_1a, k_1a))^* + \frac{(k_1a)^2 K_1^*a}{2} (J_{nn}^{(-1)}(K_1a, k_1a) \\
& - J_{nn}^{(1)}(K_1a, k_1a))^* + \frac{k_1a(K_1a)^2}{2} (J_{n+1n+1}^{(-1)}(K_1a, k_1a) - J_{n+1n+1}^{(1)}(K_1a, k_1a))^* \\
& + \frac{(k_1a)^2}{(K_1a)^2} (nK_1a J_{nn}^{(1)}(K_1a, k_1a) - (n+1)k_1^*a J_{n+1n+1}^{(1)}(K_1a, k_1a))^* \\
& \left. - \frac{1}{2} (L_n^{(1)}(k_1a, K_1a) + L_n^{(2)}(k_1a, K_1a)) \right]
\end{aligned}$$

$$S_{9n} = \frac{k_1a k_1^*a}{(K_1a)^2} (k_1^*a j'_n(k_1a) j'_n(k_1^*a) + k_1a j'_{n+1}(k_1a) j'_{n+1}(k_1^*a))$$

Where

$$\begin{aligned}
H_{nm}^{(j)}(x_1, x_2) &= \int_1^\infty y^{-j} h_n^{(1)}(x_1 y) h_m^{(2)}(x_2^* y) dy \\
&= \sum_{k=0}^n \sum_{q=0}^m B_{kq} x_1^{-(k+1)} (x_2^*)^{-(q+1)} E_M(ix_2^* - ix_1)
\end{aligned}$$

$$\begin{aligned}
J_{nm}^{(j)}(x_1, x_2) &= \int_1^\infty y^{-j} h_n^{(1)}(x_1 y) j_m^{(2)}(x_2^* y) dy \\
&= \frac{1}{2} \sum_{k=0}^n \sum_{q=0}^m B_{kq} x_1^{-(k+1)} (x_2^*)^{-(q+1)} (E_M(ix_2^* - ix_1) \\
&\quad - (-1)^{m+q} (E_M(-ix_2^* - ix_1)))
\end{aligned}$$

in which $E_M(z)$ is the exponential integral of order M . The correction to Doinikov's J_{nm} is the change of $(-1)^{m+1}$ as listed in [22] to $(-1)^{m+q}$, as shown above.

$$B_{kq} = \frac{i^{m-n} (-1)^k (n+k)! (m+q)!}{(2i)^{k+q} k! (n-k)! q! (m-q)!}$$

$$M = 2 + k + q + j; \quad j = -1, 0, 1, 2$$

$$G_n^{(l)}(k_1 a) = k_1^* a (h_n^{(1)}(k_1 a))' h_n^{(l)}(k_1^* a)' + k_1 a (h_{n+1}^{(1)}(k_1 a))' (h_{n+1}^{(l)}(k_1^* a))'$$

$$L_n^{(l)}(k_1 a, K_1 a) = k_1 a (h_n^{(l)}(k_1 a))' h_n^{(2)}(K_1^* a)' - \frac{(n+1)(k_1 a)^2}{(K_1 a)^2} (h_{n+1}^{(l)}(k_1 a))' (h_{n+1}^{(2)}(K_1^* a))$$

$$K_n^{(l)}(k_1 a, K_1 a) = \frac{(n+1)(k_1^* a)^2}{(K_1 a)^2} (h_n^{(l)}(k_1^* a))' h_n^{(1)}(K_1 a) - k_1^* a (h_{n+1}^{(l)}(k_1^* a))' (h_{n+1}^{(1)}(K_1 a))'$$

$$l = 1, 2$$
$$(h_n^{(l)}(k_1 a))' = \frac{dh_n^{(l)}(k_1 a)}{d(k_1 a)}$$

Appendix C: Elastic Scattering from a Sphere: Matrix Equations

The matrix equation used to find the Δ coefficients is shown below, followed by Δ_0 and Δ_1 .

$$\left(\begin{array}{cc} \frac{-1}{2r} \left(\frac{K_1}{k_1} \right)^2 + \frac{[l(l+1)+2]}{k_1^2 r^3} - \frac{2\partial_r}{(k_1 r)^2} & \frac{\mu_2}{\mu_1} \left(\frac{1}{2r} \left(\frac{K_2}{k_2} \right)^2 - \frac{[l(l+1)+2]}{k_2^2 r^3} + \frac{2\partial_r}{(k_2 r)^2} \right) \\ -\frac{4}{k_1^2 r^3} + \frac{2\partial_r}{(k_1 r)^2} & \frac{\mu_2}{\mu_1} \left(\frac{4}{k_2^2 r^3} - \frac{2\partial_r}{(k_2 r)^2} \right) \\ -\frac{1}{(k_1 r)^2} (1 - r\partial_r) & \frac{1}{(k_2 r)^2} (1 - r\partial_r) \\ \frac{1}{(k_1 r)^2} & -\frac{1}{(k_2 r)^2} \end{array} \right)$$

$$\left(\begin{array}{cc} -\frac{l(l+1)}{K_1 r^2} \left(\partial_r - \frac{2}{r} \right) & \frac{\mu_2 l(l+1)}{\mu_1 K_2 r^2} \left(\partial_r - \frac{2}{r} \right) \\ -\frac{2l(l+1)}{K_1 r^3} + \frac{2\partial_r}{K_1 r^2} + \frac{K_1}{r} & \frac{\mu_2}{\mu_1} \left(\frac{2l(l+1)}{K_2 r^3} - \frac{2\partial_r}{K_2 r^2} - \frac{K_2}{r} \right) \\ -\frac{l(l+1)}{K_1 r^2} & \frac{l(l+1)}{K_2 r^2} \\ -\frac{\partial_r}{K_1 r} & \frac{\partial_r}{K_2 r} \end{array} \right) \begin{bmatrix} (r\pi_L^s) \\ (r\pi_L^t) \\ (r\pi_{SV}^s) \\ (r\pi_{SV}^t) \end{bmatrix} = - \begin{bmatrix} \frac{1}{2r} \left(\frac{K_1}{k_1} \right)^2 - \frac{[l(l+1)+2]}{k_1^2 r^3} + \frac{2\partial_r}{(k_1 r)^2} \\ \frac{4}{k_1^2 r^3} - \frac{2\partial_r}{(k_1 r)^2} \\ \frac{1}{(k_1 r)^2} (1 - r\partial_r) \\ \frac{1}{(k_1 r)^2} \end{bmatrix} (r\pi_L^i)$$

$$\begin{aligned}
\Delta_0 &= \left(\frac{\mu_2}{\mu_1} - 1\right)^2 [l(l+1) - 2] \left[\frac{k_2 a j'_l(k_2 a)}{j_l(k_2 a)} \frac{K_2 a \psi'_l(K_2 a)}{\psi_l(K_2 a)} - l(l+1) \right] \left[\frac{k_1 a h'_l(k_1 a)}{h_l(k_1 a)} \frac{K_1 a \zeta'_l(K_1 a)}{\zeta_l(K_1 a)} - l(l+1) \right] \\
&+ \frac{1}{2} (K_1 a)^2 \left(\frac{\mu_2}{\mu_1} - 1\right) \left\{ \left[\frac{k_2 a j'_l(k_2 a)}{j_l(k_2 a)} \frac{K_2 a \psi'_l(K_2 a)}{\psi_l(K_2 a)} - l(l+1) \right] \left[\frac{K_1 a \zeta'_l(K_1 a)}{\zeta_l(K_1 a)} + 2 \frac{k_1 a h'_l(k_1 a)}{h_l(k_1 a)} - 2l(l+1) \right] \right. \\
&\quad \left. - \frac{\rho_2}{\rho_1} \left[\frac{k_1 a h'_l(k_1 a)}{h_l(k_1 a)} \frac{K_1 a \zeta'_l(K_1 a)}{\zeta_l(K_1 a)} - l(l+1) \right] \left[\frac{K_2 a \psi'_l(K_2 a)}{\psi_l(K_2 a)} + 2 \frac{k_2 a j'_l(k_2 a)}{j_l(k_2 a)} - 2l(l+1) \right] \right\} \\
&+ \frac{1}{4} (K_1 a)^4 \left\{ l(l+1) \left[1 - \frac{\rho_2}{\rho_1} \right]^2 - \left[\frac{k_2 a j'_l(k_2 a)}{j_l(k_2 a)} - \frac{\rho_2}{\rho_1} \frac{k_1 a h'_l(k_1 a)}{h_l(k_1 a)} \right] \left[\frac{K_2 a \psi'_l(K_2 a)}{\psi_l(K_2 a)} - \frac{\rho_2}{\rho_1} \frac{K_1 a \zeta'_l(K_1 a)}{\zeta_l(K_1 a)} \right] \right\}
\end{aligned}$$

$$\begin{aligned}
\Delta_1^L &= \frac{j_l(k_1 a)}{h_l(k_1 a)} \left\{ \left(\frac{\mu_2}{\mu_1} - 1 \right)^2 [l(l+1) - 2] \left[\frac{k_2 a j_l'(k_2 a)}{j_l(k_2 a)} \frac{K_2 a \psi_l'(K_2 a)}{\psi_l(K_2 a)} - l(l+1) \right] \left[\frac{k_1 a j_l'(k_1 a)}{j_l(k_1 a)} \frac{K_1 a \zeta_l'(K_1 a)}{\zeta_l(K_1 a)} - l(l+1) \right] \right. \\
&+ \frac{1}{2} (K_1 a)^2 \left(\frac{\mu_2}{\mu_1} - 1 \right) \left\{ \left[\frac{k_2 a j_l'(k_2 a)}{j_l(k_2 a)} \frac{K_2 a \psi_l'(K_2 a)}{\psi_l(K_2 a)} - l(l+1) \right] \left[\frac{K_1 a \zeta_l'(K_1 a)}{\zeta_l(K_1 a)} + 2 \frac{k_1 a j_l'(k_1 a)}{j_l(k_1 a)} - 2l(l+1) \right] \right. \\
&\quad \left. \left. - \frac{\rho_2}{\rho_1} \left[\frac{k_1 a j_l'(k_1 a)}{j_l(k_1 a)} \frac{K_1 a \zeta_l'(K_1 a)}{\zeta_l(K_1 a)} - l(l+1) \right] \left[\frac{K_2 a \psi_l'(K_2 a)}{\psi_l(K_2 a)} + 2 \frac{k_2 a j_l'(k_2 a)}{j_l(k_2 a)} - 2l(l+1) \right] \right\} \right. \\
&+ \left. \frac{1}{4} (K_1 a)^4 \left\{ l(l+1) \left[1 - \frac{\rho_2}{\rho_1} \right]^2 - \left[\frac{k_2 a j_l'(k_2 a)}{j_l(k_2 a)} - \frac{\rho_2}{\rho_1} \frac{k_1 a j_l'(k_1 a)}{j_l(k_1 a)} \right] \left[\frac{K_2 a \psi_l'(K_2 a)}{\psi_l(K_2 a)} - \frac{\rho_2}{\rho_1} \frac{K_1 a \zeta_l'(K_1 a)}{\zeta_l(K_1 a)} \right] \right\} \right\}
\end{aligned}$$

Bibliography

- [1] Alexander Sedov and Lester W. Jr. Schmerr. The time domain elastodynamic Kirchhoff approximation for cracks: the inverse problem. Wave Motion, 8:15–26, 1986.
- [2] L.D. Landau and E.M. Lifshitz. Fluid Mechanics, volume 6. Pergamon Press, 1987.
- [3] A.A. Doinikov. Acoustic radiation pressure on a rigid sphere in a viscous fluid. Proceedings of the Royal Society of London, 447(1931):447–466, 1994.
- [4] A.A. Doinikov. Acoustic radiation force on a spherical particle in a viscous heat-conducting fluid. i. general formula. Journal of the Acoustical Society of America, 101(2):713–721, 1997.
- [5] Paul S. Epstein and Richard R. Carhart. The absorption of sound in suspensions and emulsions. Journal of the Acoustical Society of America, 25(3):553–565, 1953.
- [6] Wen H. Lin and A.C. Raptis. Thermoviscous effects on acoustic scattering by thermoelastic solid cylinders and spheres. Journal of the Acoustical Society of America, 74(5):1542–1554, 1983.
- [7] F.D. Murnaghan. Finite deformations of an elastic solids. American Journal of Mathematics, 59(2):235–260, 1937.
- [8] J.L. Rose. Ultrasonic Waves in Solid Media. Cambridge University Press, 1999.
- [9] H. Kolsky and L.S. Douch. Experimental studies in plastic wave propagation. Journal of the Mechanics and Physics of Solids, 10:195–223, 1962.
- [10] Karl F. Graff. Wave Motion in Elastic Solids. Dover, 1991.
- [11] V.V. Varadan, A. Lakhtakia, and V.K. Varadan. Field Representations and Introduction to Scattering. Elsevier Science Publishers B.V., New York, 1991.
- [12] R.D. Spence and Sara Granger. The scattering of sound from a prolate spheroid. Journal of the Acoustical Society of America, 23(6):701–706, 1951.
- [13] M. Abramowitz and I.A. Stegun. Handbook of Mathematical Functions. Dover, New York, ninth dover printing, tenth gpo printing edition, 1964.
- [14] C.M. Linton and P.A. Martin. Multiple scattering by random configurations of circular cylinders: Second-order corrections for the effective wavenumber. Journal of the Acoustical Society of America, 117(6):3413–3424, 2005.

- [15] Vijay K. Varadan, Vasundara V. Varadan, and Yih-Hsing Pao. Multiple scattering of elastic waves by cylinders of arbitrary cross section. 1. sh waves. Journal of the Acoustical Society of America, 63(5):1310–1320, 1977.
- [16] Rene Marklein. The Finite Integration Technique as a General Tool to Compute Acoustic, Electromagnetic, Elastodynamic, and Coupled Wave Fields, pages 201–244. IEEE Press and John Wiley and Sons, Piscataway and New York, 2002.
- [17] F. Schubert, A. Peiffer, B. Kohler, and T. Sanderson. The elastodynamic finite integration technique for waves in cylindrical geometries. Journal of the Acoustical Society of America, 104:2604–2614, 1998.
- [18] L.V. King. On the acoustic radiation pressure on spheres. Proceedings of the Royal Society of London, 147:212–240, 1934.
- [19] K. Yosioka and Y. Kawasima. Acoustic radiation pressure on a compressible sphere. Acustica, 5:167–173, 1955.
- [20] T. Hasegawa. Comparison of two solutions for acoustic radiation pressure on a sphere. Journal of the Acoustical Society of America, 61:1445–1448, 1977.
- [21] T. Hasegawa and K. Yosioka. Acoustic radiation force on a solid elastic sphere. Journal of the Acoustical Society of America, 46:1139–1143, 1969.
- [22] A.A. Doinikov. Acoustic radiation pressure on a compressible sphere in a viscous fluid. Journal of Fluid Mechanics, 267:1–21, 1994.
- [23] Andrei Dukhin and Philip Goetz. Bulk viscosity and compressibility measurement using acoustic spectroscopy. Journal of Chemical Physics, 130(12), 2009.
- [24] Robert G. Hohlfeld. Sonic debubbler for liquids. Technical report, U.S. Patent No. 5022899, June 11 1991.
- [25] T. Hasegawa, T. Kido, T. Iizuka, and C. Matsuoka. A general theory of rayleigh and langevin radiation pressures. Journal of the Acoustical Society of Japan, 21(3):145–152, 2000.
- [26] Max Born and Emily Wolf. Principles of Optics. Pergamon Press, New York, 6 edition, 1980.
- [27] John David Jackson. Classical Electrodynamics. John Wiley and Sons, New York, 3 edition, 1998.
- [28] Stanley J. Farlow. Partial Differential Equations for Scientists and Engineers. Dover, Mineola, NY, 1993.
- [29] T. Hasegawa and Y. Watanbe. Acoustic radiation pressure on an absorbing sphere. Journal of the Acoustical Society of America, 63:1733–1737, 1978.
- [30] V.S. Kalambur, Han Bumsoo, Bruce E. Hammer, Thomas W. Shield, and John C. Bischof. In vitro characterization of movement, heating and visualization of magnetic nanoparticles for biomedical applications. Nanotechnology, 16:1221–1233, 2005.

- [31] D.R. (Ed.) Lide. Handbook of Chemistry and Physics. CRC Press/Taylor and Francis, Boca Raton, FL, 89, internet edition edition, 2009.
- [32] Herbert Uberall (ed). Acoustic Resonance Scattering. Gordon and Breach Science Publishers, 1992.
- [33] Craig Bohren and Donald Huffman. Absorption and Scattering of Light by Small Particles. John Wiley and Sons, 1983.
- [34] David L. Heckmann and Steven L. Dvorak. Numerical computation of hankel functions of integer order for complex-values arguments. Radio Science, 36(6):1265–1270, 2001.
- [35] Liang-Wu Cai. On the computation of spherical Bessel functions of complex arguments. Computer Physics Communications, 2010.
- [36] K Shann, D Likosky, J Murkin, R Baker, Y Baribeau, G DeFoe, T Dickinson, T Gardner, H Grocott, G O'Connor, D Rosinski, F Sellke, and T Willcox. An evidence-based review of the practice of cardiopulmonary bypass in adults: A focus on neurologic injury, glycemic control, hemodilution, and the inflammatory response. Journal of Thoracic and Cardiovascular Surgery, 132(2):283–290, 2006.
- [37] RE Clark, J Brillman, DA Davis, MR Lovell, TR Price, and GJ Magovern. Microemboli during coronary artery bypass grafting. genesis and effect on outcome. Journal of Thoracic Cardiovascular Surgery, 109(2):249–257, 1995.
- [38] W Pugsley, L Klinger, C Pashalis, T Treasure, M Harrison, and S Newman. The impact of microemboli during cardiopulmonary bypass on neuropsychological functioning. Stroke, 25(7):1393–1399, 1994.
- [39] DA Stump, AT Rogers, JW Hammon, and SP Newman. Cerebral emboli and cognitive outcome after cardiac surgery. Journal of Cardiothoracic and Vascular Anesthesia, 10(1):113–119, 1996.
- [40] G Djaiani, L Fedorko, M Borger, R Green, J Carroll, M Marcon, and J Karski. Continuous-flow cell saver reduces cognitive decline in elderly patients after coronary bypass surgery. Circulation, 116(17):1888–1895, 2007.
- [41] Serdar Gunaydin. Air handling and cardiac surgery EDAC^(R) Quantifier introduces new concepts in solving an old problem. AmSect Today, Journal of ExtraCorporeal Technology, page 11, 2008.
- [42] D van Dijk, M Spoor, R Hijman, H.M. Nathoe, C. Borst, E.W. Jansen, D.E. Grobbee, P.P. de Jaegere, and C.J. Kakman. Cognitive and cardiac outcomes 5 years after off-pump vs on-pump coronary artery bypass graft surgery. Journal of the American Medical Association, 297(7):701–708, 2007.
- [43] MF Newman, JP Mathew, HP Grocott, GB Mackensen, T Monk, KA Welsh-Bohmer, JA Blumenthal, DT Laskowitz, and DB Mark. Central nervous system injury associated with cardiac surgery. Lancet, 368(9536):694–703, 2006.

- [44] M Barak and Y. Katz. Microbubbles: Pathophysiology and clinical implications. Chest, 128:2918–2932, 2005.
- [45] John Lynch, Alison Pouch, Randi Sanders, Mark Hinders, Kevin Rudd, and John Se-vick. Gaseous microemboli sizing in extracorporeal circuits using ultrasound backscatter. Ultrasound in Medicine and Biology, 33(10):1661–1675, 2007.
- [46] JE Lynch and JB Riley. Microemboli detection on extracorporeal bypass circuits. Perfusion, 23(1):23–32, 2008.
- [47] K Schwarz, C Church, P Serrino, and R Meltzer. The acoustic filter: An ultrasonic blood filter for the heart-lung machine. Cardiovascular Surgery, 104:1647–1653, 1992.
- [48] Tjeerd Romer, James Brennan, Maryann Fitzmaurice, Michael Feldstein, Geurt Deinum, Johnathan Myles, John Kramer, Robert Less, and Michael Feld. Histopathology of human coronary atherosclerosis by quantifying its chemical composition with Raman spectroscopy. Circulation, 97:878–885, 1998.
- [49] David Machin and Chris Allsager. Principles of cardiopulmonary bypass. Continuing Education in Anesthesia, Critical Care and Pain, 6(5):176–181, 2006.
- [50] A. Disalvo and S.A. Simon. Permeability and Stability of Lipid Bilayers. CRC Press, Boca Raton, FL, 1995.
- [51] Daniela Negrini, Anna Candiani, Federica Boshetti, Beatrice Cristafulli, Massimo Del Fabbro, Dario Bettinelli, and Giuseppe Miserocchi. Pulmonary microvascular and perivascular interstitial geometry during development of mild hydraulic edema. American Journal of Physiology - Lung Cellular and Molecular Physiology, pages L1464–L1471, 2001.
- [52] G. Emanuel. Bulk viscosity of a dilute polyatomic gas. Physics of Fluids A, 2:2252–2254, 1990.
- [53] Hwai-Shen Liu, Wu-Cheng Chiung, and Yu-Chi Wang. Effect of lard oil, olive oil, castor oil on oxygen transfer in an agitated fermenter. Biotechnology Techniques, 8(1):17–20, 1994.
- [54] R.E. Graves and B.M. Argrow. Bulk viscosity: past to present. Journal of Thermophysics and Heat Transfer, 13:337–342, 1999.
- [55] D.K. Kaul, M.E. Fabry, P. Windisch, S. Baez, and R.L. Nagel. Erythrocytes in sickle cell anemia are heterogeneous in their rheological and hemodynamic characteristics. Journal of Clinical Investigation, 72:22–31, 1983.
- [56] M. Sugihara-Seki and B.M. Fu. Blood flow and permeability in microvessels. Fluid Dynamics Research, 37(1/2):82–132, 2005.
- [57] Samuel Temkin. Elements of Acoustics. Wiley and Sons, 1981.
- [58] Lawrence Crum. Acoustic force on a liquid droplet in an acoustic stationary wave. Journal of the Acoustical Society of America, 50:157–163, 1971.

- [59] Ko Higashitani, Masahiro Fukushima, and Yoshizo Matsuno. Migration of suspended particles in plane stationary ultrasonic field. Chemical Engineering Science, 36(12):1877–1882, 1981.
- [60] Larisa Kuznetsova and W.T. Coakley. Microparticle concentration in short path length ultrasonic resonators: Roles of radiation pressure and acoustic streaming. Journal of the Acoustical Society of America, 116(4):1956–1965, 2004.
- [61] T. Hasegawa. Acoustic radiation force on a sphere in a quasistationary wave field-theory. Journal of the Acoustical Society of America, 65(1):32–40, 1979.
- [62] Rouke Bosma, Wim van Spronsen, Johannes Tramper, and René Wijffels. Ultrasound, a new separation technique to harvest microalgae. Journal of Applied Phycology, 15(2/3):14–153, March 2003.
- [63] Larisa Kuznetsova and W.T. Coakley. Applications of ultrasound streaming and radiation force in biosensors. Biosensors and Bioelectronics, 22:1567–1577, 2007.
- [64] Andreas Nilsson, Filip Petersson, Henrik Jonsson, and Thomas Laurell. Acoustic control of suspended particles in micro fluidic chips. Lab on a Chip, 4(2):131–135, 2004.
- [65] E.H. Trinh. Compact acoustic levitation device for studies in fluid dynamics and material science in the laboratory and microgravity. Review of Scientific Instruments, 56(11):2059–2065, 1985.
- [66] W.J. Xie, C.D. Cao, Y.J. Lu, and B. Wei. Levitation of iridium and liquid mercury by ultrasound. Physical review letters, 89(10):104304–1 – 104304–4, 2002.
- [67] Robert Gould, W.T. Coakley, and Martin Grundy. Upper sound pressure limits on particle concentration in fields of ultrasonic standing-wave at megahertz frequencies. Ultrasonics, 30(4):239–244, 1992.
- [68] Teruyuki Kozuka, Toru Tuziuti, and Hideto Mitome. Micromanipulation using a focused ultrasonic standing wave field. Electronics and Communications in Japan, Part 3, 83(1):1654–1659, 2000.
- [69] Muhammet Kursad Araz, Chung-Hoon Lee, and Amit Lal. Ultrasonic separation in microfluidic capillaries. IEEE Ultrasonics Symposium, pages 1066–1069, 2003.
- [70] Gregory Kaduchak, Greg Goddard, and et al. Ultrasonic analyte concentration and application in flow cytometry. US Patent 7,340,957, Mar. 11, 2008.
- [71] J.J. Hawkes and W.T. Coakley. A continuous flow ultrasonic cell-filtering method. Enzyme and Microbial Technology, 19:57–62, 1995.
- [72] Johannes Spengler and Martin Jekel. Ultrasound conditioning of suspensions - studies of streaming influence on particle aggregation on a lab- and pilot - plant scale. Ultrasonics, 38:624–628, 2000.

- [73] A. Kundt and O. Lehmann. Longitudinal vibrations and acoustic figures in cylindrical columns of liquids. Annalen der Physik and Chemie (Pogendorff's Annalen), 153:1, 1874.
- [74] K. Sollner and C. Bondy. The mechanism of coagulation by ultrasonic waves. Transactions of the Farady Society, 32:616–623, 1936.
- [75] Robert Gould and W.T. Coakley. The effects of acoustic forces on small particles in suspension. Finite-amplitude wave effects in fluids, Proceeds of the 1973 Symposium (Copenhagen), pages 252–257, 1974.
- [76] O. Doblhoff-Dier, Th. Gaida, H. Katinger, W. Burger, M. Groschl, and E. Benes. A novel ultrasonic resonance field device for the retention of animal cells. Biotechnology Progress, 10:428–432, 1994.
- [77] Martin Groschl. Ultrasonic separation of suspended particles - part I: Fundamentals. Acustica, 84:432–447, 1998.
- [78] Filip Petersson, Andreas Nilsson, Cecilia Holm, Henrik Jonsson, and Thomas Laurell. Continuous separation of lipid particles from erythrocytes by means of laminar flow and acoustic standing wave forces. Lab on a Chip, 5(1):20–22, 2005.
- [79] Zenon Mandralis and Donald Feke. Continuous suspension fractionation using acoustic and divided-flow fields. Chemical Engineering Science, 48(23):3897–3905, 1993.
- [80] Dwayne Johnson and Donald Feke. Methodology for fractionating suspended particles using ultrasonic standing wave and divided flow fields. Separations Technology, 5:251–258, 1995.
- [81] Filip Petersson, Andreas Nilsson, Cecilia Holm, Henrik Jonsson, and Thomas Laurell. Separation of lipids from blood utilizing ultrasonic standing waves in microfluidic channels. Analyst, 129(10):938–943, 2004.
- [82] Henrik Jonsson, Cecilia Holm, Andreas Nilsson, Filip Petersson, Per Jonsson, and Thomas Laurell. Particle separation using ultrasound can radically reduce embolic load to brain after cardiac surgery. The Annals of Thoracic Surgery, 78(5):1572–1577, November 2004.
- [83] J.J. Hawkes and W.T. Coakley. Force field particle filter, combining ultrasound standing waves and laminar flow. Sensors and Actuators B, 75(3):213–222, 2001.
- [84] E. Benes, M. Groschl, H. Nowotny, F. Trampler, T. Keijzer, H. Bohm, S. Radel, L. Gherardini, J.J. Hawkes, R. Konig, and Ch. Delouvroy. 2001 IEEE Ultrasonics Symposium. Proceedings. IEEE, Atlanta, GA USA, 2001.
- [85] Kenji Yasuda, Shin-ichiro Umemura, and Kazuo Takeda. Concentration and fractionation of small particles in liquid by ultrasound. Japanese Journal of Applied Physics, 34:2715–2720, May 1995.
- [86] Martin Groschl. Ultrasonic separation of suspended particles - part II: Design and operation of separation devices. Acustica, 84:632–642, 1998.

- [87] Greg Goddard and Gregory Kaduchak. Ultrasonic particle concentration in a line-driven cylindrical tube. Journal of the Acoustical Society of America, 2005.
- [88] Rebecca E. McIntosh. A biofuels consortium. Innovation, Dec 2009/Jan 2010.
- [89] RDDaily. Sound-wave technology strikes a chord with algal biofuels. accessed: 4 Aug 2010, September 2009.
- [90] W.T. Coakley, D.W. Bardsley, M.A. Grundy, F. Zamani, and D.J. Clarke. Cell manipulation in ultrasonic standing wave fields. Journal of Chemical Technology and Biotechnology, 44:43–62, 1988.
- [91] G. Whitworth, M.A. Grundy, and W.T. Coakley. Transport and harvesting of suspended particles using modulated ultrasound. Ultrasonics, 29(6):439–444, 1991.
- [92] A.A. Doinikov. Acoustic radiation interparticle forces in a compressible fluid. Journal of Fluid Mechanics, 444:1–21, 2001.
- [93] Johannes Spengler and Martin Jekel. Ultrasonic phase separation. In T.J. Mason and A. Tiehm, editors, Advances in Sonochemistry, Volume 6: Ultrasound in Environmental Protection, pages 181–220. JAI Press Inc, UK, 2001.
- [94] M. Saito, N. Kitamura, and M Terauchi. Ultrasonic manipulation of locomotive microorganisms and evaluation of their activity. Journal of Applied Physics, 92(12):7581–7586, 2002.
- [95] Felix Trampler, Stefan Sonderhoff, Phylis Pui, Douglas Kilburn, and James Piret. Acoustic cell filter for high density perfusion culture of hybridoma cells. Nature Biotechnology, 12:281–284, 1994.
- [96] Sonosep. Sonosep, BioSep. www.sonosep.com, 2005.
- [97] Johannes F. Spengler and W. Terence Coakley. Ultrasonic trap to monitor morphology and stability of developing microparticle aggregates. Langmuir, 19:3635–3642, 2003.
- [98] Stephen C. Peterson, Owen D. Brimhall, Thomas J. McLaughlin, Charles D. Baker, and Sam L. Sparks. Methods and apparatus for moving and separating materials exhibiting different physical properties. US Patent No. 4,983,189, Jan. 8, 1991.
- [99] Ramesh Varadaraj. Demulsification of water-in-oil emulsions. US Patent No. 6,716,358, Apr. 6, 2004.
- [100] N.D. Srinivas, R.S. Barhate, K.S.M.S Raghavarao, and Paul Todd. Acoustic field assisted enhanced demixing of aqueous two-phase systems. Biochimica et Biophysica, 1524:38–44, 2000.
- [101] Martyn Hill and Robert Wood. Modelling in the design of a flow-through ultrasonic separator. Ultrasonics, 38:662–665, 2000.

- [102] Phylis W.S. Pui, Felix Trampler, Stefan Sonderhoff, Martin Groeschl, Douglas Kilburn, and James Piret. Batch and semicontinuous aggregation and sedimentation of hybridoma cells by acoustic resonance fields. Biotechnology Progress, 11:146–152, 1995.
- [103] N Riley. Acoustic streaming. Theoretical and Computational Fluid Dynamics, 10:349–356, 1998.
- [104] Larisa Kuznetsova and W.T. Coakley. Applications of ultrasound streaming and radiation force in biosensors. Biosensors and Bioelectronics, 22:1567–1577, 2007.
- [105] Wesley Nyborg. Acoustic streaming near a boundary. Journal of the Acoustical Society of America, 30(4):329–339, 1958.
- [106] Hideto Mitome. The mechanism of generation of acoustic streaming. Electronics and Communications in Japan, 81(10):1–8, 1997.
- [107] James Lighthill. Waves in Fluids. Cambridge University Press, 1978.
- [108] Jad Mouawad. Big rise seen in demand for energy. The New York Times, July 19 2007.
- [109] Michael Grunwald. The clean energy scam. Time, March 27 2008.
- [110] Timothy Searchinger, Ralph Heimlich, R.A. Houghton, Fengxia Dong, Amani Elobeid, Jacinto Fabiosa, Simla Tokgoz, Dermot Hayes, and Tun-Hsiang Yu. Use of U.S. croplands for biofuels increases greenhouse gases through emissions from land-use change. Science, 319(5867):1238–1240, 2008.
- [111] Sukhvinder S. Phull and Timothy J. Mason. Advances in Sonochemistry, volume 5, chapter Use of Ultrasound in Microbiology. JAI Press, 1999.
- [112] Yusuf Chisti. Biodiesel from microalgae. Biotechnology Advances, 25:294–306, 2007.
- [113] Peer Schenk, Skye Thomas-Hall, E Stephens, UC Marx, JH Mussgnug, C Posten, O Kruse, and B Hankamer. Second generation biofuels: High efficiency microalgae for biodiesel production. Bioenergy Research, 1(1):20–43, 2008.
- [114] AS Carlsson, J B van Beilen, R Moller, D Clayton, and D Ed. Bowles. Micro- and Marco-algae Utility for Industrial Applications. CPL Press, UK, 2007.
- [115] Stephanie Joyce. The dead zones: Oxygen-starved coastal waters. Environmental Health Perspectives, 108(3):A120–A125, 2000.
- [116] Robert Diaz and Rutger Rosenber. Spreading dead zones and consequences for marine ecosystems. Science, 321:926–929, August 15 2008.
- [117] Josphe McClain. ChAP: Biofuel from aquatic algae. <http://www.wm.edu/research/ideation/science-and-technology/algae-biofuel-two-007.php>, accessed: Feb 15 2011.

- [118] Y Zhang, FX Fu, E Whereat, K Coyne, and D Huthcins. Bottom-up controls on a mid-species hab assemblage: A comparison of sympatric *chattonella subsalsa* and *heterosigma akashiwo* isolates from the delaware inlang bays, usa. Harmful Algae, 5:310–320, 2006.
- [119] Maria F. Montero, Manuela Aristizabal, and Ghillermo Garcia Reina. Isolation of high-lipid content strains of the marine microagla *tetraselmis suecica* for biodiesel production by flow cytometry and single-cell sorting. Journal of Applied Phycology, 2010.
- [120] Laura Barsanti and Paolo Gualtieri. Algae Anatomy, Biochemistry, and Biotechnology. CRC Press, 1 edition, 2005.
- [121] Glenn Elert. Physics factbook: Density of seawater. <http://hypertextbook.com/facts/2002/EdwardLaValley.shtml>, accessed: March 1, 2010.
- [122] A.G. Avetisyan, V.S. Arakelyan, O.V. Bagdasaryan, and A.K. Dudoyan. On heavy particle behaviour in viscous liquid in a standing ultrasonic wave field. Akusticheskii Z, 31:385–386, 1985.
- [123] Kane Yee. Numerical solution of inital boundary value problems involving maxwell’s equations in isotropic media. IEEE transactions on antennas and propagation, 14(3):302, 1966.
- [124] Shuozhong Wang. Finite-difference time-domain approach to underwater acoustic scattering problems. Journal of the Acoustical Society of America, 99(4):1924–1931, 1996.
- [125] A. Peiffer and B. Kohler. The acoustic finite integration technique for waves of cylindrical symmetry (cafit). Journal of the Acoustical Society of America, 102(2):697–706, 1997.
- [126] Kevin Rudd. Parallel 3D Acoustic and Elastic Wave Simulation Methods with Applications in Nondestructive Evaluation. PhD thesis, College of William and Mary, June 2007.
- [127] Joe D. Hoffman. Numerical Methods for Engineers and Scientists. Marcel Dekker, New York, 2 edition, 2001.
- [128] Kevin Rudd and Mark Hinders. Simulation of incident nonlinear sound beam and 3d scattering from complex targets. Journal of Computational Acoustics, 16(3):427–445, 2008.
- [129] Suhas V. Patankar. Numerical Heat Transfer and Fluid Flow, chapter 6. Hemisphere Publishing Corporation, 1980.
- [130] Frank Schubert, Alexander Peiffer, and Bernd Kohler. The elastodynamic finite integration technique for waves in cylindrical geometries. Journal of the Acoustical Society of America, 104(5):2604–2614, 1998.

- [131] Jill Bingham and Mark Hinders. Lamb wave characterization of corrosion-thinning in aircraft stringers: Experiment and three-dimensional simulation. Journal of the Acoustical Society of America, 126(1):103–113, July 2009.
- [132] Anjani Achanta, Mark McKenna, Joseph Heyman, Kevin Rudd, and Mark Hinders. Non-linear acoustic concealed weapons detection. Proceeding of the 34th applied imagery and pattern recognition workshop, 2005.
- [133] H.M. Hertz. Standing-wave acoustic trap for nonintrusive positioning of microparticles. Journal of Applied Physics, 78(8):4845–4849, 1995.
- [134] M. Wiklund, S. Nilsson, and H.M. Hertz. Ultrasonic trapping in capillaries for trace-amount biomedical analysis. Journal of Applied Physics, 90(1):421–426, 2001.
- [135] Martyn Hill, Rosemary Townsend, and Nicholas Harris. Modelling for the robust design of layered resonators for ultrasonic particle manipulation. Ultrasonics, 48:521–528, 2008.
- [136] Kevin Leonard and Mark Hinders. Lamb wave tomography of pipe-like structures. Ultrasonics, 43:574–583, 2005.
- [137] Eugene Malyarenko and Mark Hinders. Fan beam and double crosshole lamb wave tomography for mapping flaws in aging aircraft structures. Journal of the Acoustical Society of America, 108(4):1631–1639, 2000.
- [138] Jill Bingham and Mark Hinders. Lamb wave characterization of corrosion-thinning in aircraft stringers: Experiment and three-dimensional simulation. Journal of the Acoustical Society of America, 126(1):103–113, 2009.
- [139] T Weiland. A discretization method for the solution of maxwell’s equations for six-component fields. Electronic Communications (AEU), 31(3):116–120, 1977.
- [140] P. Fellingner. A Method for the Numerical Solution of Elastic Wave Propagation Problems in the Time Domain by Direct Discretization of Elastodynamic Governing Equations. PhD thesis, University of Kassel, Germany, 1991.
- [141] Frank Schubert, Bernd Koehler, and Pavel Zinin. Numerical time-domain simulation of wave propagation and scattering in acoustic microscopy for subsurface defect characterization. Proceedings of SPIE, 5766(106):106–117, 2005.
- [142] K. Nakahata, S. Hirose, F. Schubert, and B. Kohler. Image based efit simulation for nondestructive ultrasonic testing of austenitic steel. Journal of Solid Mechanics and Materials Engineering, 3(12):1256–1262, 2009.
- [143] D. Algernon, B. Grafe, F. Mielentz, B. Kohler, and F. Schubert. Imaging of the elastic wave propagation in concrete using scanning techniques: application for impact-echo and ultrasonic echo methods. Journal of Nondestructive Evaluation, 27:83–97, 2008.
- [144] R. Marklein. Efit simulations for ultrasonic NDE. In Proceedings of the 8th ECNDT 2002 Conference, 2002.

- [145] Rene Marklein, Prashanth Kumar Chinta, Hartmut Hintze, and Weddo Plankert. Numerical modelling of ultrasonic ndt of a wheel shaft of and ICE train. European Conference on Nondestructive Testing Proceedings, 2006.
- [146] Kevin Rudd, Kevin Leonard, Jill Bingham, and Mark Hinders. Simulation of guided waves in complex piping geometries using the elastodynamic finite integration technique. Journal of the Acoustical Society of America, 121(3):1449–1458, 2007.
- [147] D.C. Calvo, Rudd. K.E., M. Zampolli, Sanders. W.M., and L.D. Bibee. Simulation of acoustic scattering from an aluminum cylinder near a rough. Wave Motion, doi:10.1016/j.wavemoti.2010.05.002, 2010.
- [148] Lester W. Schmerr Jr. Fundamentals of Ultrasonic Nondestructive Evaluation. Plenum Press, 1998.
- [149] M.K. Hinders. Extinction of sound by spherical scatterers in a viscous fluid. Physical Review A, 43(10):5628–5636, 1991.
- [150] P. Fellingner, R. Marklein, K.J. Langenberg, and S. Klaholz. Numerical modeling of elastic wave propagation and scattering with efite - elastodynamic finite integration technique. Wave Motion, 21:47–66, 1995.
- [151] Jill Bingham. Ultrasonic guided wave interpretation for structural health inspections. PhD thesis, College of William and Mary, 2008.
- [152] Jill Bingham and Mark Hinders. 3d elastodynamic finite integration technique simulation of guided waves in extended built-up structures containing flaws. Journal of Computational Acoustics, 18(2):1–28, 2010.
- [153] F. Fellingner and K.J. Langenberg. Numerical techniques for elastic wave propagation and scattering. Elastic waves and ultrasonic nondestructive evaluation: Proceedings of IUTAM Symposium on Elastic Wave Propagation and Ultrasonic Evaluation, pages 81–86, July-Aug 1990.
- [154] K.E. Rudd, K.R. Leonard, J.P. Bingham, and M.K. Hinders. Simulation of guided waves in complex piping geometries using the elastodynamic finite integration technique. Journal of the Acoustical Society of America, 121:1449–1458, 2007.
- [155] M.K. Hinders. Plane-elastic wave scattering from an elastic sphere. Nuovo Cimento, 106B(7):799–818, 1991.
- [156] D. Brill and G. Guanaur. Resonance theory of elastic waves ultrasonically scattered from an elastic sphere. Journal of the Acoustical Society of America, 81(1):1–21, 1986.
- [157] Steven W. Smith. Digital Signal Processing: A Practical Guide for Engineers and Scientists. Newnes, 2003.
- [158] C.F. Ying and R. Truell. Scattering of a plane longitudinal wave by a spherical obstacle in an isotropically elastic solid. Journal of Applied Physics, 27:1086–1097, 1956.

- [159] Jill Bingham and Mark Hinders. 3d elastodynamic finite integration technique simulation of guided waves in extended built-up structures containing flaws. Journal of Computational Acoustics, 18(2):165–192, 2010.
- [160] US Geological Survey. Earth quake glossary, accessed: Sept. 28 2010.
- [161] Eugene Malyarenko and Mark Hinders. Ultrasonic lamb wave diffraction tomography. Ultrasonics, 39:269–281, 2001.
- [162] R.R. Whymark. Acoustic field positioning for containerless processing. Ultrasonics, 13(6):251–261, 1975.
- [163] Jeremy J Hawkes, Joseph J Cefai, David A Barrow, W Terence Coakley, and L Greg Briarty. Ultrasonic manipulation of particles in microgravity. Journal of Physics D: Applied Physics, 31:1673–1680, 1998.
- [164] F. Priego-Capote and Luque de Castro. Ultrasound-assisted levitation: Lab-on-a-drop. Trends in Analytical Chemistry, 25(9), 2006.
- [165] M.F. Culpin. The viscosity of liquid indium and liquid tin. Proceedings of the Physical Society B, 70:1069–1078, 1957.
- [166] UK Trade and Investment. Space "drum" uses sound for ultra-pure experiments. <http://www.ukti.gov.uk/uktihome/localisation/104442.html>, accessed: Dec 6 2010.
- [167] NASA. Space dynamically responding ultrasonic matrix system (space-drums). http://www.nasa.gov/mission_pages/station/research/experiments/SpaceDRUMS.html, accessed: Dec 6 2010.
- [168] D'Arcy J Hart, Ron Davidson, Meaghan Miron, and Jacques Y. Guigne. High temperature advanced materials development on the international space station. 55th International Astronautical Congress, pages 1–9, 2004.
- [169] Ruth Marlaire. Nasa develops algae bioreactor as a sustainable energy source. <http://www.nasa.gov/centers/ames/news/releases/2009/09-147AR.html>, accessed: Dec 9 2010.
- [170] E. Domany, J.A. Krumhansl, and S. Teitel. Quasistatic approximation to the scattering of elastic waves by a circular crack. Journal of Applied Physics, 45(5):2599–2604, 1978.
- [171] D.A. Mendelsohn, J.D. Achenbach, and L.M. Keer. Scattering of elastic waves by a surface-breaking crack. Wave Motion, 2:277–292, 1980.
- [172] David W. Eaton. Backscattering from spherical elastic inclusions and accuracy of the kirchhoff approximation for curved interfaces. Geophysical Journal International, 166:1249–1258, 2006.
- [173] NASA Ceramics Branch. http://www.grc.nasa.gov/WWW/StructuresMaterials/Ceramics/research_structural.html, accessed: Dec 9 2010.

- [174] Frank Schubert and Bernd Koehler. Numerical time-domain simulation of diffusive ultrasound in concrete. Ultrasonics, 42:781–786, 2004.
- [175] Fengqiu Tang, Hiroshi Fudouzi, Tetsuo Uchikoshi, and Yoshio Sakka. Preparation of porous materials with controlled pore size and porosity. Journal of the European Ceramic Society, 24:341–344, 2004.
- [176] R. Marklein, R. Barmann, and K.J. Langenberg. The ultrasonic modeling code EFIT as applied to inhomogeneous dissipative isotropic and anisotropic media. Review of progress in quantitative nondestructive evaluation, 14:251–258, 1995.
- [177] E. Hrcir and J. Rosina. Surface tension of blood. Physiological Research, 46(4):319–321, 1997.
- [178] Leopoldo Rodriguez and Donald Leeber. Normal range of blood surface tension of men. DTIC, School of Aerospace Medicine Brooks AFB, Sep 1970.